PROPULSION AND STEERING OF ARTIFICIAL

FLAGELLATED MICRO-SWIMMERS

LIU JINAN

PhD

The Hong Kong Polytechnic University

2024

The Hong Kong Polytechnic University

Department of Mechanical Engineering

Propulsion and Steering of Artificial Flagellated Micro-swimmers

Liu Jinan

A thesis submitted in partial fulfilment of the requirements for the degree of Doctor of Philosophy

Mar 2024

CERTIFICATE OF ORIGINALITY

I hereby declare that this thesis is my own work and that, to the best of my knowledge and belief, it reproduces no material previously published or written, nor material that has been accepted for the award of any other degree or diploma, except where due acknowledgement has been made in the text.

_____ (Signed)

_____Liu Jinan_____ (Name of student)

Abstract

This thesis achieves a quantitative model of artificial flagellated micro-swimmers (AFMSs) to predict the motility and steerability of an acoustically actuated AFMS. We first summarized the historical achievements and theoretical perspectives on microorganisms and their propulsion mechanisms, then reviewed the progress in actuation strategies of AFMSs, and finally focused on a simple sperm-like micro-swimmer geometry, composed of an ellipsoidal head and a flagellum (tail) with the length of hundreds of micrometers. We argue that these AFMSs can swim by inducing head oscillations that beat the flagellum to achieve wavy motion and thus the propulsion in a low Reynolds number (LRN) Newtonian fluid environment.

We provided the quantitative relation between head oscillation amplitude and acoustic pressure and frequency, and the theoretical account of how the flagellum is whipped, bringing about propulsion. The one-dimensional (1D) equations of motion (EOM) for a flagellum, treated as an Euler-Bernoulli viscoelastic beam, were then derived based on the resistive force theory (RFT) and solved by using the Galerkin method. In order to make our theoretical model applicable for designing the AFMS, we have involved the inertia term and material damping in the 1D EOM and considered the tapered cross-section of a flagellum. The numerical results reveal that the micro-swimmer actuated by ultrasound can achieve a perceptible velocity, especially at resonance. Influences of nondimensional parameters, such as the resonance index, sperm number, and material damping coefficient, were discussed and a comparison with reported experimental results demonstrates the validity of the proposed 1D model.

To deal with the steerability of micro-swimmers under magneto-acoustic actuation with significant non-linearity in EOM, we proposed a bar-joint model based on the

corrected resistive force theory (CRFT) for studying AFMSs propelled in a 2D acoustic field or with a rectangular cross-section. Note that the classical RFT for 3D cylindrical flagellum leads to over 90% deviation in terminal velocities from those of 2D fluid-structure interaction (FSI) simulations, while the proposed CRFT bar-joint model can reduce the deviation to below 5%; hence, it enables a reliable prediction of the 2D locomotion of an acoustically actuated AFMS with a rectangular cross-section, which is the case in many experiments. Introduced in the CRFT is a single correction factor K determined by comparing the linear terminal velocities under acoustic actuation obtained from the CRFT with those from simulations. After the determination of K, detailed comparisons of trajectories between the CRFT-based bar-joint AFMS model and the FSI simulation were presented, exhibiting excellent consistency. Finally, a numerical demonstration of the purely acoustic or magneto-acoustic steering of an AFMS based on the CRFT was presented, which can be one of the choices for future AFMS-based precision therapy.

Experimentally, AFMSs can be manufactured based on digital light processing (DLP) of UV-curable resins. We first determined the viscoelastic properties of a UV-cured resin through dynamic mechanical analysis (DMA). The high-frequency storage moduli and loss factors were obtained based on the assumption of time-temperature superposition (TTS), which were then applied in theoretical calculations. Though the extrapolation based on the TTS implied the uncertainty of high-frequency material response and there is limited accuracy in determining head oscillation amplitude, the differences between the measured terminal velocities of the AFMSs and the predicted ones are less than 50%, which, to us, is well acceptable. These results indicate that the motions of acoustic AFMS can be predicted, and thus, designed, which pave the way for their long-awaited applications in targeted therapy.

Publications arising from the thesis

Published papers:

[1]. **Jinan Liu,** and Haihui Ruan. "Modeling of an acoustically actuated artificial micro-swimmer." *Bioinspiration & Biomimetics* 15, no. 3 (2020): 036002.

[2]. **Jinan Liu,** Yiqiang Fu, Xiongjun Liu, and Haihui Ruan. "Theoretical perspectives on natural and artificial micro-swimmers." *Acta Mechanica Solida Sinica* (2021): 1-27.

[3]. **Jinan Liu,** Yiqiang Fu, Xiongjun Liu, and Haihui Ruan. "A bar-joint model based on the corrected resistive force theory for artificial flagellated micro-swimmers propelled by acoustic waves." *Bioinspiration & Biomimetics* 18, no. 3 (2023): 035003.

Submitted paper:

[1]. **Jinan Liu,** Yiqiang Fu, Yifei Wu, Haihui Ruan. "Propulsion mechanism of artificial flagellated micro-swimmers actuated by acoustic waves – theory and experimental verification." *Lab on a Chip*. (2024)

Acknowledgments

I would like to thank my thesis supervisor Dr. Haihui RUAN, the associate professor of Department of Mechanical Engineering, the Hong Kong Polytechnic University, for his patient guidance, kind suggestions, and great support to my PhD thesis. His consistent enthusiasm for science and positive mindset profoundly influenced me.

I would also like to acknowledge Mr. Suo Zhang, Dr. Jianbiao Wang, Dr. Xu Wang and Dr. Chen Lin, who are my colleagues, and are helpful for me because of their constructive suggestions on my reach work and academic career. I would also like to thank my group members Dr. Awais Akhtar, Dr. Yiqiang Fu, Mr. Yi Yang, Mr. Yifei Wu, Mr. Wei Wang, Mr. Yuzhou Zhang, Ms. Junju Xu, and all the other group members. I am extremely grateful to them.

My deepest gratitude to The Hong Kong Polytechnic University and NSFC/RGC Joint Research Scheme (Project number: N_PolyU519/19) for the funding and support received throughout the four years of my PhD studies in Hong Kong. Lastly and most importantly, I am really grateful to my parents for their ceaseless support on my whole student life. Thanks a million.

Table of contents

List of figures

List of tables

Nomenclature

A	surface area of the micro-swimmer regards the acoustic radiation force
A_s	area of the cross-section of the flagellum
$\mathbf{A}$	resistive matrices of bars in the bar-joint model
$\mathbf{A}_0$	resistive matrices of the head in the bar-joint model
$\mathbf{A}_{\text{acou}}$	acoustic displacement field
A_{acou}	amplitude of the fluid particle in the acoustic displacement field
$\mathbf{a}_i$	transformed matrix of local coefficients of resistive forces of the ith bar
$\mathbf{B}$	matrix of kinematic constraints in the bar-joint model
$\mathbf{B_0}$	matrix of kinematic constraints between the first bar and head
$\mathbf{b}$	external magnetic field
$b_1/\, b_2/\, b_3$	three non-zero constants to derive the conventional RFT
$\mathbf{C}$	resistive tensor between the relative fluid velocity and Stokeslets
$\mathbf{C}_i$	tensor of resistive coefficients for the ith bar in the bar-joint model
C_1	the first constant in the WLF equation
C_2	the second constant in the WLF equation
c_0	sound velocity in the fluid
$c_\parallel$	tangential coefficient of resistive force
$c_\perp$	normal coefficient of resistive force
c_H	translational coefficient of resistance of the head
c_{HR}	rotational coefficient of resistance of the head
$\overline{c}$	relative resistance between the head and the flagellum in the 1D model
$\tilde{c}$	non-dimensional coefficients of resistive forces
$\tilde{c}_H$	non-dimensional translational coefficient of resistance of the head
$\tilde{c}_{HR}$	non-dimensional rotational coefficient of resistance of the head

D	matrix of moment balance related to the bars in the bar-joint model
$\mathbf{D}_0$	matrix of moment balance related to the head in the bar-joint model
$\mathbf{D}_{0i}$	vector of the ith component of $\mathbf{D}_{0i}$ in the bar-joint model
D	distance between two ends of a droplet-like or sphero-cylinder head
d_s	diameter of a flagellum with a circular cross-section
E	storage Young's modulus in the viscoelastic material
E_{effi}	actuation efficiency in the 1D model
$\tilde{E}$	non-dimensional storage Young's modulus in the viscoelastic material
$\mathbf{e}_1/\ \mathbf{e}_2/\ \mathbf{e}_3$	three unit vectors along three axes
$\mathbf{F}_0$	vector of the external actuation in the bar-joint model
$\mathbf{F}_E$	vector of internal torques in the bar-joint model
$\boldsymbol{F}_f$	vector of fluid forces in Stokes flow
$\mathbf{F}_{\mathrm{flu}0}$	vector of total fluid forces on the head in the bar-joint model
$\mathbf{F}_{\mathrm{flu}i}$	vector of total fluid forces of the ith bar in the bar-joint model
$\mathbf{F}_m$	magnetic forces
$F_{f\parallel}$	tangential component of fluid forces in Stokes flow
$F_{f\perp}$	normal component of the forces in Stokes flow
F_A	acoustic radiation force
F_a	amplitude of the external oscillating force
F_{Ei}	the ith component of $\mathbf{F}_E$ in the bar-joint model
$F_{\mathrm{ext}x}$	horizontal force arising from external actuation
$F_{\mathrm{ext}y}$	vertical force arising from external actuation
F_{head}	fluid force of the spherical head in the 1D model
$\overline{F}_{\mathrm{prop}}$	time-averaged propulsive force in Wiggins' theory
$\tilde{F}$	non-dimensional forces in the bar-joint model
$\mathbf{f}_f$	vector of local fluid forces on the flagellum

$\mathbf{f}_{\mathrm{flu}i}$	vector of local fluid forces on the ith bar in the bar-joint model
f	actuation frequency of the acoustic field
f_0	resonant frequency of the gas bubble for a bubble-based micro-swimmer
$f_{f\parallel}$	tangential component of local fluid forces on the flagellum
$f_{f\perp}$	normal component of local fluid forces on the flagellum
f_e	normal elastic force in Wiggins' theory
f_n	the nth natural frequency of a cantilever beam in the 1D model
f_{prop}	local propulsive force in the 1D model
f_{tran}	local transverse force in the 1D model
$\mathbf{G}$	Green's function to Stokes flow
G	physical property representing E and γ in the principle of TTS
G_n	the nth coefficient to analytically solve linear partial differential equation
H	non-dimensional inertial term in the 1D model
h	tapering equation of the flagellum
$\mathbf{I}$	identity tensor
$\mathbf{I}_a$	augmented identity matrix
I	second moment of area of the flagellum
I_{acou}	acoustic filed intensity
I_i	second moment of area of the ith bar in the bar-joint model
$\tilde{I}$	non-dimensional second moment of area in the bar-joint model
J	non-dimensional second moment of area in the 1D model
$\mathbf{K}$	correction tensor of the resistive force theory in the CRFT model
K	correction factor of the resistive force theory in the CRFT model
K_u	coefficients of proportionality for translation in the head simulation
K_θ	coefficients of proportionality for rotation in the head simulation
L	total length of the flagellum of the micro-swimmer

L_0	length of a liquid column outside the bubble-based micro-swimmer
L_B	bubble length for a bubble-based micro-swimmer
l	half-length of each bar in the bar-joint model
M	bending moment of the flagellum in the 1D model
M_i	moment induced by the torsion spring at the ith joint in the bar-joint model
$\mathbf{m}$	magnetization of the head
N	total number of bars in the bar-joint model
$\mathbf{n}$	normal unit vector of a micro-swimmer regards the acoustic radiation force
n_m	number of modal superpositions based on the Galerkin method
$\mathbf{P}$	coordinates along the body centerline in Stokes flow
$\mathbf{P}_0$	vector of coordinates of the head center in the bar-joint model
$\mathbf{P}_i$	vector of coordinates of the centerline of the ith bar in the bar-joint model
$\mathbf{P}_{s\delta}$	distance vector (from the arclength s to $s + \delta$) in Stokes flow
P_B	initial pressure inside the bubble for a bubble-based micro-swimmer
p	amplitude of the acoustic pressure
p_f	fluid pressure in Stokes flow
Q_n	the nth coefficient of the steady-state solution based on the Galerkin method
q_n	the nth generalized coordinates based on the Galerkin method
Re	Reynolds number
R_H	equivalent head radius of the micro-swimmer
$\tilde{R}_H$	non-dimensional equivalent head radius of the micro-swimmer
r_1	radius of the large end of a droplet-like or sphero-cylinder head
r_2	radius of the small end of a droplet-like or sphero-cylinder head
r_n	the nth root of the characteristic equation based on the Galerkin method
$r_{\text{PDE}n}$	the nth root to analytically solve linear partial differential equation
r_s	radius of a flagellum with a circular cross-section
$\mathbf{S}$	distribution of Stokeslets in Stokes flow

$S_{\parallel}$	tangential component of Stokeslets in Stokes flow
$S_{\perp}$	normal component of Stokeslets in Stokes flow
S_n	the nth integral parameter based on the Galerkin method
S_p	sperm number
s	arclength along the centerline of the flagellum
$\tilde{s}$	non-dimensional arclength along the centerline of the flagellum
$\mathbf{T}_{Ri}$	transformation matrix of rotation of the ith bar in the bar-joint model
$\mathbf{T}_{V}$	matrix of kinematic constraints of neighboring bars in the bar-joint model
$\mathbf{T}_{Vi}$	transformation matrix of local velocity of the ith bar in the bar-joint model
T	temperature in the WLF equation
T_0	reference temperature in the WLF equation
T_{σ}	kinetic energy of the flagellum in the 1D model
t	time
$\tilde{t}$	non-dimensional time
$\mathbf{U}$	relative fluid velocity field with respect to the slender body in Stokes flow
U	characteristic velocity in the expression of the Reynolds number
U_{σ}	strain energy of the flagellum in the 1D model
$\mathbf{u}$	velocity field of the fluid
$\mathbf{u}_i$	local velocity field of the fluid on the ith bar in the bar-joint model
$u_{\parallel}$	tangential component of the velocity field of the fluid
$u_{\perp}$	normal component of the velocity field of the fluid
u_{ix}	horizontal component of the local velocity field of the fluid on the ith bar
u_{iy}	vertical component of the local velocity field of the fluid on the ith bar
$\tilde{u}$	non-dimensional fluid velocities in the bar-joint model
$\mathbf{V}$	vector of the translational velocities of the flagellum
$\mathbf{V}_i$	vector of the translational velocities of the ith bar in the bar-joint model

y_{cr}	relative lateral displacement of the flagellum centerline in the 1D model
y_{0a}	amplitude of translational displacement of the wiggly head
y_i	ordinate of the midpoint of the ith bar in the bar-joint model
y_s	vertical component of the flagellum displacement field in the 1D model
$\hat{\mathbf{y}}$	unit vector normal to the flagellum
Z	non-dimensional drag term in the 1D model
α	flagellum slenderness
α_T	shift factor in the WLF equation
β	non-dimensional parameter of flagellum's hydrodynamics in CRFT model
Γ	Euler's constant
γ	ratio of loss to storage modulus in the viscoelastic material (loss factor)
δ	variable of integration in the expression of Stokeslets
$\boldsymbol{\varepsilon}$	Cauchy strain tensor of the flagellum in the 1D model
ε	the longitudinal normal strain of the flagellum
η	viscosity coefficient of material damping in the viscoelastic material
$\tilde{\eta}$	non-dimensional viscosity coefficient of material damping
Θ	slope angle of the flagellum in the 1D model
θ_0	angle of rotation of the head
θ_{0a}	amplitude of the rotational angle of the wiggly head
θ_i	angle of rotation of the ith bar in the bar-joint model
$\boldsymbol{\kappa}$	functional of slenderness
κ	the halfwidth of a flagellum with unit length (the half of slenderness)
κ_B	frequency-dependent parameter for a bubble-based micro-swimmer
κ_e	curvature of the flagellum in Wiggins' theory
Λ	power of tapering of the flagellum
λ	tapering index of the flagellum
μ	dynamic viscosity of the fluid

Ξ	shear elastic force of the flagellum in the 1D model
ξ_c	non-dimensional lateral displacement of flagellum centerline in 1D model
ξ_{cr}	non-dimensional relative lateral displacement of 1D flagellum centerline
ξ_{0a}	non-dimensional amplitude of translational displacement of the wiggly head
Π	dimensionless product in the Buckingham π theorem
ρ_0	fluid density
ρ_1	the first order of fluid density regards the acoustic radiation force
ρ_s	density of flagellum
σ	the longitudinal normal stress of the flagellum
$\boldsymbol{\sigma}_2$	fluid stress tensor due to the microstreaming regards acoustic radiation force
$\boldsymbol{\tau}_m$	magnetic torques
τ_{ext}	torques about origin arising from external actuation
$\tilde{\tau}$	non-dimensional torques
Φ_n	the nth vibration mode of a cantilever beam based on the Galerkin method
φ_i	incident angle of the sound wave
φ_h	phase difference between the translational and rotational motion of the head
Ψ_n	the nth phase of the steady-state solution based on the Galerkin method
ψ	functional of Stokeslets
ω	angular frequency of the external actuation
ω_{ns}	resonance index
Ω	volume of flagellum in the 1D model
$\partial\Omega_1$	micro-swimmer surface regards the acoustic radiation force

Chapter 1. Introduction

1.1 Background

In 1959, Richard Feynman conceived nanotechnology in his famous talk [1] and envisioned that maneuverable machines at an exceedingly small scale would be very useful in many fields. Although people have ever since fantasized about micro-robotics [2], the actuation and manipulation of micro-scaled robots have not been realized until the recent decade with the booming development of microfabrication. Among many potential applications, medical implementation could be the most significant impetus to develop microbotics [3]. For example, some commercialized swallowable medical devices [4] have been available. They can move inside the human body for diagnosis or surgery. The structure we focus on in this thesis is an artificial flagellated micro-swimmer (AFMS), which incorporates a relatively rigid head and a flexible tail, where the tail is commonly named a flagellum in microbiology [5]. Herein, We focus on the flagellated, a.k.a. sperm-like, structure because its rigid head has the potential for cargo delivery, which can lay the foundation of targeted therapy for cancer treatment [6]. Besides, this design is simple to fabricate through layer-by-layer photocuring (i.e., 3D printing) [7, 8], which will be presented in this thesis.

It should be noted that even if remotely controllable capsule endoscopes have been proposed in the past several years, these devices are still in millimeter scale to accommodate various functionalities, such as power supply, propulsion, navigation, imaging, signaling, and so forth [9]. As a result, the so-called milli-swimmers can only move in sufficiently large biological ducts, and the medical implementation such as the targeted therapy is restricted. Fortunately, the possibility of further downscaling these devices has been demonstrated with the advent of submillimeter micro-swimmers [6].

Therefore, more medical applications can be anticipated. For example, we envision that a swarm of micro-swimmers could be direct to the position of the focus along the esophagus under an external excitation, as shown in Figure 1-1. There, they would release medicines into the inflammation site or kill cancer cells by utilizing the magneto-caloric effect.
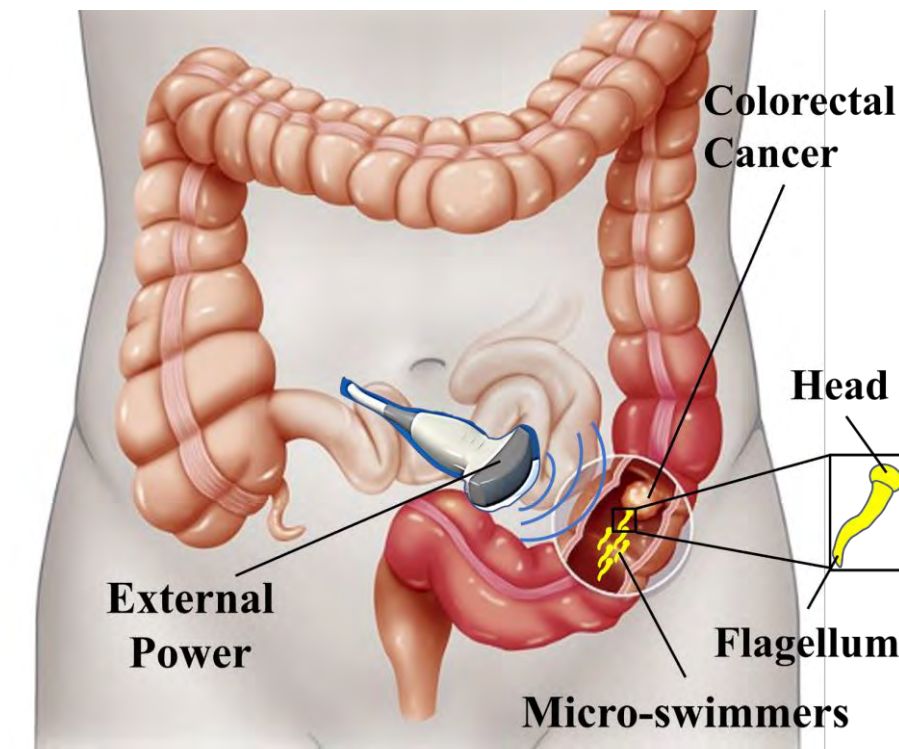
Figure 1-1. Sketch map of the application scenario about medical cargo delivery.

1.2 Objectives and methodology of this thesis

The objective of this thesis is to achieve a quantitative model of AFMSs to predict their motility and steerability under external actuation. For the motility of an AFMS, we attempt to first answer the questions on (i) the motion of the head under acoustic actuation, (ii) parameter optimization of the flagellum, (iii) the effect of inertia, (iv) the

effect of material damping, (v) the effect of the non-uniform flagellum. These questions are crucial because the answers to them can pave the road to far-reaching medical applications. The motion of the head acts as a bridge between the external actuation and the locomotion of the micro-swimmer; the parameter optimization is meaningful to the design and can assist us in the cost trade-off; inertia is the agent of energy conversion and the cause of resonance; material damping is the inherent property of the polymeric flagellum; the non-uniform flagellum provides a possibility for the geometric optimization of the flagellum. After the analysis of one-dimensional (1D) propulsion, in our analytical attempt to resolve the turn performance of an AFMS, it is found that the geometric nonlinearity leads to the coupled governing partial differential equations (PDEs) of the flagellum dynamics. Disentangling them was difficult and led to non-convergent results. Therefore, for the steerability of an AFMS, we attempt to establish a 2D model of the flagellum to predict the trajectory of motion. This model should be simple to solve numerically and can be verified by our experiments.

Concerning medical applications, the propulsion strategies that are apparently harmful, such as the chemical and electrical actuations, have been excluded, which has brought our attention to acoustic and magnetic ones. Generally speaking, the magnetically actuated devices are more maneuverable as reported in [10, 11], nevertheless, the driving strategy is limited to the acoustic actuation due to the requirements of bio-compatibility and medium-independence [12]. The directional motions of AFMSs under the acoustic actuation were observed in some experiments [7, 13]. Authors therein considered that the propulsion arose from the strong acoustic streaming around sharp edges of AFMSs, which is a well-established mechanism for propelling swimmers excited by acoustic waves [14-16]. However, it is generally complex to obtain acoustic streaming surrounding a micro-swimmer (mainly via

numerical simulation based on the perturbation technique [16]), which gives rise to the difficulty of theoretical analyses, and sometimes, leads to significant discrepancies (e.g., the resonance frequency of the simulated value differs from the experimental observation in [13]). Fortunately, if a body is slender (i.e., the ratio of the characteristic width to length is less than 0.1 [17]), an asymptotic expression of fluid forces around solid boundaries can be obtained under a low Reynolds number (LRN), known as the resistive force theory (RFT) [18-24]. Gray and Hancock [25] and Lighthill [26] developed the RFT to describe LRN swimming problems. Recently, in the analyses of artificial micro-swimmers, the RFT is the most adopted [27-29]. For example, studied in [28] and [29] were the micro/nano-rods propelled by ultrasound, wherein the complex effect of acoustic waves was simplified into forces estimated based on the drags calculated using the RFT owing to the LRN, which avoids the analysis of complexed acoustic streaming.

The above achievements and difficulties inspired us to develop the model of acoustically actuated AFMSs. Indeed, the footage of the sperm-like artificial micro-swimmers provided in Ref. [7] is reminiscent of the swimming of natural spermatozoa [30-32]. Figure 1-2 is a recap of a sequence of tail deformation of the AFMS described in Ref. [7], which is very similar to the wiggling of a biological flagellum. Such a wiggling motion provides the propulsive force that can be determined based on the theories developed in the LRN regime. In this regime, the inertia of fluid can be neglected because the inertial force is much less than the viscous force [33]; and propulsion can only be achieved by breaking the time-reversal invariance [34], known as the 'scallop theorem'. The wiggling of the flagellum as shown in Figure 1-2 is such a motion that provides forward thrust. Though microorganisms beat their flagella through the action of molecular motors embedded in the filaments [30, 35], it has been

shown that beating a flagellum at one of its ends can also give rise to the forward thrust, which has been theoretically studied [36-38] and experimentally verified [39].

Note that the effect of acoustic streaming cannot be neglected, which is near the tip of a flagellum. Intuitively, the effect of the acoustic streaming can be treated as forces causing flagellum wiggling but from the tail tip instead of the head. It is thus clear that the RFT can be widely employed to analyze the propulsion of an AFMS under the swimming mechanism we proposed. For the steering problem, one may derive the 2D governing PDEs of a flagellum via Hamilton's principle [40] if the dynamic profile of the flagellum is a known function [41]. Unfortunately, in swimming, the wiggling profile of a flagellum is not *ad hoc*. In addition, a flagellum becomes curved in turning [42], bringing about geometric nonlinearly, and the influence of the rigid-body motion further increases the nonlinearity of the problem. Therefore, a discrete flagellum model was developed to solve the 2D swimming problem (aka. the bar-joint model) [43]. The problem with these studies is that the derivation of RFT is based on circular cross-sections, but the cross-sections of many artificial micro-swimmers are non-circular. For example, if layer-by-layer photocuring is applied to fabricate AFMSs, the cross-section of the flagellum is more like a rectangle [7]. Hence, we proposed a corrected RFT (CRFT) model to correct the classical RFT for 2D cases or flagellum with rectangular cross-sections. The theoretical process leads to a single correction factor K which can be determined by comparing the terminal swimming velocities obtained from the bar-joint model based on the CRFT with those from 2D fluid-structure interaction (FSI) simulations. Nevertheless, the experimental verification of this theory is still unachieved.

In the following chapters, we will first summarize the historical achievements and theoretical perspectives on microorganisms and their propulsion mechanisms, then

review the progress in actuation strategies of AFMSs in Chapter 2. After that, in Chapter 3, the 1D equations of motion (EOM) for a flagellum, treated as an Euler-Bernoulli viscoelastic beam, will be derived based on the RFT and solved by using the Galerkin method. In order to make our theoretical model applicable to the design of an AFMS, we will involve the inertia term and material damping in the 1D EOM and consider the tapered cross-section of a flagellum. Influences of nondimensional parameters, such as the resonance index, sperm number, and material damping coefficient, will be discussed and a comparison with reported experimental results will also be demonstrated. Next, in Chapter 4, we will develop the 2D EOM of an AFMS based on a discrete bar-joint model for the flagellum and the CRFT for the AFMS with rectangular cross-sections. Therein, we will first state the swimming problem of corresponding FSI simulations, and then examples of convergence analyses of FSI simulation will be presented. After that, the correction factor K will be determined in terms of different geometrical, materials, and acoustic-actuation parameters. Comparisons of swimmer's trajectories between the CRFT-based bar-joint model and the FSI simulation will then be presented as a verification of our theory, and a demonstration of the acoustic or magneto-acoustic steering strategy for the AFMS will be shown as the examples of applications. In Chapter 5, we aim to verify the CRFT models by comparing terminal velocities of AFMSs observed in experiments to those predicted by theoretical calculation. Therein, we will describe the fabrication of AFMSs, the corresponding materials characterization, the experimental platform for acoustic actuation and observation, and the comparison between experiments and theoretical calculations (i.e., FSI simulations and CRFT models). Finally, we will conclude and discuss the future work of this research in Chapter 6.
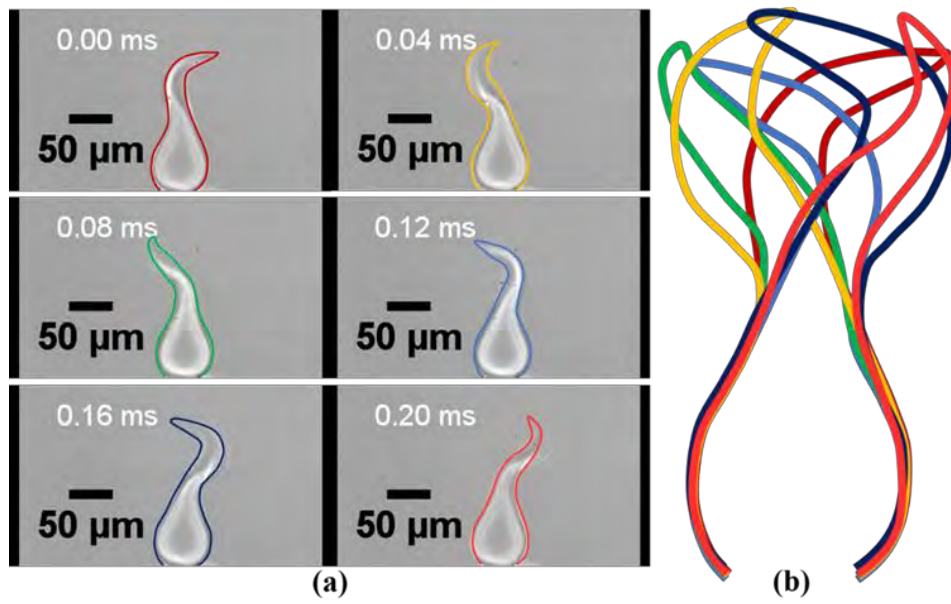
Figure 1-2. Kaynak et al.'s artificial micro-swimmer [7] beats the flagellum in an acoustic field: (a) the footage of swimming provided in [7]; (b) the overlapped profiles of the micro-swimmer showing the flagellum wiggling.

Chapter 2. Literature review

2.1 Observations of microorganisms

We define a "swimmer" as a creature or an object that moves by periodically changing its body configuration. This type of swimmer in nature, if the size is sufficiently small to be invisible to the naked eye, is usually called a microorganism. The biological observation of microorganisms began with the invention of the optical microscope in the 17th century when Anthony van Leeuwenhoek first observed swimming bacteria [44]. Since then, people have discovered that our world is full of swimming microorganisms like sperms, bacteria, protozoa, and algae.

In accordance with the comprehensive review article [5], many tiny swimmers use one or more appendages to advance. The appendage can be a rather hard spiral that can rotate. For example, the motor organelles of Escherichia coli and Salmonella typhimurium are bacterial flagella, which consist of a rotating motor, a spiral filament, and a hook that connects the motor to the filament [31, 45, 46]. The diameter of the filament is around 20 nm with a 10-μm contour length of helix [37]. Each cell usually has several flagella. When the motor rotates counterclockwise, the filaments are wrapped in a bundle and the cell is pushed forward at a speed of 25–35 μm/s [47]. When the motor runs clockwise, the corresponding filaments get unbundled and undergo a "polymorphic" transformation, in which the helix's chirality changes; and these transformations can change the direction of cell movement [37]. Aside from the helical filament, the appendage can also be a flexible filament that undergoes whip-like motion driven by molecular motors, such as the sperms of many species [48].

As shown in Figure 2-1, swimming bacteria have various flagellar configurations. For example, F. crescentus has a single right-handed spiral filament that is driven by a

rotating motor and can be turned in any direction. The motor rotates clockwise preferentially and drives the filament to make the body move forward [49]. When rotating counterclockwise, the filament pulls the body instead of pushing it. The motor of Rhodobacter sphaeroides only rotates in one direction, but it stops periodically [50]. The flagellar filaments form a tight coil prior to a stop and then extend into a spiral at a stop. Besides, a fraction of bacteria do not have flagella, they can also move slowly by sliding [51].

Eukaryotic flagella and cilia are much larger than bacterial flagella, with a diameter of about 200 nm and a complex internal structure [48]. The most common structure has a molecular motor or dynein which slides back and forth causing fluctuations that propagate along the flagella. The beat pattern and length between eukaryotic flagella and cilia are very different. For example, Chlamydomonas reinhardtii have both cilia and flagella. Cilia are short and have random or non-synchronized motions [48], while flagella's motion has a clear pattern. During the power stroke, each flagellum stretches and bends at the bottom, which is a bit reminiscent of the motion of our arms in breaststroke. During the recovery stroke, the flagella regain their folding, causing less resistance underneath.

Flagellated microorganisms, such as sperms, are more researched in the biomechanics community because of their simplicity—often involving only one flagellum for propulsion—and their large size which simplifies observation. One can notice two kinds of flagellar wave motions, helical and planar, and two corresponding trajectories of organisms. When the flagella move in a helical way, the overall trajectory is, in general, a straight line, though there exists helical rotation around the line [52-55]. It is interesting that in the case of planar flagellar motion, the trajectory turns out to be circular rather than linear [52, 54-57]. Further analysis demonstrates that the greater the

asymmetry of the flagellar wave motions, the smaller the radius of curvature [55]. This indicates the existence of a strong connection between the circular path and the asymmetric tail beating [58]. However, more detailed interpretations of the results of biological observation are requisite, especially for biomimicking. This is the reason why the investigations on the fundamental physics of natural micro-swimmers are emerging in an endless stream.
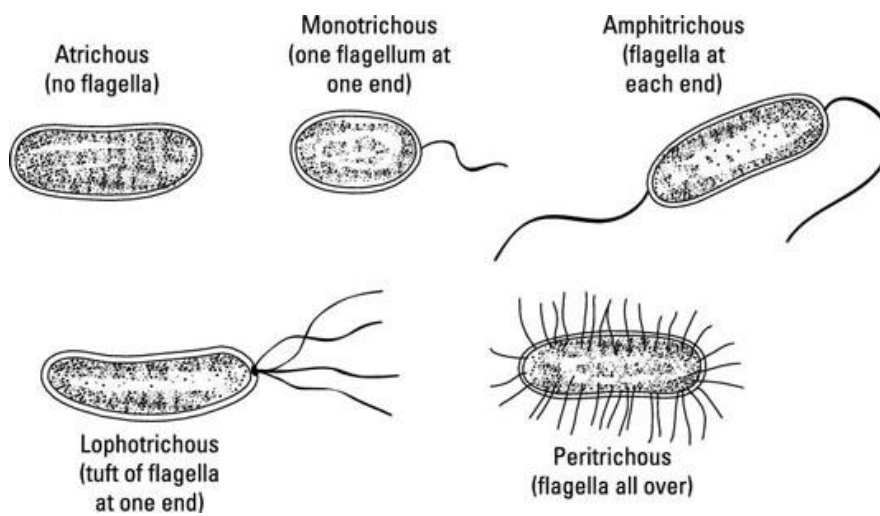
Figure 2-1. Sketches of microscopic swimmers. Reproduced with permission [59]. Copyright 2019, Wiley.

2.2 Swimming mechanisms of natural micro-swimmers

2.2.1 Principles of swimming on micro-scale

The physics of microscopic swimming is distinct from the macroscopic one. The world of microorganisms is "a world with the LRN", where inertia hardly plays a role and viscous damping is predominant. A general definition of the Reynolds number is $Re = \rho_0 UL/\mu$, where ρ_0 is the fluid density, μ the dynamic viscosity of the fluid, U and L the characteristic velocity and the length of the fluid, respectively. The specific

Reynolds numbers for natural micro-swimmers are worth comparison [60]. In water, with fluid parameters $\rho_0 \approx 1000$ kg/m^3 and $\mu \approx 10^{-3}$ Pa·s, a swimming bacterium, such as E. coli, with $U \approx 10$ µm/s and $L \approx 0.1$ µm is of a Reynolds number Re $\approx 10^{-5}$–10^{-4}. A human sperm with $U \approx 200$ µm/s and $L \approx 50$ µm moves at Re $\approx 10^{-2}$. Some larger ciliates, such as Paramecium, with $U \approx 1$ mm/s and $L \approx 100$ µm can have Re ≈ 0.1 [61]. It is noted that a micro-swimmer with a speed around 1000 µm/s is reasonable in nature. Furthermore, for some much larger swimmers, such as fishes, birds, and insects, it is noted that their Reynolds numbers are usually very large, and thus, their swimming strategies will not work on a small scale [60, 62-66].

The study of the mechanisms of locomotion at LRNs has a long history. In 1930, Ludwig [67] remarked that microorganisms that swing their stiff arms like paddles cannot perform net movements. After that, there have been some classical reviews from different perspectives. Some were from the perspective of fluid mechanics at LRNs [26, 34, 61, 68, 69]; some focused on the general animal locomotion [70]; and others found incentive from the investigations of the biophysics and biology of cell mobility [46, 71]. In general, one can simplify the sophisticated hydrodynamic problems at LRNs by studying the limit case Re = 0, in which the Navier-Stokes equations reduce to the Stokes equations [72] following:

$$-\nabla p_f + \mu \nabla^2 \mathbf{u} = 0, \quad \nabla \cdot \mathbf{u} = 0 , \tag{2.1a, b}$$

where $\mathbf{u}$ is the velocity field, and p_f the fluid pressure. Since the Stokes equations, i.e., Eqs. (2.1a, b), are linear, the classical linear superposition method is practicable to solve the fluid field and pressure distribution. The Green's function to Stokes flow $\mathbf{G}[\mathbf{P}(s) - \mathbf{P}(s + \delta)]$ can be solved analytically [68] and is expressed as:

$$G\left[\mathbf{P}(s) - \mathbf{P}(s+\delta)\right] = \frac{1}{8\pi\mu}\left(\frac{\mathbf{I}}{|\mathbf{P}_{s\delta}|} + \frac{\mathbf{P}_{s\delta}\mathbf{P}_{s\delta}}{|\mathbf{P}_{s\delta}|^3}\right), \tag{2.2}$$

where $\mathbf{I}$ is the identity tensor, and the distance vector $\mathbf{P}_{s\delta} = \mathbf{P}(s) - \mathbf{P}(s + \delta)$. Physically, $G[\mathbf{P}(s) - \mathbf{P}(s + \delta)]$ represents the velocity field at position $\mathbf{P}(s)$ due to a singularity force $\mathbf{F}_f$ acting on the fluid domain at position $\mathbf{P}(s + \delta)$, and that is $\mathbf{u}[\mathbf{P}(s)] = G[\mathbf{P}(s) - \mathbf{P}(s + \delta)]\cdot\mathbf{F}_f[\mathbf{P}(s + \delta)]$ based on the linear superposition. Evidently, the flow velocity is inversely proportional to the spatial distance, allowing the neglect of the far-field effect.

A significant solution to Eqs. (2.1a, b) in terms of locomotion is denominated as directional anisotropy. For example, for a 2D problem, if there is a force $\mathbf{F}_f = \left(F_{f\parallel}, 0\right)$ exerted at $\mathbf{P}(s + \delta) = (\delta, 0)$, i.e., $s = 0$, one can derive the flow field $\mathbf{u}$ at $\mathbf{P}(s) = (0, 0)$ as $\mathbf{u} = \left[F_{f\parallel}/(4\pi\mu\delta), 0\right]$ from Eq. (2.2); if $\mathbf{F}_f = \left(0, F_{f\perp}\right)$, $\mathbf{u}$ will then become $\mathbf{u} = \left[0, F_{f\perp}/(8\pi\mu\delta)\right]$. That is, for the same applied force ($F_{f\parallel} = F_{f\perp}$), the flow velocity in the parallel direction is twice that in the perpendicular one ($u_{\parallel} = 2u_{\perp}$). Alternatively, in order to obtain the same speed, it is imperative to apply a force twice greater in the vertical direction than in the parallel direction ($2F_{f\parallel} = F_{f\perp}$). In this case, one may note that the corresponding drag coefficients $c_{\parallel}$ and $c_{\perp}$ (the coefficient of proportionality between the local force and velocity) are different (typically $c_{\perp}/c_{\parallel} \approx 2$), i.e., the drag anisotropy. As we mentioned earlier, most biological swimmers apply elongated appendages, known as flagella, to swim. These slender filaments can intuitively remind us that the fundamental principle of swimming through resistance-based thrust is just the use of drag anisotropy at LRNs. To illustrate these ideas, we can take an undulating filament as an example, as depicted in Figure 2-2. An infinitesimal element of the filament can be considered as rigid, and it moves at a speed of $\mathbf{V}$ which is at an angle

of Θ with regard to the whole filament. The horizontal component of the drag force f_{prop}, which propels the swimmer, is expressed as:

$$f_{\text{prop}} = \left(c_{\parallel} - c_{\perp} \right) |\mathbf{V}| \sin\Theta\cos\Theta \,. \tag{2.3}$$

With Eq. (2.3), only if the drag is anisotropic, e.g., $c_{\perp}/c_{\parallel} \approx 2$, there will be a net force in the propulsive direction. This resistance-based thrust theory is the so-called RFT.

The feasibility of resistance-based thrust mainly depends on the following two important physical inferences: first, due to the existence of drag anisotropy, a micro-swimmer can generate propulsion in the direction perpendicular to the local movement direction of the filament; second, although the filament deforms reciprocally, it can still produce a non-zero time-averaged propulsive force [25, 73]. It should be accentuated that the periodic deformation of the filament needs to meet certain conditions to produce a non-zero time-averaged force as per Purcell's scallop theorem [34]. Purcell took scallops as an example for the explanation. Under LRNs, reciprocating motion cannot be used for movement; this is analogous to a scallop whose shell opens and closes alternatively while resulting in zero net displacements. Nevertheless, it is worth emphasizing that Purcell's scallop theorem is strictly valid only under the limited condition that all relevant Reynolds numbers in the swimming problem are zero. Many recent studies have been devoted to a more general issue by involving the inertia theorem (the Euler regime), and it has been found that the continuity of transition from the Stokerian regime to the Euler regime is normally dependent on the spatial symmetry of the problem [74-78].
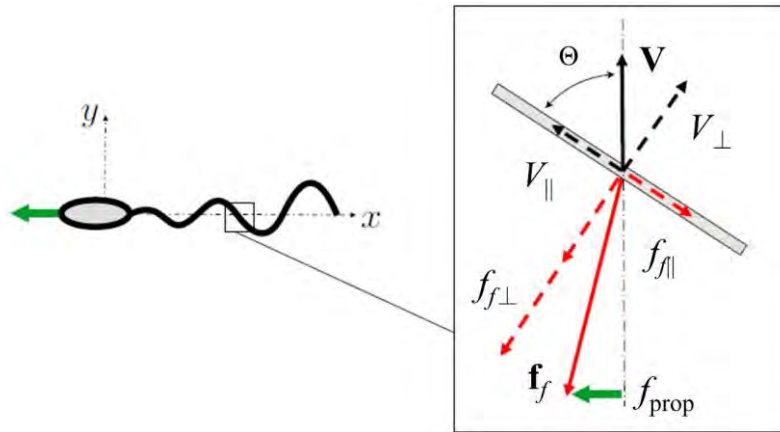
Figure 2-2. Understanding of drag anisotropy for slender filaments. Reproduced with permission [5]. Copyright 2009, IOP Publishing.

2.2.2 Swimming mechanisms

Gray and Hancock [25] and Lighthill [26] developed the aforementioned RFT to describe LRN swimming problems. This theory has been used to model the propulsion generated by spermatozoa [41], small earthworms [79], Chlamydomonas reinhardtii [80], and some swimmers in a granular material [81]. However, the drag coefficients were usually revised to better fit the observations rather than using the theoretical values given in Refs. [25] and [26]. This theory has also been employed to interpret the propulsion mechanisms of helical flagella [80, 82-87] and nanobots [33, 88-90]. However, the RFT ignores the long-range hydrodynamic interaction and only regards the viscous force acting on the immersed body as a function of local velocity [17]. Thus, the slender body theory (SBT) [26, 91], as well as its advanced version, the regularized Stokeslet theory [92], have been proposed to improve the accuracy of modeling. Intuitively, applying the SBT to a micro-swimmer with an undulating flagellum (whose propulsion is usually estimated by the RFT) can be straightforward. According to the derivation of SBT [18], appropriate geometries of flagella require two properties: a

small thickness-to-length ratio and a small displacement amplitude (compared with the wavelength) of the flagellum undulating. Fortunately, within an acceptable range, the predictions of SBT have shown great conformance with experimental observation [93] and the results of more complicated models established by the finite-element method [94], the regularized Stokeslet method [23], the boundary element method [95], etc. The equivalence between the SBT and the RFT has also been explored. For example, for helical flagella, the RFT was employed to express the forces and torques in terms of the translational and rotational velocities [25, 26]. Ref. [23] then experimentally examined the reliability of RFT and compared the experimental results with the theoretical predictions of the more involved SBT. All the theoretical predictions were in good accordance with experimental observations.

It is noted that these studies usually assumed idealized modeling conditions, for example, the filament model was assumed to be sufficiently slender, with a prescribed dynamic profile, and far from the boundary to satisfy the SBT. Subsequent research has mainly focused on the dynamics of swimmers close to the non-skid or free-skiing boundary adopting boundary element methods [96-98]. Rorai et al. [17] investigated the dynamics of a flagellated micro-swimmer, which is, more specifically, a sperm-like swimmer as demonstrated in Figure 2-3, in an infinite domain by finite element simulation, and an excellent agreement between the regularized Stokeslet method and the finite element simulation was demonstrated. However, their simulation did not consider a fully coupled FSI where the whole structure can have a rigid body motion, thus it became difficult to imitate the holistic locomotion of the swimmer. Curatolo et al. [99] proposed an approach to coupling the overall rigid body motion with the FSI for a fish-like swimmer by employing the automatic remeshing technique, as shown in Figure 2-4. However, they did not test the reliability of the RFT. Obviously, the

geometry of the numerical model should be varied for a more comprehensive assessment of the analytical models, but the convergence of simulation can be a problem. Therefore, further research is needed to improve the numerical model of micro-swimmers through the FSI simulation.

According to the aforementioned Purcell's scallop theorem [34], the breakthrough of the swimming problem for natural swimmers at LRNs is to find a nonreciprocal deformation approach. In 1951, Taylor found that a swimmer who deforms in a wave fashion can advance in an opposite direction to its traveling wave, and such a swimmer was named Taylor's swimming sheet thereafter [36]. Generally speaking, all the 3D wave-like deformations can cause net propulsion, especially the spiral wave of flexible flagella [100]. It is noted that the original model of Taylor's swimming sheet is infinitely long. Nevertheless, the Taylor sheet calculation is of great importance because it can be extended to finite objects. For example, to mimic the movement of ciliates such as opal and paramecium, Lighthill introduced an "envelope model", where a traveling surface wave was exploited to simulate the swinging cilia embedded in the cell [101-103]. It is worth noting that the influence of inertia can be directly considered in the sheet calculation. In addition, it has been shown that if the flow separation is ignored, the swimming speed decreases with the increase of Reynolds number, and the asymptotic value at high Reynolds number is half of Taylor's result [104, 105]. When the Reynolds number is zero and the waveform is prescribed, the nearby rigid wall, if exists, can increase the swimming speed if the gap between them is reduced [104].
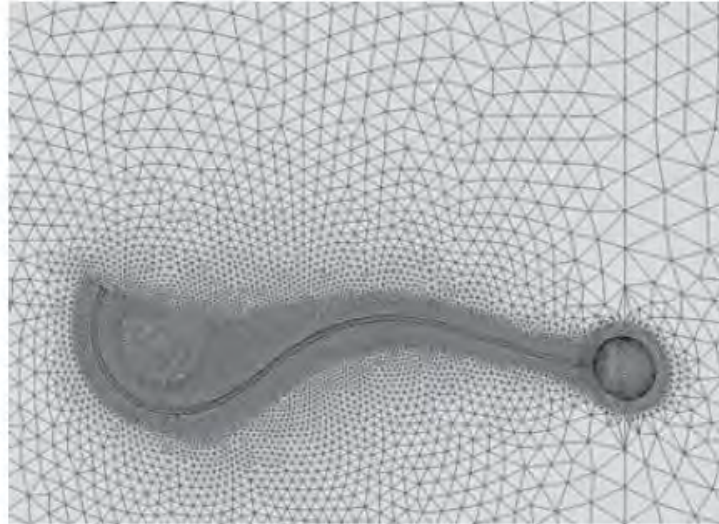
Figure 2-3. Numerical simulations of natural swimmers: finite-element mesh around the sperm-like swimmer. Reproduced with permission [17]. It is an open access article that does not need to seek permission.
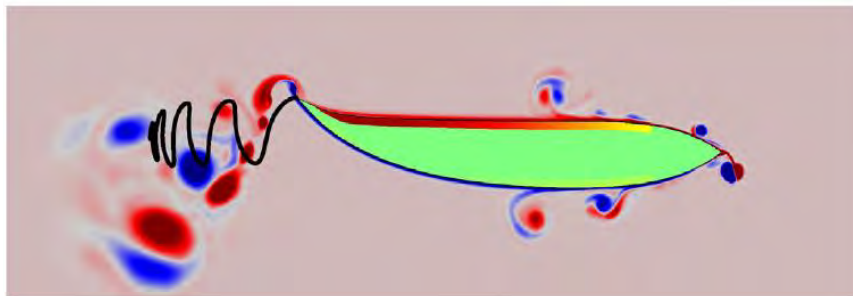
Figure 2-4. Numerical simulations of natural swimmers: onset of vorticity of the fish-like swimmer. Reproduced with permission [99]. Copyright 2016, Elsevier.

2.2.3 Dynamic behaviors of flagellated micro-swimmers

Inspired by Taylor's swimming sheet, one may have an intuitive understanding of the general problem of the self-propelled motion of flagellated swimmers at LRNs. For such micro-swimmers, their dynamic behaviors mainly arise from the interplay between the internal and external forces acting on them. Internal forces are normally

from elastic properties and can resist the bending of flagella and ensure the inextensibility of their bodies, while external forces are mainly due to the fluid viscosity (which can be estimated from the RFT or the SBT) that can cause deformations of flagella and hence non-trivial dynamic behaviors. In an earlier study, Machin [106] found that the amplitude of the bending wave decayed exponentially with the length of a flagellum due to the fact that the LRN corresponds to overdamping. However, Machin scrutinized the fact that the swing amplitude of the sperm flagella did not attenuate but gradually increased with the distance from the head. Therefore, he concluded that in order to be consistent with experimental observations, there must be an internal actuation torque distribution along flagella, which turns out to be actin filaments afterward. Their study lays the foundation for many subsequent FSI problems at LRN [38, 106-113] and has been further extended to the estimation of the actin filament's persistence length [114, 115]. Wiggins et al. [38] followed Machin's work and established the so-called hyper-diffusion equation with boundary conditions in terms of the normal drag coefficient $c_\perp$ and the bending modulus EI for a flagellum with constant cross-section, which is given by

$$
\begin{cases}
c_\perp \left(\partial y_c / \partial t \right) = -EI \left(\partial^4 y_c / \partial x^4 \right), \ 0 \le x \le L \ ; \\
\text{at } x = 0 : y = y_{0a} \sin \omega t \ , \ \partial y_c / \partial x = \theta_{0a} \sin \omega t \ ; \\
\text{at } x = L : \partial^2 y_c / \partial x^2 = 0 \ , \ \partial^3 y_c / \partial x^3 = 0 \ .
\end{cases}
\tag{2.4}
$$

In which, y_c is the lateral displacement of the flagellum centerline with length L and is a function of time t and longitudinal coordinate x; y_{0a} and θ_{0a} are the translational and rotational amplitudes of the wiggly head; and ω is the angular frequency. Eq. (2.4) can be solved analytically by assuming y_c as the following:

$$
y_c \left(x, t \right) = \sum_{n=1}^{4} G_n e^{r_{\text{PDE}n} x} e^{-i\omega t} ,
\tag{2.5}
$$

where the four characteristic roots $r_{\text{PDE}n}$ are determined by

$$r_{\text{PDE}n} = \sqrt[4]{\frac{i\omega c_\perp}{EI}} \, , \, n = 1,2,3,4 . \tag{2.6}$$

It can be seen that Eq. (2.5) conforms to the above-mentioned Machin's solution [106], i.e., the fluctuation amplitude decays exponentially along the flagellum. Wiggins et al. [38] calculated the propulsive force by integrating the projected elastic force density along the flagellum because there was no other external force exerted on it. The expression of the normal elastic force f_e is:

$$f_e = EI\left(\partial^2 \kappa_e / \partial s^2 + \kappa_e^3 / 2\right), \tag{2.7}$$

where κ_e denotes the curvature of the flagellum at the arc coordinate s. By integrating f_e over the whole length L, the time-averaged propulsive force $\overline{F}_{\text{prop}}$ for the case of the translational boundary condition (i.e., $\theta_{0a} = 0$) is expressed as:

$$\overline{F}_{\text{prop}} = \frac{1}{2} y_{0a}{}^2 c_\perp \omega Y\left(S_p\right), \tag{2.8}$$

where Y is a function of the sperm number S_p, and they are both non-dimensional. The relation between Y and S_p is exhibited in Figure 2-5. For the case of pivoting prosthesis (i.e., $y_{0a} = 0$), $\overline{F}_{\text{prop}}$ has a similar expression in terms of Y_p, which is also a function of the sperm number S_p as shown in Figure 2-5. It is noted that based on Eq. (2.6), the real part of the characteristic root $\sqrt[4]{\omega c_\perp / EI}$ is of great significance and will influence the dynamic behavior of a sperm-like micro-swimmer. In fact, S_p is defined as $L\sqrt[4]{\omega c_\perp / EI}$, which is the most popular non-dimensional parameter used in micro-swimmer studies [38, 106, 116] because it indicates the interplay between viscous and elastic forces on the flagellum.

19

In addition, the computed propulsive force based on the head movement has also been experimentally verified [110]. The propulsive force for a variable cross-section flagellum is proposed by Singh et al. [117]. One can first obtain the elastic force as:

$$f_e = EI\kappa_e^{3} - EI\left(\partial^2 \kappa_e / \partial s^2\right) - 2E\left(\partial I / \partial s\right)\left(\partial \kappa_e / \partial s\right) - E\left(\partial^2 I / \partial s^2\right)\kappa_e, \tag{2.9}$$

where EI is a function of the arc length s. The propulsive force can then be estimated by integrating f_e. If the diameter of the cross-section varies linearly, one can first derive the analytical solution of the EOM and then calculate the propulsive force by the RFT. When such a micro-swimmer is placed in a fluid field, the effects of external forces, fluid viscous stresses, and internal bending moments can lead to complex dynamic deformations of the flagellum, which successively influences the swimming properties of the micro-swimmer. There have been many experimental and theoretical studies on the dynamics of such swimmers with regard to different sorts of microscale flows, such as extensional flows [118-120], vortex arrays [121-123], simple shear flow [124-129], pressure-driven channel flows [130], and other micro-fluidic flows [131, 132]. Some investigations have involved more complicated external or internal forces, such as forces at the ends of filaments [38, 133], two-body interactions [134], internal actuation [111, 135, 136], and self-attraction due to capillary interactions [137].
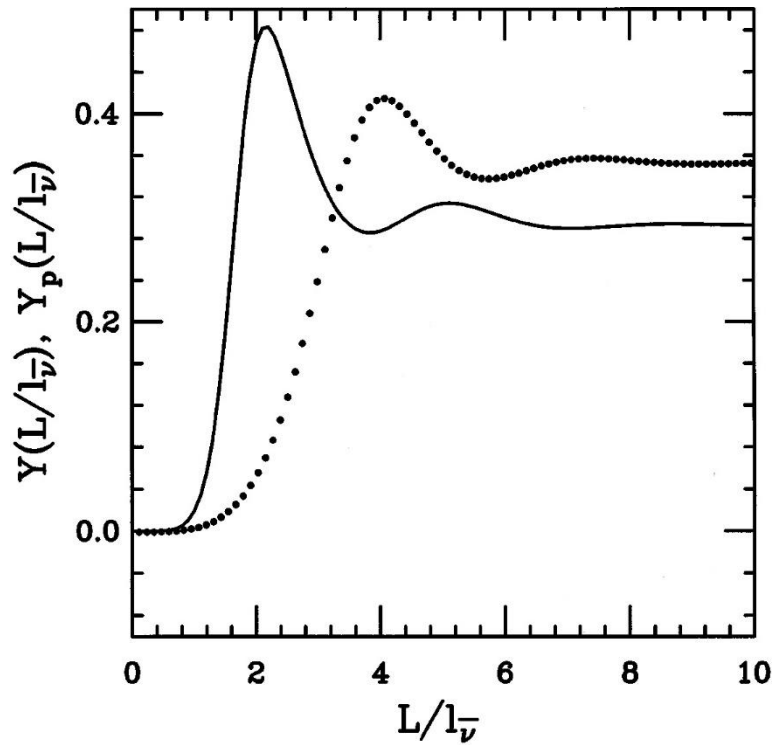
Figure 2-5. Scaling functions Y and Y_p for propulsive force versus the sperm number S_p (which equals $L/l_{\bar{v}}$). Dotted (Y) and solid lines (Y_p) indicate functions for the translational and pivoting prosthesis, respectively. Adapted with permission [38]. Copyright 1998, American Physical Society.

2.3 Experimental achievements of artificial micro-swimmers

2.3.1 Self-propulsion approach

Artificial micro-swimmers or microrobots swim in an LRN regime just like microorganisms, requiring swimming strategies that are distinct from those of macroscale swimmers. Researchers have proposed various propulsion mechanisms, many of which are biomimetic, to drive and control artificial micro-swimmers remotely. It is noted that some mechanisms are not biomimicking; however, as they can move microdevices in the fluid, the latter were also called micro-swimmers. In this sense, the concept of swimming has been expanded to describe all artificial microdevices

propelled in the fluid. They are generally classified into three categories: self-propulsion, external propulsion, and a combination of them [138].

The foundation of the self-propulsion approach is energy conversion. If there are local chemical reactions at the surface of a nano- or micro-swimmer, the chemical energy can be converted into kinetic energy. This energy transformation can eventually bring about the locomotion of artificial swimmers [139-144]. The first fully artificial self-propelled nano-engine was synthesized by Paxton et al. [145] in 2004 and then followed by Fournier-Bidoz et al. [146] Motivated by these achievements, some synthetic self-propelled micro-motors driven by catalytic reactions have been proposed [147-150]. While these autonomous swimmers can move at speeds close to 1.5 cm/s, they are not steerable. As a result, the application of these self-propelled micro-swimmers normally limits to imprecise manipulations, which makes them incompetent for medical applications. To accurately control the movement of a swimmer, one may consider using field-propulsion rather than self-propulsion, and the field(s) can be magnetic, acoustic, photonic, thermal, or any combination of them [141, 151, 152].

2.3.2 Magnetic actuation

The most renowned micro-robots actuated by rotating magnetic fields are helical swimmers [153, 154]. In 2007, Bell et al. [153] first reported a spiral-shaped magnetic swimmer that had a magnetic head and a spiral semiconductor tail made of a thin GaAs bilayer film as shown in Figure 2-6. This swimmer is an artificial duplicate of bacteria in terms of not only the dimensions but also the propulsion mechanism. Then, in 2012, Schuerle et al. reported a process to fabricate these magnetic swimmers by coating self-assembled phospholipidic helices with a magnetic CoNiReP alloy using electroless

deposition [155]. After that, Gao et al. [156] developed a bio-template technique to manufacture magnetic microrobots through helical plant vessels in 2014. Recently, Nelson's team has proposed soft micro-swimmers composed of stimuli-responsive hydrogel bilayers [157-159], where the layer of poly-N-isopropylacrylamide (PolyNIPAM) is thermally responsive. The blending of magnetic nanoparticles and PolyNIPAM enables the hydrogel to move under magnetic manipulations. Moreover, by exploiting magnetic fields or near-infrared radiation, such magnetic nanoparticles can also generate heat, which is able to deform the temperature-sensitive PolyNIPAM layer. Magnetic nanoparticles can also be exploited to control the rolling direction of the hydrogel and produce magnetic shape anisotropy through appropriate design. These flexible micro-swimmers can adapt the surrounding environment and be actuated by rotating magnetic fields (direction changes with time), revealing the prospects in medical applications [159].

Another widely applied magnetic actuation method is the oscillating magnetic field (intensity changes with time) which is usually perpendicular to the trajectory of the swimmer. Dreyfus et al. [116] fabricated a magnetic micro-swimmer that had a flexible filament composed of DNA-linked chains of paramagnetic colloidal beads and investigated its behaviors under the actuation of an oscillating magnetic field. Misra and co-workers demonstrated a sperm-like magnetic micro-swimmer composed of an ellipsoidal CoNi head and a soft flagellum made of SU-8 [160]. The on-off mechanism was also employed to actuate and control artificial micro-swimmers [161]. As shown in Figure 2-7, the repeated switch between "on" and "off" can generate a planar oscillating magnetic field. The basic driving principle of these microrobots is based on the "dual-mass-spring system" which consists of four main components: a gold head, two nickel segments as the body, and a gold tail. These segments are connected by three

springs, which are made of flexible silver, as demonstrated in Figure 2-7. When the magnetic field is "on", the micro-swimmer is bent due to the magnetic forces on each segment. When "off", the springs tend to restore the linkage to the original configuration. The transition during the "on/off" switching of the magnetic field brings about various instant configurations. When the magnetic field oscillates near the resonant frequency of the swimmer, the dynamic response of the micro-swimmer can result in a net displacement. When the magnetic field oscillates near the resonant frequency of the swimmer, the dynamic response of the micro-swimmer can result in a net displacement.
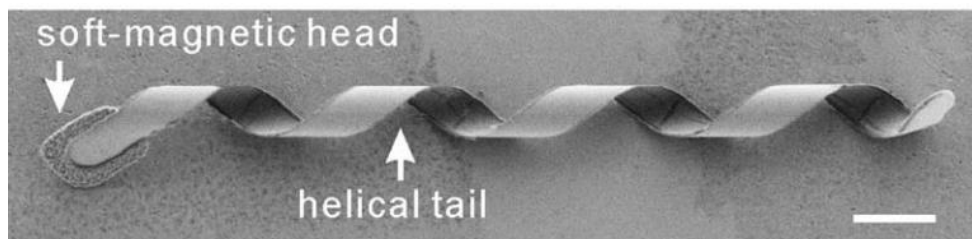
Figure 2-6. Some examples of magnetic micro-swimmers: an artificial flagellum fabricated from a self-rolled semiconductor. Reproduced with permission [11]. Copyright 2009, AIP Publishing.
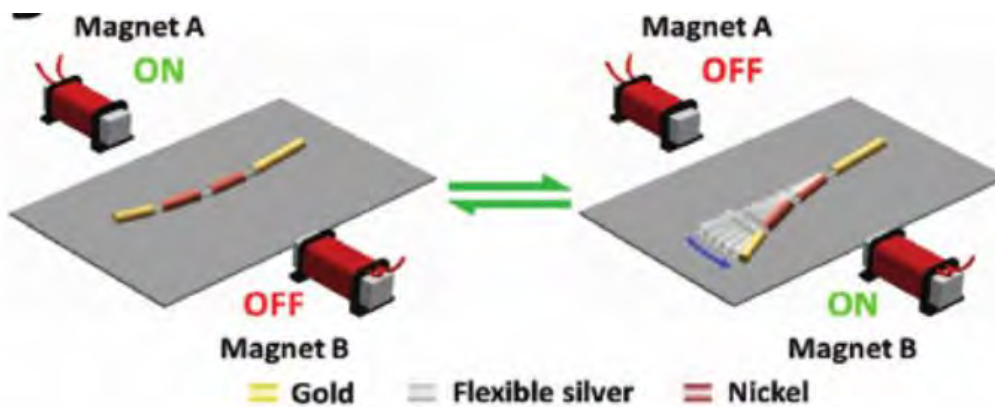
Figure 2-7. Some examples of magnetic micro-swimmers: magnetic propulsion of an artificial nano-fish using a planar oscillating magnetic field. Reproduced with permission [161]. Copyright 2016, Wiley.

2.3.3 Acoustic actuation

Recently, acoustic actuation has been a considerably prevailing driving strategy for generating substantial propulsive force and has attracted much attention in terms of medical applications and lab-on-chip devices. Nevertheless, in consideration of its superb biocompatibility, the mechanisms of acoustic propulsion and precise manipulation deserve deep exploration.

As exhibited in Figure 2-8, some early acoustic artificial nano-swimmers are designed as geometrically asymmetric and composed of rigid metallic nanorods [28], which can be suspended by an acoustic standing wave. Such an acoustic field, in which a series of nodes and antinodes are established from the bottom to the top, can be generated by the cooperation of a piezo transducer and a reflector. These nodes are also the extreme points of the acoustic pressure of the standing wave. If the compressibility and the density of a nano-swimmer are greater than those of its surrounding fluid, the swimmer will be propelled toward the nodes. Wang et al. [28, 162] found that the metallic nanorods could achieve a speed of around 200 μm/s. Moreover, they discovered that these nanorods exhibited striking interactions between nanorods. The manipulation of an acoustic nano-swimmer was realized by incorporating Ni into the electrochemically grown nanorods [163, 164], but it required to import an external magnetic field with a strength of 40–50 mT to steer the nanorods, which was too strong to be implemented in bio-applications. Although acoustic-based artificial swimmers have been considered feasible in various medical circumstances, further studies are

required to determine their driving mechanism and to predict their dynamic behaviors in biological environment.

Another type of acoustically propelled device employs the resonant behavior of micro-scale trapped bubbles within polyethylene-glycol-based cavities under acoustic actuation [165, 166]. The trapped bubble will oscillate if it is subject to a long-wavelength acoustic wave, especially when the wavelength is much larger than the bubble diameter. Based on this principle, some micro-swimmers embedded with bubbles of different sizes have been designed to navigate under acoustic actuation [165, 166]. However, the controllability is poor due to the limitations of coupling between bubbles and the finite resonant region [165]. Recently, Ahmed et al. developed a hybrid magneto-acoustic soft microrobot [167]. As shown in Figure 2-9, their design includes an acoustic bubble at the center of the swimmer, and some superparamagnetic particles are carefully aligned along the length of the swimmer within a polymer matrix. Significant propulsive forces generated by these bubble-based swimmers are demonstrated, and the capability of swimming in viscous fluids makes practical applications more promising. However, the air bubbles can only remain stable for a few hours. Bubble-based swimmers for the next generation require more robust bubbles, and this may be achieved via the polymeric coating technique.

We have mentioned in Chapter 2.1 that many microorganisms swim based on the flagellum, which could be a helix that rotates for propulsion or a flexible filament that wiggles for locomotion [5]. By mimicking the latter, Ahmed et al. [168] demonstrated the first flagellated artificial micro-swimmer (i.e., the AFMS) propelled by acoustically actuated flagellum motion in 2016. They have shown that the flagellated micro-swimmer can be ten times faster than those propelled by acoustic streaming (i.e., without flagella). In the next year, as shown in Figure 2-10, Kaynak et al. [7]

synthesized a larger sperm-like swimmer (~180 × 60 μm) that can achieve the terminal speed of 1.2 mm/s. These two experimental studies suggest that an artificial micro-swimmer with high motility must have one or several flagella; however, the mechanism of acoustic propulsion was not apparently elaborated therein. To comprehend it, we later proposed a driving mechanism based on head oscillation, which will be discussed in detail in Chapter 3.
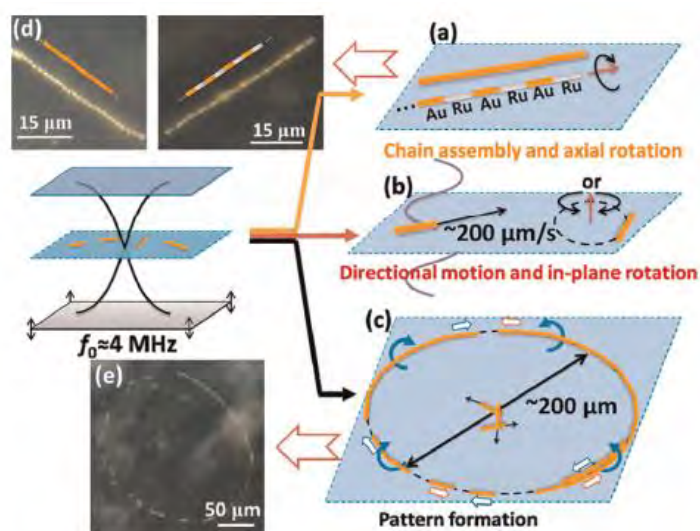
Figure 2-8. Some examples of acoustic micro-swimmers: schematics of the experimental setup and the acoustic propulsion of the nanorods. Reproduced with permission [28]. Copyright 2012, American Chemical Society.
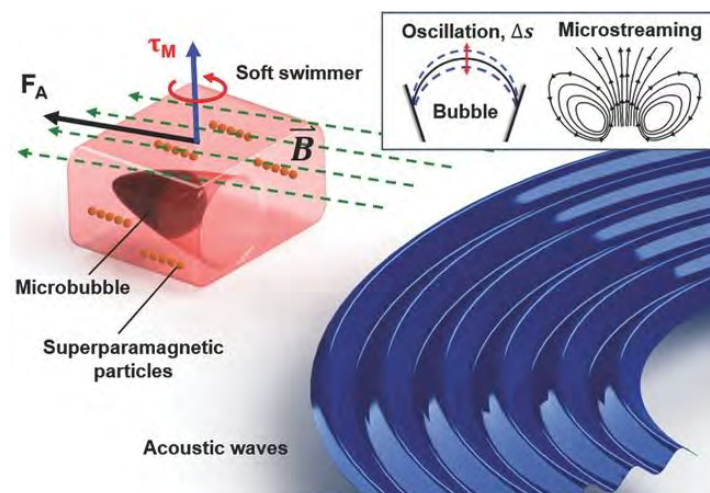
Figure 2-9. Some examples of acoustic micro-swimmers: schematic illustrates the swimming mechanism of the magneto-acoustic soft microrobot. Reproduced with permission [167]. Copyright 2017, Wiley.
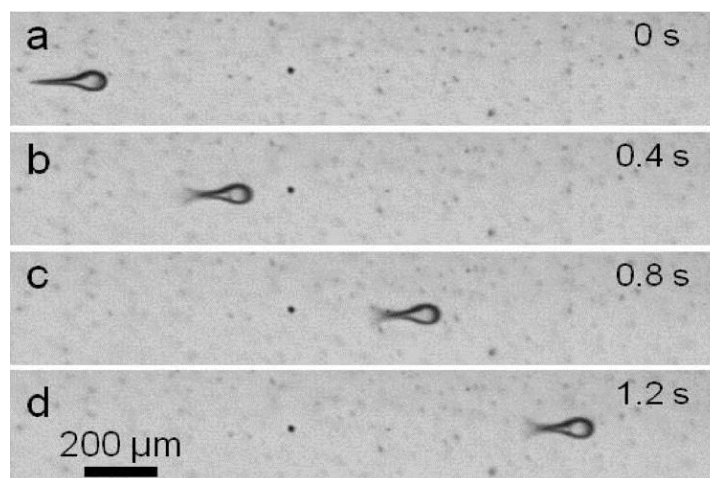
Figure 2-10. Some examples of acoustic micro-swimmers: the experimental observation of flagellated micro-swimmers' directional movement. Reproduced with permission [7]. Copyright 2017, Royal Society of Chemistry.

2.3.4 Other actuation strategies

The possibility of employing optical and thermal energies for micro-swimmer actuation has also been explored. The first optically actuated micro-swimmer was fabricated by Jiang et al. [169], in which micro-swimmers were coated with a thin layer of Au onto silica hemispheres. This layer can absorb light and then generate a local temperature gradient which propels the micro-swimmers by thermophoresis. The further optical micro-swimmers exploit photocatalysis in which the propulsion arises from the light-induced catalytic reaction [170]. When the photocatalytic part of a micro-swimmer in a solution is illuminated, electron-hole pairs are generated by the photons. These holes and electrons are distributed on the surface of the photocatalytic material where they can react with the surrounding solution, and meanwhile, byproducts will be produced. This mechanism is similar to the conventional chemically catalytic propulsion strategy [140]. The collective behavior under light illumination has also been noted. For example, Ibele et al. demonstrated the collective behavior of micro-sized AgCl particles exposed to ultraviolet light in deionized water [171, 172].
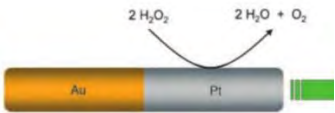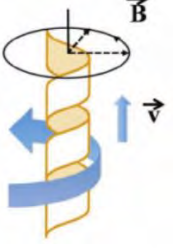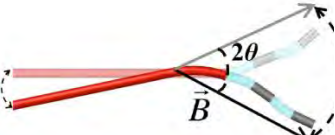
Due to the difficulty of heat transfer, the strategy of heat-actuated micro- or nano-motors has seldom been reported. One possible way of employing heat to propel micro-swimmers is to incorporate an array of micro-heaters, which has been used in the study of a micro-swimmer consisting of shape memory alloy (SMA) components. During heating, the deformation of SMA parts can actuate the microrobot [173-175]. The attempt of propelling micro-objects, such as bubbles and droplets, by the temperature gradient technique has also been reported [176, 177].
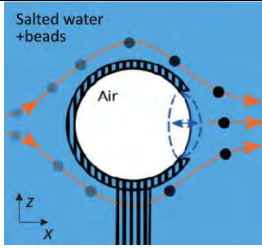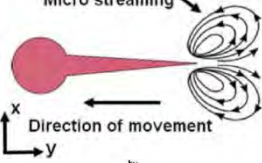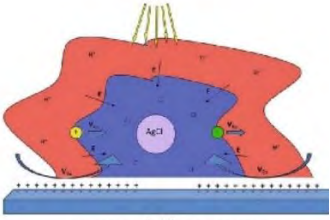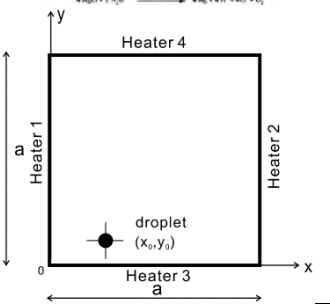
In general, combinations of some of the aforementioned methods may enhance the propulsion and manipulation of small-scale swimmers. Sitti and Schmidt et al. have recently proposed the application of bioengineered and biohybrid bacteria in drug delivery systems [178, 179]. We can also find several realizations of micro-swimmers

that use magnetic power for control purposes (rather than for propulsion), for example, the micromotors that are self-driven in hydrogen peroxide (H_2O_2) solutions but magnetically navigated [180, 181]. Our study shown in Chapter 4 can be another example of the combination of acoustic and magnetic strategies.

We have introduced many actuation strategies so far. To have a comparison of them, the representative references are summarized in Table 2-1. One may notice that the characteristic velocities and dimensions vary remarkably from one actuation mechanism to another. Among them, acoustic bubble oscillation provides the highest speed, but the micro-swimmers propelled through acoustic flagellum whipping probably have the most balanced combination of speed, dimension, and easiness of manufacturing.

Table 2-1. Comparison of different actuation mechanisms.

Actuation mechanism	Representative sketch	Characteristic velocity (μm/s)	Characteristic dimension (μm)	Ref.
self-electrophoresis		5	2×0.4	[147]
Magnetically actuated helical rotation		0.5	10×2	[155]
Magnetically actuated flagellum whipping		10	15×0.1	[182]

Acoustic bubble oscillation		10000	$50 \times R10$	[183]
Acoustically actuated flagellum whipping		500	$200 \times R30$	[7]
Optical actuation		3	R1	[172]
Thermal actuation		100	R500	[177]

2.4 Theoretical studies of artificial micro-swimmers

2.4.1 Theoretical studies on propulsion mechanisms

Most of the basic mechanisms of propulsion strategies have been reviewed in the above context. In this chapter, we briefly describe the theoretical foundation of different propulsion strategies.

Micro-swimmers with bubbles have been widely studied. It has been unveiled that the driving forces, arising from the bubble oscillation, can be induced by H_2O_2 decomposition. The bubble-based micro-swimmer introduced in [146] has a nickel segment acting as the catalyst for H_2O_2 decomposition, i.e.,

$$2H_2O_2(l) = O_2(g) + 2H_2O(l). \tag{2.10}$$

Alternatively, if the O_2 gas generated based on Eq. (2.10) can be forced to flow along a prescribed direction, a micro-swimmer can also be propelled. This is the case of Pt-Au bimetallic nanorods [148], as demonstrated in Figure 2-11, which utilizes the difference in the catalytic effects of these two metals. On the Pt surface, oxidation occurs and O_2 is produced. The electrons flow along the metallic nanorod towards the Au side where reduction occurs. In this case, O_2 is pushed toward the Au side because of the proton gradient (H^+ ions are produced on the Pt side and consumed on the Au side), and the bimetallic nanorod moves in the opposite direction.

Magnetic power is one of the most often employed propulsive strategies for artificial micro-swimmers due in large part to its prospect of remote and wireless operation, directional movement, and biocompatibility. In a magnetic field $\mathbf{b}$, a permanent magnet or a magnetic dipole with the magnetization of $\mathbf{m}$ is subjected to a magnetic torque $\boldsymbol{\tau}_m$, which is the cross product of $\mathbf{m}$ and $\mathbf{b}$, expressed as [184, 185]:

$$\boldsymbol{\tau}_m = \mathbf{m} \times \mathbf{b}. \tag{2.11a}$$

If the magnetic gradient $\nabla \mathbf{b}$ is nonzero, the magnet $\mathbf{m}$ is subjected to a magnetic force:

$$\mathbf{F}_m = \left(\mathbf{m} \cdot \nabla \right) \mathbf{b}. \tag{2.11b}$$

This is the reason why either a non-uniform or an oscillating magnetic field is applied to propel a magnetic micro-swimmer.

As for the acoustically actuated artificial micro-swimmers, the understanding of the driving mechanism behind the locomotion is still fragmented to date. A prevailing view regards the acoustic radiation force F_A as the streaming-induced Stokes drag subject to the micro-swimmer surface $\partial \Omega_1$, and the integral form is expressed as [168]:

32

$$F_A = \oint_{\partial\Omega_1} \langle \boldsymbol{\sigma}_2 \rangle \cdot \mathbf{n} \mathrm{d}A - \oint_{\partial\Omega_1} \rho_1 \langle \mathbf{v}_1 \mathbf{v}_2 \rangle \cdot \mathbf{n} \mathrm{d}A, \qquad (2.12)$$

where $\mathbf{v}_1$ and $\mathbf{v}_2$ are the vibration velocity of a micro-swimmer and the corresponding streaming velocity, respectively; A is the area of the micro-swimmer surface, and ρ_1 the first order of fluid density vibration. The velocity field can be solved by the perturbation expansion approach [16, 168]. The bracket $<\cdot>$ denotes the time-averaging within an acoustic period. The stress, $\boldsymbol{\sigma}_2$, is interlinked to $\mathbf{v}_2$. The first term in Eq. (2.12) arises from the acoustic microstreaming and the second is due to the structural vibration of the micro-swimmer. However, in most cases, Eq. (2.12) cannot be straightforwardly used to solve the swimming problem. The finite element simulation is helpful, but it is often ill-conditioned due to the complex FSI circumstance.

Hence, more simplified models for theoretical calculation are needed for acoustic actuation. It is noted that the structure resonance of a micro-swimmer (related to the second term of Eq. (2.12)) may play an important role in propulsion (that is the reason why we consider the effect of the mass of the AFMS in Chapter 3). For example, for a bubble-based acoustic micro-swimmer, as shown in Figure 2-12 [186], the theoretical resonant frequency f_0 of the gas bubble can be estimated by [187]:

$$f_0 = \frac{1}{2\pi} \sqrt{\frac{\kappa_B P_B}{\rho_0 L_0 L_B}}, \qquad (2.13)$$

where κ_B is a frequency-dependent parameter related to the thermodynamic process, P_B the initial pressure inside the bubble, ρ_0 the fluid density, L_B the bubble length, and L_0 the length of a liquid column outside the bubble (see Figure 2-12). If the surface tension effect is considered, a correction factor, which is in connection with the geometry of the bubble and the surface tension of the water-air interface, will be introduced into Eq.

(2.13) [188]. The oscillation amplitude and the propulsive force can also be estimated at resonance [189].

For a flagellated microrobot, e.g., a sperm-like artificial micro-swimmer, the dynamic behavior is more difficult to predict. Nevertheless, the review of natural microorganisms reminds us that we can convert this problem into a simple so-called hyper-diffusion problem [38], in which the drag force and the elastic force on the tail are balanced. Specifically, the simplification can bring about a PDE that governs the oscillation of a cantilever beam (the flagellum) which has oscillatory boundary conditions at its clamped end (the head), which will be further discussed in Chapter 3.

As we have mentioned, many artificial micro-swimmers are bio-inspired. However, most studies only focus on the actuation strategies, fabrication processes, or experimental techniques; and the theoretical aspect (i.e., the principles of design and optimization) based on the swimming mechanisms at LRN is insufficiently addressed. Hence, as listed in Table 2-2, we categorized the references of natural and artificial micro-swimmers based on the types of propulsion mechanisms to remind the close relationship between them. Among them, the success in the theoretical description of microorganisms propelled by oscillating flagella [25, 38, 80, 190, 191] has inspired our preliminary work on AFMSs described in the next chapters.
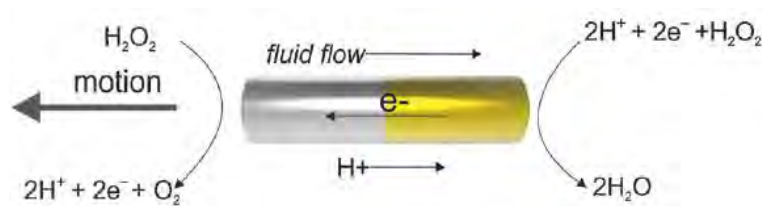
Figure 2-11. Some examples of theoretical studies of artificial micro-swimmers: schematic of motion of a Pt–Au nanorod driven by the catalytic decomposition of hydrogen peroxide. Reproduced with permission [140]. Copyright 2015, Wiley.
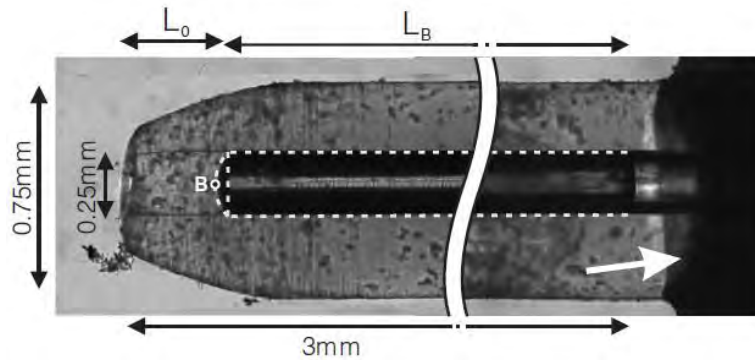
Figure 2-12. Some examples of theoretical studies of artificial micro-swimmers: a detailed image of an acoustic bubble actuator with the middle part removed, and the dark cylinder in the tube being the air bubble. Reproduced with permission [186]. Copyright 2006, IOP Publishing.

Table 2-2. Categorized references of theoretical studies on propulsion mechanisms of microorganisms and their artificial counterparts.

Propulsion mechanisms	References of natural micro-swimmers	References of artificial micro-swimmers
Helical filament	[23, 31, 82-84, 86, 87, 192-198]	[10, 11, 156, 199-203]
Undulating flagellum	[17, 25, 27, 38, 80, 106, 117, 190, 191]	[7, 41, 73, 110, 116, 168, 202, 204, 205]
Cilia (multiple flagella)	[61, 88, 206-209]	[210, 211]
Propagation of kinks (without flagellum)	[212-214]	[161, 215]

2.4.2 Theoretical studies on the modeling of steering the AFMS

It should be noted that the models of the AFMS are usually 1D, which confines the swimmer's motion to a straight line. Considering the need for manipulation or steering

in applications, such a 1D model is insufficient. Establishing at least a 2D AFMS model to address plane motion is therefore indispensable.

Inspired by Purcell's three-link swimmer [34], a flexible flagellum has been modeled by using multiple rigid bars linked by flexible joints (aka. the bar-joint model) [43], which intrinsically fulfills the inextensible constraints of a flexible tail [216, 217]. As for the bar-joint model, let us shed some light on the possible strategies for steering a flagellated micro-swimmer propelled acoustically. We focus on this micro-swimmer because of the anticipation of its great potential in medical applications, considering the facts that ultrasound systems have been the most adopted clinical tools for diagnosis and therapy and a sperm-like structure is effortless to fabricate through 3D printing. It is noted that the governing equations for 2D flagellar dynamics are normally of significant non-linearity due to the geometric nonlinearity of the flagellum and the influence of the rigid body motion. Besides, decoupling of the equations is generally difficult and may involve improper simplification and render convergence problems. Therefore, a discrete flagellum model is desired to solve the swimming problem. In 1976 [34], Purcell proposed a symmetric linkage with three links articulated at two hinges, known as Purcell's three-link swimmer, which could be regarded as the "simplest animal" that could achieve locomotion at LRNs. Purcell demonstrated that this swimmer would be propelled along a straight line over one cycle of sequentially moving its front and rear bars. The dynamics of Purcell's three-link swimmer has been further investigated since then [73, 218-221]. Inspired by Purcell's three-link swimmer, using multi-link bars or bar-joint models, the dynamics of flexible flagella has been modeled. Alouges et al. [43] proposed a slender magneto-elastic swimmer, along which the magnetic-induced torques were distributed, and the governing equations of the elastic tail were reduced to a system of ordinary differential equations (ODEs). Their

group has also investigated the optimal stroke of a multi-link swimmer based on the criterion of optimal energy efficiency [222]. Moreau et al. [223] compared the classical elasto-hydrodynamic formulation with the bar-joint model via the coarse-graining formalism and demonstrated that the latter could achieve better numerical performance.

It is generally nontrivial to verify and correct micro-swimmer models experimentally because geometries and material properties are often uncertain (or undermined in literature). In addition, the wiggling profile of a flagellum is difficult to capture under a microscope. Hence, numerical simulations dealing with FSI, which are usually based on the finite element method (FEM), were more desirable to verify a simplified micro-swimmer model. As we have mentioned before, Rorai et al. [17] studied a sperm-like micro-swimmer in a 3D infinite domain by FEM and demonstrated an excellent agreement between the SBT and the FSI simulations in terms of the propulsive matrix coefficients (see Figure 2-3). Nevertheless, the dynamic motion of the flagellum was specified *a priori*, and the swimmer for each time was fixed, i.e., the elasticity of the flagellum and the resultant rigid-body motion were not investigated. Curatolo et al. [99] employed the automatic remeshing technique [224, 225] to couple the structure's rigid-body motion with FSI simulations for a fish-like swimmer (see Figure 2-4). However, they did not compare their simulation results with those of RFT or SBT.

Undoubtedly, differences exist between the results of FSI simulations and the RFT or SBT models due to various reasons. For example, the RFT and SBT can hardly address fluid problems around a flagellum tip or a head-flagellum joint [17]. The fluid force exerted on a head is also difficult to estimate because the head is normally neither a sphere nor a slender body. Most importantly, the RFT and SBT are initially established for a slender cylindrical body, but the flagellum in 2D simulations

(considering that 3D simulations are computationally too demanding) approximates a slender body with rectangular cross-sections, which is often the case in experiments (e.g., [7]). In addition, the most prevailing AFMS fabrication is based on layer-by-layer photocuring (i.e., 3D printing) [8], which leads to flagella with rectangular cross-sections and hence, the need for modifying SBT and RFT for them.

The SBT for arbitrary cross-section has been developed by adding a dimensionless coefficient tensor **K** [226], depending only on the cross-sectional geometry, to the fluid velocity field. Borker et al. [227] extended this method to particle dynamics in shear flows and determined the magnitudes of components of **K** through FSI simulations. However, such a geometry-dependent **K** is insufficient to predict the locomotion of an AFMS because of the aforementioned complexities. In particular, when dealing with AFMS turning, the corrected SBT is still very difficult to solve [228]. Hence, we argue that a correction to RFT, considering both the effect of the non-circular cross-section and the match of the linear terminal speed with the corresponding FSI simulation, may be a better strategy for approximation.

2.5 Summary

In the first part of this chapter, we have recapitulated the historical studies and theoretical perspectives on natural micro-swimmers such as sperms, bacteria, protozoa, and algae. They use one or more appendages to advance, which can be relatively hard spirals that can rotate or flexible filaments that undergo whip-like motion. The fundamental principle of swimming through resistance-based thrust is the use of drag anisotropy at LRNs. RFT, SBT, and FEM simulations have also been developed to address more details of hydrodynamics. In short, a periodic nonreciprocal deformation

that can generate net propulsion arises from the interplay between the internal and external forces acting on each of the appendages, which has been clearly unveiled in the modeling of flagellated micro-swimmers.

In the second part of this chapter, the actuation methods of artificial micros-swimmers, classified into self-propulsion, external propulsion, and a combination of them, have been reviewed. A self-propulsion approach is generally based on local (electro-) chemical reactions, e.g., H_2O_2 decomposition at the surface of a nano- or micro-swimmer, by which the chemical energy can be converted into kinetic energy. External propulsions may involve magnetic, acoustic, optical, and thermal fields. Magnetic power is most employed because of its prospect of remote and wireless operation, directional movement, and biocompatibility. A magnetic micro-swimmer can be propelled via either a non-uniform or an oscillating magnetic field. Recently, acoustic actuation has been a considerably popular driving strategy because of its potential for medical applications and lab-on-chip devices. We have introduced acoustic microrobots driven by acoustic standing waves, resonant trapped bubbles, microstreaming, and head oscillation, which can generate substantial propulsive forces. The employment of optical and thermal energies and combinations of some of the aforementioned methods for micro-swimmer actuation have also been introduced in this chapter. The approach of establishing a 2D AFMS model to address plane motion has been finally mentioned, where a correction to the RFT is necessary.

Chapter 3. 1D model of AFMS based on the RFT —— straight motion

3.1 Problem statement for acoustic propulsion

An experimental system for actuating an AFMS is sketched in Figure 3-1. The actual experimental system is generally built on a glass slide [7, 13], and an acoustic transducer adheres to the glass slide to generate sound waves. Because the acoustic transducer is much larger than the microchannel, the acoustic wave inside the microchannel can be simplified as a plane wave that propagates along a prescribed wave vector. The micro-swimmer is composed of an ellipsoidal rigid head and a slenderly flexible tail which is designated as a flagellum here. The micro-swimmer suspends in an aqueous solution and swims headwards at a speed v_{prop} propelled by the sound-induced flagellum whipping. Following the theoretical works [38] on the actuation induced by head wiggling, we denote the motion of the rigid head by the translational displacement $y_0(t)$ and a rotational angle $\theta_0(t)$, as shown in Figure 3-2. Under the acoustic actuation, it is intuitive to presume that both $y_0(t)$ and $\theta_0(t)$ should be periodic with the acoustic frequency f. The wall of the microchannel is assumed to be the sound hard wall. A sound hard wall is a kind of ideal acoustic medium with a large acoustic impedance so that the incident waves can be completely reflected. Accordingly, standing waves may come forth in the microchannel, which will be assumed in our simulation of the head motion.

We assume that the AFMS wiggles and whips its flagellum in the plane of acoustic wave propagation. This concurs with the experimental observation [13]. In biological systems, most observation of flagellum whipping also indicates that the motion is 2D [30, 41, 229]. We further assume that the Euler-Bernoulli beam theory is sufficiently

accurate to elucidate the flagellum motion and propulsion, following Refs. [35, 38, 230]. It should be remarked that the results derived from this linear assumption are conceivably to be highly in agreement with the large-amplitude ones [39], despite that the actual flagellum deflection is not small [35]. As shown in Figure 3-3, the head of the micro-swimmer is assumed to be a rigid end with a prescribed translation and rotation. Thus, the flagellum is considered as a cantilever beam agitated by the motion of the clamped end. For the expected medical application and also because of the experiments described, the materials of the micro-swimmer are assumed to be a kind of organic polymer, such as the polypyrrole (PPy) in Ref. [13] and the polyethylene glycol (PEG) in Ref. [7]. Thus, we employ the Kelvin-Voigt viscoelastic model to account for the inherent viscous effect.

Inertia is inconsequential to a living microorganism in the LRN regime [26, 34] so that the mass was not involved in the past models [33, 35, 38, 230]. This gives a misconception that all the inertial terms in both fluid and solid domains can be neglected upon the LRN assumption. Nevertheless, the foundation of the RFT is the Stokes equation, wherein only the inertia of fluid is neglected. In addition, the expression of the Reynolds number is related to the density of the fluid but irrelevant to that of a flagellum. Therefore, it is necessary to scrutinize the effect of inertia of a flagellum based on the RFT especially when the flagellum whips at a high frequency under external actuation. Accordingly, in order to clarify the frequency dependence of the terminal velocity and the motility of the AFMS in the following sections, we take into account the density of the flagellum in our model.
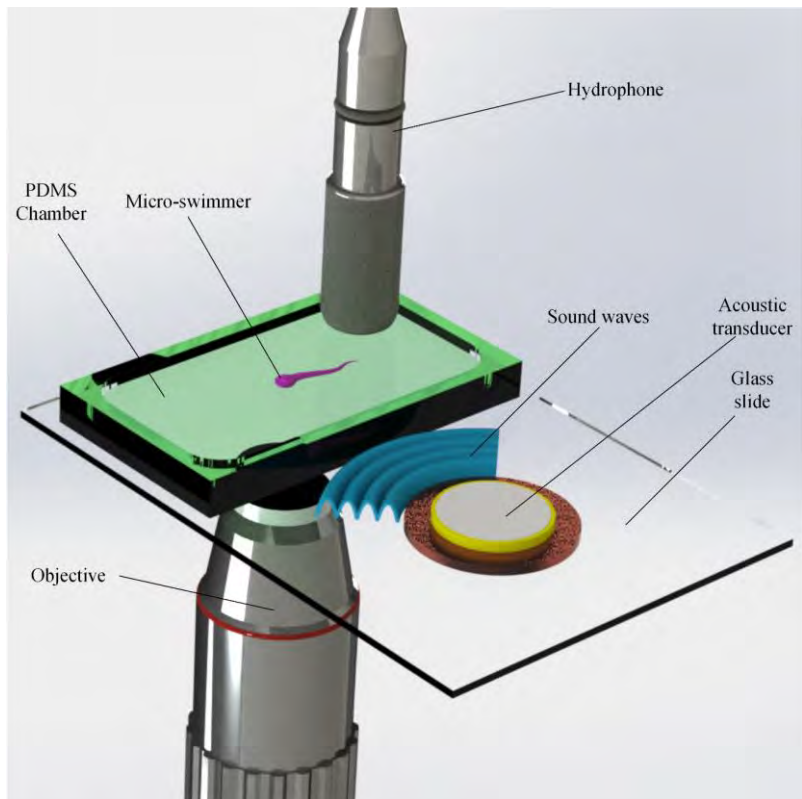
Figure 3-1. Sketch of the experimental system for 1D propulsion.
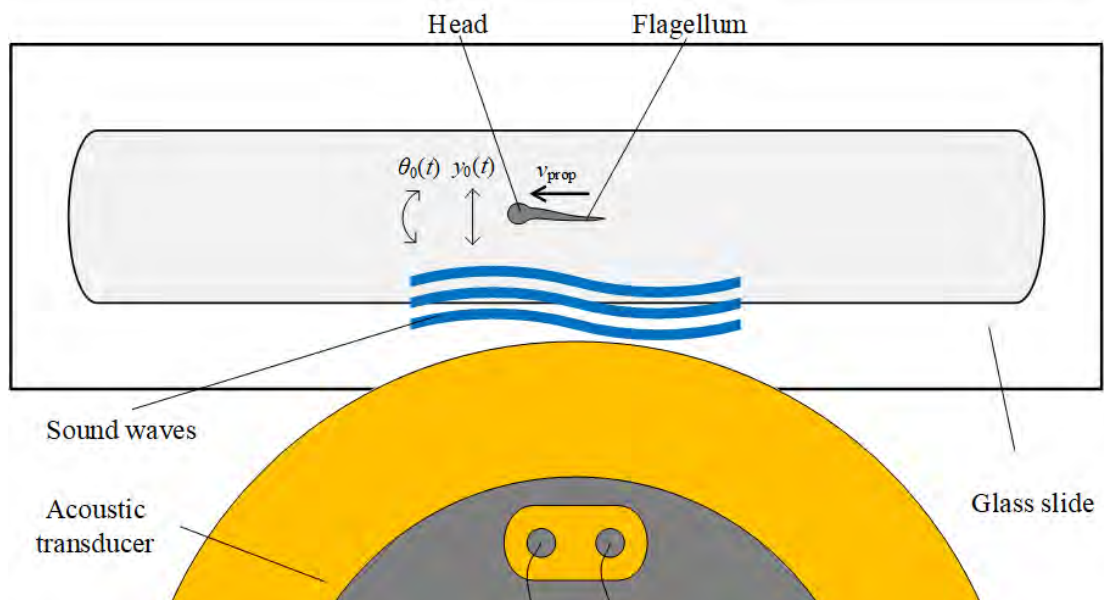
Figure 3-2. Diagrammatic sketches of the presumptive experimental scene for the problem statement.

3.2 Simulation of head wiggling under acoustic waves

In order to understand the actuation mechanism, a 3D FEM simulation for the head motion is carried out by using the COMSOL Multiphysics Pressure Acoustics module and Multibody Dynamics module. The two physical modules are coupled by the Acoustic-Structure Boundary module [231]. Following Kaynak et al. [7], we first consider the cone-shaped head with two hemispherical ends (a.k.a. the droplet-like shape), as depicted in Figure 3-3. One transient sound pressure distribution is exhibited in Figure 3-4, which is as a case of the overall configuration of the simulation. A droplet-like head is initially placed at the center of a $1000 \times 500 \times 200$ μm^3 box. The cubical box is assumed to be full of viscous fluids at room temperature. The head is featured by the radius r_1, r_2 ($r_1 > r_2$) of the end spheres and the distance D between their centers, and the line between the two centers is set to be the longitudinal axis of the head. It is prescribed to be only able to translate perpendicular to its longitudinal axis and rotate in the plane of acoustic wave propagation. Besides, it is considered as a rigid body with a sound hard wall to scatter the acoustic waves.

As shown in Figure 3-4, a plane wave is incident from the lower boundary to the upper one. To form standing sound waves, the left, right, and upper boundaries of the simulation box are set to be sound hard walls; only the lower boundary is set as a plane wave radiation border. On this border, a sinusoidal sound pressure with the amplitude p, the frequency f and the incident angle φ_i is applied. φ_i is set to be the angle between the wave vector and the longitudinal axis of the head, as shown in Figure 3-4. To specify the values of p and f, we refer to the clinical therapeutic ultrasound. As reviewed by Ter H.G. [232], the acceptable sound intensity I_{acou} is in the range from 0.125 W/cm^2 to 3 W/cm^2, and the frequency f from 0.75 MHz to 5 MHz. The frequency range we adopt in our simulation is from 0.75 MHz to 3.75 MHz. The amplitude of sound pressure is

43

then calculated using the relation between the acoustic pressure and the sound intensity for a plane wave [233], which is expressed as:

$$p = \sqrt{2I_{\text{acou}}\rho_0 c_0} \ , \tag{3.1}$$

where ρ_0 and c_0 denote the density and sound velocity of the acoustic medium, respectively. The product $\rho_0 c_0$ is called the characteristic acoustic impedance. In the human body, the tissue impedance is about 1.5×10^6 kg/m^2/s [234], which is close to that of water. Therefore, we set $\rho_0 = 10^3$ kg/m^3 and $c_0 = 1500$ m/s in our simulation. The amplitude of acoustic pressures, estimated from Eq. (3.1), can vary between 60 kPa and 300 kPa. In the simulation, the shear and bulk viscosity of the fluid domain are set according to the gastric fluid [235] to be 0.01 Pa·s and 0.002 Pa·s, respectively.

A battery of time-dependent simulations were carried out under two parametric sweeps, i.e., the sound pressure p from 60 kPa and 300 kPa, and the frequency f from 0.75 MHz to 3.75 MHz. The results of the head translation and rotation at two extreme frequencies for $\varphi_i = 90°$ are exhibited in Figure 3-5 and Figure 3-6, where the upward displacement and anticlockwise rotation are defined to be positive. Numerical simulations confirm that the displacement and rotating angle of the head are both harmonic functions of time with frequencies identical to the acoustic frequency, that is $y_0(t) = y_{0a} \sin \omega t$ and $\theta_0(t) = \theta_{0a} \sin(\omega t + \varphi_h)$, where $\omega = 2\pi f$ is the angular frequency of the actuation. The phase angle difference between the translational and rotational movement is denoted by φ_h. The amplitudes of the translational and rotational motion depend on the acoustic pressure and frequency, as shown in Figure 3-7 and Figure 3-8, respectively. The results indicate that the oscillating amplitude of the head is proportional to the sound pressure p and the reciprocal of acoustic frequency $1/f$. Thus, y_{0a} and θ_{0a} can be expressed as:

44

$$y_{0a} = K_u \frac{p}{f} \ , \ \theta_{0a} = K_\theta \frac{p}{f} \, , \tag{3.2a, b}$$

where K_u and K_θ denote the two coefficients of proportionality for the translation and rotation, respectively.

It should be noted that Eq. (3.2a) does tally with the theoretical expression of the displacement amplitude A_{acou} of an acoustic particle of a plane wave [233]:

$$A_{acou} = \frac{p}{\omega \rho_0 c_0} \, , \tag{3.3}$$

which expects that K_u is in the same order as $1/(2\pi\rho_0 c_0)$. It is apparent that the head can be approximately treated as a particle inside the acoustic medium because the sound wavelength is on the order of 1 mm under the prescribed conditions, far larger than the dimensions of the head. Therefore, the head oscillates in accordance with the acoustic wave. On the other hand, as one may notice from Figure 3-5 and Figure 3-6, the mean value of the displacement is different from zero in a period. It is a nonlinear phenomenon named the Stokes drift [236]. It is also due to the relatively small dimension of the head which will travel with the acoustic flow and move a net distance in each period. However, the effect of Stokes drift is ignored herein because we are not concerning about the small lateral trajectory of AFMSs in this thesis. Based on our simulation of a head referring to the actual acoustic micro-swimmer [7] with $r_1 = 25$ μm, $r_2 = 12.5$ μm and $D = 25$ μm, we can obtain different values of K_u (in the unit of μm/Pa/s), K_θ (in the unit of rad/Pa/s) and φ_h with different incident angles φ_i, as listed in Table 3-1. φ_h could be 180° if the acoustic wave vector is perpendicular to the longitudinal axis of the head at $t = 0$, which is the case of $\varphi_i = 90°$ in Table 3-1. And it is actually not far away from 180° at other φ_i. K_u and K_θ will slightly differ when φ_i

changes a little. This phenomenon may be dependent on the specific outline of the head, which determines the pattern of the scattered field. The final acoustic scattered field will influence the values of K_u and K_θ, which brings about the fluctuations of the amplitude of head oscillation, resulting in the error bars as shown in Figure 3-7 and Figure 3-8. It is seen that K_u, K_θ, and φ_h vary with the geometry of the head. As listed in Table 3-2, the rotational motion strictly vanishes if a head is symmetric about a transverse plane (i.e., $r_1 = r_2$), but becomes nonnegligible with φ_h being 180° for a droplet-like (i.e., $r_1 > r_2$) head. Note that the phase angle difference φ_h could deviate from 180° if the acoustic wave vector is not normal to the longitudinal axis of the head. The droplet-like head has the largest K_u and nonvanishing K_θ, it is expected that the droplet-like head would be the best choice for propulsion. Nevertheless, according to Table 3-1, the coefficients of the amplitude can almost remain steady for a given head under different incident angles of sound waves, despite the influence of the lateral trajectory of the micro-swimmer herein.
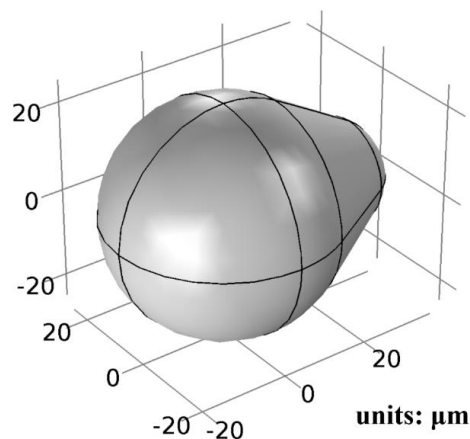
Figure 3-3. A three-dimensional model of the head with a droplet-like shape.
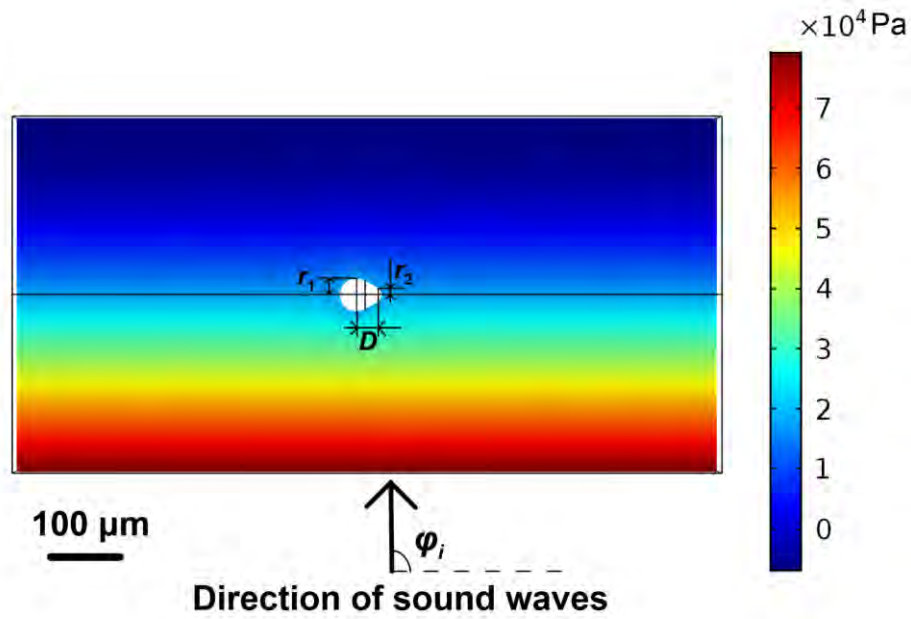
Figure 3-4. Instantaneous sound pressure distribution for the fluid domain.
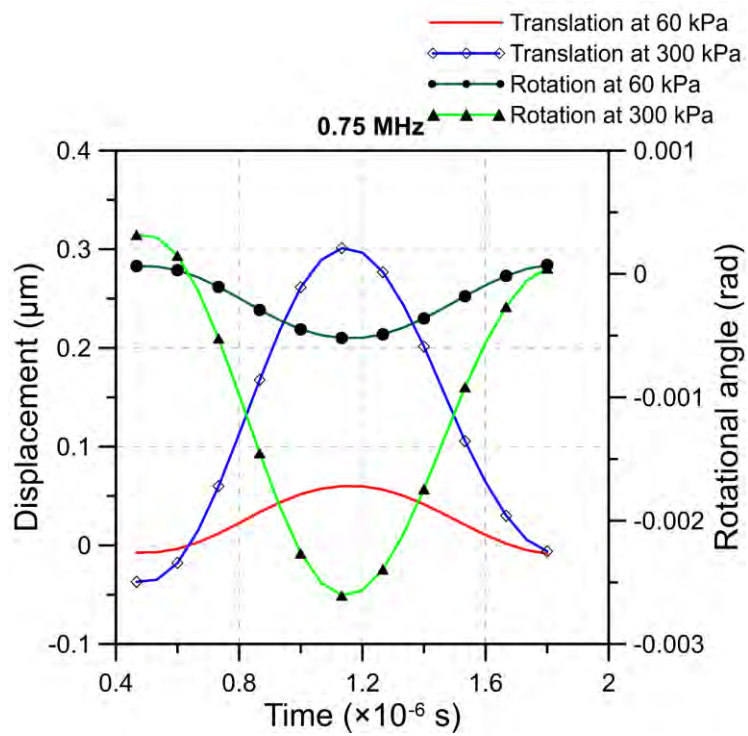
Figure 3-5. Amplitude vs. time at 0.75 MHz for one period at $\varphi_i = 90°$ of the head with a droplet-like shape.
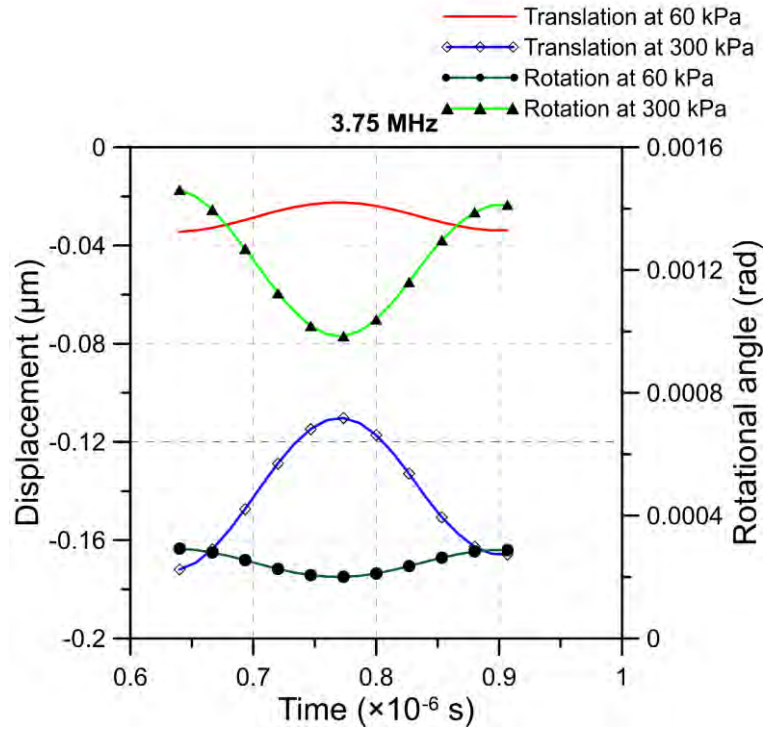
Figure 3-6. Amplitude vs. time at 3.75 MHz for one period at $\varphi_i = 90°$ of the head with a droplet-like shape.
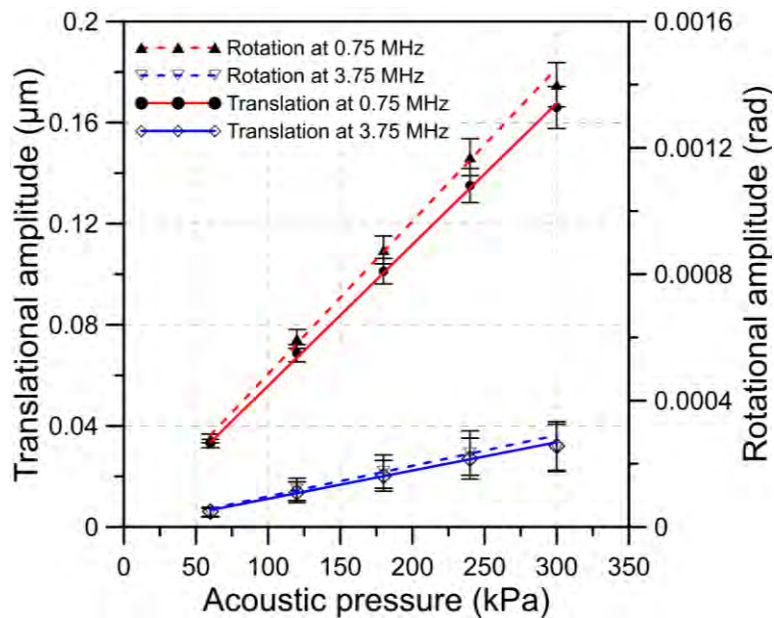
Figure 3-7. Amplitude for each sound pressure under two extreme frequencies at $\varphi_i = 90°$ of the head with a droplet-like shape.
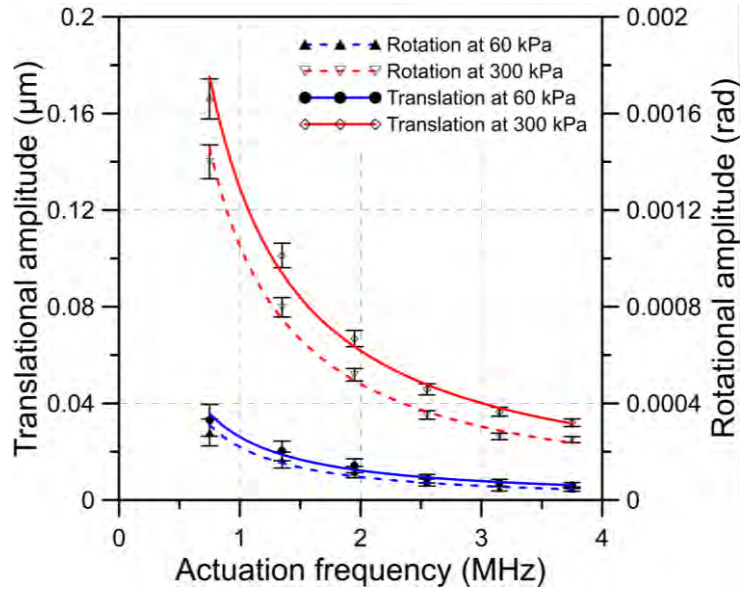
Figure 3-8. Amplitude for each actuation frequency under two extreme sound pressures at $\varphi_i = 90°$ of the head with a droplet-like shape.

Table 3-1. Values for the actuation parameters K_u, K_θ and φ_h of the droplet-like head with different φ_i.

φ_i	K_u (µm/Pa/s)	K_θ (rad/Pa/s)	φ_h
90°	0.419	0.00363	180°
89.983°	0.416	0.00360	179.973°
90.017°	0.407	0.00361	180.011°

Table 3-2. Values for the actuation parameters K_u, K_θ and φ_h with different head shapes at $\varphi_i = 90°$.

Shape	r_1 (µm)	r_2 (µm)	D (µm)	K_u (µm/Pa/s)	K_θ (rad/Pa/s)	φ_h
Droplet	25	12.5	25	0.419	0.00363	180°
Spherocylinder	25	25	25	0.373	0	/
Sphere	25	25	0	0.396	0	/

49

3.3 The governing equations of the flagellum for the continuous model

As indicated in Figure 3-9, the longitudinal axis and the transverse axis of the flagellum with the origin at the fixed end are denoted as the x-axis and y-axis, separately; the length and the area of the cross-section are denoted by L and $A_s(x)$, respectively. The longitudinal and lateral displacement fields, designated as x_s and y_s, respectively, are assumed as:

$$x_s = -y\Theta(x,t), \; y_s = y_c(x,t), \tag{3.4a, b}$$

where $\Theta(x,t)$ and $y_c(x,t)$ denote the rotational angle and the lateral displacement of the centerline of the flagellar profile, respectively. And the Cauchy strain $\boldsymbol{\varepsilon}$ for the Euler-Bernoulli beam can be expressed as:

$$\boldsymbol{\varepsilon} = \frac{1}{2}(\mathbf{x} \otimes \nabla + \nabla \otimes \mathbf{x}), \tag{3.5}$$

where ∇ is the Hamiltonian differential operator, and $\mathbf{x} = [x_s, y_s]^{\mathrm{T}}$ the displacement vector, $\otimes$ the outer products. Then the substitution of the small-rotating-angle assumption for the Euler-Bernoulli beam, which is given by

$$\Theta(x,t) = \frac{\partial y_c}{\partial x}, \tag{3.6}$$

will reach the expression of the longitudinal normal strain ε given by

$$\varepsilon = -y\frac{\partial^2 y_c}{\partial x^2}. \tag{3.7}$$

The material of the micro-swimmer is considered to be a kind of isotropic polymer. As per Ref. [237], the Kelvin-Voigt viscoelastic model is employed, i.e., the constitutive relation of normal stress σ and the normal strain ε is expressed as:

$$\sigma = E\varepsilon + \eta\frac{\partial\varepsilon}{\partial t}, \tag{3.8}$$

where E and η are Young's modulus and the material viscosity coefficient, respectively [238-240]. Hence, the strain energy U_σ over the whole volume Ω can be expressed as:

$$U_\sigma = \int_\Omega \left(\int_\varepsilon \sigma d\varepsilon \right) d\Omega, \tag{3.9}$$

and the kinetic energy T_σ in terms of the linear density ρ_s of the flagellum is given by

$$T_\sigma = \frac{1}{2}\int_0^L \rho_s A_s(x) \left(\frac{\partial y_c}{\partial t} \right)^2 dx, \tag{3.10}$$

then, the work done by nonconservative forces W_σ is expressed as:

$$W_\sigma = \int_0^L \int_{y_c} f_{f\perp}(x,t) dy_c dx + \int_{y_c} F_{exty} dy_c \Big|_{x=0} + \int_\Theta \tau_{ext} d\Theta \Big|_{x=0}, \tag{3.11}$$

where $f_{f\perp}(x,t)$ represents the vertical fluid force distribution for the unit length of the flagellum, which is perpendicular to the longitudinal axis of the flagellum; F_{exty} and τ_{ext} denote the external torque and vertical force at the clamped end of the flagellum, respectively. Now we can apply the variational techniques to reach the variations of the above energies, which are expressed as:

$$\delta U_\sigma = \int_0^L \frac{\partial^2}{\partial x^2}\left[EI(x)\frac{\partial^2 y_c}{\partial x^2} \right]\delta y_c dx + \int_0^L \frac{\partial^2}{\partial x^2}\left[\eta I(x)\frac{\partial^3 y_c}{\partial x^2 \partial t} \right]\delta y_c dx$$
$$+ \left[EI(x)\frac{\partial^2 y_c}{\partial x^2} + \eta I(x)\frac{\partial^3 y_c}{\partial x^2 \partial t} \right]\delta \frac{\partial y_c}{\partial x}\Big|_0^L - \frac{\partial}{\partial x}\left[EI(x)\frac{\partial^2 y_c}{\partial x^2} + \eta I(x)\frac{\partial^3 y_c}{\partial x^2 \partial t} \right]\delta y_c \Big|_0^L \tag{3.12}$$

$$\delta T_\sigma = \frac{\partial}{\partial t}\left[\int_0^L \rho_s A_s(x)\frac{\partial y_c}{\partial t}\delta y_c dx \right] - \int_0^L \rho_s A_s(x)\frac{\partial^2 y_c}{\partial t^2}\delta y_c dx, \tag{3.13}$$

$$\delta W_{\sigma} = \int_{0}^{L} f_{f\perp}(x,t)\delta y_{c}\mathrm{d}x + F_{\mathrm{ext}y}\delta y_{c}\Big|_{x=0} + \tau_{\mathrm{ext}}\delta \frac{\partial y_{c}}{\partial x}\Big|_{x=0} \; , \quad (3.14)\mathrm{where} \quad I(x) = \int_{A_{s}} y^{2}\mathrm{d}A_{s} \quad \mathrm{is}$$

the second moment of area of the flagellum cross-section, which is a function of x in case the flagellum is non-uniform. Now, we can substitute Eqs. (3.12), (3.13) and (3.14) into Hamilton's principle [40]:

$$\delta \int_{t_{1}}^{t_{2}} \left(T_{\sigma} - U_{\sigma} + W_{\sigma} \right) \mathrm{d}t = 0 , \tag{3.15}$$

then we will reach the EOM of the flagellum, which is expressed as:

$$\rho_{s} A_{s}(x)\frac{\partial^{2} y_{c}}{\partial t^{2}} + \frac{\partial}{\partial x^{2}}\left(EI(x)\frac{\partial^{2} y_{c}}{\partial x^{2}} + \eta I(x)\frac{\partial^{3} y_{c}}{\partial x^{2}\partial t} \right) = f_{f\perp}(x,t), \quad 0 \le x \le L . \tag{3.16}$$

We can also obtain the internal bending moment M and shear force Ξ for the unit length of the flagellum from Eq. (3.12), which are expressed as:

$$\begin{cases} M(x,t) = EI(x)\dfrac{\partial^{2} y_{c}}{\partial x^{2}} + \eta I(x)\dfrac{\partial^{3} y_{c}}{\partial x^{2}\partial t} \; ; \\[2mm] \Xi(x,t) = -\dfrac{\partial}{\partial x}\left[EI(x)\dfrac{\partial^{2} y_{c}}{\partial x^{2}} + \eta I(x)\dfrac{\partial^{3} y_{c}}{\partial x^{2}\partial t} \right] . \end{cases} \tag{3.17}$$

To avoid the complex analysis of external torque τ_{ext} and force $F_{\mathrm{ext}y}$ at the head end (actually, they will be addressed in Chapter 4), the boundary conditions are employed instead. The associated boundary conditions for this cantilever beam are formulated as:

$$\begin{cases} \mathrm{at}\ x = 0 : y_{c} = y_{0a}\sin\omega t \; , \quad \dfrac{\partial y_{c}}{\partial x} = \theta_{0a}\sin\left(\omega t + \varphi_{h}\right) \; ; \\[2mm] \mathrm{at}\ x = L : M(L,t) = 0 \; , \quad \Xi(L,t) = 0 \; . \end{cases} \tag{3.18}$$

It is noteworthy that the clamped end wiggles with the head with the amplitude determined by Eqs. (3.2a, b), and the phase angle difference φ_{h} could deviate from 180° if the acoustic wave vector is not normal to the longitudinal axis of the head.

In order to simplify the problem, the shape of the cross-section is simplified to be circular; and the diameter d_s of the cross-section is assumed to be much smaller than the length of the tail. Under such restrictions, the tail appears to be sufficiently slender, and the vertical linear fluid force $f_{f\perp}$ would be proportional to the local lateral velocity in light of the so-called SBT [18, 21, 26, 241]. In the LRN regime, the fluid force can be analytically solved by adding the Stokeslet (Green's function for a Stokes flow) and dipole strength together to satisfy the boundary conditions at the fluid-structure interface. Eventually, the fluid force perpendicular to the flagellum can be expressed as:

$$f_{f\perp}(x,t) = -c_\perp \frac{\partial y_c}{\partial t}, \qquad (3.19)$$

where the minus sign is owing to the fact that fluid force always hinders the local movement of the flagellum. The normal drag coefficient $c_\perp$ is expressed as [21]:

$$c_\perp(x) = \frac{4\pi\mu}{\ln(2L/d_s(x)) - 1/2 + \ln 2 - (1 - \pi^2/12)/\ln(2L/d_s(x))}. \qquad (3.20)$$

The tangent drag coefficient $c_\parallel$ can be derived in a similar technique, which is given by [21]:

$$c_\parallel(x) = \frac{2\pi\mu}{\ln(2L/d_s(x)) - 3/2 + \ln 2 - (1 - \pi^2/12)/\ln(2L/d_s(x))}. \qquad (3.21)$$

It is more convenient to deduct the rigid motion of the flagellum from y_c as:

$$y_{cr} = y_c - y_{0a}\sin\omega t - x\theta_{0a}\sin(\omega t + \varphi_h). \qquad (3.22)$$

Considering brevity, the following non-dimensional terms are now imported:

$$X = \frac{x}{L} \ , \ \tilde{t} = ft \ , \ \gamma = \frac{\eta \omega}{E} \ , \ \xi_{0a} = \frac{y_{0a}}{L} \ ,$$

$$\xi_c\left(X,\tilde{t}\right) = \frac{y_c\left(x,t\right)}{L} \ , \ \xi_{cr}\left(X,\tilde{t}\right) = \frac{y_{cr}\left(x,t\right)}{L} \ , \tag{3.23}$$

$$H\left(X\right) = \frac{\rho_s A_s\left(x\right) f^2}{E} \ , \ Z\left(X\right) = \frac{c_\perp\left(x\right) f}{E} \ , \ J\left(X\right) = \frac{I\left(x\right)}{L^4} \ .$$

In which, γ denotes the ratio of loss modulus to storage modulus for a Kelvin-Voigt model [237], i.e., the material damping. The substitution of Eqs. (3.17), (3.18), (3.19), (3.22) and (3.23) into Eq. (3.16) leads to the following non-dimensional equations governing the flagellum motion:

$$\left| \begin{array}{l} H \dfrac{\partial^2 \xi_{cr}}{\partial \tilde{t}^2} + Z \dfrac{\partial \xi_{cr}}{\partial \tilde{t}} + \dfrac{\partial^2}{\partial X^2}\left(J \dfrac{\partial^2 \xi_{cr}}{\partial X^2} + \dfrac{\gamma J}{2\pi} \dfrac{\partial^3 \xi_{cr}}{\partial^2 X \partial \tilde{t}} \right) \\[3mm] = \xi_{0a}\left(4\pi^2 H \sin 2\pi\tilde{t} - 2\pi Z \cos 2\pi\tilde{t} \right) \\[2mm] \quad + X\theta_{0a}\left[4\pi^2 H \sin\left(2\pi\tilde{t} + \varphi_h\right) - 2\pi Z \cos\left(2\pi\tilde{t} + \varphi_h\right) \right] \ , \ 0 \le X \le 1 \ ; \\[3mm] \text{at } X = 0 : \xi_{cr} = 0 \ , \ \dfrac{\partial \xi_{cr}}{\partial X} = 0 \ ; \\[3mm] \text{at } X = 1 : J \dfrac{\partial^2 \xi_{cr}}{\partial X^2} + \gamma J \dfrac{\partial^3 \xi_{cr}}{\partial X^2 \partial \tilde{t}} = 0 \ , \ \dfrac{\partial}{\partial X}\left(J \dfrac{\partial^2 \xi_{cr}}{\partial X^2} + \dfrac{\gamma J}{2\pi} \dfrac{\partial^3 \xi_{cr}}{\partial X^2 \partial \tilde{t}} \right) = 0 \ . \end{array} \right. \tag{3.24}$$

Note that the variable ξ_{cr} in Eq. (3.24) is not the non-dimensional lateral displacement ξ_c of the flagellum, and there are only Dirichlet boundary conditions in Eq. (3.24), which are different from those in Eq. (3.18). Based on Eq. (3.22), ξ_c is expressed as:

$$\xi_c\left(X,\tilde{t}\right) = \xi_{cr}\left(X,\tilde{t}\right) + \xi_{0a} \sin 2\pi\tilde{t} + X\theta_{0a} \sin\left(2\pi\tilde{t} + \varphi_h\right) . \tag{3.25}$$
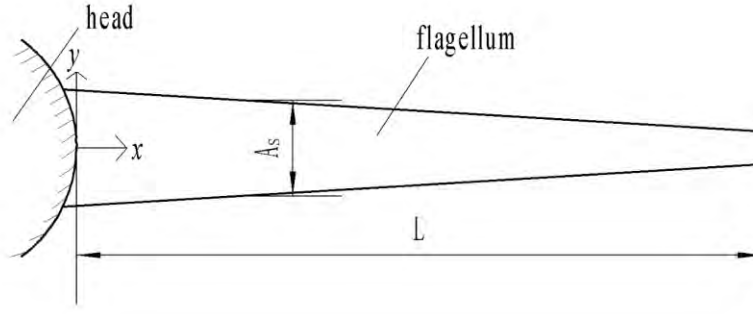
Figure 3-9. The mechanical model for the flagellum.

3.4 The terminal speed of a flagellated micro-swimmer along a straight line

To calculate the speed of the artificial micro-swimmer based on the lateral displacement of the flagellum $\xi_c\left(X,\tilde{t}\right)$, the RFT [17, 31, 68] is employed, which is a simple yet sufficiently accurate theory to estimate the propulsive force of microorganisms [38].

As shown in Eq. (3.19), the fluid force is in nature a sort of drag, which is always opposite to the direction of the local velocity $\partial y_c / \partial t$. As illustrated in Figure 3-10, the forward propulsion f_{prop} within an infinitesimal flagellum segment, dx, is determined by the difference between the horizontal components of two forces $f_{f\perp}$ and $f_{f\parallel}$ as follows:

$$f_{\text{prop}} = f_{f\parallel}\cos\Theta - f_{f\perp}\sin\Theta , \tag{3.26}$$

where Θ is the slope angle of the flagellum, which is approximately equal to $\partial y_c / \partial x$, and expressions for $f_{f\perp}$ and $f_{f\parallel}$ are similar to Eq. (3.19). Typically, the velocity v_{prop} of the AFMS is proportional to the total propulsive force $\int_L f_{\text{prop}} dx$ with the scale factor

$c_{\parallel}$. However, the drag of the head F_{head} cannot be neglected due to the sizable radius in contrast to that of the flagellum. Simplifying the head to be a sphere with a larger radius $R_H = r_1$, the drag of the head can be given by [68]

$$F_{\text{head}} = 6\pi\mu R_H v_{\text{prop}} . \tag{3.27}$$

Taking into account the resistance of the head, the balance of the fluid forces over the whole micro-swimmer is given by

$$\int_L f_{\text{prop}} dx = F_{\text{head}} + \int_L v_{\text{prop}} \left(c_{\parallel} \cos^2 \Theta + c_{\perp} \sin^2 \Theta \right) dx \simeq F_{\text{head}} + \int_L c_{\parallel} v_{\text{prop}} dx . \tag{3.28}$$

Substituting Eqs. (3.26) and (3.27) into Eq. (3.28), and taking the average value over a period, the time-averaged terminal velocity $\bar{v}_{\text{prop}}$ is expressed as:

$$\bar{v}_{\text{prop}} = \frac{1}{\int_0^L c_{\parallel} dx + 6\pi\mu R_H} \int_0^{\frac{2\pi}{\omega}} \frac{\omega}{2\pi} \int_0^L \left| \left(c_{\parallel} - c_{\perp} \right) \frac{\partial y_c}{\partial t} \frac{\frac{\partial y_c}{\partial x}}{1 + \left(\frac{\partial y_c}{\partial x} \right)^2} \right| dx dt . \tag{3.29}$$

Using the dimensionless terms given in Eq. (3.23), Eq. (3.29) will be recast to

$$\bar{v}_{\text{prop}} = \frac{1}{L\int_0^1 c_{\parallel} dX + 6\pi\mu R_H} \int_0^1 \frac{L^2\omega}{2\pi} \int_0^1 \left| \left(c_{\parallel} - c_{\perp} \right) \frac{\partial \xi_c}{\partial \tilde{t}} \frac{\frac{\partial \xi_c}{\partial X}}{1 + \left(\frac{\partial \xi_c}{\partial X} \right)^2} \right| dX d\tilde{t} . \tag{3.30}$$

Ultimately, the substitution of $\xi_c\left(X, \tilde{t}\right)$ determined by Eqs. (3.24) and (3.25) into Eq. (3.30) leads to the terminal velocity of the micro-swimmer.

There are certainly more accurate theories to evaluate the propulsive force based on the singular solutions for the equations of a Stokes flow such as the Regularized Stokeslet method [92] and Lighthill SBT [26]. Nonetheless, if the wavelength of the

profile is greater than a quarter of the tail, or the ratio of length to radius for the tail is larger than 10, the RFT does not differ much from other theories [17, 23]. This condition will be enforced in our succeeding studies to ensure the accuracy of Eq. (3.30).

Following the convention in [242, 243], the motility of the micro-swimmer V_{cs} can be defined as:

$$V_{cs} = \bar{c}\,\frac{\bar{v}_{prop}}{Lf},$$

(3.31)

where the factor $\bar{c}$ reflects the relative resistance between the head and the flagellum. In case that the flagellum is sufficiently slender, i.e., $c_\perp = 2c_\parallel$ according to Ref. [68], and not connected with a head, $\bar{c} = 1$. For a uniform flagellum, the motility V_{cs} and the factor $\bar{c}$ are respectively expressed as:

$$V_{cs} = \int_0^1 \int_0^1 -\left(\partial \xi_c / \partial \tilde{t}\right) \cdot \left(\partial \xi_c / \partial X\right) \Big/ \left[1 + \left(\partial \xi_c / \partial X\right)^2\right] dX d\tilde{t},$$

(3.32)

$$\bar{c} = \frac{1 + 6\pi\mu R_H / \left(Lc_\parallel\right)}{c_\perp / c_\parallel - 1},$$

(3.33)

where V_{cs} only depends on the normalized wiggling profile of the flagellum.

In addition to the optimal speed, one may concern the impact of kinematic parameters on actuation efficiency. According to Wiggins et al. [38], we can estimate the actuation efficiency E_{effi} of a flagellated micro-swimmer by comparing the power $\int_L f_{prop} v_{prop} dx$ for longitudinal propulsion to the power arising from the local transverse drag $f_{tran} = f_{f\parallel} \sin\Theta + f_{f\perp} \cos\Theta$ dissipated in transverse motions over a period, which is expressed as:

$$
\begin{aligned}
E_{\text{effi}} &= \int_0^{\frac{2\pi}{\omega}} \frac{\omega}{2\pi} \frac{\int_0^L f_{\text{prop}} v_{\text{prop}} \, dx}{\int_0^L f_{\text{tran}} \frac{\partial y_c}{\partial t} \, dx} \, dt \\
&= \int_0^{\frac{2\pi}{\omega}} \frac{\omega}{2\pi} \frac{v_{\text{prop}} \int_0^L \left(f_{f\parallel} \cos\Theta - f_{f\perp} \sin\Theta \right) dx}{\int_0^L \left(f_{f\parallel} \sin\Theta + f_{f\perp} \cos\Theta \right) \frac{\partial y_c}{\partial t} \, dx} \, dt \\
&= \int_0^{\frac{2\pi}{\omega}} \frac{\omega}{2\pi} \frac{v_{\text{prop}} \int_0^L \left[\left(c_\parallel - c_\perp \right) \frac{\partial y_c}{\partial t} \dfrac{\frac{\partial y_c}{\partial x}}{1 + \left(\frac{\partial y_c}{\partial x} \right)^2} \right] dx}{\int_0^L \left\{ \left[\left(c_\parallel - c_\perp \right) \left(\frac{\partial y_c}{\partial x} \right)^2 + c_\perp \right] \left(\frac{\partial y_c}{\partial t} \right)^2 \right\} dx} \, dt \\
&= \int_0^{\frac{2\pi}{\omega}} \frac{\frac{\omega}{2\pi} \left\{ \int_0^L \left[\left(c_\parallel - c_\perp \right) \frac{\partial y_c}{\partial t} \dfrac{\frac{\partial y_c}{\partial x}}{1 + \left(\frac{\partial y_c}{\partial x} \right)^2} \right] dx \right\}^2}{\left(\int_0^L c_\parallel \, dx + 6\pi\mu R_H \right) \int_0^L \left\{ \left[\left(c_\parallel - c_\perp \right) \left(\frac{\partial y_c}{\partial x} \right)^2 + c_\perp \right] \left(\frac{\partial y_c}{\partial t} \right)^2 \right\} dx} \, dt
\end{aligned}
\tag{3.34}
$$

Using the dimensionless terms given in Eq. (3.23), Eq. (3.34) will be recast to

$$
E_{\text{effi}} = \int_0^1 \frac{L \left\{ \int_0^1 \left[\left(c_\parallel - c_\perp \right) \frac{\partial \xi_c}{\partial \tilde{t}} \dfrac{\frac{\partial \xi_c}{\partial X}}{1 + \left(\frac{\partial \xi_c}{\partial X} \right)^2} \right] dX \right\}^2}{\left(L \int_0^1 c_\parallel \, dX + 6\pi\mu R_H \right) \int_0^1 \left\{ \left[\left(c_\parallel - c_\perp \right) \left(\frac{\partial \xi_c}{\partial X} \right)^2 + c_\perp \right] \left(\frac{\partial \xi_c}{\partial \tilde{t}} \right)^2 \right\} dX} \, d\tilde{t}
\tag{3.35}
$$
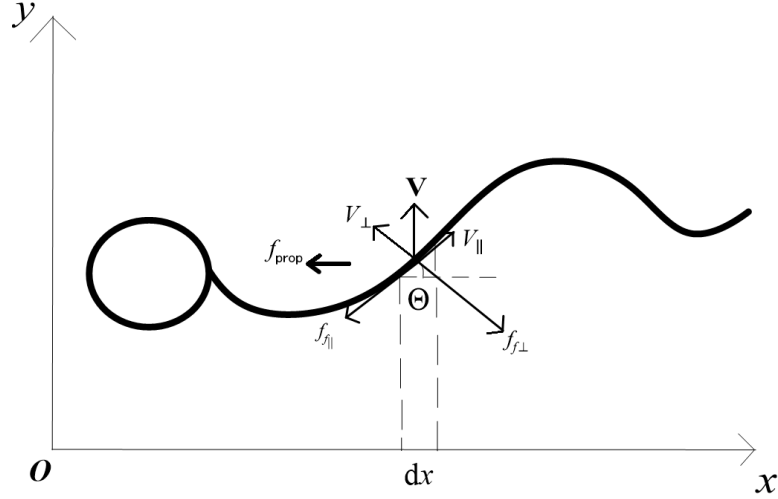
Figure 3-10. Derivation for the propulsive force based on the RFT.

3.5 Semi-analytical solutions for the 1D model

In what follows, to solve the inhomogeneous PDE (3.24) with boundary conditions, Eq. (3.24) will be truncated to an ODE without any boundary condition. This technique is in the light of the Galerkin method [238-240, 244], then Eq. (3.24) can be solved by numerical method directly. As a result, the dependent variable ξ_{cr} can be decomposed by a convergent series of basis functions in terms of the nth vibration mode Φ_n, expressed as:

$$\xi_{cr}\left(X,\tilde{t}\right)=\sum_{n=1}^{n_m}\Phi_n\left(X\right)q_n\left(\tilde{t}\right), \tag{3.36}$$

where n_m represents the number of terms to be accumulated, or in other words, the number of modal superpositions; q_n is the generalized coordinates which are explicit functions of the dimensionless time. To eliminate the boundary conditions for the cantilever beam, Φ_n is expressed with respect to the constant G_n as follows:

$$\Phi_n\left(X\right) = G_n\left[\cosh r_n X - \cos r_n X + \frac{\sin r_n - \sinh r_n}{\cosh r_n + \cos r_n}\left(\sinh r_n X - \sin r_n X\right)\right], \qquad (3.37)$$

where r_n are the solutions of the equation given by

$$\cosh r_n \cos r_n = -1. \qquad (3.38)$$

Eqs. (3.37) and (3.38) are the mode functions of an elastic cantilever beam with a uniform cross-section [245], which are normally exploited as the basis functions for non-uniform ones [239]. Optionally, r_n can be estimated by a fitting formula: $r_n = \left(n-0.5\right)\pi$. The constant G_n is to normalize the nth modal function, i.e., let:

$$\int_0^1 \Phi_n \Phi_m \mathrm{d}X = \begin{cases} 0, & n \neq m \\ 1, & n = m \end{cases}. \qquad (3.39)$$

Substituting Eq. (3.36) into Eq. (3.24), multiplying the resultant equation with Φ_j on both sides, and then, integrating the resultant equations over the whole flagellum, an equation set for $q_n\left(\tilde{t}\right)$ is resulted as:

$$\begin{aligned}
&\sum_{n=1}^{n_m} S_{Hjn}\frac{\partial^2 q_n}{\partial \tilde{t}^2} + \sum_{n=1}^{n_m}\left(S_{Zjn} + \frac{\gamma}{2\pi}S_{Jjn}\right)\frac{\partial q_n}{\partial \tilde{t}} + \sum_{n=1}^{n_m} S_{Jjn}q_n \\
&= \left(4\pi^2\xi_{0a}S_{Hj} + 4\pi^2\theta_{0a}S_{xHj}\cos\varphi_h + 2\pi\theta_{0a}S_{xZj}\sin\varphi_h\right)\sin 2\pi\tilde{t} \\
&\quad - \left(2\pi\xi_{0a}S_{Zj} - 4\pi^2\theta_{0a}S_{xHj}\sin\varphi_h + 2\pi\theta_{0a}S_{xZj}\cos\varphi_h\right)\cos 2\pi\tilde{t}, \quad j = 1,2,...,n_m,
\end{aligned} \qquad (3.40)$$

where the integral constants

$$S_{Hjn} = \int_0^1 H\Phi_j\Phi_n\mathrm{d}X \,, \quad S_{Zjn} = \int_0^1 Z\Phi_j\Phi_n\mathrm{d}X \,, \quad S_{Jjn} = \int_0^1 \Phi_j\frac{\partial^2}{\partial X^2}\left(J\frac{\partial^2\Phi_n}{\partial X^2}\right)\mathrm{d}X \,,$$

$$S_{Hj} = \int_0^1 H\Phi_j\mathrm{d}X \,, \quad S_{Zj} = \int_0^1 Z\Phi_j\mathrm{d}X \,, \quad S_{xHj} = \int_0^1 XH\Phi_j\mathrm{d}X \text{ and } S_{xZj} = \int_0^1 XZ\Phi_j\mathrm{d}X$$

are parameters that can be precalculated. The ODEs Eq. (3.40) can be solved by using the built-in ODE solver *ode15s* in MATLAB [246]. If we only focus on the time-averaged quantities and the steady-state response, the particular solutions for Eq. (3.40) will be of great importance. Thereupon, we presume that q_n is a sinusoidal function with a frequency identical to the actuation one, expressed as:

$$q_n = Q_{n1} \sin\left(2\pi\tilde{t} - \psi_{n1}\right) - Q_{n2} \cos\left(2\pi\tilde{t} - \psi_{n2}\right), \tag{3.41}$$

where the coefficients Q_{n1}, Q_{n2}, ψ_{n1} and ψ_{n2} can be obtained by solving a set of algebraic equations as follows:

$$\begin{cases} \sum_{n=1}^{n_m} \left[\left(S_{Jjn} - 4\pi^2 S_{Hjn}\right) Q_{n1} \cos\psi_{n1} + \left(\gamma S_{Jjn} + 2\pi S_{Zjn}\right) Q_{n1} \sin\psi_{n1} \right] \\ = 4\pi^2 \xi_{0a} S_{Hj} + 4\pi^2 \theta_{0a} S_{xHj} \cos\varphi_h + 2\pi\theta_0 S_{xZj} \sin\varphi_h \\ \sum_{n=1}^{n_m} \left[\left(S_{Jjn} - 4\pi^2 S_{Hjn}\right) Q_{n1} \sin\psi_{n1} - \left(\gamma S_{Jjn} + 2\pi S_{Zjn}\right) Q_{n1} \cos\psi_{n1} \right] = 0 \\ \sum_{n=1}^{n_m} \left[\left(S_{Jjn} - 4\pi^2 S_{Hjn}\right) Q_{n2} \cos\psi_{n2} + \left(\gamma S_{Jjn} + 2\pi S_{Zjn}\right) Q_{n2} \sin\psi_{n2} \right] \\ = 2\pi\xi_{0a} S_{Zj} - 4\pi^2 \theta_{0a} S_{xHj} \sin\varphi_h + 2\pi\theta_{0a} S_{xZj} \cos\varphi_h \\ \sum_{n=1}^{n_m} \left[\left(S_{Jjn} - 4\pi^2 S_{Hjn}\right) Q_{n2} \sin\psi_{n2} - \left(\gamma S_{Jjn} + 2\pi S_{Zjn}\right) Q_{n2} \cos\psi_{n2} \right] = 0 \end{cases}, \tag{3.42}$$

$$j = 1, 2, ..., n_m.$$

For a uniform flagellum, the orthogonality condition, i.e. Eq. (3.39), can be exploited to simplify the calculation so that q_n can be analytically solved and given by

$$q_n = Q_{nu1} \sin\left(2\pi\tilde{t} - \psi_{nu}\right) - Q_{nu2} \cos\left(2\pi\tilde{t} - \psi_{nu}\right), \tag{3.43}$$

where the three coefficients are expressed as:

$$Q_{nu1} = \frac{\omega_{ns}^2 \xi_{0a} S_{n1} + \omega_{ns}^2 \theta_{0a} S_{n2} \cos\varphi_h + S_p^4 \theta_{0a} S_{n2} \sin\varphi_h}{\sqrt{\left(r_n^4 - \omega_{ns}^2\right)^2 + \left(S_p^4 + \gamma r_n^4\right)^2}}, \tag{3.44}$$

61

$$Q_{nu2} = \frac{S_p^{\,4}\xi_{0a}S_{n1} - \omega_{ns}^{\,2}\theta_{0a}S_{n2}\sin\varphi_h + S_p^{\,4}\theta_{0a}S_{n2}\cos\varphi_h}{\sqrt{\left(r_n^{\,4} - \omega_{ns}^{\,2}\right)^2 + \left(S_p^{\,4} + \gamma r_n^{\,4}\right)^2}}\,, \tag{3.45}$$

$$\psi_{nu} = \arctan\frac{S_p^{\,4} + \gamma r_n^{\,4}}{r_n^{\,4} - \omega_{ns}^{\,2}}\,, \tag{3.46}$$

where $S_{n1} = \int_0^1 \Phi_n \mathrm{d}X$ and $S_{n2} = \int_0^1 X\Phi_n \mathrm{d}X$. In the above equations, we have introduced the following two non-dimensional parameters:

$$S_p = \sqrt[4]{2\pi Z/J}\,, \tag{3.47}$$

$$\omega_{ns} = 2\pi\sqrt{H/J}\,, \tag{3.48}$$

which are named the sperm number [108] and the resonance index, respectively. The sperm number is the most frequently used parameter in the field of the sperm-like swimmer, which indicates the relative importance of viscous to elastic stresses on the filament [35, 38, 242]. Intuitively, it is proportional to the ratio of the length of the flagellum to the wavelength of the profile [35]. The resonance index ω_{ns} renders the ratio between the actuation and the nth-order natural frequency of a cantilever beam f_n [233], which is given by

$$f/f_n = \omega_{ns}/r_n^{\,2}\,, \tag{3.49}$$

where the quantity r_n is determined by Eq. (3.38). In this chapter, ω_{ns} will be used to illustrate the effect of resonance on the motility of an acoustically actuated AFMS.

3.6 Optimized micro-swimmer with a uniform elastic flagellum

The AFMS can be regarded as an energy-harvesting device that collects the acoustic energy and converts it to its kinetic energy. Thus, the dynamic response of the swimmer in an acoustic field severely influences the swimming performance. It is apparent that the energy conversion efficiency will reach an extreme if the actuation frequency approaches a resonance frequency of flagellum. However, the terminal speed $\bar{v}_{prop}$ of the micro-swimmer is not a monotonic function of the resonant frequency but maximizes at a certain value.

Figure 3-11 shows an example of the terminal velocity for the micro-swimmer with a uniform elastic flagellum within a specific frequency band. The width of the frequency band f is set in the range of 1 - 3 MHz, which is the range of therapeutic ultrasound [232]. The amplitude of the sound pressure p is stipulated as 60 kPa based on this reference as well. The viscosity of the fluid μ is set according to the gastric fluid [235] to be 0.02 Pa·s. The shape of the head is prescribed as the droplet, and the parameters of head motion are according to Eqs. (3.2a, b) with $K_u = 0.419$, $K_\theta = 0.00363$ and $\varphi_h = 180°$ at $\varphi_i = 90°$, as listed in Table 3-1 (or in Table 3-2). These parameters related to the head motion are also employed in this chapter. Other parameters are listed in Table 3-3 titled initial parameters, where the value of f denotes the actuation frequency at the maximal terminal velocity, and the value of $\bar{v}_{prop}$ denotes the maximal terminal velocity within the parameter sweep. It is noted that the resonance can occur at three actuation frequencies, and the terminal speed maximizes at the second one, which is equal to 74.19 μm/s. Figure 3-12 illustrates the case of the terminal velocity for a micro-swimmer versus the flagellum length L in the range of 100 - 500 μm, which is selected as the probable range of the length of the artificial micro-swimmer. Other

parameters are the same as Figure 3-11, except that f is fixed at 1.94 MHz based on the results of Figure 3-11. According to Eqs. (3.23) and (3.49), the resonance frequency f_n is proportional to the reciprocal of L^2, thus, the plot for L vs. $\bar{v}_{\text{prop}}$ can also embody the frequency response of the micro-swimmer. We can find that the maximal terminal velocity is not located at the extreme value of L at resonance. Parallel analyses are implemented in Figure 3-13 and Figure 3-14. Figure 3-13 illustrates the case of the terminal velocity versus Young's modulus in the range of 10 - 1000 MPa, whereas Figure 3-14 illustrates the case of the terminal velocity versus the density of the flagellum in the range of 1000 - 2000 kg/m^3, which are selected from Table 3-3 and all related to the natural frequency. Other parameters are the same as Figure 3-11, except that f is fixed at 1.94 MHz. The results from Figure 3-11, Figure 3-12, Figure 3-13 and Figure 3-14 verify that the terminal speed $\bar{v}_{\text{prop}}$ of the micro-swimmer is not a linear function of the resonant frequency nor other design parameters.

Because the effects of design parameters are nonlinear, let us exercise a design optimization to explore a parametric space. For the optimization, we only consider a uniform elastic flagellum because its terminal velocity, as well as the motility, can be analytically solved. In the subsequent two chapters, we will further describe the effects of resonance and the material damping of the flagellum on the motility of the micro-swimmer.

The optimization objective is to maximize the terminal velocity $\bar{v}_{\text{prop}}$ within a specific frequency band. The parameters to be optimized are the flagellum's density ρ_s, Young's modulus E, diameter d_s, and length L, as well as the actuation frequency f. The ranges of these parameters are shown in Table 3-3. These parametric ranges should have covered the most probable range of AFMSs made by an organic polymer. For

example, Young's modulus varies in the range of 10 - 10^3 MPa, which covers most polymers [247, 248]; The ratio d_s/L is set to be less than 0.1, which meets the applicability condition of the RFT; the ranges of remaining design parameters are the same as Figure 3-11 and Figure 3-12. A multi-island genetic algorithm [249] is utilized in our optimization. After iteration for 600 steps, the optimum combination of parameters is also shown in Table 3-3 titled Optimized parameters. It is noted that the optimized terminal speed is 740.9 μm/s, which is much greater than the results shown in Figure 3-11 and Figure 3-12. It is noted that natural micro-swimmers (such as sperms) generally swim at a speed in the order of 100 μm/s, which is slower than the predicted swimming speed of the AFMS. A frequency sweep based on the optimized flagellum indicates that the high speed is owing to the resonance response of vibration mode, as shown by the red solid line in Figure 3-15. This phenomenon indicates the essentiality of introducing the mass term into the swimming problem. Since the optimization is implemented with $\varphi_h = 180°$, in Figure 3-15, the effect of diverse actuation phase difference φ_h is also illustrated. The values of φ_h are selected from Table 3-1 in Chapter 3.2 with corresponding K_u and K_θ, meanwhile, the remaining design parameters stay unchanged. It is observed from Figure 3-15 that at the actuation frequency for the maximal terminal velocity, the value of $\bar{v}_{\text{prop}}$ with $\varphi_h = 180°$ prevails over the other φ_h. Nevertheless, the deviation of the results for different φ_h is not conspicuous. Therefore, the actuation phase difference φ_h is always set to be 180° for all the subsequent parts of this chapter.

It should be noted that the optimum speed given in Table 3-3 is achieved by resonance at the frequency of a high-vibration mode of the flagellum, which is around the fourteenth order of resonance. In this case, the acoustic frequency must be identical to the resonant frequency. In Figure 3-15, we can find that the full width of half

65

maximum (FWHM) of the highest velocity peak is only 0.011 MHz. That is, a 0.4% deviation in the frequency brings down the speed to half of the optimum magnitude. A further deviation of 1.9% leads to a 99% reduction of the terminal speed. In reality, the uncertainties in the mechanical properties and geometry of flagellum bring about the uncertainty of resonant frequency. Therefore, the design of the flagellum must allow a sufficiently large width of actuation frequency to achieve a reasonably high propulsive velocity. A preliminary design is to take the material damping into account. Figure 3-16 exhibits the effect of the material damping on the frequency response, where all the design parameters are identical to the ones in Figure 3-15 except the ratio of loss modulus to storage modulus $\gamma = 0.01$. It is observed that the FWHM of the highest velocity peak increases to 0.036 MHz, and the half-peak frequency deviation increases to 1.2%. Although the peak value decreases to 120 μm/s, it is still acceptable for the medical application. That is, an appropriate combination of the parameters related to the resonance and material damping will enhance the motility V_{cs}. To make clear this point, the influence of resonance and material damping is discussed in the following sections.

In Figure 3-11, Figure 3-15 and Figure 3-16, dotted lines therein represent the values for natural frequencies determined by Eq. (3.49), where all the formants lie on the natural frequencies. This spectrum of steady motion makes it clear that it is the theory of forced vibration that can be exploited to explain the dynamic properties of the flagellum, and the optimized velocity is just actuated at the 14th order of natural frequency in this case. This phenomenon indicates the essentiality of introducing the mass term into the swimming problem. Figure 3-17 demonstrates the actuation efficiency of the AFMS (estimated from Eq. (3.35)) in terms of the actuation frequency, where the natural frequencies (also represented by dotted lines) and other parameters

are the same as those in Figure 3-15. The natural frequency for the largest actuation efficiency in Figure 3-17 is just the same frequency for the largest terminal velocity in Figure 3-15, which indicates that a high terminal velocity may embody a condition of high efficiency. Thus, we will not discuss the actuation efficiency in the following sections in this thesis, instead, the terminal velocity and the motility of the AFMS will be considered.
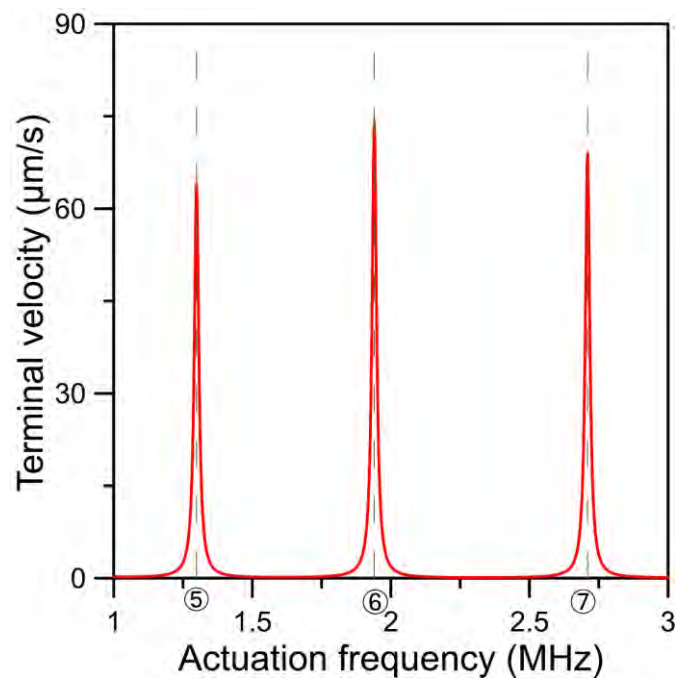
Figure 3-11. The frequency response within 1~3 MHz for the initial parameters.
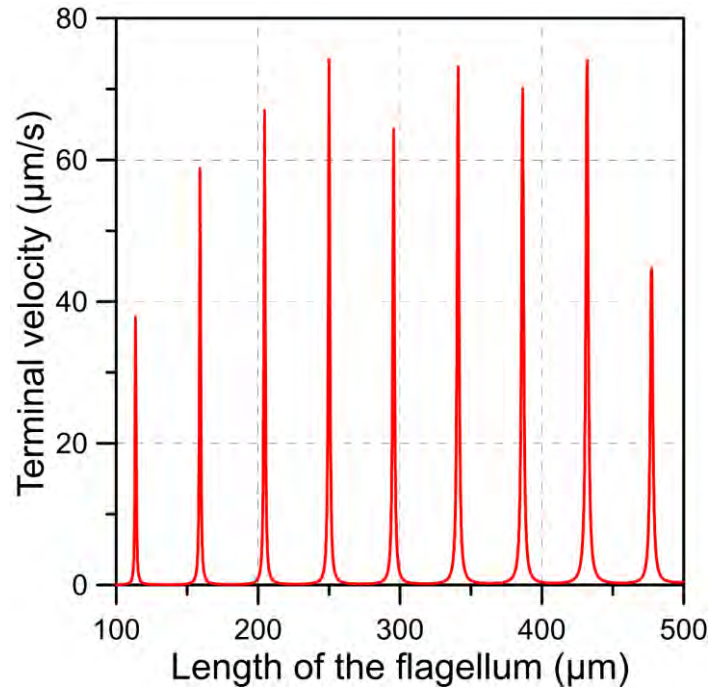
Figure 3-12. L vs. $\overline{v}_{\text{prop}}$ at 1.94 MHz for the parameters in Figure 3-11.
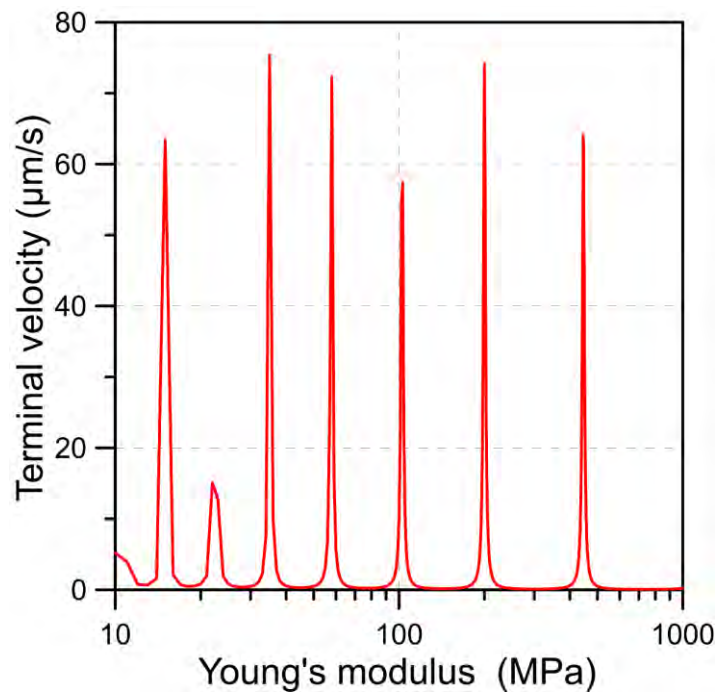
Figure 3-13. E vs. $\overline{v}_{\text{prop}}$ at 1.94 MHz for the parameters in Figure 3-11.

68
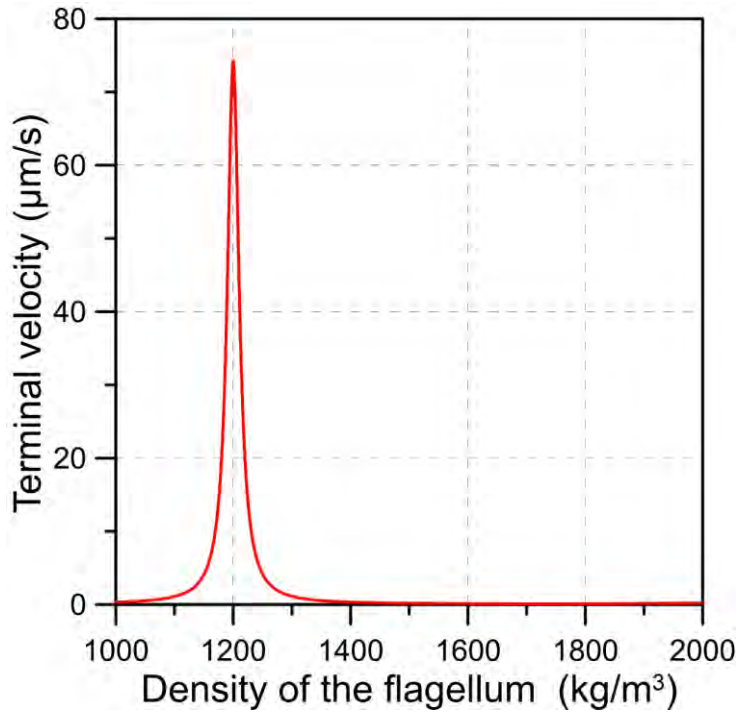
Figure 3-14. ρ_s vs. $\overline{v}_{\text{prop}}$ at 1.94 MHz for the parameters in Figure 3-11.
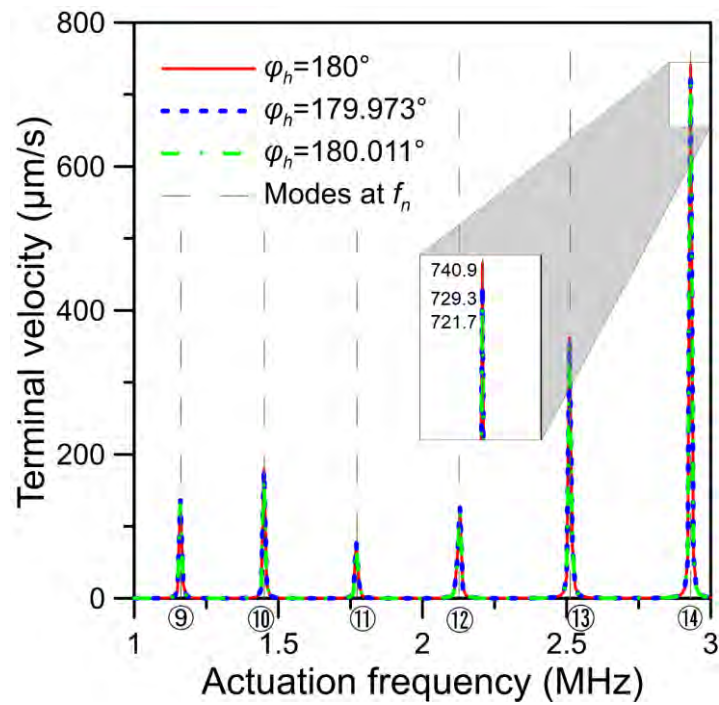
Figure 3-15. The frequency response within 1~3 MHz at optimized parameters with $\gamma = 0$ for three φ_h.
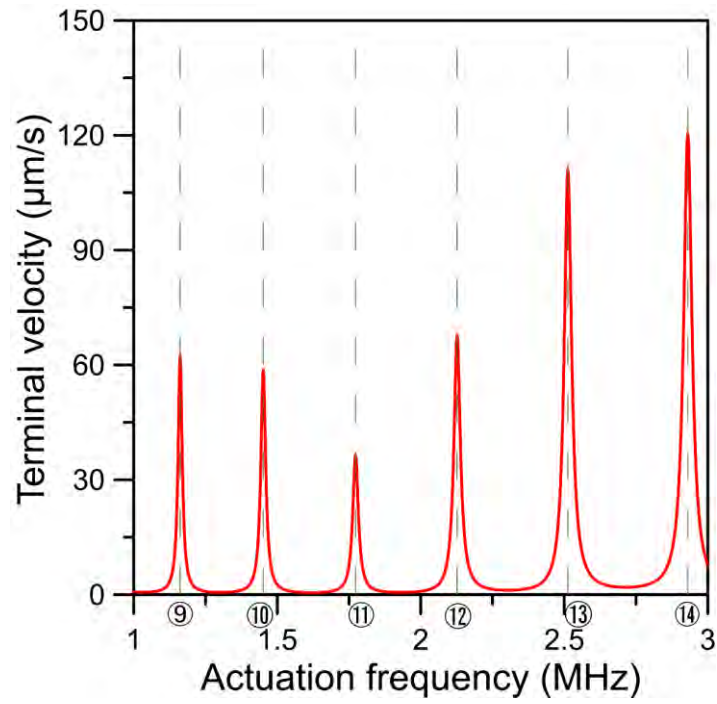
Figure 3-16. The frequency response within 1~3 MHz at optimized parameters with $\gamma = 0.01$ for $\varphi_h = 180°$.
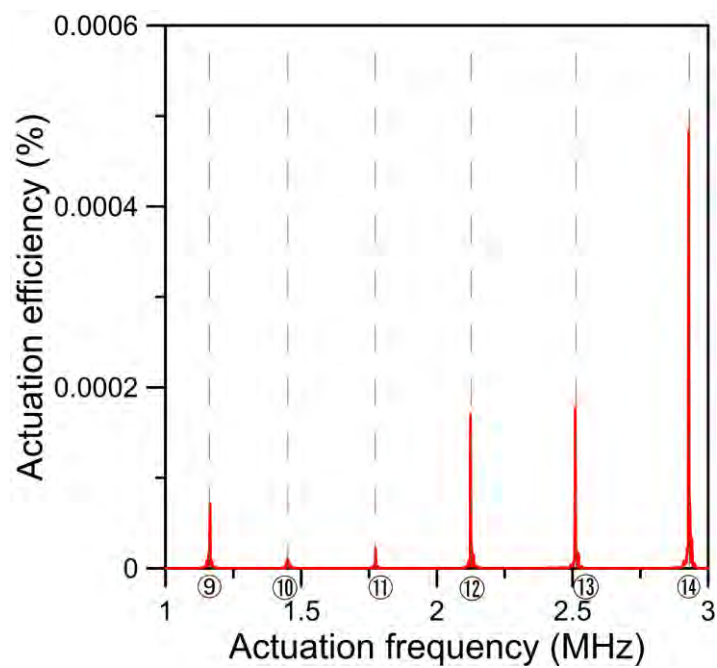
Figure 3-17. The actuation efficiency within 1~3 MHz at optimized parameters with $\gamma = 0$ for $\varphi_h = 180°$.

Table 3-3. The parametric ranges and results for the initial and optimized parameters for $\varphi_h = 180°$.

Parameters	E (MPa)	d_s/L	L (μm)	ρ_s (kg/m³)	f (MHz)	$\overline{V}_{prop}$ (μm/s)
Minimum values	10	0.01	100	1000	1	
Maximum values	1000	0.1	500	2000	3	
Initial parameters	200	0.1	250	1200	1.94	74.19
Optimized parameters	57.9	0.093	399	1865	2.93	740.9

3.7 Effect of resonance

In order to explicate the effect of resonance on V_{cs} of a uniform elastic flagellum, we explored the variation of V_{cs} in terms of two dimensionless parameters, i.e., the sperm number S_p given by Eq. (3.47) and the resonance index ω_{ns} given by Eq. (3.48). The calculation was performed with a few prescribed head actuations. In Figure 3-18, the results of $\xi_{0a} = 10^{-4}$, $\theta_{0a} = 10^{-4}$ and $\varphi_h = 180°$ are presented. Based on Eqs. (3.2a, b) and (3.23), it is noted that $\xi_{0a}/\theta_{0a} = K_u/K_\theta/L$. If the geometry of the head is prescribed, K_u and K_θ will be constants. Therefore, the quotient ξ_{0a}/θ_{0a} determines the length of flagellum L. For example, if $\xi_{0a}/\theta_{0a} = 1$ and the actuation parameters are given by the row of $\varphi_h = 180°$ in Table 3-1, the length of the flagellum is determined to be 115 μm. This length is close to the one reported in [7]. With this prescription, the motility V_{cs} can be calculated from Eq. (3.31) and is affected by S_p and ω_{ns}, which lead to various combinations of E, d_s, ρ_s and f. Note that when $\omega_{ns} = 0$, our model reduces to the case of the massless one, and the analytical expressions of the profile and velocity have been studied in [35, 38].

In Figure 3-18, S_p and ω_{ns} are varied in the ranges of 0 - 20 and 0 - 1400, respectively, based on the parametric ranges given in Table 3-3. It is observed that the motility V_{cs} maximizes in several resonance bands (red zones) and that V_{cs} could also be zero (white zones). As shown in Figure 3-19, the enlarged view of a resonant region for ω_{ns} from

280 to 320, if S_p is very small, the resonant V_{cs} regions will be very narrow for a certain S_p. This is an indication that the resonance-induced high-speed motion is very unstable. Results in Figure 3-18 and Figure 3-19 reveal that resonance could lead to motility higher than 2. However, these regions are narrow in terms of the band of ω_{ns}. For example, the largest band of ω_{ns} for $V_{cs} \geq 2$ in Figure 3-19 is from 297.5 to 299.5 at S_p = 5. Such a narrow frequency band renders a tight tolerance of the geometrical and material property variation, which is impractical. Instead, one may reduce the requirement of V_{cs} to trade for a larger frequency band of efficient actuation. Let us suppose that the satisfactory motility is $V_{cs} = 1$. With $d_s = 10$ μm, $L = 115$ μm, $f = 3$ MHz, $R_H = 25$ μm and $\mu = 0.02$ Pa.s, the terminal velocity $\bar{v}_{prop}$ is about 54 μm/s according to Eq. (3.31), which could have been adequate in a medical application (one may increase the acoustic pressure to obtain much larger speed). Thus, the band of ω_{ns} for $V_{cs} \geq 1$ denotes the satisfactory frequency band (SFB) of the actuation. It is observed from Figure 3-18 and Figure 3-19 that the width of SFB increases with S_p and order of resonance, i.e., an appropriate selection of S_p can help to broaden the SFB. For example, when $\omega_{ns} = 296$ and 301, the maximum SFB is achieved at $S_p = 6$, as depicted in Figure 3-19. That is, a 1.7% deviation in the actuation frequency is acceptable with respect to the motility of the micro-swimmer, which is better than the index FWHM. It can be used to assess the effect of manufacturing error. For example, according to Eq. (3.23) and (3.48), ω_{ns} is inversely proportional to the diameter of the flagellum d_s. If the accuracy of manufacturing of d_s is ±1%, the deviation of ω_{ns} will be 0.99% - 1.01%, which is less than the maximum SFB. That is, the error of manufacturing is acceptable if the micro-swimmer is designed at a maximum SFB.

Figure 3-20 and Figure 3-21 highlight the influence of ω_{ns} on the V_{cs} - S_p curves. The values of ω_{ns} in Figure 3-20 are selected to be at low-, moderate- and high-order resonance, respectively. Based on Eq. (3.49), where $\omega_{ns} = r_n^2$ represents the case of resonance, we choose n = 4, 8 and 12 in Figure 3-20. With the increase of the resonant ω_{ns} (or the acoustic frequency), the extreme point of S_p for the V_{cs} - S_p curve increases, and the peak value for V_{cs} is first increased and then decreased. However, at the region for $S_p > 10$, V_{cs} at all the three resonance conditions almost vanish. It can be understood by the physical meaning of the sperm number S_p. Because S_p is just the ratio of the fluid resistive force to the elastic force acting on the flagellum [108], a large S_p represents a considerable resistance, which is adverse to the behavior of resonance. But, if S_p is too small, the propulsive force will be scanty based on the RFT [25], meanwhile, a large bending modulus will block the generation of the wave along the flagellum, thus, the motility will be small according to the 'scallop theorem' in the LRN regime [34, 36]. Therefore, there will be a peak value at the V_{cs} - S_p curve. On the other hand, a larger ω_{ns} at resonance indicates a smaller bending modulus according to Eq. (3.48), which results in a larger S_p. Hence, the extreme value of S_p becomes larger with the increase of the resonant ω_{ns}. As a result, an opportune S_p should be selected discreetly to achieve high motility. Outside the resonance bands, the detailed influence of S_p on V_{cs} is shown in Figure 3-21. All the selected ω_{ns} in Figure 3-21 are pertaining to non-resonant scenarios. It is noted that the peak value of V_{cs} at the non-resonance region ($\omega_{ns} = (r_3^2 + r_4^2)/2 \approx 100$) is thousands of times less than that at the resonance region. For the massless case ($\omega_{ns} = 0$), the motility increases with S_p and approaches a saturated value of 0.014. The case of $\omega_{ns} = 1$ in Figure 3-21 is used to verify the accuracy of our numerical model by comparing this small-mass result with the massless one, for which

the profile can be solved analytically based on the so-called hyper-diffusion equation [35, 38]. The error of our numerical model is acceptable, as shown in Figure 3-21. Note that if we neglect the mass, or the density of the flagellum is extremely small, the motility will be, in theory, very poor, even compared with the case of the non-resonance one. This is a demonstration that for the artificial sperm-like micro-swimmer actuated by ultrasound, the inertia effect is not negligible.
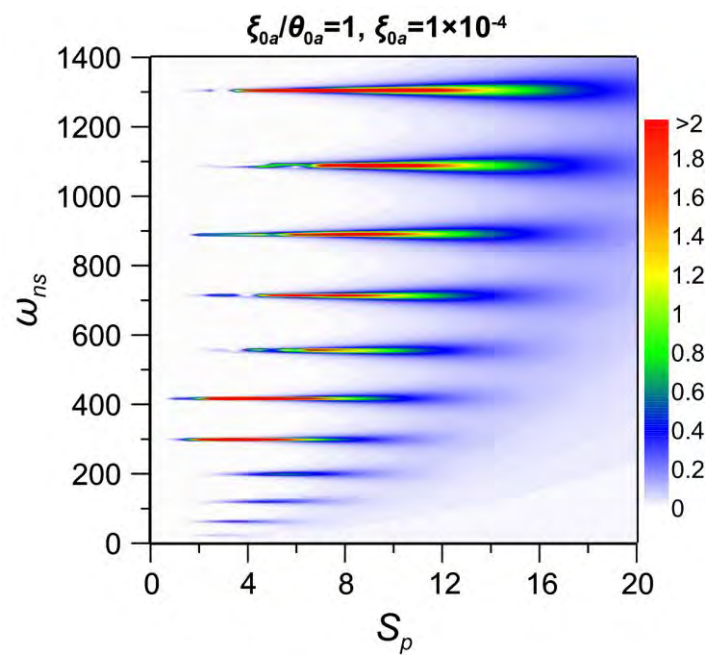
Figure 3-18. The contour map of V_{cs} in terms of S_p and ω_{ns} at a fixed actuation, where $\xi_{0a}/\theta_{0a} = 1$ and $\xi_{0a} = 1\times10^{-4}$.
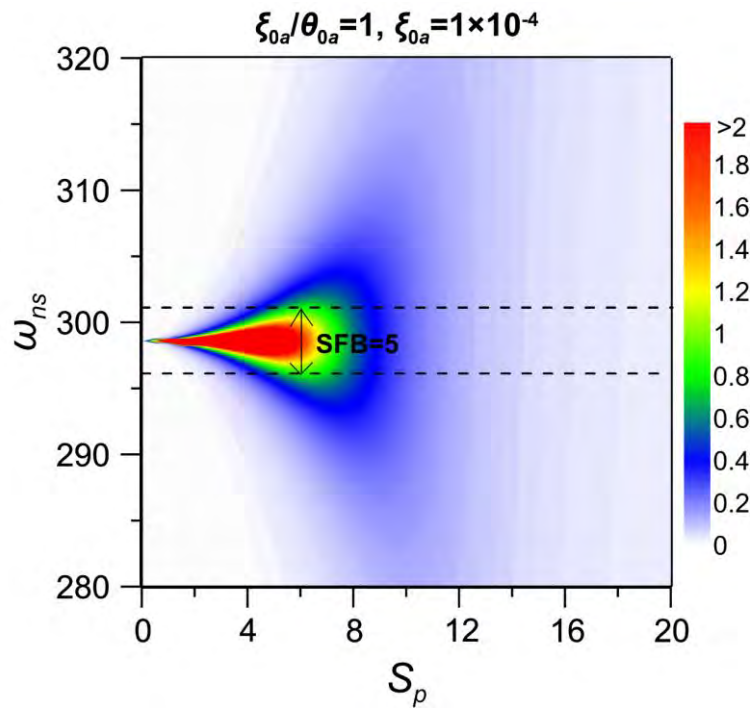
Figure 3-19. The detailed view of Figure 3-18 at ω_{ns} = 280 - 320.
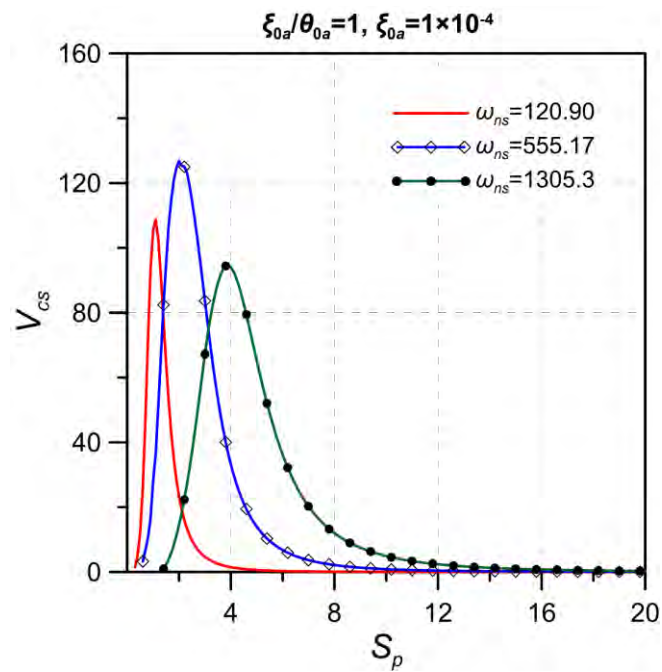
Figure 3-20. The correlation between V_{cs} and S_p for different ω_{ns} at the resonant zones.
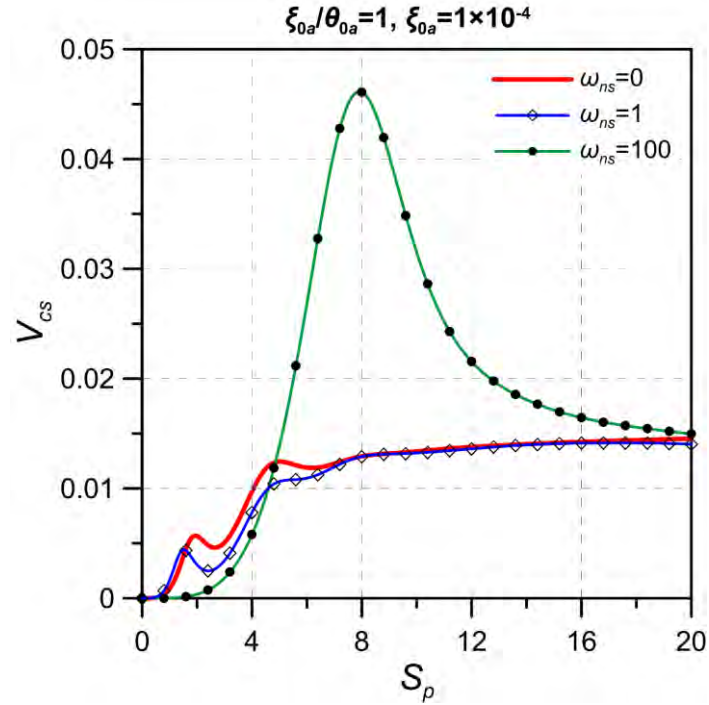
Figure 3-21. The correlation between V_{cs} and S_p at different ω_{ns} which are far away from the resonant as well as $\omega_{ns} = 0$.

3.8 Effect of material damping

The inherent damping in most polymers is nonnegligible [237]. Therefore, it is necessary to quantify the effect of the material damping on the motility of a micro-swimmer. We assume that the material of the flagellum, generally an organic polymer, can be described by the Kelvin–Voigt model, in which the damping property is designated by γ, defined as the ratio of loss to storage moduli $\eta\omega/E$ [250], at the acoustic frequency ω. The range of γ is from 0 to 0.1 according to [237]. In this chapter, the parameters associated with the actuation, i.e., ξ_{0a}/θ_{0a}, ξ_{0a}, K_u, K_θ and φ_h, are the same as those in the last chapter. Consequently, we also demonstrate a map of motility based on the parameters S_p and ω_{ns} with $\gamma = 0.01$, as shown in Figure 3-22, to compare with Figure 3-18. It is noted that the zones of $V_{cs} > 2$ (red areas) are shifted to the lower S_p side after $\gamma = 0.01$ is applied. This effect is more significant for the higher-order

resonance zones. As a result, the width of SFB for a small S_p, e.g., $S_p = 2$, is significantly increased at $\gamma = 0.01$. Figure 3-23 demonstrates the effect of γ from 0.0001 to 0.1 at $S_p = 2$, which represents a design of a micro-swimmer with a rather large bending modulus or small fluid viscosity [242]. In this case, if the material damping is not involved, V_{cs} is less than unity, as shown in Figure 3-18. However, with γ ranging from 0.001 to 0.01, V_{cs} in resonance zones becomes greater than one. Both Figure 3-22 and Figure 3-23 indicate that a moderate γ benefits the short flagellum design, especially in the cases where the motility V_{cs} is required to be a reasonable value and the larger SFB is more desired. It should be noted that an excessively large value of γ will significantly reduce V_{cs}. When $\gamma > 0.05$, $V_{cs} < 1$. Thereupon, a moderately but not extremely large γ is beneficial to the flagellum designed at a large bending modulus or small fluid viscosity.

Figure 3-24 and Figure 3-25 illustrate in more detail the variation of V_{cs} with S_p and resonant ω_{ns}. For the purpose of contrast, ω_{ns} are selected to be the same as those in Figure 3-20. The difference between Figure 3-24 and Figure 3-25 is the magnitude of γ, i.e., $\gamma = 0.001$ in Figure 3-24 and $\gamma = 0.01$ in Figure 3-25. It is noted from Figure 3-24 and Figure 3-25 that all the extreme points vanish and the maximum value point of V_{cs} is located at the minimum value of S_p. The V_{cs} - S_p curve at resonance is changed into the monotonically decreasing one with the existence of the material damping. When $\gamma = 0.001$, the maximum V_{cs} for the three ω_{ns} decreases to about 1/3 or 1/4 of the original peak values in Figure 3-20; when $\gamma = 0.01$, these fractional numbers become 1/30 or 1/40. It is also observed from Figure 3-24 that the maximum values of V_{cs} for $\omega_{ns} = 555.17$ and $\omega_{ns} = 1305.3$ are nearly the same, whereas this value for $\omega_{ns} = 555.17$ is greater than the one for $\omega_{ns} = 1305.3$, as depicted in Figure 3-25. That is, the decrement of the motility for the higher resonance index will be more significant than the one for the lower resonance index if the material damping is quite large. It is noted

that the maximum values of V_{cs} are relatively centered, thereupon, if we extract all the maximum V_{cs} for each order of ω_{ns} at γ from 0.001 to 0.01, we will plot a maximum V_{cs} - γ curve, as shown in Figure 3-26. The percentages in Figure 3-26 denote the distributional error of the maximum V_{cs} at different ω_{ns} for a given γ, and they are all around 10%. This implies that the maximum V_{cs} for different resonant ω_{ns} can be concentrated within a reasonable bound and comply with the same rule in terms of γ. Note that the axes in Figure 3-26 are logarithmic, therefore, the straight line represents an exponential relationship. The slope of the line is -1, which indicates that the maximum V_{cs} at resonance is inversely proportional to γ.

Outside the resonance bands, the detailed influence of γ on the V_{cs} - S_p curve is depicted in Figure 3-27. ω_{ns} is chosen to be the average of the 9th- and the 10th-order resonance index, which is $\omega_{ns} = \left(r_9^2 + r_{10}^2 \right)/2 = 801.91$, therefore pertaining to a non-resonant scenario. It is observed from Figure 3-27 that V_{cs} can remarkably increase for all the ranges of S_p when γ is at the maximum value ($\gamma = 0.1$) for the region far away from resonance. In other cases of γ, values of V_{cs} nearly remain the same. This indicates that we can select the material damping as large as possible if the AFMS is working at a non-resonant zone. All the phenomena associated with the material damping can be explained by the expressions of the amplitude of a uniform elastic flagellum, i.e., Eqs. (3.43), (3.44), (3.45) and (3.46). It is noted that the term γ always appears together with S_p, and the summation of them can be regarded as a whole term. Thus, the increase of γ is equivalent to the increase of S_p. The V_{cs} - S_p curve for resonant ω_{ns} with γ (Figure 3-24 and Figure 3-25) corresponds to the one without γ (Figure 3-20) at a large S_p range; if the equivalent S_p is greater than the position of the extremum, the peak points will vanish and the curve becomes monotonic. In addition, in Eqs. (3.44), (3.45) and (3.46), γ always times r_n^4 which is equivalent to the resonant ω_{ns}, so the influence of γ is more

78

remarkable for a higher order of ω_{ns}. It is observed from Figure 3-27 that the extreme point of S_p on a non-resonant condition is quite large because the resistive force is predominant for the propulsion of the flagellum. The increase of γ is just corresponding to a larger S_p, therefore, it is easy to understand the reason why the existence of material damping benefits the motility at a low sperm number. It can help us to determine the optimal intervals of S_p and then, we can restrainedly take advantage of γ to exalt the motility of the AFMS.
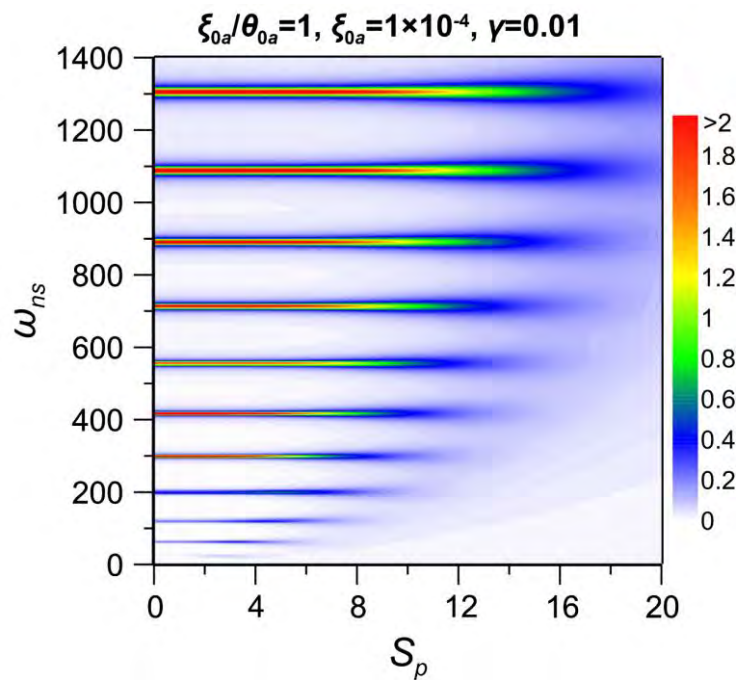
Figure 3-22. The contour map of V_{cs} in terms of S_p and ω_{ns} at a fixed material damping where $\gamma = 0.01$.
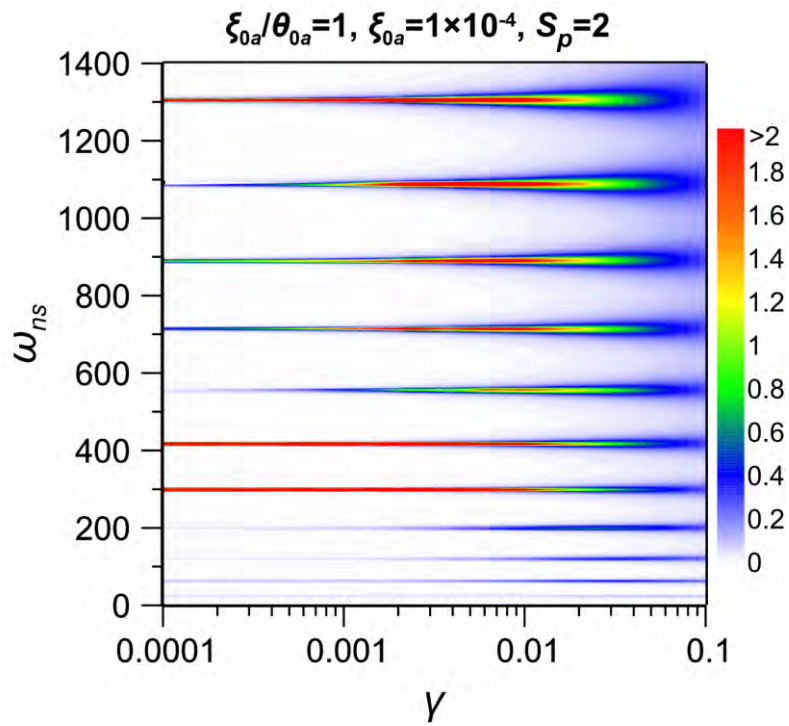
Figure 3-23. The contour map of the effect of the material damping on the resonance at a fixed $S_p = 2$.
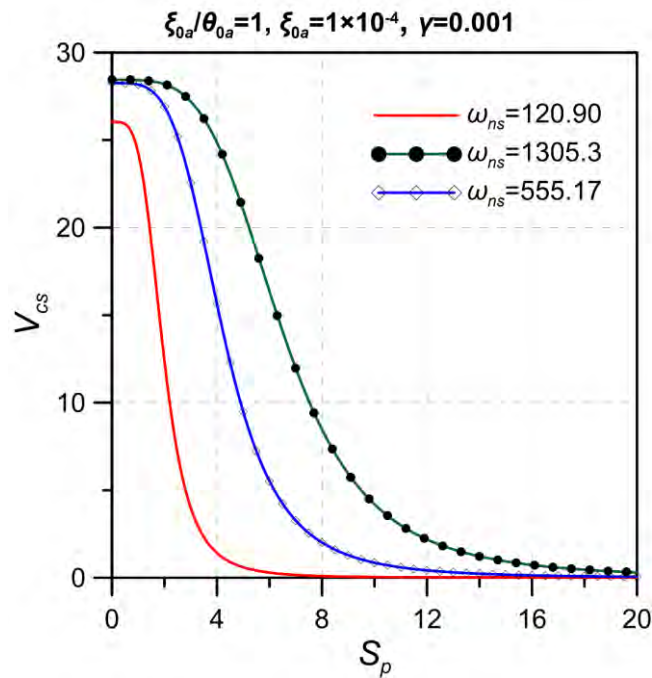
Figure 3-24. The correlation between V_{cs} and S_p for different ω_{ns} at three resonant zones where $\gamma = 0.001$.
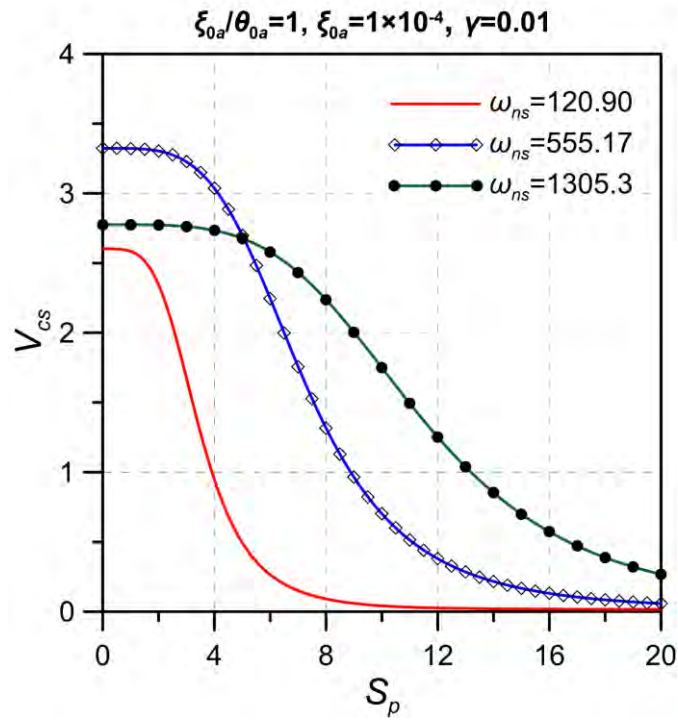
Figure 3-25. The correlation between V_{cs} and S_p for different ω_{ns} at three resonant zones where $\gamma = 0.01$.
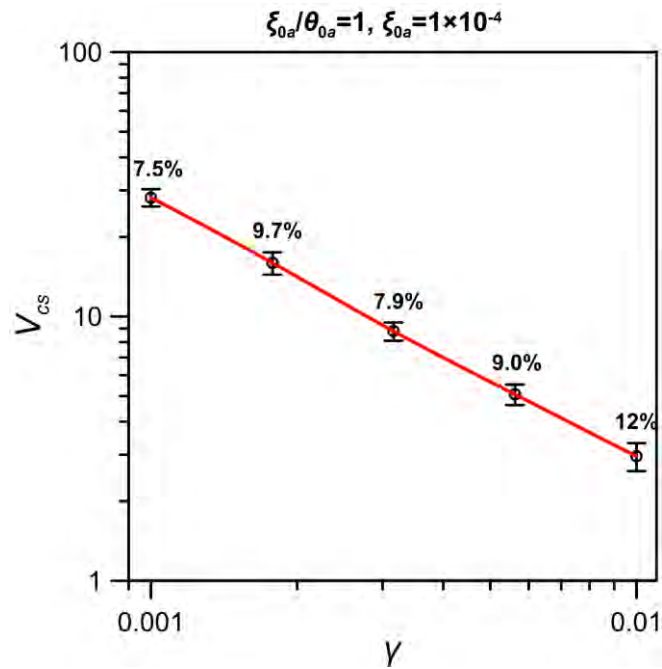
Figure 3-26. The maximum V_{cs} for all the ω_{ns} except the first order at different γ.

81
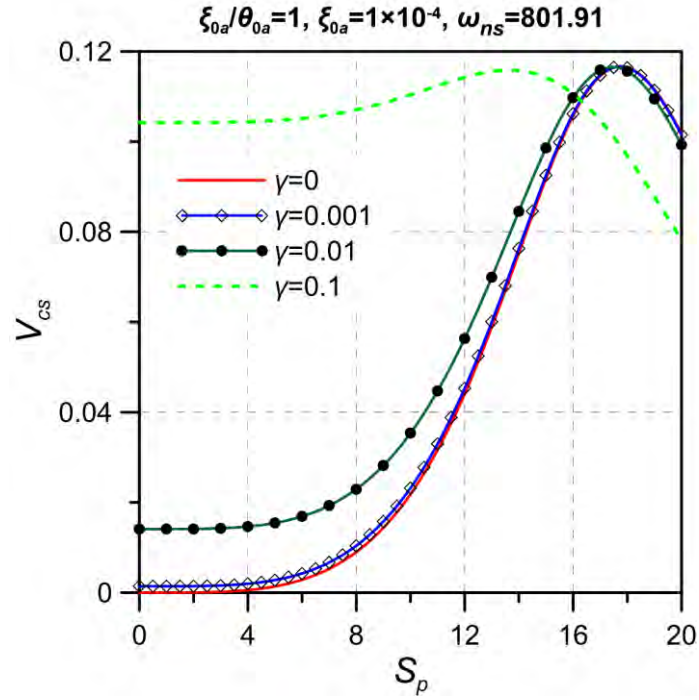
Figure 3-27. The correlation between V_{cs} and S_p for different γ at the region far away from the resonant zones where $\omega_{ns} = 801.91$.

3.9 Effect of tapering and comparison with existing experiments

In this chapter, the effect of the non-uniform circular cross-section flagellum is elucidated. As mentioned in Chapter 3.3, the diameter of the circular cross-section is denoted by d_s, and d_s is herein defined as the function of the dimensionless abscissa X. The non-uniform cross-section influences two physic quantities, the area of the circular cross-section A_s and the second moment of area I. Here, A_s, I and the diameter d_s can be expressed as:

$$A_s(X) = \frac{\pi d_s(X)^2}{4},$$
(3.50)

$$I(X) = \frac{\pi d_s(X)^4}{64},$$
(3.51)

$$d_s(X) = d_s(0)h(X),$$ (3.52)

$$h(X) = 1 - \lambda X^\Lambda,$$ (3.53)

where $d_s(0)$ represents the maximal value of d_s, which is also the diameter of the flagellum at the head end; h denotes the tapering equation for the diameter of the cross-section; λ is the relative slope of h, which is the index of the tapering; Λ denotes the power of h function. If $\Lambda = 1$, the diameter of the cross-section is linearly varied with the length of the flagellum. Taking into account the condition $0 \le X \le 1$, it is easy to obtain that $0 \le \lambda < 1$. For the convenience of directly demonstrating the effects of the variable cross-section and comparing with the experimental results in Ref. [7], the design parameters for our numerical calculation in this chapter are selected in the vicinity of the ones in Ref. [7] as possible. Accordingly, we prescribe the parameters in Figure 3-28, Figure 3-29, Figure 3-30 and Figure 3-31 as $d_s(0) = 25$ μm, $L = 180$ μm, $E = 10$ MPa, $\rho_s = 1200$ kg/m³, $\Lambda = 1$ and $f = 4600$ Hz, along with a head for $R_H = 25$ μm and the fluid dynamic viscosity $\mu = 1$ Pa·s. We neglect the rotation of the head, i.e., $\theta_{0a} = 0$ in this chapter.

In Figure 3-28, we choose $\lambda = 0.9$, and the head amplitude y_{0a} is taken from 10 μm to 40 μm, which is based on the experimental data reported in [7]. In Figure 3-29, λ can be varied from 0 to 1, and the head amplitude $y_{0a} = 40$ μm. Otherwise, if we neglect the inertial term ($\rho_s = 0$), the governing equation of the elastic flagellum with a linearly non-uniform cross-section will be translated into a conventional Cauchy-Euler equation, and it can be solved analytically (see Appendix A). To compare the results of our numerical model to the analytical one, where the material damping is not considered, we take γ as 0 in Figure 3-28 and Figure 3-29. They illustrate the terminal velocity for different flagellum density ρ_s versus the head amplitude y_{0a} and the relative slope λ,

respectively. It is noted that the results for $\rho_s = 1200$ kg/m^3 and $\rho_s = 1$ kg/m^3 are almost identical, as depicted in Figure 3-28 and Figure 3-29. It indicates that the AFMS is actuated at a non-resonant scenario. Therefore, this chapter is mainly exploring the locomotion of the AFMS far away from the resonance. The errors between the small-mass results ($\rho_s = 1$) and the analytical one ($\rho_s = 0$) are shown in Figure 3-28 and Figure 3-29, which are less than 5% for both the $\bar{v}_{\text{prop}}$ - y_{0a} curve and the $\bar{v}_{\text{prop}}$ - λ curve. It demonstrates that our numerical model for the non-uniform flagellum case is reliable to a certain extent. It is noted that the terminal velocity will increase with λ, as illustrated in Figure 3-29.

The contrast to the experiments in terms of the terminal velocity and the profiles of the micro-swimmer are respectively shown in Figure 3-30 and Figure 3-31, where we take the material damping γ as 5. γ normally ranges from 0.001 to 0.01 at the unity frequency, and it will increase with the vibration frequency [251]. As for the actuation frequency herein (4600 Hz), $\gamma = 5$ is acceptable to some extent. As illustrated in Figure 3-30, the blue spots are the experimental results reported in [7]. A uniform cross-section case ($\lambda = 0$) and a tapered case ($\lambda = 0.9$) are selected to be compared with the experimental one. It is noted that results for $\lambda = 0.9$ adequately match the experimental results in [7]. In addition, the $\bar{v}_{\text{prop}}$ - y_{0a} curve for our numerical model seems like a parabola, which does just tally with the expectation in Ref. [38]. However, the result for $\lambda = 0$ shows very poor agreement with the experimental one. This indicates the necessity of the consideration of the non-uniform flagellum. The profiles of the micro-swimmer for y_{0a} equal to 12 μm within one oscillating period are demonstrated in Figure 3-31. Different colors embody the sequence of motions which are divided into 6 instants for a period to externalize the spatial-temporal movement of the micro-swimmer. As

depicted in Figure 3-31, the head ends are merged into one to be analogous to the configuration of Figure 1-2(b). It is noted that the wavelength of the flagellum is greater than a quarter of its length, which conforms to the application condition for the RFT stated in Chapter 3.4. Moreover, the obtained results indicate that the amplitude of the tail is small enough compared with the length of the flagellum, which is conforming to the linear assumption in Chapter 3.1. The above results to a certain degree give the verification to the present model.

Figure 3-32 demonstrates the effect of γ for different L at $y_{0a} = 40$ μm and Figure 3-33 illustrates the effect of λ for diverse tapering power Λ still at $y_{0a} = 40$ μm. Other design parameters are the same as Figure 3-30. As plotted in Figure 3-32, the terminal velocity declines rapidly only when $\gamma > 0.1$. As for the effect of L, there is almost no difference for $L < 200$, whereas the terminal velocity will decrease with L if $L > 200$. However, this difference is not very large when $\gamma > 0.1$. Various laws of the tapering equation of the flagellum, which is embodied by Λ, can also influence the terminal velocity, as depicted in Figure 3-33. $\bar{v}_{\text{prop}}$ decreases with the value of Λ but increases with λ. It accords with the description in Figure 3-29. That is, the non-uniform cross-section is indeed conducive to the enhancement of the swimming velocity, and a larger slope of the tapered cross-section is recommended.
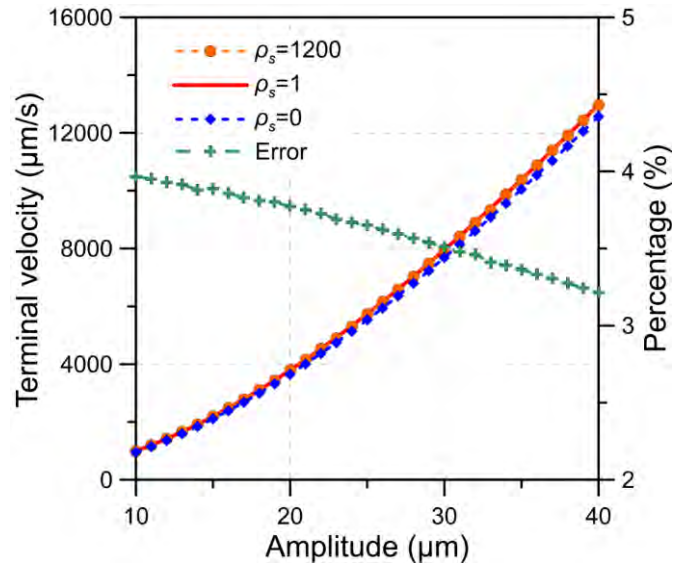
Figure 3-28. Head amplitude vs. terminal velocity at $\lambda = 0.9$ for the cases with inertia and without inertia.
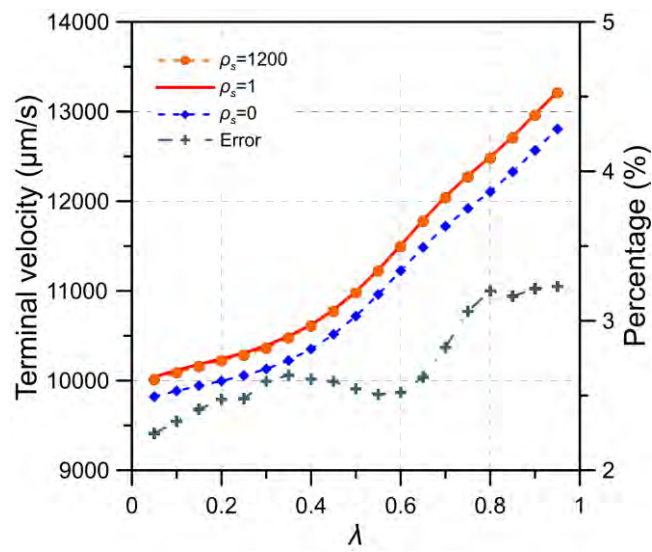
Figure 3-29. λ vs. terminal velocity at actuation $y_{0a} = 40$ μm for the cases with inertia and without inertia.
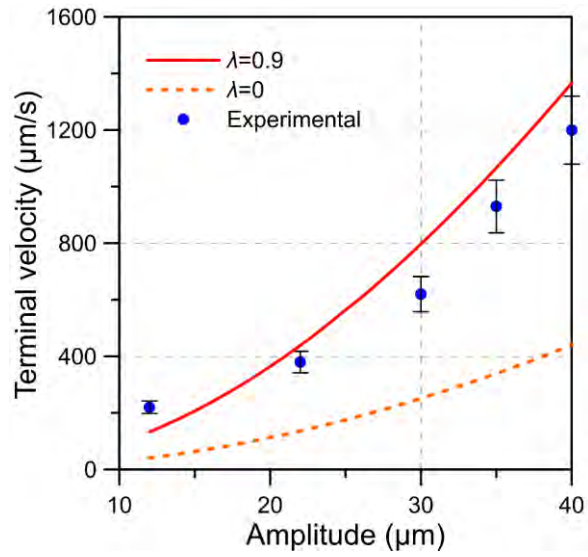
Figure 3-30. The comparison between experimental [7] and theoretical results.

Figure 3-31. The combination of the profiles at a head amplitude equal to 12 μm for the parameters the same as $\lambda = 0.9$ in Figure 3-30.
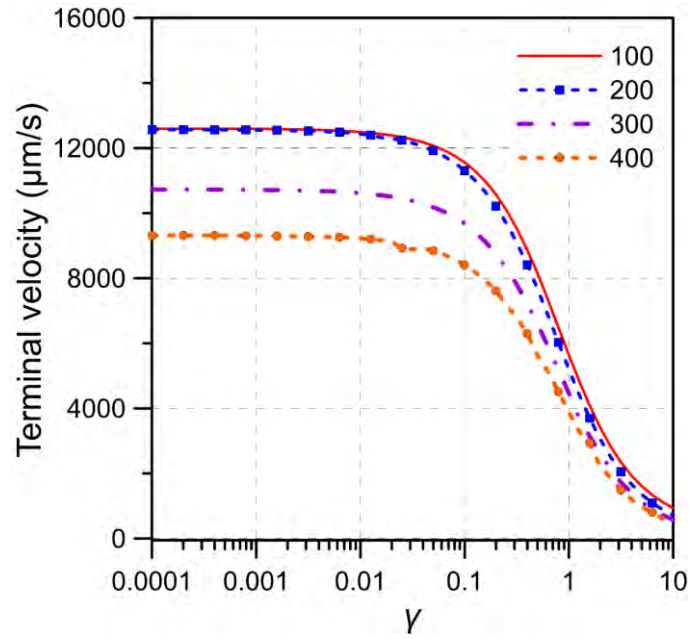
Figure 3-32. γ vs. terminal velocity for different L at y_{0a} = 40 μm.
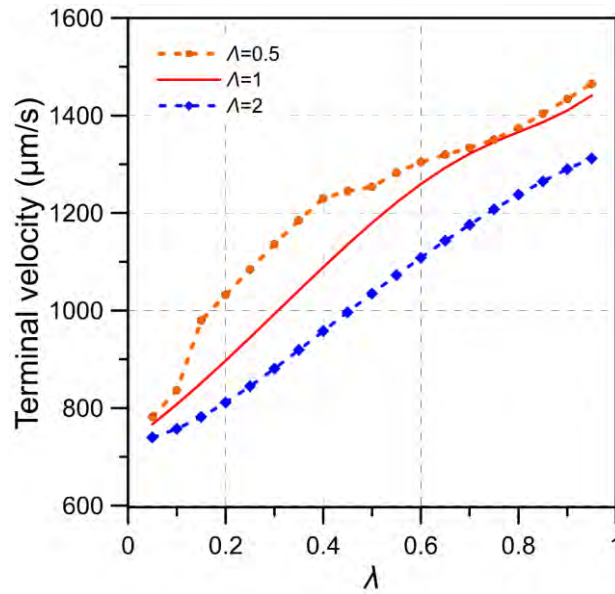
Figure 3-33. λ vs. terminal velocity for different Λ at γ = 5 and y_{0a} = 40 μm.

3.10 Summary

In this chapter, we investigated a 1D theoretical model to estimate the speed of straight-line motion of an acoustically actuated AFMS based on the head-actuated mechanism, where an undulating flagellum was actuated by acoustic waves and treated as a clamped boundary condition in simulation. We found that the oscillating amplitude of the head depends linearly on the sound pressure while it is inversely proportional to the actuation frequency. The incident angle of the sound wave can slightly influence the proportionality factor. Then, an acceptable terminal velocity can be reached in the light of the head-inspired model. Taking into account the inertial term and the material damping, the continuous lateral EOM for the non-uniform flagellum was set up and the propulsive velocity was deduced from the RFT.

Numerical solutions were achieved with the assistance of the Galerkin method. The results revealed that the actuation frequency of the optimal velocity lies on the natural frequency; thus, the inertial term cannot be neglected especially at resonance. However, the relationship between the terminal velocity and the order of the resonance is not monolithic. The optimal range for the sperm number will increase with the resonance index, and a considerably large sperm number will be adverse to the motility; but, a relatively large sperm number is beneficial to broaden the SFB. Thus, an opportune sperm number should be selected discreetly. A moderate value of the material damping for the material will broaden the SFB at a low sperm number as well as promote motility at the non-resonant region. However, excessive material damping results in considerably bad performance of the micro-swimmer. The maximum motility at resonance is inversely proportional to the material damping, and a small value of sperm number is profitable on this condition. It is preferred to design and fabricate an AFMS with a non-uniform flagellum of a larger slope of the tapered cross-section, and the

recommended tapering equation for the diameter is of a square root relation. The numerical results of the relationship between the terminal velocity and the head amplitude based on our theoretical model are in good agreement with the experimental results reported in [7]. The numerical results also coincide well with the ones from the analytical models which neglect the inertial term, including the hyper-diffusion model with uniform cross-section [35, 38] and the massless model with a linearly tapered flagellum. The novelty of our work in this chapter is to provide a theoretical model of actuation and propulsion of the AFMS, whose directional swimming has been experimentally observed before but lack of theoretical elaboration. Note that the RFT we employed for modeling is essentially a 3D theory, thus, the model we proposed in this chapter has the possibility of extrapolating our relevant research findings to the study of microrobots swimming in 3D space by adding the 3D rigid body motion of head as dependent variables to the EOM.

Chapter 4. 2D model of AFMS based on the CRFT —— rotation and steerability

4.1 Problem statement for the steering

We consider an AFMS requiring acoustic excitations to propel. The concerned AFMS is composed of a rigid head and a flexible slender flagellum, as exhibited in Figure 4-1, where the structure has been meshed for the FSI simulation. The AFMS suspends in an aqueous solution and swims under an acoustic actuation that leads to the oscillations of the head and the whipping of the flagellum. According to the study in Chapter 3, the effect of periodic acoustic excitation for an AFMS can be assumed to be a periodic force F_{ext} acting on the head with the actuation frequency f (or angular frequency ω), that is $F_{ext}(t) = F_a \cos \omega t$, where F_a is the amplitude of force. The head oscillation induced by F_{ext} whips the flagellum, giving rise to the advancement of the AFMS at a terminal average speed of V_{ave}. We focus firstly on the swimming problem that the average displacement of the micro-swimmer during several actuation periods keeps a straight line. It has been demonstrated both experimentally [7, 252] and theoretically [38, 43] that the micro-swimmer tends to align itself perpendicular to the direction of F_{ext}. Hence, in the following FSI simulations, the only boundary condition is that the centroid of the head (or the end of the flagellum if the micro-swimmer has no head) is subject to a transverse harmonic force F_{ext}. Consequently, the head oscillates transversely with an amplitude y_{0a}.

Figure 4-1 shows the mesh of the FSI model that was simulated using a built-in fully coupled 2D FSI solver in COMSOL Multiphysics [253]. The whole geometry can be divided into two domains: a rectangular fluid domain of $2000 \times 500 \ \mu m^2$ (capacious enough for a micro-swimmer) and a solid one for the AFMS in the center of the fluid.

The radius of the circular head and the length of the flagellum are denoted by R_H and L, respectively. For a 2D simulation, the cross-section of the flagellum is rectangular. The flagellar width W_y can be either uniform or tapered with a maximum of W_{y0} at the root (the joint between the head and the flagellum). The micro-swimmer is assumed to have a uniform thickness of W_z.
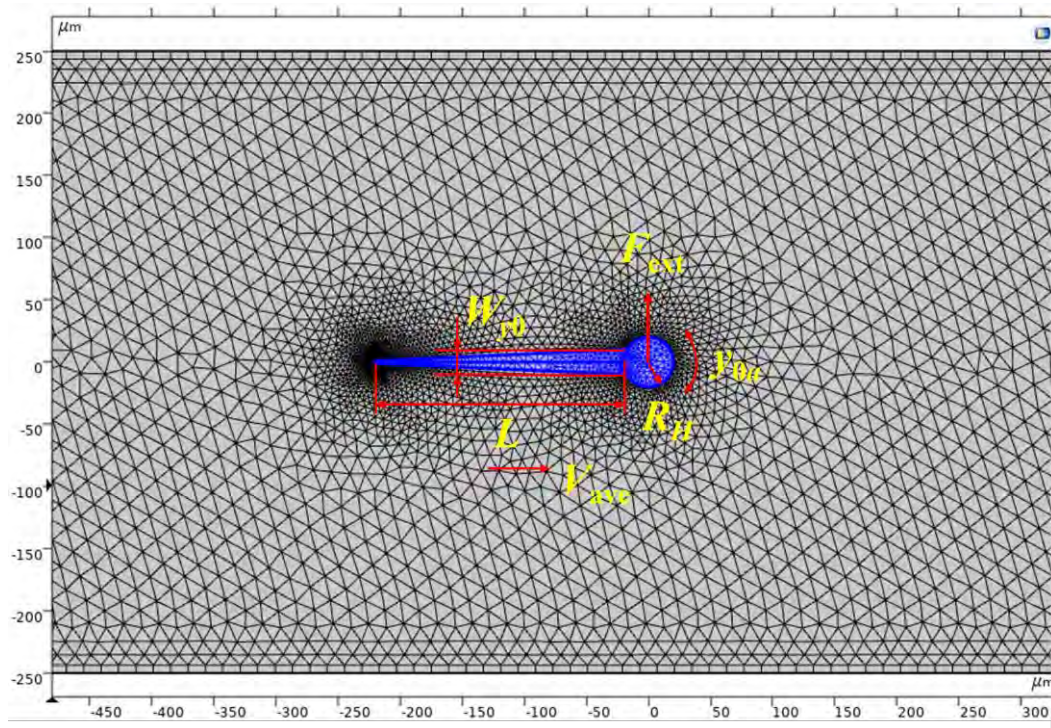
Figure 4-1. The configuration of an FSI simulation, wherein the gray area represents a mesh result of the fluid, and the blue area illustrates the deformable AFMS domain.

4.2 The convergence analyses of FSI simulations

We investigate the steady-state swimming performances using the trajectory of the center of the head (or the right end of the flagellum). In the numerical simulations, the incompressible creeping flow module without the inertial term (Stokes flow) is employed for the fluid domain, while the solid mechanics module with plane strain

approximation for the solid domain (also without inertial term because it will not be at resonance in most cases according to the results of Chapter 3, and there is no inertial term in our CRFT model in this chapter) [254]. The micro-swimmer consists of two material models: a viscoelastic material for the flagellum and a rigid domain for the head [237]. Considering the expected medical applications and the current experiments, as we have mentioned in Chapter 3, the flagellar material is assumed to be a Kelvin-Voigt viscoelastic material for representing an organic polymer, such as the PPy employed in Ref. [13] and the PEG employed in Ref. [7] as well as in our experiment. F_{ext} is applied along the y-direction to the centroid of the head. If headless, F_{ext} is applied to the right end of the flagellum. The automatic remeshing technique is employed to tackle the problems induced by large rigid-body motions, where the fluid domain (i.e., the gray area in Figure 4-1) is set as the moving mesh region based on the Winslow smoothing method [255], in which the mesh distortion parameter is set to unity.

We first exemplify 2D simulations of two AFMS models as shown in Figure 4-2 and Figure 4-3. The first (Figure 4-2) one is a uniform flagellum (without head) with dimensions: $L = 200$ μm, $W_z = 40$ μm, and $W_y = 12$ μm, and swims in a fluid with the dynamic viscosity: $\mu = 0.1$ Pa·s. The second one (Figure 4-3) is a sperm-like micro-swimmer referring to the AFMS described in Ref. [7]. It has a thickness $W_z = 20$ μm, a cylindrical head with a radius $R_H = 20$ μm, a tapered flagellum $L = 200$ μm, the width $W_y = W_{y0}(1 - \lambda X)$, where $0 \leq X \leq 1$ is the length normalized by L, $W_{y0} = 20$ μm, and the tapering index $\lambda = 0.9$ (see Chapter 3.9 for the power $\Lambda = 1$). Both micro-swimmers have the material properties: the storage Young's modulus $E = 10$ MPa, material viscosity coefficient $\eta = 10$ Pa·s, and it is in the static fluids ($\mathbf{u} = 0$).

Figure 4-2 and Figure 4-3 illustrate the fluid pressure distribution at t = 0.005 s. A vertical acoustic force F_{ext} was applied at the right with a frequency of f = 1000 Hz and an amplitude of 2.7 μN and 4 μN, for the uniform flagellum (Figure 4-2) and the sperm-like micro-swimmer (Figure 4-3), respectively, to maintain an amplitude of y_{0a} = 20 μm at the actuated end. It is observed that the average trajectory within a period of acoustic excitation is nearly a straight line parallel to the x-axis. The average (over one period) velocity in the first two periods varies (transient motion) and afterward stabilizes at 383.4 μm/s (Figure 4-2) or 5537 μm/s (Figure 4-3). For the micro-swimmer herein, considering the fluid density $\rho_0 \sim 10^3$ kg/m³, which leads to the Reynolds number Re = $\rho_0 LU/\mu$ = 7.668 × 10⁻⁴, which is sufficiently small to warrant the employment of the RFT (for the comparisons of Re, see Chapter 2.2.1). The stabilized terminal velocity V_{ave} is obtained with the simulation domain having around 10^4 elements (Figure 4-2) or 2 × 10^4 elements (Figure 4-3). Figure 4-4 illustrates the relative errors for the cases without and with head, respectively, in terms of the number of elements used in the FSI simulations. It is noted that the simulation results have converged (i.e., the deviation is within 5%) when the number of elements is more than 10^4, indicating that the FSI simulation is convergent and stable.
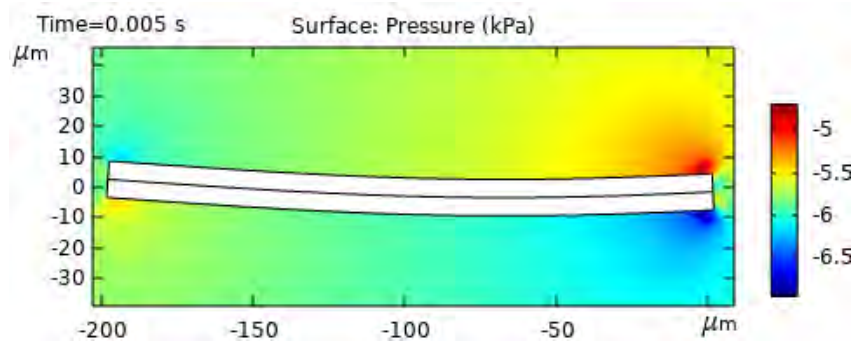
Figure 4-2. Examples of convergence analyses of the FSI simulation with common parameters $L = 200$ μm, $E = 10$ MPa, $\eta = 10$ Pa·s, $\mu = 0.1$ Pa·s, $y_{0a} = 20$ μm, and $f = 1000$ Hz: the pressure distribution of a uniform flagellum without head at the end of the fifth actuation period ($t = 0.005$ s) with $R_H = 0$, $\lambda = 0$, $W_{y0} = 12$ μm, $W_z = 40$ μm, and $F_a = 2.7$ μN.
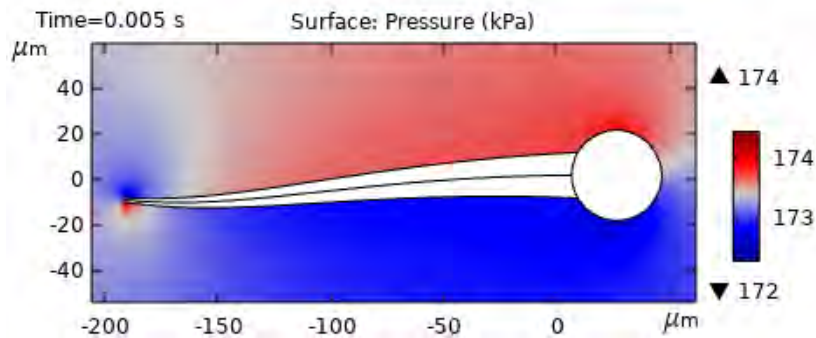
Figure 4-3. Examples of convergence analyses of the FSI simulation with common parameters $L = 200$ μm, $E = 10$ MPa, $\eta = 10$ Pa·s, $\mu = 0.1$ Pa·s, $y_{0a} = 20$ μm, and $f = 1000$ Hz: the pressure distribution of a tapered flagellum with head at the end of the fifth actuation period ($t = 0.005$ s) with $R_H = 20$ μm, $\lambda = 0.9$, $W_{y0} = 20$ μm, $W_z = 20$ μm, and $F_a = 4$ μN.
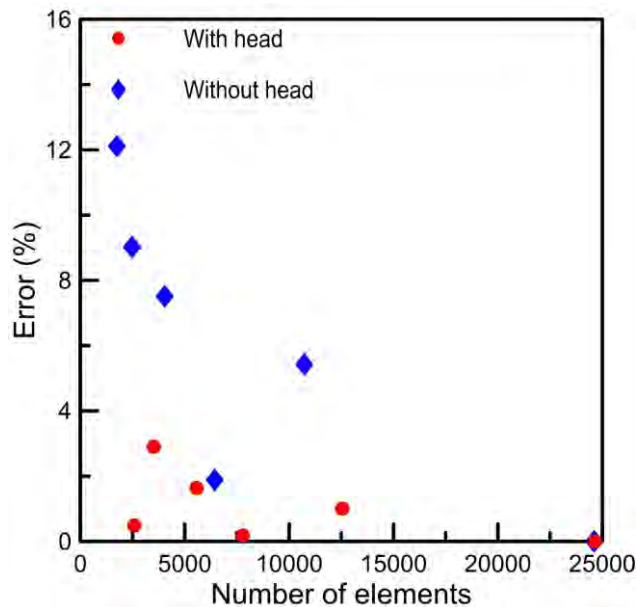
4.3 Correction to the RFT

The correction of RFT for the case of non-circular cross-section has been developed in Ref. [226]. Here we briefly introduce the concept and then simplify it to a more convenient form, i.e., the CRFT. As we have mentioned before, in an LRN regime, the Navier-Stokes equations of fluid reduce to the linear Stokes equations [26] given by Eqs. (2.1a, b) in Chapter 2. Considering a slender body of unit length, let $\mathbf{S}(s) = \left[S_{\parallel}(s), S_{\perp}(s) \right]^{\mathrm{T}}$ be the distribution of Stokeslets [256], where the superscript T denotes transpose and $0 \leq s \leq 1$ is the arclength along the body centerline. Applying the linear superposition method (for Eqs. (2.1a, b) are linear) to solve the fluid field and pressure distribution, the total fluid force $\mathbf{F}_f$ acting on a flagellum of unit length can be obtained as:

$$\mathbf{F}_f = -8\pi\mu \int_0^1 \mathbf{S}(s)\,\mathrm{d}s . \tag{4.1}$$

Let $\mathbf{P}(s)$ and $\kappa(s)$ be the coordinates and the half-width of the body at the position s along the body centerline, where $\kappa(s)$ also indicates how slender the body is. If κ is sufficiently small and the cross-section is circular, one can obtain the classical expression of $\mathbf{S}$ in terms of the fluid field $\mathbf{u}(s)$ based on the SBT [21]:

$$\mathbf{S}(s) = \frac{2\mathbf{I} - \hat{\mathbf{x}}(s)\hat{\mathbf{x}}(s)}{4\ln\kappa(s)} \cdot \left\{ \mathbf{u}(s) - \mathbf{V}(s) + S_{\perp}(s)\hat{\mathbf{y}}(s) \right.$$
$$+ \ln\left[4s(1-s)\right]\mathbf{S}(s) + S_{\parallel}(s)\left\{\ln\left[4s(1-s)\right] - 2\right\}\hat{\mathbf{x}}(s)$$
$$+ \int_{-s}^{1-s}\left[\frac{\mathbf{S}(s+\delta)}{|\mathbf{P}_{s\delta}|} - \frac{\mathbf{S}(s)}{|\delta|} + \frac{\mathbf{P}_{s\delta}\mathbf{P}_{s\delta}\cdot\mathbf{S}(s+\delta)}{|\mathbf{P}_{s\delta}|^3} - \frac{S_{\parallel}(s)\delta^2\hat{\mathbf{x}}(s)}{|\delta|^3}\right]\mathrm{d}\delta\right\} \qquad (4.2)$$

where $\hat{\mathbf{x}}(s)$ and $\hat{\mathbf{y}}(s)$ are orthogonal unit vectors that are tangential and normal to the body centerline, respectively, $\mathbf{I}$ the identity matrix, $\mathbf{P}_{s\delta} = \mathbf{P}(s) - \mathbf{P}(s + \delta)$ the distance vector, and $\mathbf{V}(s)$ the local translational velocity of the body.

To deal with arbitrary flagellum cross-sections or 2D problems (i.e., with rectangular cross-sections), we follow the method proposed in [226] to introduce a dimensionless coefficient tensor $\mathbf{K}$ to the expression of the fluid velocity field. Based on the SBT for circular flagellum cross-section, the relative fluid velocity field can be expressed as: $\mathbf{U} = \mathbf{C} \cdot \mathbf{S}$, where $\mathbf{U}(s) = \mathbf{u}(s) - \mathbf{V}(s)$ represents the relative velocity of the fluid with respect to the flagellum part at point s. For non-circular ones, it is assumed that the relative fluid velocity for the non-circular case is: $\mathbf{U} = (\mathbf{C} + \mathbf{K}) \cdot \mathbf{S}$, where $\mathbf{C}$ is the resistive tensor, and the Stokeslets $\mathbf{S}$ is still based on the expression for a slender body with a circular cross-section. Note that the revised expression of $\mathbf{U}$ can still meet the zero-divergence condition for fluid velocity (i.e., Eq. (2.1b)) as long as $\mathbf{K}$ is a symmetric tensor with zero divergence.

In Ref. [226], $\mathbf{K}$ depends only on the shape of the cross-section, which can be directly estimated for some special shapes without performing FSI simulations. Nevertheless, in most cases, FSI simulations are required to determine $\mathbf{K}$ because the dynamics of a solid body (e.g., the wiggling profile of a flagellum), which affects $\mathbf{U}$ and $\mathbf{K}$, cannot be determined *a priori*, as reported by Borker et al. [227]. Hence, we

assume that $\mathbf{K} = [K_{ij}]$ (i, j = 1, 2 for 2D problems) is the only correction tensor to determine and that it must be determined based on the comparison between the FSI simulation and the SBT model. In the following, we reduce the corrected SBT to the corrected RFT by neglecting interactions between different parts of a flagellum. This is generally an acceptable simplification in the study of micro-swimmers [21] considering the limited accuracy in experimental observation. In RFT, the fluid forces $\mathbf{F}_f$ acting on a slender body are assumed to be proportional to the local velocities of the body. We shall then include $\mathbf{K}$ in the coefficients of proportionality to establish the CRFT.

For shorthand, we recast Eq. (4.2) as:

$$\mathbf{S}(s) = \boldsymbol{\kappa}(s) \cdot \left\{ \mathbf{U}(s) + \psi\left[\mathbf{S}(s)\right] \right\}, \tag{4.3}$$

where $\boldsymbol{\kappa}(s) = \left[2\mathbf{I} - \hat{\mathbf{x}}(s)\hat{\mathbf{x}}(s) \right] / \left[4\ln\kappa(s) \right]$, and $\psi[\mathbf{S}(s)]$ is the functional of Stokeslets $\mathbf{S}(s)$ and $\psi(\mathbf{0}) = \mathbf{0}$. Taking the correction term $\mathbf{K} \cdot \mathbf{S}$ into account, Eq. (4.3) is rewritten as:

$$\mathbf{S}(s) = \boldsymbol{\kappa}(s) \cdot \left\{ \mathbf{U}(s) + \mathbf{K} \cdot \mathbf{S}(s) + \psi\left[\mathbf{S}(s)\right] \right\}. \tag{4.4}$$

The approximation of Eq. (4.4) can be made based on the scenario of a straight flagellum of a uniform cross-section. In this scenario, $\mathbf{U}$ and $\boldsymbol{\kappa}$ are constants, and the direction vectors $\hat{\mathbf{x}}$ and $\hat{\mathbf{y}}$ are independent of position s, i.e., $\mathbf{P}(s) = s\hat{\mathbf{x}}$, and $\mathbf{P}_{s\delta} = -\delta\hat{\mathbf{x}}$, which greatly simplifies the solution. An iterative procedure can then be adopted. In this case, Eq. (4.4) can be simplified as:

$$
\begin{aligned}
\mathbf{S}(s) = \frac{2\mathbf{I} - \hat{\mathbf{x}}\hat{\mathbf{x}}}{4\ln\kappa} \bullet \Big\{ & \mathbf{U} + \mathbf{K}\bullet\mathbf{S}(s) + S_\perp(s)\hat{\mathbf{y}} \\
& + \ln\big[4s(1-s)\big]\mathbf{S}(s) + S_\parallel(s)\big\{\ln\big[4s(1-s)\big]-2\big\}\hat{\mathbf{x}} \\
& + \int_{-s}^{1-s}\bigg[(\mathbf{I}+\hat{\mathbf{x}}\hat{\mathbf{x}})\bullet\frac{\mathbf{S}(s+\delta)-\mathbf{S}(s)}{|\delta|}\bigg]\mathrm{d}\delta \Big\}
\end{aligned}
\tag{4.5}
$$

Denoted by $U_\parallel(s)$ and $U_\perp(s)$ the components of $\mathbf{U}(s)$ tangential and normal to the local centerline of a flagellum, respectively, the corresponding fluid forces in the RFT are formulated as:

$$
F_{f\parallel} = c_\parallel U_\parallel, \quad F_{f\perp} = c_\perp U_\perp.
\tag{4.6a, b}
$$

When the body moves tangentially to its centerline, resulting in the Stokeslet vector $\mathbf{S}(s) = S_\parallel(s)\hat{\mathbf{x}}$, and the relative velocity $\mathbf{U} = U_\parallel\hat{\mathbf{x}}$, then Eq. (4.5) is recast as (note we have assumed that $K_{22} = -K_{11}$ due to the property of zero divergence of the tensor $\mathbf{K}$):

$$
S_\parallel(s) = \frac{1}{2\ln\kappa}\left\{ \frac{U_\parallel}{2} + S_\parallel(s)\left[\frac{K_{11}}{2} + \ln(4s - 4s^2) - 1\right] + \int_{-s}^{1-s}\frac{S_\parallel(s+\delta)-S_\parallel(s)}{|\delta|}\mathrm{d}\delta \right\}.
\tag{4.7}
$$

The zeroth iterative of Eq. (4.7) is expressed as:

$$
S_\parallel^{(0)}(s) = \frac{U_\parallel}{4\ln\kappa}.
\tag{4.8}
$$

Replacing $S_\parallel(s)$ on the right side of Eq. (4.7) with the right-hand side of Eq. (4.8) reaches the first iterative of the tangential Stokeslet, expressed as:

$$
S_\parallel^{(1)}(s) = \frac{U_\parallel}{4\ln\kappa}\left\{1 + \frac{1}{2\ln\kappa}\left[\frac{K_{11}}{2} + \ln(4s - 4s^2) - 1\right]\right\}.
\tag{4.9}
$$

Replacing $S_\parallel(s)$ on the right side of Eq. (4.7) with the right-hand side of Eq. (4.9) reaches the second iterative of the tangential Stokeslet, expressed as:

$$S_\parallel^{(2)}(s) = \frac{U_\parallel}{4\ln\kappa}\left\{1 + \frac{K_{11}}{4\ln\kappa} + \left(\frac{K_{11}}{4\ln\kappa}\right)^2 + \left(\frac{1}{2\ln\kappa} + \frac{K_{11}}{4\ln^2\kappa}\right)\left[\ln\left(4s - 4s^2\right) - 1\right]\right.$$

$$\left. + \left[\frac{\ln\left(4s - 4s^2\right) - 1}{2\ln\kappa}\right]^2 + \int_{-s}^{1-s} \frac{\ln\left[4(s+\delta)(1-s-\delta)\right] - \ln\left(4s - 4s^2\right)}{(2\ln\kappa)^2}\frac{d\delta}{|\delta|}\right\}. \quad (4.10)$$

The second-order approximation is normally accurate enough for the RFT [21]. Then the total tangential fluid force of the slender body of unit length can be obtained based on Eq. (4.1) and is expressed as:

$$F_{f\parallel} = -8\pi\mu\int_0^1 S_\parallel^{(2)}(s)\,ds$$

$$= -8\pi\mu\frac{U_\parallel}{4\ln\kappa}\left\{1 + \frac{K_{11}}{4\ln\kappa} + \left(\frac{K_{11}}{4\ln\kappa}\right)^2\right.$$

$$+ \left(\frac{1}{2\ln\kappa} + \frac{K_{11}}{4\ln^2\kappa}\right)\int_0^1\left[\ln\left(4s - 4s^2\right) - 1\right]ds$$

$$+ \frac{1}{(2\ln\kappa)^2}\int_0^1\left[\ln\left(4s - 4s^2\right) - 1\right]^2 ds$$

$$\left. + \frac{1}{(2\ln\kappa)^2}\int_0^1\int_{-s}^{1-s}\frac{\ln\left[4(s+\delta)(1-s-\delta)\right] - \ln\left(4s - 4s^2\right)}{|\delta|}\,d\delta ds\right\}. \quad (4.11)$$

$$= -2\pi\mu\frac{U_\parallel}{\ln\kappa}\left\{1 + \frac{K_{11}}{4\ln\kappa} + \left(\frac{K_{11}}{4\ln\kappa}\right)^2 + \left(\frac{1}{2\ln\kappa} + \frac{K_{11}}{4\ln^2\kappa}\right)(2\ln 2 - 3)\right.$$

$$\left. + \frac{1}{(2\ln\kappa)^2}\left[4\left(\frac{3}{2} - \ln 2\right)^2 + 4 - \frac{\pi^2}{3}\right] + \frac{1}{(2\ln\kappa)^2}\left(-2.724\times10^{-8}\right)\right\}$$

$$= 2\pi\mu U_\parallel\left[\frac{1}{\ln(1/\kappa)} + \frac{\frac{3}{2} - \ln 2 - \frac{K_{11}}{4}}{\ln^2(1/\kappa)} + \frac{\left(\frac{3}{2} - \ln 2 - \frac{K_{11}}{4}\right)^2 + 1 - \frac{\pi^2}{12}}{\ln^3(1/\kappa)}\right]$$

The tangential coefficient of resistive force $c_\parallel$ in the CRFT can be obtained from Eq. (4.11) by setting $K_{11} = K$, which is expressed as:

$$c_{\parallel} = 2\pi\mu \left[\frac{1}{\ln\left(1/\kappa\right)} + \frac{\frac{3}{2} - \ln 2 - \frac{K}{4}}{\ln^2\left(1/\kappa\right)} + \frac{\left(\frac{3}{2} - \ln 2 - \frac{K}{4}\right)^2 + 1 - \frac{\pi^2}{12}}{\ln^3\left(1/\kappa\right)} \right]. \tag{4.12}$$

It is found that the influence of δ on the integral is negligible ($\sim 10^{-8}$), which justifies RFT. To compare this expression with the classical one, we can construct the identical equation with non-zero constants b_1, b_2, and b_3, which is expressed as:

$$\frac{1}{b_3} + \frac{b_1}{b_3^2} + \frac{b_2}{b_3^3} = \frac{1}{b_3 - b_1 + \left(b_1^2 - b_2\right)/b_3} + \frac{b_1^3 - 2b_1b_2 + \left(b_1^2 b_2 - b_2^2\right)/b_3}{b_3^4 - b_1 b_3^3 + \left(b_1^2 - b_2\right)b_3^2}. \tag{4.13}$$

If $b_3 = \ln(1/\kappa)$ is much larger than b_1 and b_2, we can only keep the first term of the right side of Eq. (4.13), and accordingly, Eq. (4.12) will be simplified to

$$F_{f\parallel} = 2\pi\mu U_{\parallel} \left\{ \left[\frac{1}{\ln\left(1/\kappa\right)} - \frac{3}{2} + \ln 2 + \frac{K}{4} - \left(1 - \frac{\pi^2}{12}\right) \middle/ \ln\left(1/\kappa\right) \right]^{-1} + O\left[\frac{1}{\ln^4\left(1/\kappa\right)} \right] \right\}. \tag{4.14}$$

When $K = 0$, Eq. (4.14) reduces to the classical RFT expression (cf. Eq. (19) in Ref. [21] or Eq. (3.21) in Chapter 3). However, in our work, $\ln(1/\kappa)$ is around 3, and K is uncertain. Therefore, the approximation of Eq. (4.14) does not work; instead, Eq. (4.11) should be used.

When the body moves perpendicularly to its centerline, resulting in the Stokeslet vector $\mathbf{S}(s) = S_{\perp}(s)\hat{\mathbf{y}}$, and the relative velocity $\mathbf{U} = U_{\perp}\hat{\mathbf{y}}$, then Eq. (4.5) is recast as:

$$S_{\perp}(s) = \frac{1}{2\ln\kappa} \left\{ U_{\perp} + S_{\perp}(s)\left[K_{22} + \ln\left(4s - 4s^2\right) + 1 \right] + \int_{-s}^{1-s} \frac{S_{\perp}(s+\delta) - S_{\perp}(s)}{|\delta|} d\delta \right\}. \tag{4.15}$$

The zeroth iterative of Eq. (4.15) is expressed as:

$$S_{\perp}^{(0)}(s) = \frac{U_{\perp}}{2\ln\kappa}.$$

(4.16)

Replacing $S_{\perp}(s)$ on the right side of Eq. (4.15) with the right-hand side of Eq. (4.16) renders the first iterative of the normal Stokeslet, expressed as:

$$S_{\perp}^{(1)}(s) = \frac{U_{\perp}}{2\ln\kappa}\left\{1 + \frac{1}{2\ln\kappa}\left[K_{22} + \ln\left(4s - 4s^2\right) + 1\right]\right\}.$$

(4.17)

Replacing $S_{\perp}(s)$ on the right side of Eq. (4.15) with the right-hand side of Eq. (4.17) reaches the second iterative of the normal Stokeslet, expressed as:

$$\begin{aligned}
S_{\perp}^{(2)}(s) = \frac{U_{\perp}}{2\ln\kappa}\Bigg\{ & 1 + \frac{K_{22}}{2\ln\kappa} + \left(\frac{K_{22}}{2\ln\kappa}\right)^2 + \left(\frac{1}{2\ln\kappa} + \frac{K_{22}}{2\ln^2\kappa}\right)\left[\ln\left(4s - 4s^2\right) + 1\right] \\
& + \left[\frac{\ln\left(4s - 4s^2\right) + 1}{2\ln\kappa}\right]^2 + \int_{-s}^{1-s}\frac{\ln\left[4(s+\delta)(1-s-\delta)\right] - \ln\left(4s - 4s^2\right)}{\left(2\ln\kappa\right)^2}\frac{\mathrm{d}\delta}{|\delta|}\Bigg\}.
\end{aligned}$$

(4.18)

Then the total fluid force normal to the slender body of unit length can be expressed based on Eq. (4.1), which is expressed as:

$$F_{f\perp} = -8\pi\mu\int_0^1 S_\perp^{(2)}(s)\,ds$$

$$= -8\pi\mu\frac{U_\perp}{2\ln\kappa}\left\{1 + \frac{K_{22}}{2\ln\kappa} + \left(\frac{K_{22}}{2\ln\kappa}\right)^2\right.$$

$$+\left(\frac{1}{2\ln\kappa} + \frac{K_{22}}{2\ln^2\kappa}\right)\int_0^1\left[\ln(4s-4s^2)+1\right]ds + \frac{1}{(2\ln\kappa)^2}\int_0^1\left[\ln(4s-4s^2)+1\right]^2 ds$$

$$\left.+\frac{1}{(2\ln\kappa)^2}\int_0^1\int_{-s}^{1-s}\frac{\ln\left[4(s+\delta)(1-s-\delta)\right]-\ln(4s-4s^2)}{|\delta|}\,d\delta ds\right\}$$

$$= -4\pi\mu\frac{U_\perp}{\ln\kappa}\left\{1 + \frac{K_{22}}{2\ln\kappa} + \left(\frac{K_{22}}{2\ln\kappa}\right)^2 + \left(\frac{1}{2\ln\kappa} + \frac{K_{22}}{2\ln^2\kappa}\right)(2\ln 2 - 1)\right.$$

$$\left.+\frac{1}{(2\ln\kappa)^2}\left[4\left(\frac{1}{2}-\ln 2\right)^2 + 4 - \frac{\pi^2}{3}\right] + \frac{1}{(2\ln\kappa)^2}\left(-2.724\times 10^{-8}\right)\right\}$$

$$= 4\pi\mu U_\perp\left[\frac{1}{\ln(1/\kappa)} + \frac{\frac{1}{2}-\ln 2-\frac{K_{22}}{2}}{\ln^2(1/\kappa)} + \frac{\left(\frac{1}{2}-\ln 2-\frac{K_{22}}{2}\right)^2+1-\frac{\pi^2}{12}}{\ln^3(1/\kappa)}\right]$$

.(4.19)

The normal coefficient of resistive force $c_\perp$ can be obtained from Eq. (4.19) by setting $K_{22} = -K$ due to the zero divergence of **K**, which is expressed as:

$$c_\perp = 4\pi\mu\left[\frac{1}{\ln(1/\kappa)} + \frac{\frac{1}{2}-\ln 2+\frac{K}{2}}{\ln^2(1/\kappa)} + \frac{\left(\frac{1}{2}-\ln 2+\frac{K}{2}\right)^2+1-\frac{\pi^2}{12}}{\ln^3(1/\kappa)}\right]. \tag{4.20}$$

Similarly, Eq. (4.19) can also be simplified under the condition of sufficiently large $\ln(1/\kappa)$, which is expressed as:

$$F_{f\perp} = 4\pi\mu U_\perp\left\{\left[\frac{1}{\ln(1/\kappa)} - \frac{1}{2} + \ln 2 - \frac{K}{2} - \left(1-\frac{\pi^2}{12}\right)\Big/\ln(1/\kappa)\right]^{-1} + O\left[\frac{1}{\ln^4(1/\kappa)}\right]\right\}. \tag{4.21}$$

When $K = 0$, Eq. (4.21) reduces the classical RFT expression (cf. Eq. (20) in Ref. [21] or Eq. (3.20) in Chapter 3). However, we use Eq. (4.19) in our work because $\ln(1/\kappa)$ is

not large, and K is uncertain. The proposed CRFT is then applicable to formulate the governing equations of an AFMS based on the bar-joint model.

4.4 The governing equations of the flagellum for the bar-joint model

Figure 4-5 demonstrates the bar-joint model of the AFMS. The flagellum is simplified into rigid bars with a constant length of $2l$. They are indexed (denoted by i) from 1 to N and connected with linear torsion springs [43]. The ith spring joint connects the bars i and $(i + 1)$ and the first $(i = 1)$ bar is assumed to be rigidly connected to the head. The motion of the ith bar and the head $(i = 0)$ can be represented by the vector of time-dependent variables $\mathbf{X}_i(t) = (x_i, y_i, \theta_i)^\mathrm{T}$, where x_i and y_i are coordinates of the midpoint of the ith bar (or the center of the head), and θ_i the angle of rotation with respect to the x-axis (anticlockwise rotation is taken as positive). Correspondingly, the velocity vector of the head $(i = 0)$ and bars $(i > 0)$ can be represented by $\dot{\mathbf{X}}_i = \left(\dot{x}_i, \dot{y}_i, \dot{\theta}_i \right)^\mathrm{T}$, where the overhead dot denotes the time derivative. A point P in the ith bar with the distance s from the joint $(i - 1)$ has the coordinate $\mathbf{P}_i(s)$ expressed as:

$$\mathbf{P}_i(s) = \left[x_i + (s - l)\cos\theta_i, y_i + (s - l)\sin\theta_i \right]^\mathrm{T}. \tag{4.22}$$

Note that the coordinates of the head center $\mathbf{P}_0 = (x_0, y_0)^\mathrm{T}$ is independent of s, which is employed to track the trajectory of the micro-swimmer. Differentiating the right-hand side of Eq. (4.22) with respect to time yields the translational velocity $\mathbf{V}_i(s)$:

$$\mathbf{V}_i(s) = \mathbf{T}_{Vi}(s)\dot{\mathbf{X}}_i = \begin{bmatrix} 1 & 0 & -(s-l)\sin\theta_i \\ 0 & 1 & (s-l)\cos\theta_i \end{bmatrix} \begin{bmatrix} \dot{x}_i \\ \dot{y}_i \\ \dot{\theta}_i \end{bmatrix}, \tag{4.23}$$

where $\mathbf{T}_{Vi}(s)$ is the transformation matrix of velocity for the points in the ith bar.

To simplify the derivation, we first assume that the swimmer suspends in a static fluid field, i.e., $\mathbf{u} = 0$. Hence, the relative velocity $\mathbf{U} = -\mathbf{V}$, and the total fluid forces on a rigid slender body, i.e., Eqs. (4.6a, b), are recast to $F_{f\parallel} = -c_{\parallel}V_{\parallel}$ and $F_{f\perp} = -c_{\perp}V_{\perp}$. Based on the RFT, the resistive coefficients $c_{\parallel}$ and $c_{\perp}$ are assumed to be constant even if the body is flexible and curved, i.e., the tangential and vertical components of local fluid forces $\mathbf{f}_f(s)$ at position s can be formulated as: $f_{f\parallel}(s) = -c_{\parallel}V_{\parallel}(s)$ and $f_{f\perp}(s) = -c_{\perp}V_{\perp}(s)$. Consequently, the tensor of resistive coefficients $\mathbf{C}_i$ for the ith bar based on the CRFT can be expressed as:

$$\mathbf{C}_i = \begin{bmatrix} -c_{\parallel i} & 0 \\ 0 & -c_{\perp i} \end{bmatrix}. \tag{4.24}$$

Note that $\mathbf{C}_i$ varies with i because the bar width may vary when considering a tapered flagellum. The fluid forces $\mathbf{f}_{\mathrm{flu}i}(s)$ at position s of the ith bar is then expressed as:

$$\begin{aligned} \mathbf{f}_{\mathrm{flu}i}(s) &= \mathbf{T}_{Ri}^{-1}\{\mathbf{C}_i[\mathbf{T}_{Ri}\mathbf{V}_i(s)]\} \\ &= \mathbf{T}_{Ri}^{-1}\mathbf{C}_i\mathbf{T}_{Ri}\mathbf{T}_{Vi}(s)\dot{\mathbf{X}}_i \quad, \\ &= \mathbf{a}_i(s)\dot{\mathbf{X}}_i \end{aligned} \tag{4.25}$$

where $\mathbf{T}_{Ri} = \begin{bmatrix} \cos\theta_i & \sin\theta_i \\ -\sin\theta_i & \cos\theta_i \end{bmatrix}$ is the transformation matrix of rotation and the 2×3 resistive matrix $\mathbf{a}_i(s)$ depends on the position s of the ith bar. We introduce the unit vectors $\mathbf{e}_1 = (1, 0, 0)^{\mathrm{T}}$, $\mathbf{e}_2 = (0, 1, 0)^{\mathrm{T}}$, and $\mathbf{e}_3 = (0, 0, 1)^{\mathrm{T}}$ to facilitate derivations and the resultant fluid force vector $\mathbf{F}_{\mathrm{flu}i}$ for the ith bar. The latter is given by

$$\mathbf{F}_{\text{flu}i} = \int_0^{2l} \left[\mathbf{I}_a \mathbf{f}_{\text{flu}i}(s) + \mathbf{P}_i(s) \times \mathbf{f}_{\text{flu}i}(s) \right] ds$$

$$= \left\{ \int_0^{2l} \left[\mathbf{I}_a \mathbf{a}_i + \sum_{j=1}^{3} \mathbf{P}_i \times (\mathbf{a}_i \cdot \mathbf{e}_j) \otimes \mathbf{e}_j \right] ds \right\} \dot{\mathbf{X}}_i , \qquad (4.26)$$

$$= \mathbf{A}_i \dot{\mathbf{X}}_i$$

where the operators $\times$ and $\otimes$ indicate cross and outer products of two vectors, respectively, the 3×3 tensor $\mathbf{A}_i$ is the fluid resistive matrix of the ith bar, and the

augmented identity matrix $\mathbf{I}_a = \begin{bmatrix} 1 & 0 & 0 \\ 0 & 1 & 0 \end{bmatrix}^{\text{T}}$ is employed to extend the number of rows

from 2 to 3 (note that the third component of $\mathbf{F}_{\text{ful}i}$ is the resultant torque about the origin of the coordinate system due to fluid forces). We assume that the hydrodynamic resultant forces and torque on the circular head $\mathbf{F}_{\text{flu}0}$ can be expressed as:

$$\mathbf{F}_{\text{flu}0} = \begin{bmatrix} -c_H & 0 & 0 \\ 0 & -c_H & 0 \\ c_H y_0 & -c_H x_0 & -c_{HR} \end{bmatrix} \begin{bmatrix} \dot{x}_0 \\ \dot{y}_0 \\ \dot{\theta}_0 \end{bmatrix} = \mathbf{A}_0 \dot{\mathbf{X}}_0 , \qquad (4.27)$$

where c_H and c_{HR} are coefficients of resistance and are dependent on the head geometry and fluid viscosity [257]. Note that for a 2D FSI simulation, a circular head is a cylinder instead of a sphere. In this case, c_H should be proportional to the thickness of W_z with a coefficient of resistance related to the Reynolds number, expressed as [258]:

$$c_H = \frac{4\pi\mu W_z}{1/2 - \Gamma - \ln(\text{Re}/8)} , \qquad (4.28)$$

where $\Gamma \approx 0.577$ is the Euler's constant, and the Reynolds number of the head Re $=$ $2\rho_0 U R_H/\mu$. For the micro-swimmer herein, considering the fluid density $\sim 10^3$ kg/m³,

and the characteristic velocity $U \sim 10^{-3}$ m/s, Re can be estimated to be $2R_H/\mu$. The rotational drag coefficient of the head c_{HR} is determined by [256]:

$$c_{HR} = 4\pi\mu R_H{}^2 W_z .$$ (4.29)

Then the equilibrium equations for the whole micro-swimmer can be given by

$$\sum_{i=1}^{n} \mathbf{A}_i \dot{\mathbf{X}}_i + \mathbf{A}_0 \dot{\mathbf{X}}_0 + \mathbf{F}_0 = \mathbf{0} ,$$ (4.30)

or in the matrix form:

$$\begin{bmatrix} \mathbf{A}_0 & \mathbf{A} \end{bmatrix} \begin{bmatrix} \dot{\mathbf{X}}_0 \\ \dot{\mathbf{X}} \end{bmatrix} + \mathbf{F}_0 = \mathbf{0} ,$$ (4.31)

where $\mathbf{A_0}$ and $\mathbf{A}$ are the resistive matrices of the head and bars (detailed expressions can be seen in Eqs. (B.4) and (B.7) in Appendix B), and $\mathbf{F}_0 = [F_{extx}, F_{exty,} \ \tau_{ext} + x_0 F_{extx} - y_0 F_{extx}]^T$ is the vector of the external actuation, containing horizontal and vertical forces (arising from the acoustic actuation) and a torque (about the origin, arising from the magnetic power) on the head.

At the ith joint, the velocities determined from the two connected bars should be equal, i.e., $\mathbf{V}_i(2l) = \mathbf{V}_{i+1}(0)$, which after substituting Eq. (4.23), gives rise to the kinematic constraints:

$$\begin{bmatrix} -\mathbf{T}_{Vi}(2l) & \mathbf{T}_{V(i+1)}(0) \end{bmatrix} \begin{bmatrix} \dot{\mathbf{X}}_i \\ \dot{\mathbf{X}}_{i+1} \end{bmatrix} = \mathbf{0} ,$$ (4.32)

where i runs from 1 to $(N-1)$. Since the first bar and the head are assumed to be rigidly connected, one can obtain the below ODEs in terms of the constraint:

$$\dot{\mathbf{X}}_0 = \mathbf{I}_a \mathbf{V}_1 \left(-R_H \right) + \left(\mathbf{e}_3 \otimes \mathbf{e}_3 \right) \dot{\mathbf{X}}_1$$
$$= \left[\mathbf{I}_a \mathbf{T}_{V1} \left(-R_H \right) + \mathbf{e}_3 \otimes \mathbf{e}_3 \right] \dot{\mathbf{X}}_1 . \tag{4.33}$$
$$= \mathbf{B}_0 \dot{\mathbf{X}}_1$$

For shorthand, Eqs. (4.32) and (4.33) can be combined as below $(2N + 1)$ equations in terms of the constraints:

$$\begin{bmatrix} \mathbf{0} & \mathbf{T}_V \\ -\mathbf{I} & \mathbf{B} \end{bmatrix} \begin{bmatrix} \dot{\mathbf{X}}_0 \\ \dot{\mathbf{X}} \end{bmatrix} = \mathbf{0}, \tag{4.34}$$

where $\mathbf{I}$ is a 3×3 identity matrix, $\mathbf{T}_V$ the matrix of kinematic constraints of neighboring bars (see Eq. (B.8)), and $\mathbf{B}$ the kinematic constraints between the first bar and the head (see Eq. (B.11)).

The polymeric (viscoelastic) flagellum is described based on the discrete beam theory [223] in which the inherent damping in most polymers is nonnegligible based on our results in Chapter 3. The material of the micro-swimmer is considered to be a kind of isotropic polymer described by the Kelvin-Voigt viscoelastic model [237]. The moment induced by the torsion spring at the ith joint M_i is expressed in a forward difference formula as:

$$M_i = E \frac{I_i + I_{i+1}}{2} \frac{\theta_{i+1} - \theta_i}{2l} + \eta \frac{I_i + I_{i+1}}{2} \frac{\dot{\theta}_{i+1} - \dot{\theta}_i}{2l}, \tag{4.35}$$

where I_i denotes the second moment of area of the ith bar, in which an average value of I between two neighboring bars is adopted to indicate the second moment of area at the ith joint in case the flagellum is non-uniform. For the moment equilibrium, as demonstrated in Figure 4-6, torques are taken about the origin. The reaction forces at the ith joint F_{Rx} and F_{Ry} can be determined by the balance of forces over the first i bars

and the head. The moment equilibrium of the structure before the ith joint leads to the below equations:

$$0 = M_i + \sum_{j=1}^{i} \left(\mathbf{F}_{\mathrm{flu}j} \bullet \mathbf{e}_3 \right) + \left(\mathbf{F}_{\mathrm{flu}0} + \mathbf{F}_0 \right) \bullet \mathbf{e}_3$$
$$- \left\{ \mathbf{P}_i \left(2l \right) \times \left[\left(\mathbf{F}_0^{\mathrm{T}} \mathbf{I}_a \right)^{\mathrm{T}} + \left(\mathbf{F}_{\mathrm{flu}0}^{\mathrm{T}} \mathbf{I}_a \right)^{\mathrm{T}} + \sum_{j=1}^{i} \int_0^{2l} \mathbf{f}_{\mathrm{flu}j} \left(s \right) \mathrm{d}s \right] \right\} \bullet \mathbf{e}_3 \quad , \tag{4.36}$$

where i runs from 1 to $(N-1)$. Substituting Eqs. (4.24), (4.25), (4.30) and (4.35) into (4.36) gives rise to the moment equilibrium of the structure, which are expressed as the below $(N-1)$ equations:

$$\begin{bmatrix} \mathbf{D}_0 & \mathbf{D} \end{bmatrix} \begin{bmatrix} \dot{\mathbf{X}}_0 \\ \dot{\mathbf{X}} \end{bmatrix} = \mathbf{F}_E \, , \tag{4.37}$$

where $\mathbf{D}$ and $\mathbf{D}_0$ are the matrix of moment balance related to the bars and head, respectively, which are expressed in Eqs. (B.13) and (B.17), and $\mathbf{F}_E$ is a list of torques, which is expressed in Eq. (B.19) in Appendix B.

Finally, combining Eqs. (4.31), (4.34), and (4.37), the governing ODEs of the bar-joint model based on the CRFT can be expressed as:

$$\begin{bmatrix} \mathbf{A}_0 & \mathbf{A} \\ \mathbf{0} & \mathbf{T}_V \\ -\mathbf{I} & \mathbf{B} \\ \mathbf{D}_0 & \mathbf{D} \end{bmatrix} \begin{bmatrix} \dot{\mathbf{X}}_0 \\ \dot{\mathbf{X}} \end{bmatrix} = \begin{bmatrix} -\mathbf{F}_0 \\ \mathbf{0} \\ \mathbf{0} \\ \mathbf{F}_E \end{bmatrix} . \tag{4.38}$$

The EOM (Eq. (4.38)) is a set of $(3N+3)$ ODEs, where the detailed expressions can be seen in Appendix B. For the swimmer suspends in a non-static fluid circumstance, i.e., $\mathbf{u} = 0$, there will be some revisions in Eq. (4.38), and the corresponding detailed expressions can also be seen in Appendix B. The non-dimensionalization of Eq. (4.38)

can be taken by choosing the half-length of a bar l, the frequency of the acoustic

actuation f, and the fluid viscosity μ as the reference variables based on the Buckingham

π theorem [259]. The detailed dimensionless quantities are in Appendix C. Eq. (4.38)

can be solved by using the built-in ODE solver *ode15s* in MATLAB [246].
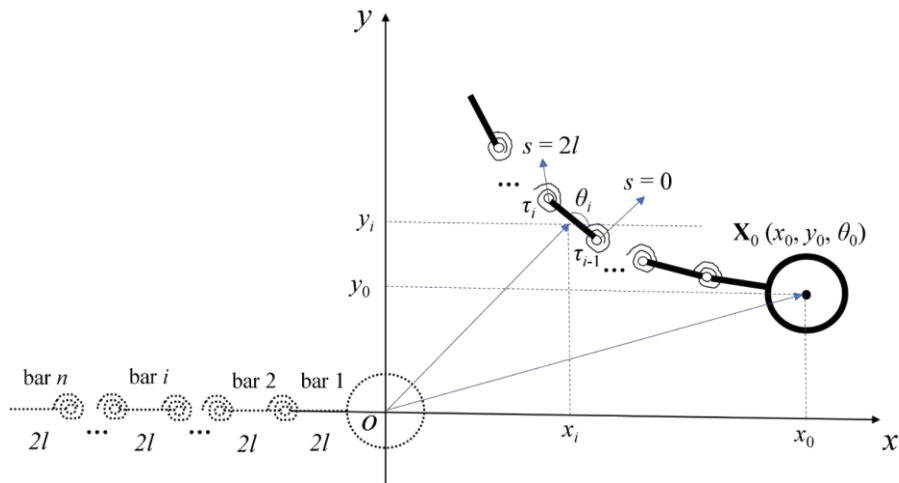
Figure 4-5. The schematic of the bar-joint model of the AFMS, where the global coordinate system is established with the origin at the centroid of the head and the x- and y-axes being the longitudinal and transverse axes of the flagellum at the initial state, respectively.
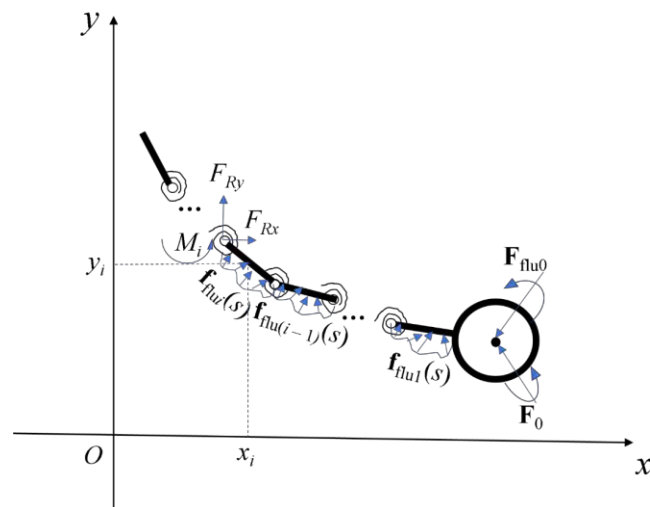
Figure 4-6. The diagram of force analysis for the bar-joint model.

110

4.5 Convergence analyses of the bar-joint model

Here we show an example of the convergence analysis of the bar-joint model. For the convenience of comparisons, all the geometric and material parameters have the same values as those in the 1D classical continuum model in Figure 3-30 in Chapter 3, in which the cross-section of the tapered flagellum is circular with the largest diameter $W_{y0} = 25$ μm and the tapering index $\lambda = 0.9$. Hence, for the bar-joint model, if we take the diameter at position $\mathbf{P}_i(0)$ of a continuum flagellum as the diameter of the ith bar, i.e., W_{yi}, of a bar-joint flagellum, then W_{yi} can be derived given by

$$W_{yi} = W_{y0}\left[1 - \lambda\frac{2l(i-1)}{L}\right], \quad i = 1, 2, ..., N. \tag{4.39}$$

The head is assumed to be a sphere with a radius of $R_H = 25$ μm, and the effect of the spherical head on locomotion is accounted for by the coefficient of resistance c_H given below as mentioned in Chapter 3:

$$c_H = 6\pi\mu R_H. \tag{4.40}$$

Other parameters in the bar-joint model are: $K = 0$ (i.e., for the circular cross-section, the CRFT reduces to the RFT), $c_{HR} = 0$ for eliminating the resistive effect of head rotation, $\mathbf{u} = 0$, $F_{extx} = 0$, $F_{exty} = F_a\cos\omega t$, $\tau_{ext} = 0$, $f = 4600$ Hz, $L = 180$ μm, $E = 10$ MPa, $\eta = 1730$ Pa·s, $\mu = 1$ Pa·s, and $F_a = 344$ μN to make $y_{0a} = 20$ μm.

For the bar-joint model of the AFMS with a head ($R_H = 25$ μm), the number of bars N varies from 2 to 60, and V_{ave} is the position change of the head in the fifth period times f. The result of V_{ave} increases with N and levels off (with fluctuations) when $N > 20$, as illustrated in Figure 4-7. Thus, we set $N = 20$ in the following sections of this

thesis. Note that the analytical result in Chapter 3 is ~350 μm/s when y_{0a} = 20 μm. The converged result of the bar-joint model is ~260 μm/s, 25% smaller than the analytical result in Chapter 3. Such a deviation is in accordance with the expectation (see discussions in Refs. [17, 23]) because the 1D analytical model cannot involve the effect of rigid-body rotation which greatly affects locomotion. Other factors, such as the ignorance of inextensibility and large deflection, also contribute substitutionally to the error of the 1D analytical model.
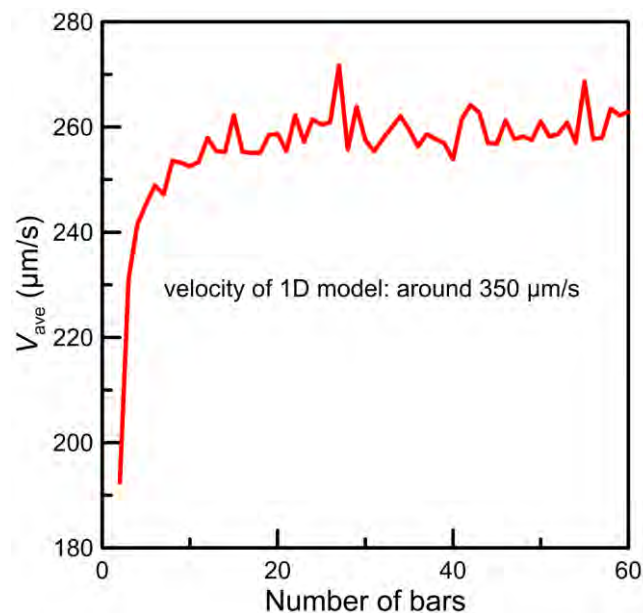
Figure 4-7. The convergence analysis of the bai-joint model in terms of the number of bars with parameters identical to results of Figure 3-30 in Chapter 3, i.e., the terminal velocity is around 350 μm/s when the amplitude is 20 μm.

4.6 Determination of *K*

The correction factor K is determined by comparing the terminal average velocities V_{ave} obtained from the FSI simulations and the CRFT-based bar-joint model. As an example, Figure 4-8 shows the results of the CRFT-based bar-joint model when K

sweeps from 0.1 to 100 for the case of a uniform flagellum without a head. In solving the bar-joint model, we also set $y_{0a} = 20$ μm and $N = 20$ to determine V_{ave} (blue dotted curve in Figure 4-8), and the deviations (red curve in Figure 4-8) from the simulation result (383.4 μm/s) has a sharp minimum at $K = 3.2$, which is less than 1%. Note that it only takes several seconds to solve our CRFT model for a certain value of K but may take several minutes to reach K for the minimum error.

In principle, adjusting K can lead to an excellent agreement between simulation and CRFT results. In the following estimate of K for different cases, we set the criterion of acceptable deviation in V_{ave} to be 5% to balance the computational efficiency and accuracy and demonstrate several relations between K and the flagellum slenderness α ($\alpha = W_y/L$) in Figure 4-9, Figure 4-10 and Figure 4-11. In order to ensure that the flagellum is still a slender body, we set α in the range of 0.05 – 0.07 [17]. Figure 4-9 and Figure 4-10 show that K varies almost linearly with α, and the slope depends on the thickness W_z, for both the uniform flagellum without a head and the sperm-like micro-swimmer with a rigid-cylindrical head, respectively. The detailed expressions of K in terms of α obtained through linear regression are listed in Table 4-1.

In Table 4-1, one can note that the existence of a head can change the slope of the linear K - α relation from a negative value to a positive one. Besides, as observed in Figure 4-10, the variation of R_H can hardly influence the K - α curve. In addition, K doubles when the depth W_z increases from 20 to 40 μm , as shown in Figure 4-9 and Figure 4-10, and also doubles when L increases from 200 to 400 μm, as shown in Figure 4-11. These results suggest that, roughly speaking, K is linearly dependent on the volume of the flagellum. In Figure 4-11, α is sampled from 0.05 to 0.1, and the fitting

113

equation obtained in the α range of 0.05 to 0.07 is used. In the 0.07 to 0.1 range, the difference between the fitting equation and the actual results of K is still below 3%.

When a tapered flagellum is discretized into a bar-joint model, these bars have uniform dimensions. In this case, the fitting equations of K for a uniform flagellum may be directly employed. For example, consider the micro-swimmer with $L = 200$ μm and $R_H = W_z = W_{y0} = 20$ μm, assume that the width of the ith bar, i.e., W_{yi}, follows the tapering equation Eq. (4.39) and that the slenderness of the ith bar, i.e., α_i, equals W_{yi}/L, the correction factor of the ith bar, i.e., K_i, can then be estimated according to the fitting curve of K in Figure 4-11. In this way, we can directly obtain the terminal average velocity V_{ave} based on the CRFT model without implementing the FSI simulation. We herein designate this method as the direct-K method. Straightforward though this method is, its outcomes can deviate from those of the FSI simulation, and the corresponding error in terms of the tapering index λ is illustrated in the blue dotted line in Figure 4-12. For the classical RFT model, i.e., $K_i = 0$ for each bar, the error exceeds 90%. For the direct-K method, it is noted that the error is around 12% for $\lambda > 0.2$, which indicates that if we directly apply the fitting expression of K arising from the case of a uniform flagellum to the case of a tapered one, the error can decrease by about 80% from the results of RFT. However, the deviation is still considerable.

More accurate results for a tapered flagellum can be achieved by assuming that all bars have identical K, i.e., $K_i = K$. In this way, we treat a tapered flagellum to be an equivalent uniform one with an effective K, and thus this method is regarded as the effective-K method. The red circles in Figure 4-12 represent the effective K at different λ, and the red solid line is the corresponding linear fitting: $K = -1.29\lambda + 6.43$. It is noted that in Figure 4-12 for $\lambda \leq 0.1$, the magnitude of the effective K is nearly identical to

that of the case of $\lambda = 0$, and the error of the effective-K method is close to 0, indicating that the effect of tapering on hydrodynamics only works when $\lambda > 0.1$.

Note that the above results of K are obtained with the specific material and actuation parameters. We find that y_{0a} and η hardly affect the determination of K, while f, E and μ can have considerable influence. For example, for the micro-swimmer as shown in Figure 4-3 in Chapter 4.2, we varied f, E and μ to check their influence on K. It is noted that the combined term $\beta = \mu f / E$ is an important non-dimensional parameter in the governing equations of flagellum's hydrodynamics. For example, β enters into the elasto-hydrodynamic penetration length [38]: $\sqrt[4]{(EI)/(2\pi c_\perp f)}$, proportional to $\sqrt[4]{1/\beta}$, and the sperm number [116]: $L\sqrt[4]{(2\pi c_\perp f)/(EI)}$, proportional to $\sqrt[4]{\beta}$. Hence, we plot the relations between K and β in Figure 4-13 with the corresponding fitting equations listed in Table 4-1. It is noted that when β is between 5 and 20, the variations of K in terms of f, E and μ collapse to the same curve. When $\beta > 20$, the effects of E and μ are still the same and tend to level off; nevertheless, the effect of head excitation frequency f tends to lean upwards. The difference in K increases with the increase in f and μ (or decrease in E) when $\beta > 20$ because raising f can considerably enhance V_{ave} (which leads to a larger K) as it can induce the change of the flagellum's wiggling profile (e.g., bringing about smaller wavelength). Instead, increasing μ or reducing E only leads to larger resistive forces under the same wiggling profile, which results in a small enhancement in V_{ave}.
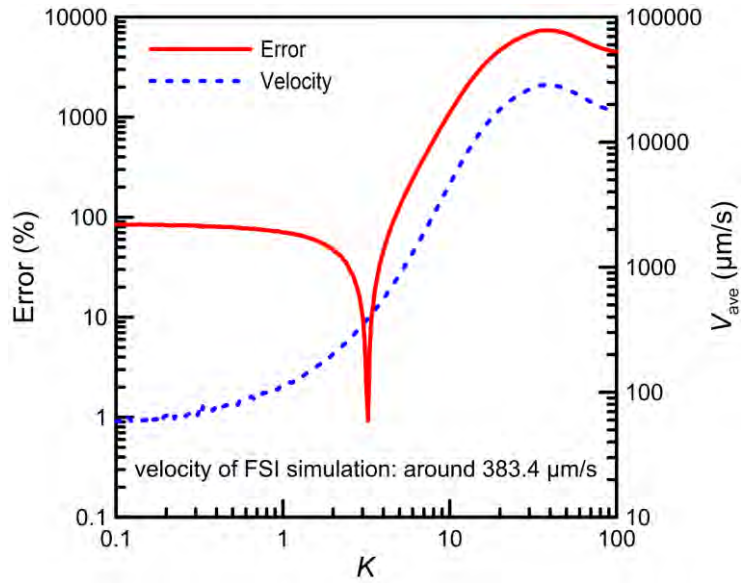
Figure 4-8. Estimate of K for uniform flagella with parameters $\eta = 10$ Pa·s, $\mu = 0.1$ Pa·s, and $y_{0a} = 20$ μm (other paramours are provided in Table 4-1.): example of the error (red solid line) V_{ave} obtained from the CRFT model (blue dashed line) based on the simulation result ($V_{ave} = 383.4$ μm/s) when K varies.
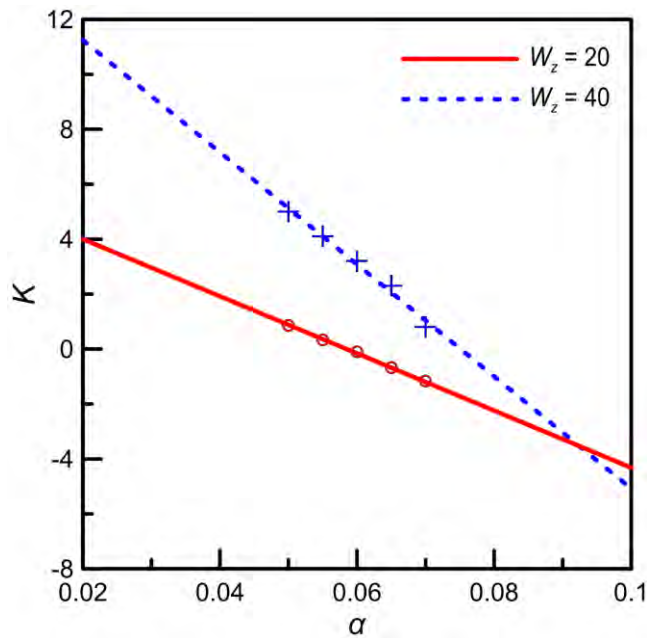
Figure 4-9. Estimate of K for uniform flagella with parameters $\eta = 10$ Pa·s, $\mu = 0.1$ Pa·s, and $y_{0a} = 20$ μm (other paramours are provided in Table 4-1.): relations between K and α for a flagellum without head.

116
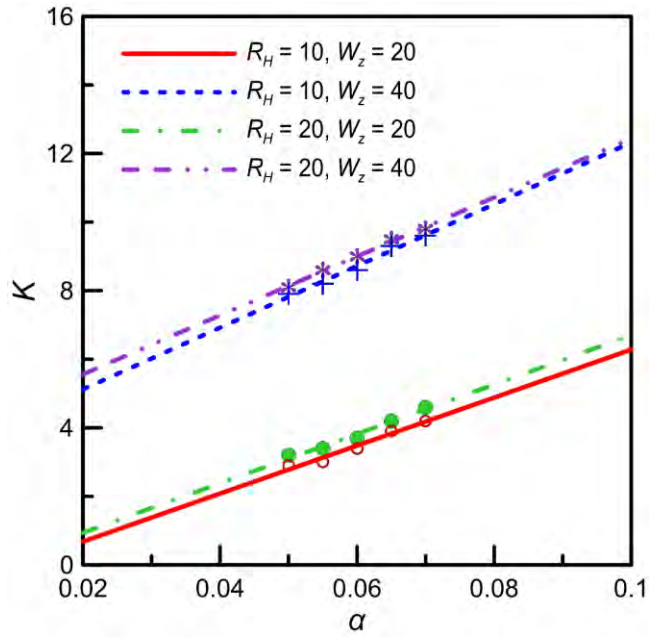
Figure 4-10. Estimate of K for uniform flagella with parameters $\eta = 10$ Pa·s, $\mu = 0.1$ Pa·s, and $y_{0a} = 20$ μm (other paramours are provided in Table 4-1.): relations between K and α for an AFMS with head.
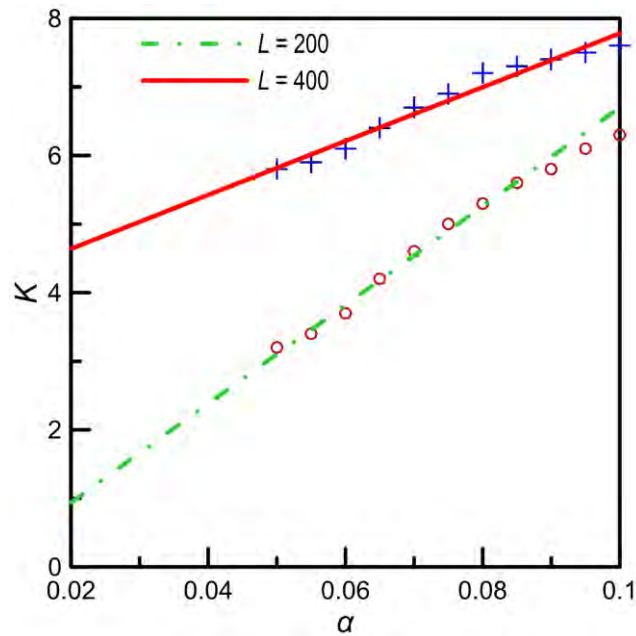
Figure 4-11. Estimate of K for uniform flagella with parameters $\eta = 10$ Pa·s, $\mu = 0.1$ Pa·s, and $y_{0a} = 20$ μm (other paramours are provided in Table 4-1.): relations between K and α for AFMSs with different flagellum length.
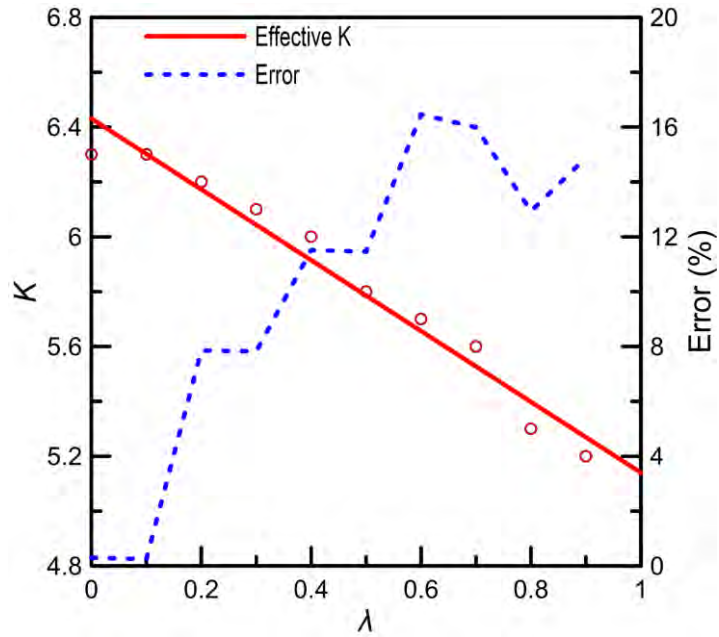
Figure 4-12. Estimate of K for tapered flagella with parameters $\eta = 10$ Pa·s, $\mu = 0.1$ Pa·s, and $y_{0a} = 20$ μm (other paramours are provided in Table 4-1.): relations between K and λ and between the error and λ, respectively, where the fitting curve of K (red solid line) is obtained by the effective-K method, and the error of V_{ave} (blue dotted line) is obtained by the direct-K method.
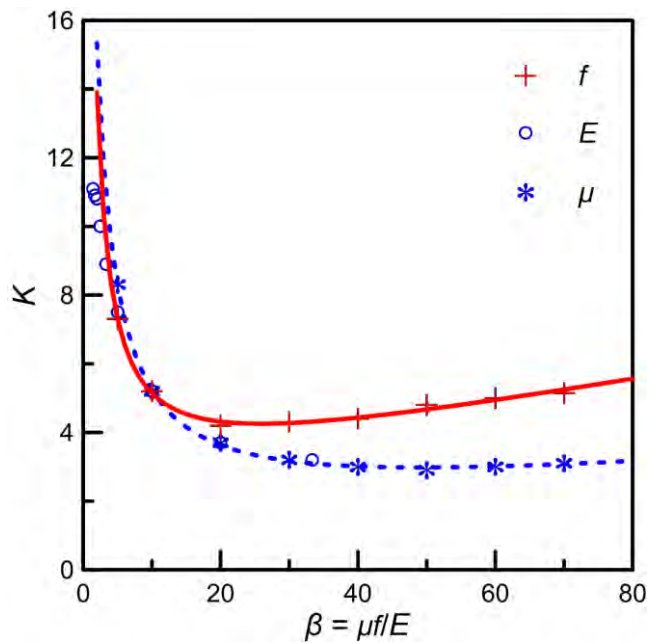
Figure 4-13. Estimate of K for tapered flagella with parameters $\eta = 10$ Pa·s, $\mu = 0.1$ Pa·s, and $y_{0a} = 20$ μm (other paramours are provided in Table 4-1.): the relation between K and β obtained by varying f (red cross), E (blue circle), or μ (blue star), respectively.

Table 4-1. The fitting expressions of K in terms of α, λ or β under different combinations of parameters.

L (μm)	R_H (μm)	W_z (μm)	W_{y0} (μm)	λ	f (Hz)	E (MPa)	μ (μm)	Expression of K	Fig.
200	0	20	10~14	0	1000	10	0.1	$K = -104\alpha + 6.08$	4-9
200	0	40	10~14	0	1000	10	0.1	$K = -204\alpha + 15.32$	4-9
200	10	20	10~14	0	1000	10	0.1	$K = 7\alpha - 0.72$	4-10
200	10	40	10~14	0	1000	10	0.1	$K = 90\alpha + 3.32$	4-10
200	20	20	10~14	0	1000	10	0.1	$K = 72\alpha - 0.5$	4-10
200	20	40	10~14	0	1000	10	0.1	$K = 86\alpha + 3.84$	4-10
400	20	20	20~40	0	1000	10	0.1	$K = 39.27\alpha + 3.854$	4-11
200	20	20	20	0.1~0.9	1000	10	0.1	$K = -1.29\lambda + 6.43$	4-12
200	20	20	20	0.9	500~7000	10	0.1	$K = (0.036\beta^2 + 2.40\beta + 24.5)/(\beta + 0.12)$	4-13
200	20	20	20	0.9	1000	3~70	0.1	$K = (0.087\beta^2 - 2.07\beta + 106)/(\beta + 7.78)$	4-13
200	20	20	20	0.9	1000	10	0.05~0.7	$K = (0.016\beta^2 + 1.40\beta + 41.4)/(\beta + 0.89)$	4-13

4.7 Examples of verification between the CRFT model and FSI simulations

In order to explicate the validity of the method for correcting RFT, we compare three head trajectories (or the trajectories of the right end of the flagellum for the case without head) calculated by FSI simulations and CRFT. All the figures in this chapter exhibit the trajectories and their errors from FSI simulations and the CRFT models for the acoustic-actuation period from 20 to 25. The corresponding geometries of AFMSs at four instances which equally divide the last period in the FSI simulation (outline) and the CRFT model (centerline) are given as the insets.

Figure 4-14, Figure 4-16 and Figure 4-18 show the trajectories of FSI simulations and CRFT models for the case of a uniform flagellum without a head, a uniform flagellum with a head, and a tapered flagellum with a head, respectively. To

approximate the trajectories based on the CRFT model, the corresponding values of K are determined to be 3.2, 6.3, and 5.2, respectively, based on the fitting equations suggested in the last chapter. It is noted that each of the trajectories obtained based on the CRFT model has an offset from the FSI-simulated one, reflecting the slight difference in the propulsive forces. This is due to the determination of K, in which we allowed a 5% tolerance in the motility difference. The distance between the positions of the AFMS head obtained from the FSI simulation and those from the CRFT solution, after dividing by the flagellum length L, is defined as the position error of the CRFT solution, which are shown in Figure 4-15, Figure 4-17 and Figure 4-19 (from 20 to 25 periods) and their insets (for first 40 periods). One may note that in Figure 4-15 and Figure 4-19, there are some small spikes, whereas in Figure 4-17 the errors are simply oscillating. Several extreme error points in Figure 4-15, Figure 4-17 and Figure 4-19 are indicated in Figure 4-14, Figure 4-16 and Figure 4-18, respectively, where the corresponding differences between the two solutions are indicated by dashed lines. It is noted that the spikes of errors are due to the oscillatory motions, resembling the interference of waves.

The insets in Figure 4-15, Figure 4-17 and Figure 4-19 show that the position errors in 40 periods are well below 4%. Because of the small motility difference (i.e., the tolerance in determining K), the trajectory deviations are caused; nevertheless, these deviations are well-bounded and remain small when normalized by the length of the flagellum. Such small errors indicate that the CRFT-based bar-joint model, as described in Chapter 4.4, renders an excellent approximation to numerical simulations. It should be noted that such position errors can be further reduced if we set a more stringent requirement for accuracy in determining K.
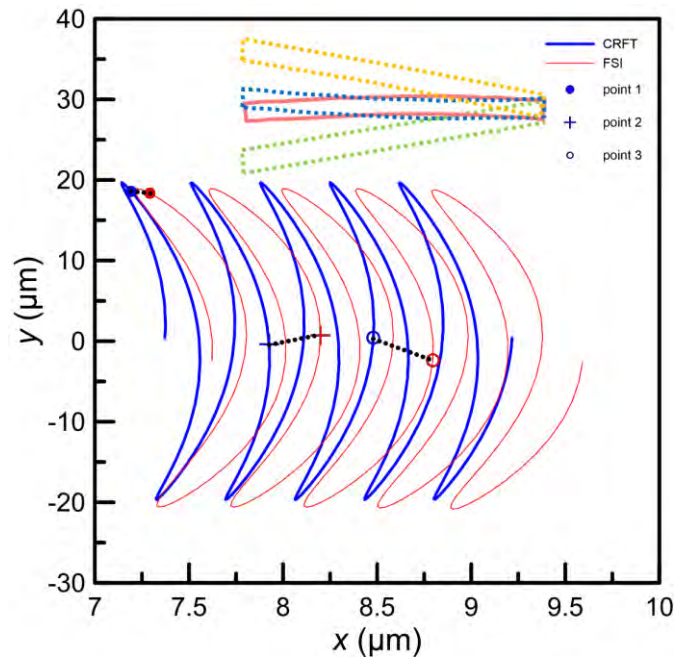
Figure 4-14. Verifications of the CRFT model: the head trajectories obtained from the FSI simulations (red lines) and CRFT-based bar-joint models (blue lines) for the cases of a uniform flagellum without the head, and marked points indicate that the trajectory errors reach their extreme values, where the corresponding distances between the pairs of trajectory points are indicated by the dashed lines. To have a clearer comparison, only the periods from 20 to 25 are shown.
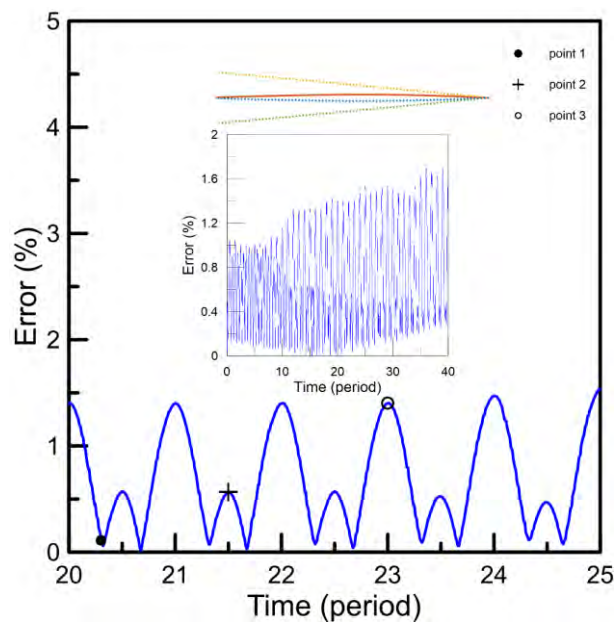
Figure 4-15. Verifications of the CRFT model: the trajectory errors obtained from the FSI simulations and CRFT-based bar-joint models for the cases of a uniform flagellum without the head, and the corresponding trajectory errors which are the distances between two head positions at the same time scaled by the length of the flagellum, respectively. The marked points indicate that the trajectory errors reach their extreme values, where the corresponding distances between the pairs of trajectory points are indicated by the dashed lines in Figure 4-14. To have a clearer comparison, only the periods from 20 to 25 are shown. The inset shows the trajectory errors for a long time (40 periods).
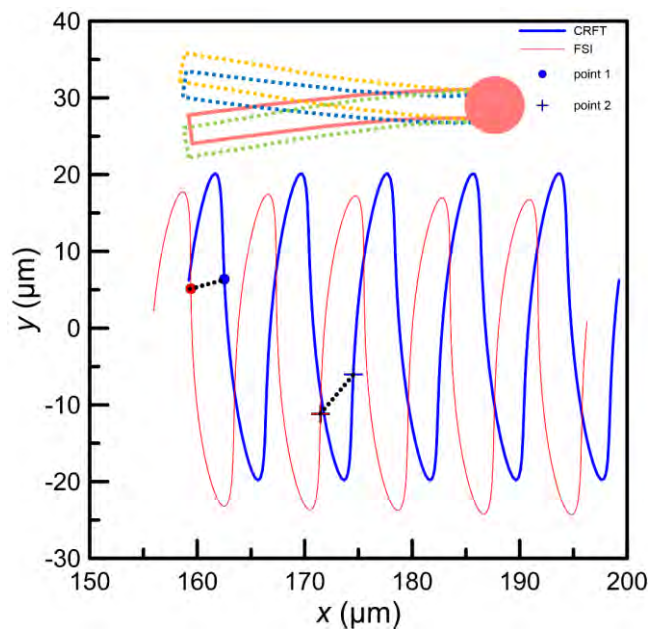
Figure 4-16. Verifications of the CRFT model: the head trajectories obtained from the FSI simulations (red lines) and CRFT-based bar-joint models (blue lines) for the cases of a uniform flagellum with the head, and marked points indicate that the trajectory errors reach their extreme values, where the corresponding distances between the pairs of trajectory points are indicated by the dashed lines. To have a clearer comparison, only the periods from 20 to 25 are shown.
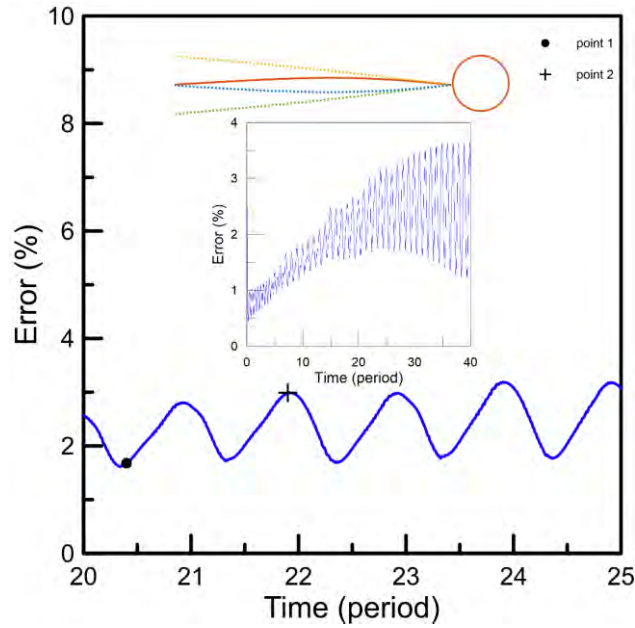
Figure 4-17. Verifications of the CRFT model: the trajectory errors obtained from the FSI simulations and CRFT-based bar-joint models for the cases of a uniform flagellum with the head, and the corresponding trajectory errors which are the distances between two head positions at the same time scaled by the length of the flagellum, respectively. The marked points indicate that the trajectory errors reach their extreme values, where the corresponding distances between the pairs of trajectory points are indicated by the dashed lines in Figure 4-16. To have a clearer comparison, only the periods from 20 to 25 are shown. The inset shows the trajectory errors for a long time (40 periods).

123
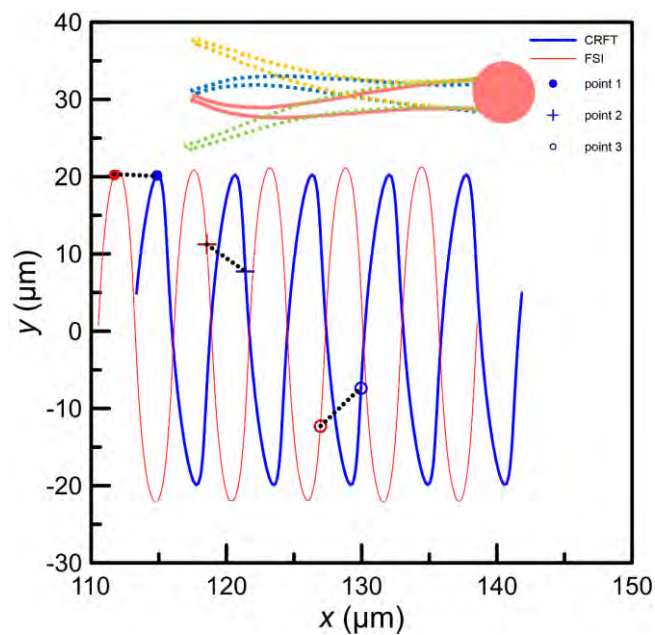
Figure 4-18. Verifications of the CRFT model: the head trajectories obtained from the FSI simulations (red lines) and CRFT-based bar-joint models (blue lines) for the cases of a tapered flagellum with the head, and marked points indicate that the trajectory errors reach their extreme values, where the corresponding distances between the pairs of trajectory points are indicated by the dashed lines. To have a clearer comparison, only the periods from 20 to 25 are shown.
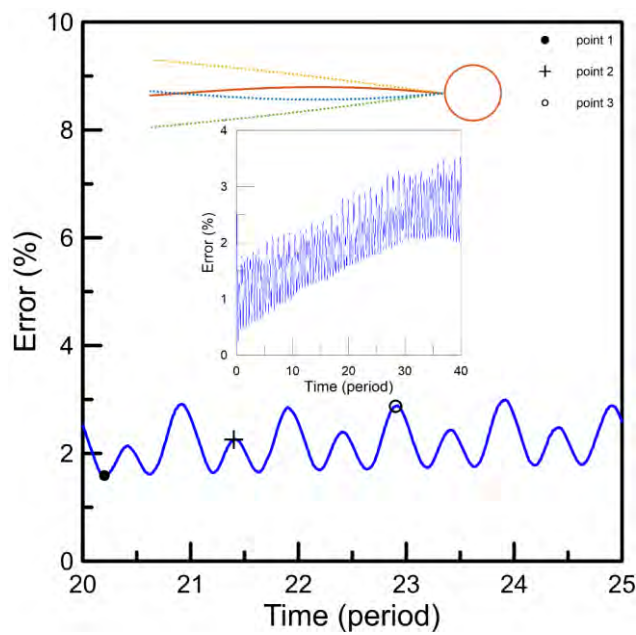
Figure 4-19. Verifications of the CRFT model: the trajectory errors obtained from the FSI simulations and CRFT-based bar-joint models for the cases of a tapered flagellum with the head, and the corresponding trajectory errors which are the distances between two head positions at the same time scaled by the length of the flagellum, respectively. The marked points indicate that the trajectory errors reach their extreme values, where the corresponding distances between the pairs of trajectory points are indicated by the dashed lines in Figure 4-18. To have a clearer comparison, only the periods from 20 to 25 are shown. The inset shows the trajectory errors for a long time (40 periods).

4.8 Steering strategies based on the CRFT-based bar-joint model

We expect that the proposed 2D CRFT-based bar-joint model can ultimately be employed for the path planning and navigation control of AFMSs because of the

excellent agreement between the FSI and the simplified model. Here, as the final demonstration, we employ CRFT to study the turning strategy for an AFMS, which is essential and inevitable in practical applications. It is noted that FSI simulation for turning is unconverted in our trials due to excessively distorted elements; hence, we only provide the results of the CRFT model.

In the following demonstration, the AFMS is identical to the one shown in Figure 4-18. We expect that the external force $\mathbf{F}_{ext}$ ($\mathbf{F}_{ext} = [F_{extx}, F_{exty}]^{T}$) can be applied to the head of an AFMS through applying acoustic waves. According to the results in Chapter 3.2, under an acoustic plane wave rendering a 2D fluid displacement field $\mathbf{A}_{acou}$ with the amplitude A_{acou}, the oscillation amplitude of the head ($R_H = 20$ μm) of the AFMS A_{amp} is approximately $1.67A_{acou}$ if the sound wavelength is far greater than the dimensions of the head. In this case, the oscillatory velocity in the fluid is nonzero, i.e., $\mathbf{u} = \partial\mathbf{A}_{acou}/\partial t$.

One may note from the trajectories in Figure 4-18 that an AFMS tends to move along the direction perpendicular to $\mathbf{F}_{ext}$ which induces head oscillations, which is also the case in the experiments of acoustic actuation [252]. Hence, steering an acoustically propelled AFMS might be achieved by rotating $\mathbf{F}_{ext}$ and we can design such a turning method using only acoustic power based on the CRFT model. Considering an acoustic plane wave that can gradually change the direction of propagation, hence changing the direction of $\mathbf{F}_{ext}$ on the head of an AFMS. As shown in Figure 4-20, we let the angle of the acoustic wavevector rotate from 90° to 60° (counterclockwise from the positive direction of the *x*-axis) in 10 periods. After the change, the angle of the micro-swimmer is around 5°. Maintaining $\mathbf{F}_{ext}$ at 60° for 100 periods, the angle of the AFMS gradually drifts to be close to 60°. Further turning $\mathbf{F}_{ext}$ to 150° in 10 periods leads the angle of the

micro-swimmer to move along the straight line of 60°. The detailed trajectory of the AFMS is shown in Figure 4-21.

The above example shows that using only acoustic power to control AFMSs is possible in theory, although the orientation relation between an AFMS and acoustic wavevector is nontrivial, depending on the parameters of the actuation and the swimmer [260]. If the direction of wavevectors can be accurately adjusted, these waves can induce head oscillation and flagellum wiggling for propulsion and steering. In these attempts, our AFMS model can provide the formalism for trajectory prediction and manipulation, which will lay the foundation for controlling micro-swimmers to carry out precision therapies for cancers and other diseases requiring non-invasive and localized treatments.

If a torque can be applied to the head of an AFMS, turning will be easier and more controllable. This can be achieved by introducing magnetic particles (MPs) into the head [202], resulting in a magnetized head along an easy axis ($\mathbf{m}$), and applying an external magnetic field ($\mathbf{b}$) unparallel with the head's easy axis, resulting in a torque $\boldsymbol{\tau}_{ext} = \mathbf{m} \times \mathbf{b}$ on the head, as sketched in the inset in Figure 4-23. Note that the acoustic power is still used for propulsion but not for steering. The external magnetic field used in hyperthermia-based therapy is usually around 10 mT [261], and the volumetric magnetic susceptibility is in the order of 10^5 for ferromagnetic MPs [262], accordingly, the magnetic-induced torque by single MP of 1 μm is around 4×10^{-12} N·m. With 5 MPs in the head, the total magnetic torque on the head is 2×10^{-11} N·m, which is assumed in the following calculation. For such a magneto-acoustic method, we design the variations of F_{extx}, F_{exty} and τ_{ext}, as shown in Figure 4-22, which results in the trajectory of the AFMS as shown in Figure 4-23. Hence, the proposed magneto-acoustic maneuver is feasible based on the existing technologies and our theoretical analysis of

magneto-acoustic steering can be employed for targeted therapies that require accurate

and rapid navigation.
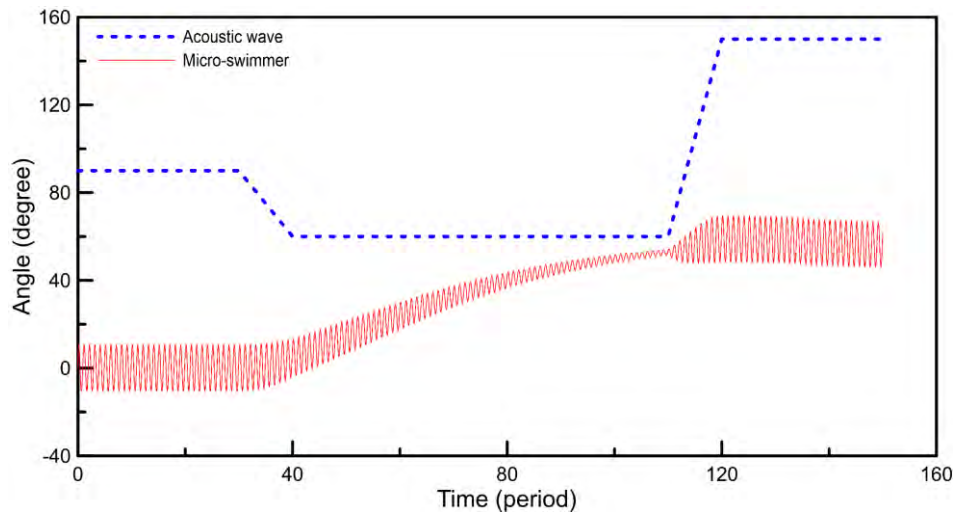
Figure 4-20. Application of the CRFT model where the AFMS is steered by acoustic waves: the rotation angle with respect to the *x*-axis in terms of actuation period for the acoustic waves (blue dashed line) and the AFMS (red solid line); the time *t* is in terms of the number of acoustic periods.
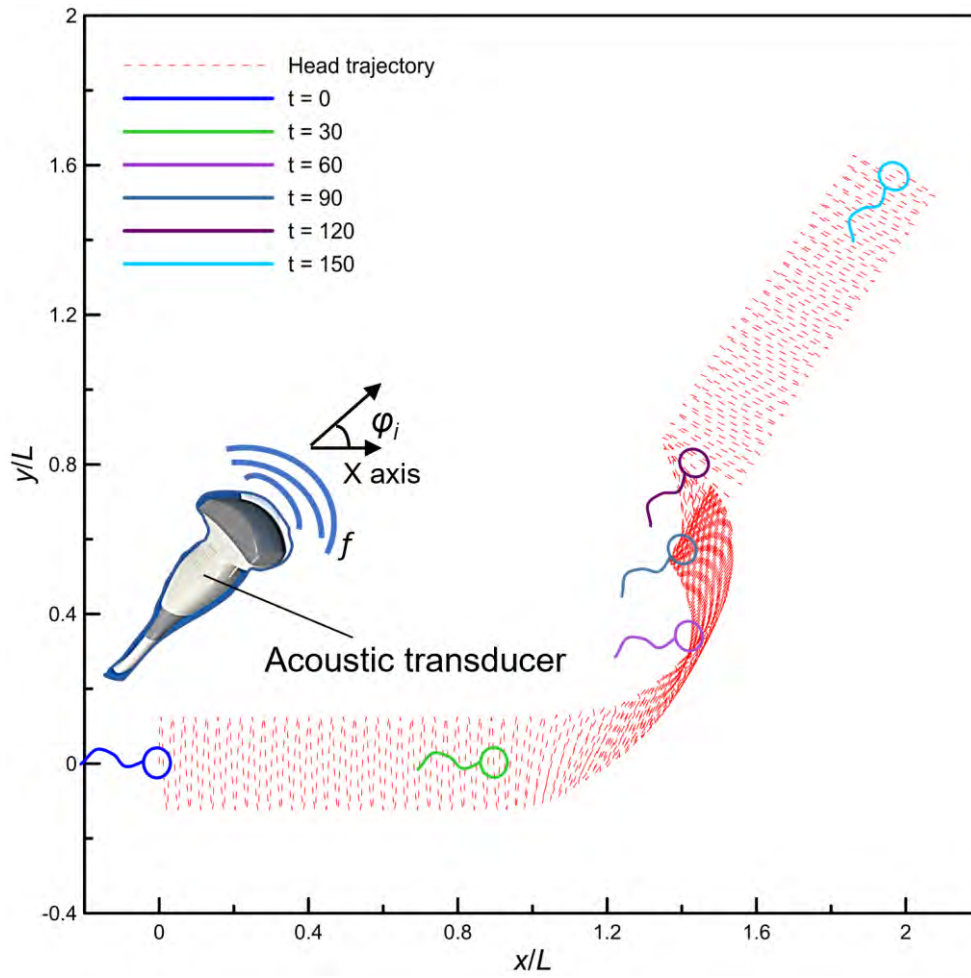
Figure 4-21. Application of the CRFT model where the AFMS is steered by acoustic waves: the trajectory and orientations of the AFMS within 150 periods; the insets sketch the acoustic steering strategy, and the time t is in terms of the number of acoustic periods.

128
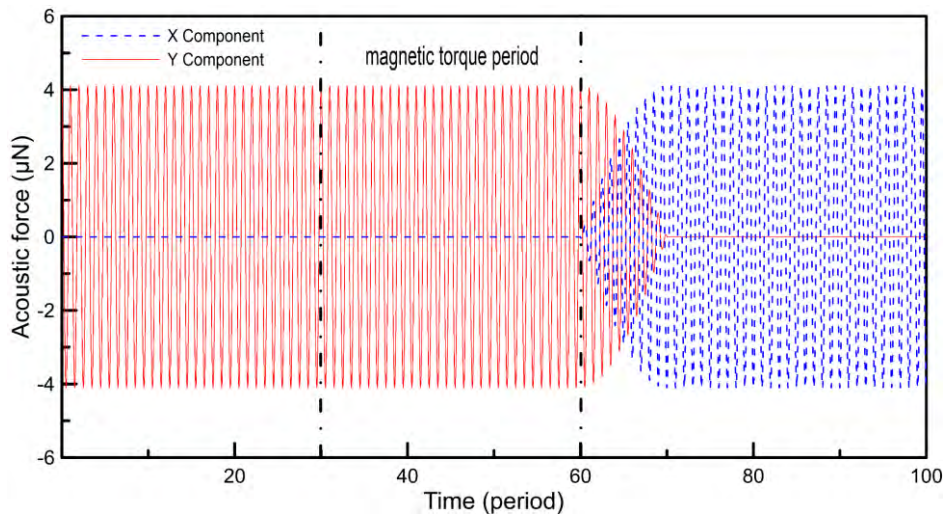
Figure 4-22. Application of the CRFT model where the AFMS is steered by a magneto-acoustic strategy: the applied acoustic forces for propulsion in terms of actuation period along *x* (blue dashed line) and *y* (red solid line) directions (Note: the actuation forces along *y* (*x*) direction linearly decreases (increases) between the 60th period and the 70th period to assist turning), and from the 30th and 60th periods, a magnetic torque is applied.
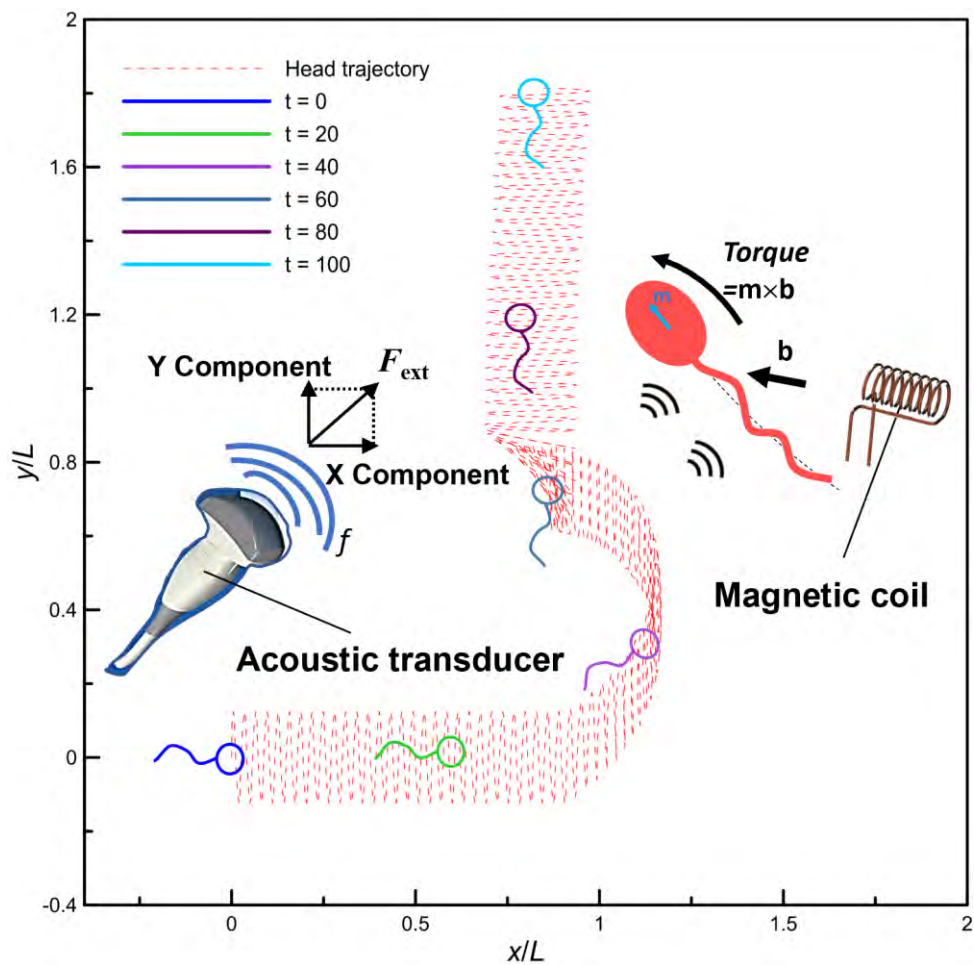
Figure 4-23. Application of the CRFT model where the AFMS is steered by a magneto-acoustic strategy: the trajectory and orientations of the AFMS within 100 periods; the insets sketch the remote magneto-acoustic steering strategy.

4.9 Summary

In this chapter, we have described a CRFT-based 2D bar-joint model for modeling AFMSs propelled by acoustic actuation. The main purpose of this work is to allow a simplified AFMS model to be correctable, verifiable, and in the future, applicable for practical applications. The CRFT is inspired by the derivation of the RFT for the non-circular flagellum and only introduced the single correction factor K. However, K depends on not only geometrical parameters but also other factors influencing a flagellum's wiggling profiles, such as material properties and actuation frequency. The physical meaning of K is the difference of fluid velocities between the case of a simple cylinder flagellum (3D case) and the case of an AFMS with a cuboid flagellum (2D case) and a rigid head. Hence, although the CRFT is derived from the non-circular SBT, K should be determined after some knowledge of the motility of an AFMS is obtained. In the exercises, we determined K by comparing the terminal average velocities obtained from the CRFT-based bar-joint models propelled by acoustic waves and those from the FSI simulations. After correction, it is shown that the difference in the detailed trajectory can be well below 4%. In our work, K is very weakly dependent on the head radius R_H and linearly dependent on the slenderness α and the tapering factor λ. Hence, it is not difficult to determine these dependencies and then employ CRFT to optimize the geometry of an AFMS for maximizing the motility. With CRFT, the controlled navigation of AFMSs can also have a high level of robustness. For this point, we have demonstrated the possible strategies for turning an AFMS using acoustic or magneto-acoustic fields, which indicates that the current CRFT model includes enough information to deal with a turning activity. Note that the accuracy of our CRFT model depends on the accuracy of the FEM simulation. The results of FEM simulation need to be verified by experiments, which will be demonstrated in the next chapter.

Chapter 5. Experimental verification

5.1 Fabrication

The main purpose of this chapter is to verify our CRFT models by comparing terminal velocities of AFMSs observed in experiments to those predicted by theoretical calculation. Firstly, we will describe the fabrication of AFMSs. A commercial ultra-violet (UV) curable resin (Phrozen Water Washable Resin, Model Gray, Phrozen, Taiwan) [7, 8] was employed to fabricate AFMSs based on the technique of digital light processing (DLP) due to its high dimensional precision and low fabrication cost. As shown in Figure 5-1, a commercial 3D printer (Sonic Mini 8K, Phrozen, Taiwan) was employed for photolithography with horizontal and vertical resolutions of 22 μm and 20 μm, respectively. Note that DLP printers can achieve higher precisions, such as those based on two-photon polymerization [263], and it may be needed in the future precision controls of AFMSs. In this work, to verify our theory, a low-cost DLP printer has suited the need.

A plate connected to a vertical guide and a lead screw is used as the base of printing, and at the bottom is a vessel containing a liquid photosensitive resin. During a layer-by-layer photocuring process at a UV wavelength of 405 nm, the plate is immersed in the resin solution. After printing, the plate can be detached from the guide and lead screw, and the product would generally be removed by a metal scraper. However, in this work, an AFMS to be printed is around 1 – 2 mm long and less than 0.5 mm thick, which is too small to be manually chipped. Therefore, we used a salt brick as the base of printing, as demonstrated in Figure 5-2, and dissolved the salt brick in water to release printed products.

Figure 5-3 exhibits a rectangular sample (used for materials characterization) adhering to the salt brick after photocuring. Immersing the salt brick in water for some time, the sample can be shed. If the AFMSs are too small to be seen with the naked eye, it will be difficult to transfer them to an experimental platform to observe their motion. Hence, Kaynak et al. [7] fabricated AFMSs *in situ*. Owing to the limitation of our laboratory equipment, transferring AFMSs from the printing stage to a testing channel is necessary (this will also be the case in future applications). Hence, we have to print AFMSs with a length over 1 mm to make them visible to human eyes and then transferable to an AFMS testing channel. Figure 5-4 and Figure 5-5 exhibit the photos of the AFMSs tested in this work, taken by using an optical microscope. They are designated as L1 (i.e., Figure 5-4 with 1 mm long) and L2 (i.e., Figure 5-5 with 2 mm long), respectively. The thicknesses of L1 and L2 are homogeneous (0.3 mm for L1 and 0.5 mm for L2), which indicates that the cross-sections of these AFMSs are rectangular. Note that such a large dimension may lead to invalidity of the RFT if using water as the testing fluid, because the Reynolds number may be not sufficiently low. Hence, we used an aqueous solution for testing AFMSs, which is sodium polyacrylate (50% concentration, Macklin, China) with a viscosity of 0.1 Pa.s at room temperature. This ensures the Reynolds number in the range of 0.009 – 0.09, satisfying the LRN condition. We also examined the PEG resin employed by Kaynak et al. [7] (the name of PEG can be seen in Chapter 3.1). However, the printed swimmer is transparent and difficult to observe (in contrast, the commercial resin is gray and can be seen easily). Thus, the PEG resin was not used to fabricate the AFMS in this work. However, the viscoelastic properties of the cured PEG resin were also characterized. The corresponding FSI simulations can be compared with the experiments [7] in terms of terminal velocities.

Figure 5-1. Fabrication of AFMSs and samples: the 3D printer for photolithography with photosensitive resin inside its vat, and the building plate is immersed in the resin.

Figure 5-2. Fabrication of AFMSs and samples: the modified building plate before photolithography, which is a rectangular cavity adhered with a salt brick.
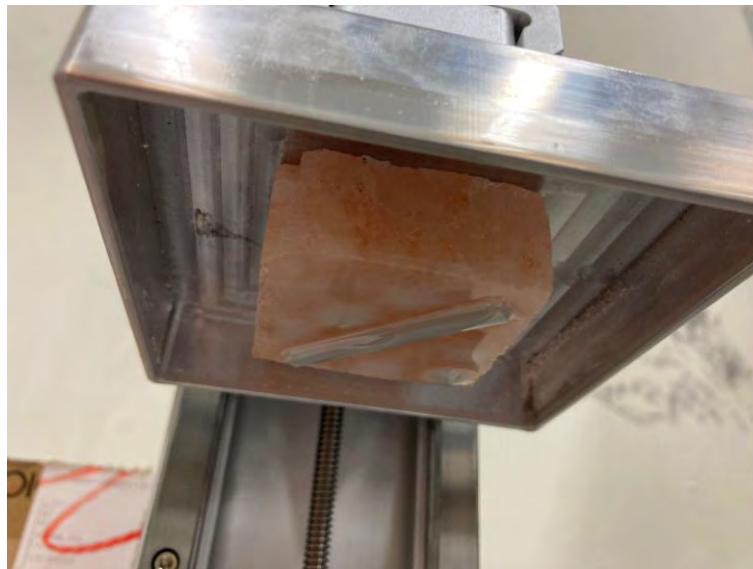
Figure 5-3. Fabrication of AFMSs and samples: after photolithography, the material sample adheres to the salt brick.

Figure 5-4. Dimensions of AFMSs and the material sample: the dimensions of AFMS L1, which is around 1 mm long and 0.3 mm thick.
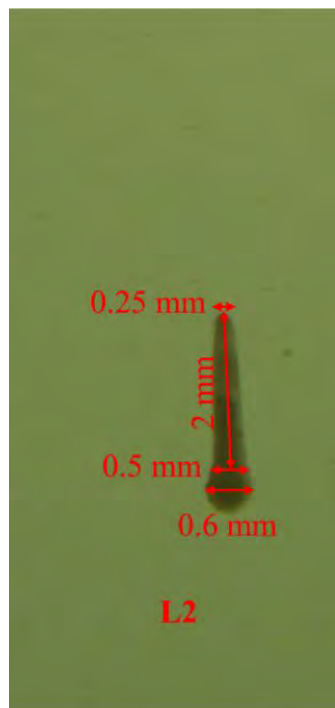
Figure 5-5. Dimensions of AFMSs and the material sample: the dimensions of AFMS L2, which is around 2 mm long and 0.5 mm thick.

5.2 Materials characterization

Because the polymer we adopted is a frequency-dependent viscoelastic material, frequency-sweeps in dynamic mechanical analysis (DMA, Thermal Analysis System DMA 1, Mettler-Toledo, Switzerland) were conducted. As we have mentioned in previous chapters, the Kelvin–Voigt model is employed to describe the response of the polymer under a periodic loading with an excitation frequency f. Thus, the relation between the stress σ and strain ε is expressed as [237]:

$$\sigma = E\varepsilon + \gamma \frac{E}{2\pi f} \frac{\partial \varepsilon}{\partial t}, \tag{5.1}$$

where E and γ are the storage modulus and the loss factor (i.e., the material damping in Chapter 3) [239] (one may note that Eq. (5.1) is equivalent to Eq. (3.8)). In DMA, a sample, as shown in Figure 5-6, was periodically loaded in the cantilever mode. The force and displacement amplitudes and their phase shift are then analyzed to determine E and γ [264].

The upper limit of the frequency sweep using the DMA is 100 Hz, but the actuation frequency for AFMS is much higher. Hence, the principle of time-temperature superposition (TTS) is employed, which states that a physical property G (representing E and γ) measured under temperature T and frequency f is equivalent to that measured under temperature T_0 and frequency $a_T f$, expressed as [251]:

$$G(f, T) = G(\alpha_T f, T_0), \tag{5.2}$$

where a_T is the shift factor. WLF equation is employed to determine a_T [265]:

$$\lg \alpha_T = -\frac{C_1 (T - T_0)}{C_2 + (T - T_0)},\tag{5.3}$$

where C_1 and C_2 are positive constants dependent on the material and the reference temperature T_0. Using TTS, E and γ measured at different temperatures and frequencies can collapse onto a master curve. Here, DMA tests were performed for both cured Phrozen and PEG resins. The reference temperature in the WLF equation (Eq. (5.3)) was preset to be room temperature (i.e., $T_0 = 25$ °C). The constants C_1 and C_2 in Eq. (5.3) were determined to let all data points collapse to a master curve with minimized deviations.
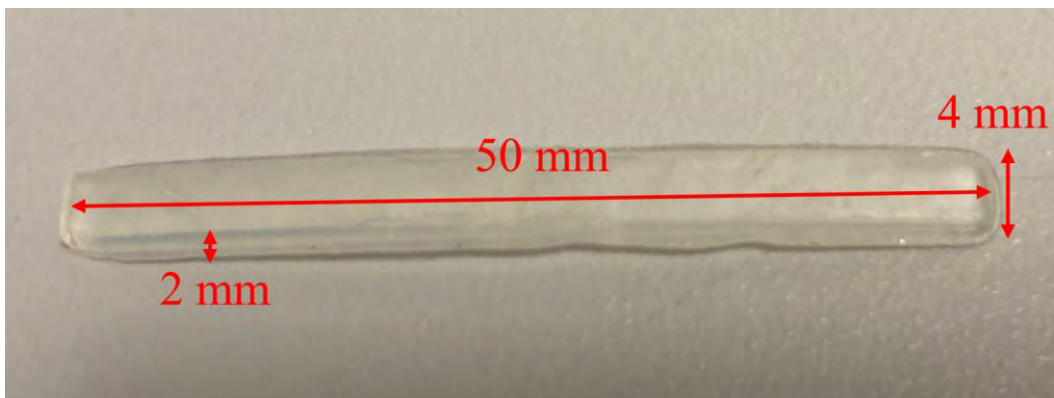
Figure 5-6. Dimensions of AFMSs and the material sample: the dimensions of the sample for material characterization.

5.3 Experimental setup

Figure 5-7 shows an experimental platform of the acoustically actuated AFMS. A polydimethylsiloxane (PDMS) plate with a through slot was fabricated using the standard soft lithography and bonded onto a glass slide to form a swimming channel. A piezoelectric transducer (PZT5 $60 \times 3 \times 0.6$ mm³, Shaoxing Shenlei Ultrasonic

Equipment, China) with a resonant frequency of 28 kHz was then attached adjacent to the PDMS channel, where acoustic waves will generate and propagate from the piezoelectric transducer to the fluid inside the channel. Because the sound impedance of the PDMS matches that of the aqueous solution inside the channel, a sound field of traveling waves will prevail if the wall of the PDMS chamber is sufficiently thick [266]. The total thickness of the wall of the chamber is designed to be 10 mm (50 × 20 mm for the outer contour and 35 × 10 mm for the channel), which is much thicker than the channel height of 2 mm and can eliminate the possible reflection of waves from PDMS boundaries.

A waveform generator (DG2052, RIGOL, China) was connected to an amplifier (ATA-2032, AIGTEK, China) to introduce a harmonic waveform to the acoustic transducer and the peak-to-peak voltage (Vpp) is determined by the combination of the generator and amplifier. A stereomicroscope (SZM-6, Weiscope, China) with a high-speed camera (E3ISPM09000KPB 186fps, Sony, Japan) was used to observe and record the motion of an AFMS. The amplitudes of actuation and swimming velocities of AFMSs can be achieved in terms of different actuation frequencies and voltages.
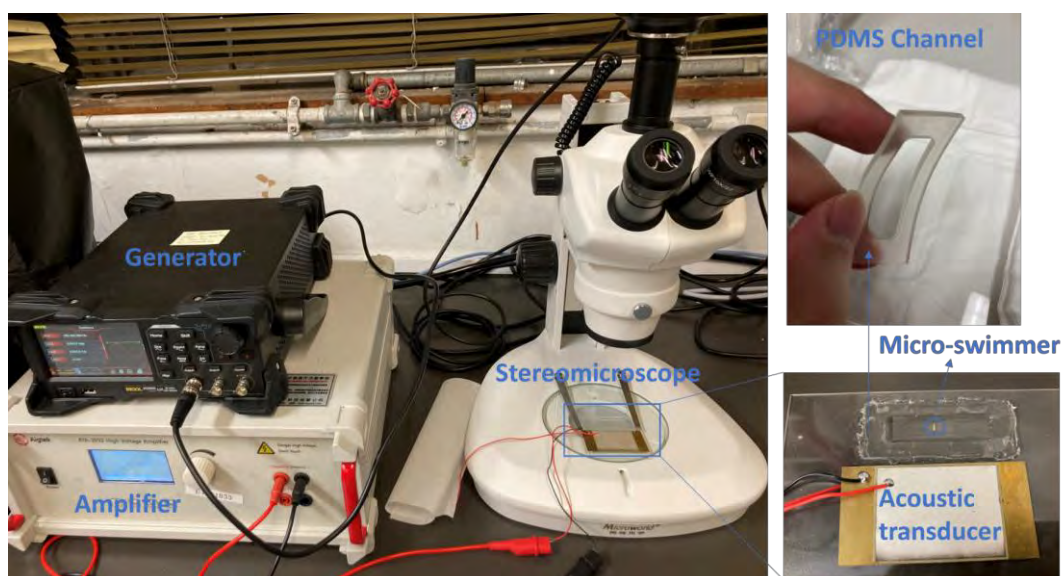
Figure 5-7. Experimental platform and devices. The inset in the upper right corner shows the flexibility of the PDMS channel; the inset in the lower right corner illustrates how to actuate the micro-swimmer by an acoustic transducer.

5.4 Results of materials characterization

Note that the storage modulus E cannot be accurately determined by DMA owing to the inaccuracy in the measurement of displacement (note that DMA is accurate in determining the phase shift between stress and strain response), we employed the impulse excitation technique (IET) to determine E at room temperature by probing the natural frequency of the primary flexural vibration mode [267].

For the Phrozen resin, the temperature range was from -10 °C to 35 °C with an interval of 5 °C (i.e., 10 sets of data). For each temperature, the loading frequency was from 0.1 Hz to 100 Hz. We determined $C_1 = 40$ and $C_2 = 290$, and the resulting master curves of storage modulus and loss factor in terms of the equivalent frequency (log base) are illustrated in Figure 5-8 and Figure 5-9, respectively. The IET test (equivalent to the lowest frequency) for E is 100 MPa, which roughly conforms to the expectation shown in Figure 5-8. For the PEG resin, the temperature range was from 5 °C to 25 °C with an interval of 5 °C. For each temperature, the loading frequency was also from 0.1 Hz to 100 Hz. We obtained $C_1 = 10$ and $C_2 = 60$, and the resulting master curves of storage modulus and loss factor in terms of the equivalent frequency are exhibited in Figure 5-10 and Figure 5-11, respectively. The IET test (equivalent to the lowest frequency) for E is around 20 MPa, which conforms to the expectation shown in Figure 5-10. It is noted that the results of γ do not fit well onto a master curve, and this implies that the TTS assumption does not work well for the PEG resin. Thus, we choose the commercial Phrozen resin as the material of the AFMS for further experiments.
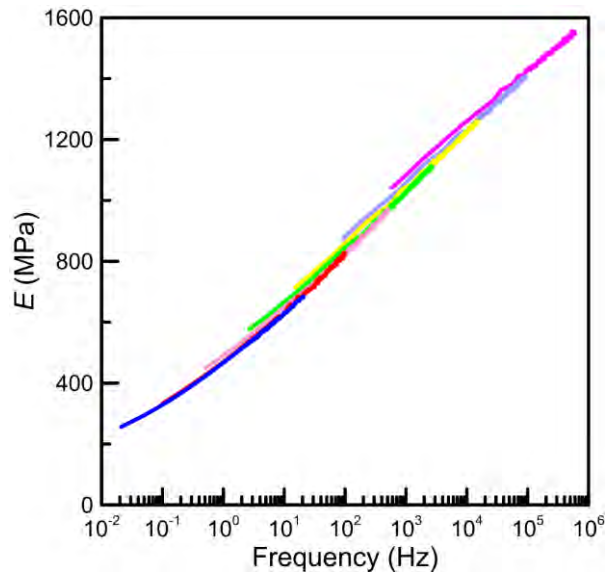
Figure 5-8. Results of material characterization by TTS test: Young's modulus in terms of the actuation frequency for the commercial photopolymer. Different colors indicate different ranges of test temperature, where the actuation frequency ranges are the same for all the tests, which are from 0.1 Hz to 100 Hz.
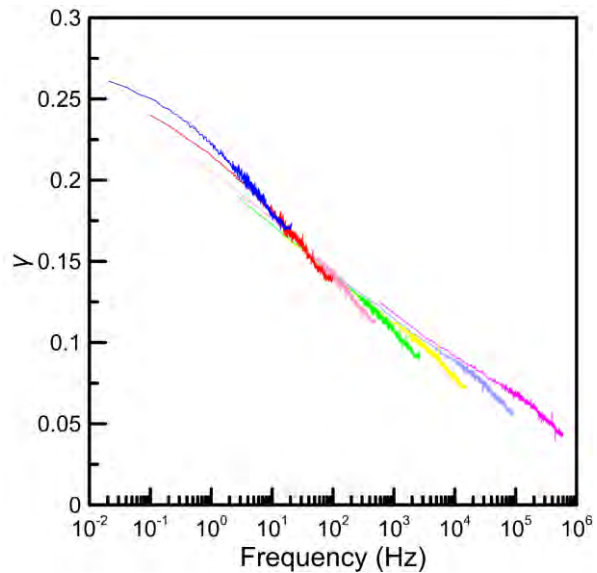
Figure 5-9. Results of material characterization by TTS test: loss factor in terms of the actuation frequency for the commercial photopolymer. Different colors indicate different ranges of test

temperature, where the actuation frequency ranges are the same for all the tests, which are from 0.1 Hz to 100 Hz.
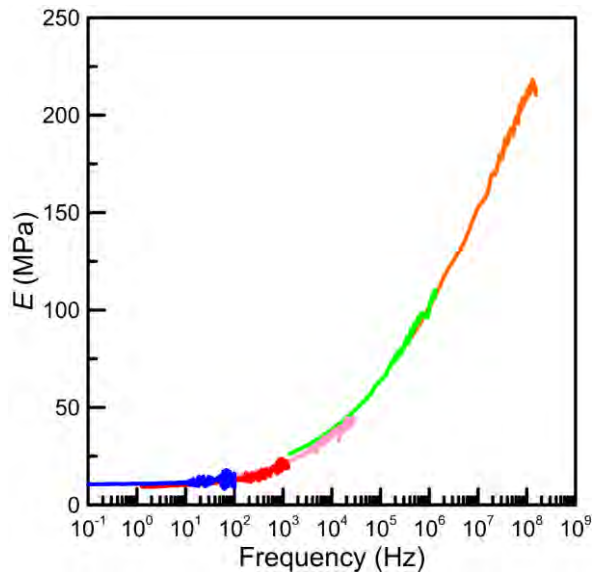
Figure 5-10. Results of material characterization by TTS test: Young's modulus in terms of the actuation frequency for PEG material. Different colors indicate different ranges of test temperature, where the actuation frequency ranges are the same for all the tests, which are from 0.1 Hz to 100 Hz.
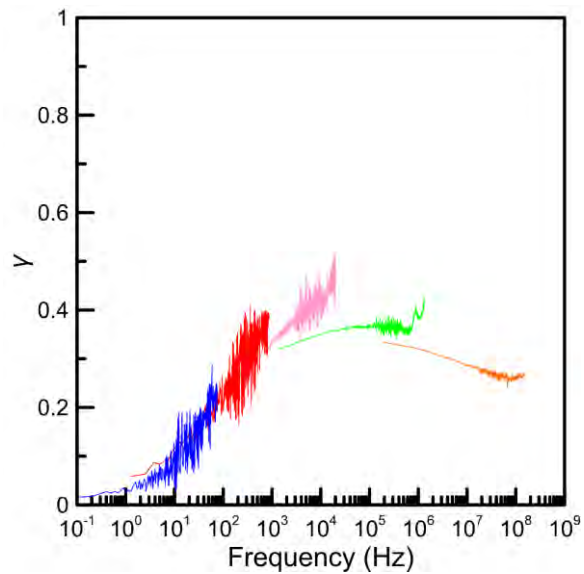
Figure 5-11. Results of material characterization by TTS test: loss factor in terms of the actuation frequency for PEG material. Different colors indicate different ranges of test temperature, where the actuation frequency ranges are the same for all the tests, which are from 0.1 Hz to 100 Hz.

5.5 Comparisons between theoretical and experimental results

Directional motions of the AFMSs of the two lengths (i.e., L1 and L2) actuated by sound waves have been observed. The acoustic frequencies were set at 100 and 500 Hz and the Vpps are from 50 to 250 V with an interval of 50 V. Figure 5-12 demonstrates the way to estimate the amplitude of the head oscillation, wherein we take L1 at 100 Hz as an example. Note that the camera on the microscope ran at 100 fps and the AFMS oscillated at 100 Hz. It means that in each frame the camera captured an overlapped image of the AFMS at different positions within one period of oscillation. Hence, the half-width of the blurred head of the AFMS image minus the half-width of the head renders the amplitude of head oscillation, as shown in Figure 5-12. The resonant frequency of the piezoelectric transducer is 28000 Hz, and the largest frequency we used herein is just 500 Hz. Therefore, the resonance of the transducer does not influence the intensity of the acoustic field. Hence, as shown in Figure 5-13, the measured oscillation amplitude of the AFMS is proportional to the input voltage. The difference in the amplitude between L1 and L2 at the same frequency and voltage is indistinguishable.

The terminal velocity averaged within one second V_{ave} can be achieved by measuring the distance of swimming captured by the camera. Figure 5-14 exhibits the movement of L1 actuated at 100 Hz and 200 Vpp. The FSI simulation and the CRFT model can be implemented based on the same actuation conditions and the material parameters characterized above. The corresponding instants of motion in the same time series of

142

the FSI simulation and the CRFT model are shown in Figure 5-15 and Figure 5-16, respectively, where colors on the AFMS in Figure 5-15 indicate total displacements, and dotted lines in Figure 5-16 indicate the centerline of the flagellum. Note that red and blue colors in Figure 5-15 represent the largest and smallest displacements, respectively The head is in greenish blue in the second picture of Figure 5-15 because the flagellum happens to swing towards the head at that moment; for other cases, the head is in red, which means the flagellum swing away from the head. The comparison among the CRFT model, simulation and experimental results suggests that the FSI simulation and the CRFT model are reliable.

Figure 5-17, Figure 5-18, Figure 5-19 and Figure 5-20 illustrate the results of terminal velocities obtained from experiments, FSI simulations and the CRFT model, respectively. Figure 5-17 and Figure 5-18 are for L1, Figure 5-19 and Figure 5-20 for L2. Among these results, the largest Reynolds number is 0.09 for L2 at 250 Vpp and 100 Hz, which indicates that the swimming problem of the AFMS herein is in the LRN regime, and the theoretical methods based on the RFT should be effective. As shown in Figure 5-17, Figure 5-18, Figure 5-19 and Figure 5-20, as expected, the results of the CRFT model conform well to the simulation results. For the experimental ones, it is noted that all the deviations between the experimental results and the simulations are less than 30% for Vpp larger than 160 V and 50% for Vpp less than 160 V. The larger deviation for smaller Vpp might be due to the tendency to enlarge the amplitude of head oscillation in experiments. Because the resolution of the image for recording the head amplitude based on a normal video camera is low, when the amplitude is not large, it is difficult to distinguish the overlapped image of the AFMS. For the same reason, a larger actuation frequency may also cause a larger deviation. In addition, deviations for L1 are overall less than those for L2. The smaller deviation for L1 might arise from the

fact that a smaller swimmer can achieve a lower Reynolds number and higher effectiveness of the RFT. One may note that both the length of the AFMS and the actuation frequency for Figure 5-20 are large, it could be understood that the deviation in Figure 5-20 is the largest within the four cases.

Several causes of deviations must be stressed. First, the extrapolated viscoelastic parameters of the AFMS material based on the TTS introduced errors; second, the head oscillation amplitude determined based on a normal video camera has limited accuracy, as shown in Figure 5-12, the images from our camera were blurred because of the low shutter speed, it is possible to obtain an inaccurate head's oscillation amplitude; and as what we have mentioned in Chapter 3, the swimmer velocity is proportional to the square of amplitude, as shown in Figure 3-30, thus, the error can also be magnified; third, the experimental AFMS has a finite depth, but the numerical model is 2D (i.e., infinite depth). These issues all contributed to the 30 - 50% errors in the prediction of the motilities of the AFMSs, and thus, we think that such a level of deviation is reasonable and acceptable.

For the PEG material, we only implemented its FSI simulation to gain V_{ave} under the same conditions as those in the literature [7] except that we do not know the fluid viscosity. As listed in Table 5-1, we tested some viscosities to achieve V_{ave} for comparison and chose the one where the error is the smallest. In this case, the fluid viscosity is 20 Pa.s. However, the accuracy of this method of viscosity estimation needs to be further verified.
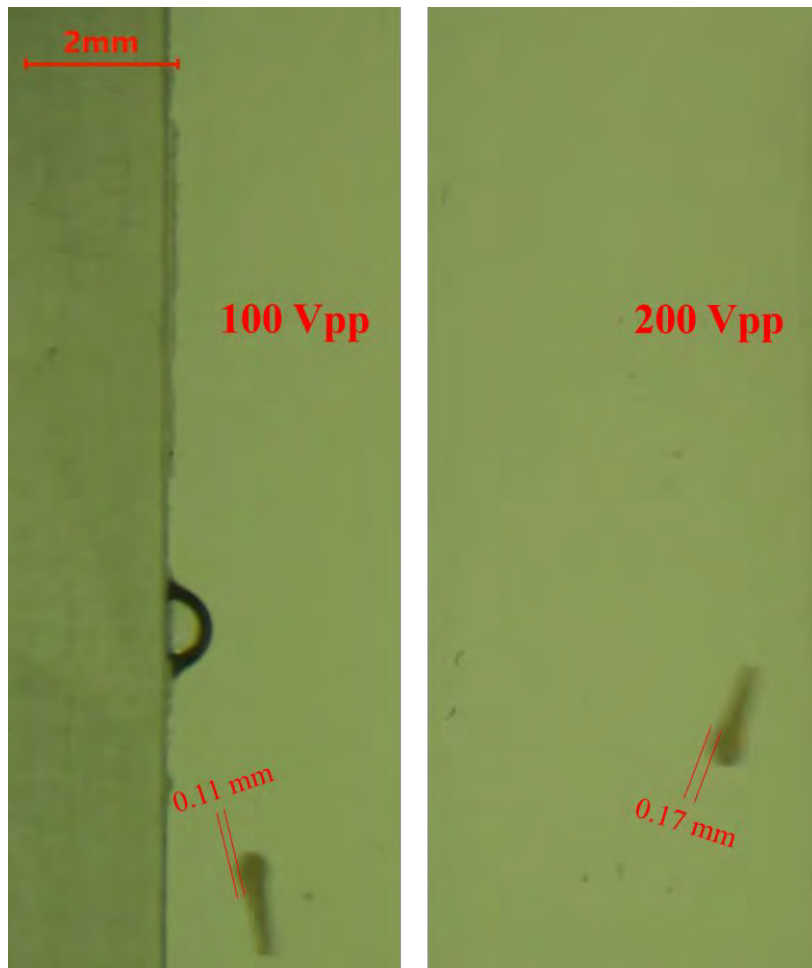
Figure 5-12. Estimate of actuation amplitudes of AFMSs: an example of extracting the amplitude of an AFMS (dimension L1), where the actuation frequency is 100 Hz, and the measured amplitudes are 0.11 mm for 100 Vpp and 0.17 mm for 200 Vpp, respectively.

145
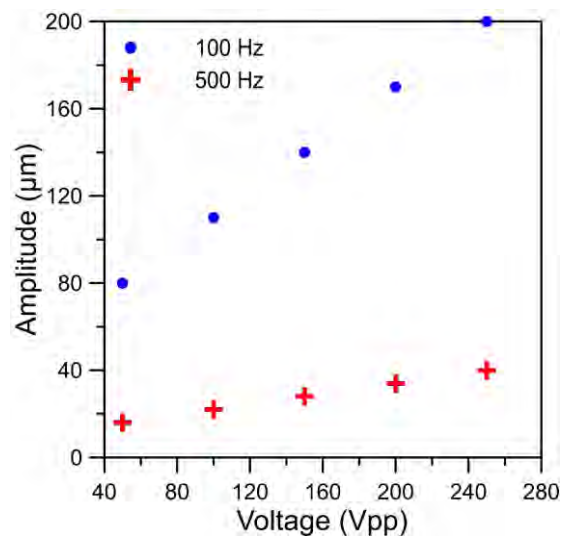
Figure 5-13. Estimate of actuation amplitudes of AFMSs: amplitudes of AFMSs under 5 actuation voltages.
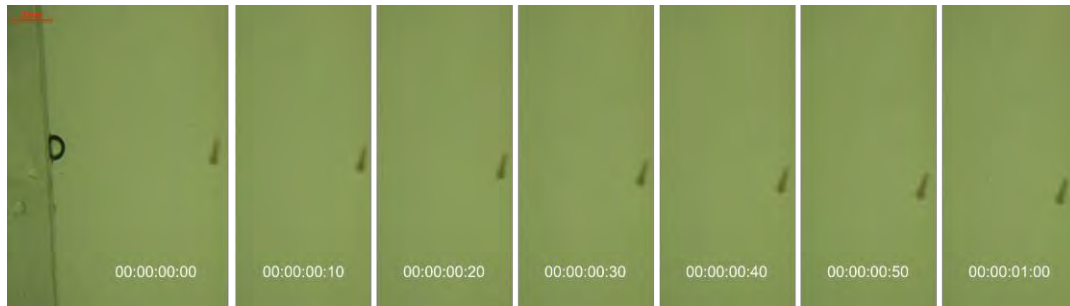
Figure 5-14. An example of how to estimate the terminal velocity of an AFMS, where the dimension is L1, actuated under 100 Hz and 200 Vpp: screenshots captured by a high-speed camera within one second.
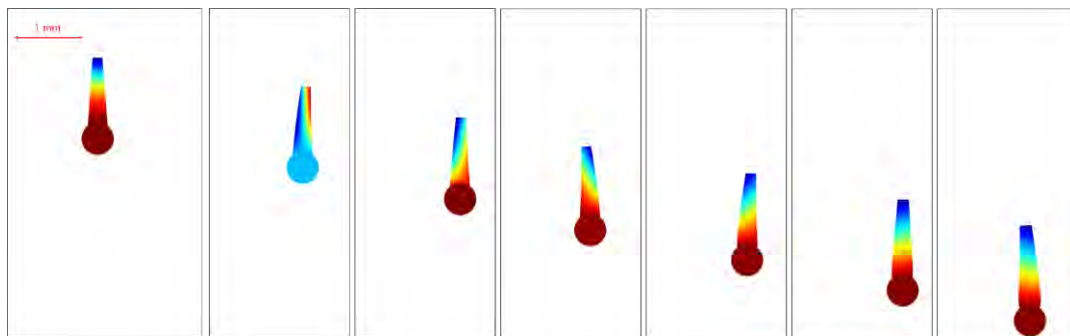
Figure 5-15. An example of how to estimate the terminal velocity of an AFMS, where the dimension is L1, actuated under 100 Hz and 200 Vpp: results of corresponding FSI simulation within one second, where colors on the swimmer indicate displacements.
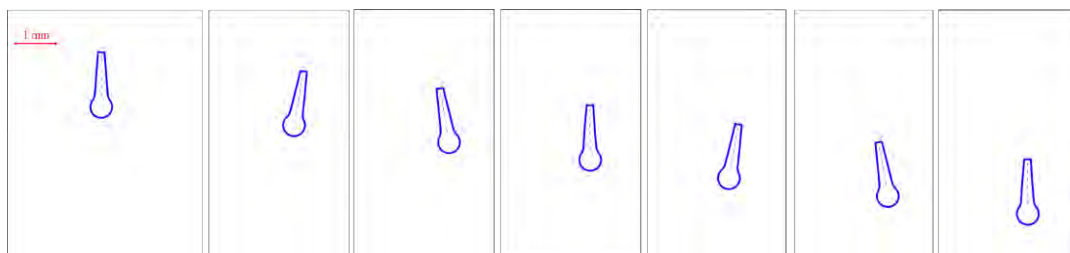
Figure 5-16. An example of how to estimate the terminal velocity of an AFMS, where the dimension is L1, actuated under 100 Hz and 200 Vpp: results of corresponding CRFT model within one second, where dotted lines indicate the centerline of the flagellum.
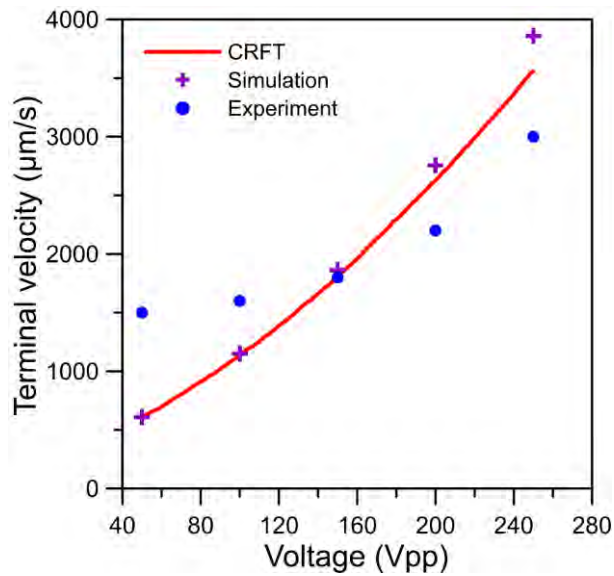
Figure 5-17. Results of terminal velocities obtained from experiments, FSI simulations and the CRFT model, respectively, with parameters of dimension L1 under 100 Hz, $K = 94$ for the CRFT model.
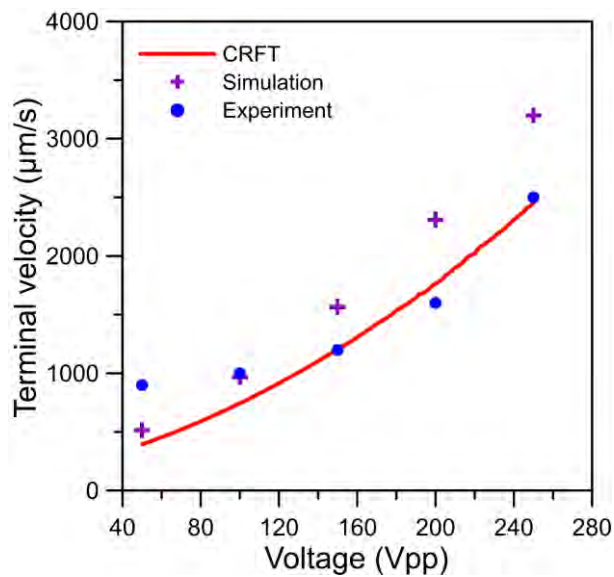
Figure 5-18. Results of terminal velocities obtained from experiments, FSI simulations and the CRFT model, respectively, with parameters of dimension L1 under 500 Hz, $K = 86$ for the CRFT model.
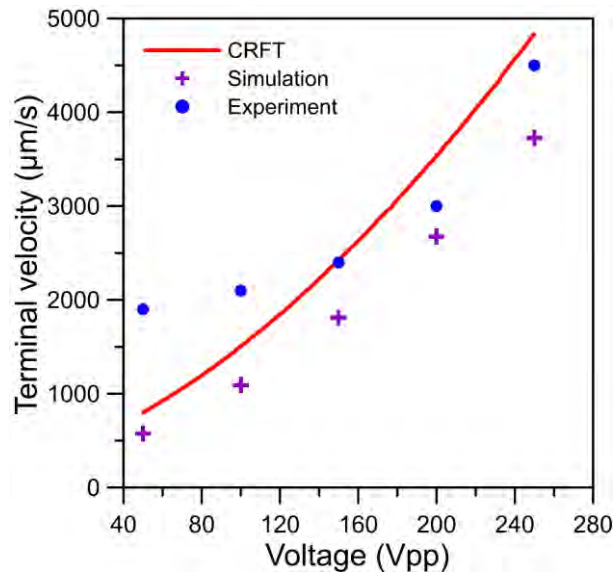
Figure 5-19. Results of terminal velocities obtained from experiments, FSI simulations and the CRFT model, respectively, with parameters of dimension L2 under 100 Hz, $K = 160$ for the CRFT model.
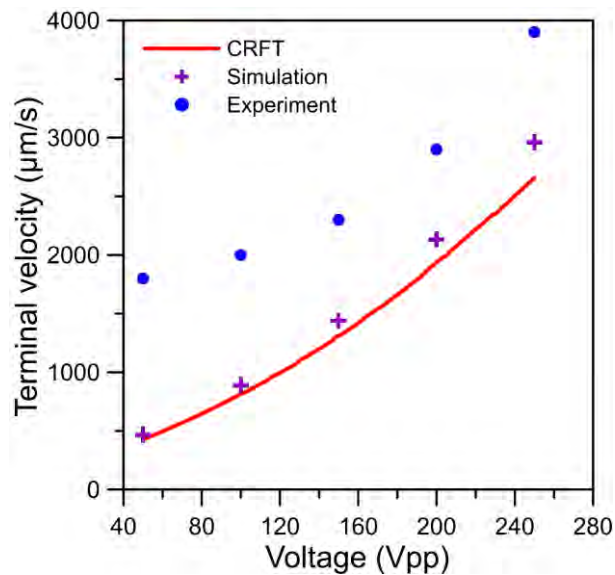
Figure 5-20. Results of terminal velocities obtained from experiments, FSI simulations and the CRFT model, respectively, with parameters of dimension L2 under 500 Hz, $K = 177$ for the CRFT model.

Table 5-1. Results of terminal velocities of AFMSs made of PEG material, which are estimated by FSI simulations and compared with the experimental results in the literature [7].

Amplitude (μm)	Velocity by simulation (μm/s)	Velocity in the Ref. [7] (μm/s)
12	234.26	220
19	595.48	380
26	1106.6	620
33	1763.6	930
40	2613.8	1200

5.6 Summary

In this chapter, we established a testing platform to experimentally verify the theoretical calculations of the AFMSs actuated by acoustic waves according to the CRFT-based bar-joint model proposed in this thesis. We demonstrated the printed AFMSs using a DLP printer and characterized the viscoelastic properties of the UV-cured resins. After that, we described the setup of the experimental platform for observing the motion of an acoustically actuated AFMS. Swimming velocities obtained from experiments, FSI simulations and CRFT models were presented and compared. The deviations are within 50%, corroborating that our theoretical treatment of the acoustic actuation for a head-flagellum structure in the previous chapters is sensible.

Chapter 6. Conclusions and suggestions for future work

6.1 Conclusions

The current research first brings to light the motility and steerability of AFMSs propelled by acoustic waves. The AFMS we considered in this thesis is composed of a rigid head and a flexible flagellum with a length of hundreds of microns. Actuated by acoustic waves, the head oscillates with an amplitude larger than fluid particles (due to the acoustic radiation), which beats the flagellum to achieve propulsion. The 1D EOM for the flagellum, treated as an Euler-Bernoulli viscoelastic beam, was derived based on the RFT to predict its linear locomotion. After that, to consider the steering performance under magneto-acoustic actuation, we developed a 2D bar-joint model based on the CRFT to predict the locomotion. A testing platform was established to experimentally verify our theoretical calculations. Several conclusions were obtained as follows:

1) The oscillating amplitude of the head depends linearly on the sound pressure and is inversely proportional to the actuation frequency. It is noted that the high motility of an AMFS is due to resonance and that a moderate material damping can broaden the SFB at a low sperm number and promote the motility at the non-resonant region. Besides, it is preferred to design and fabricate an AFMS with a non-uniform flagellum with a tapered cross-section.

2) The RFT deals with cylindrical cross-sections, therefore deviated from the micro-swimmers with rectangular cross-sections prepared through lairized printing. We developed a correction to the theory, i.e., the CRFT, and a CRFT-based bar-joint model that can reduce the deviations to below 5% in comparison with FSI simulations. The demonstration of AFMSs turning using acoustic or magneto-acoustic fields indicates that the possible means to steer AFMSs.

150

3) Deviations between the experiments and CRFT model in the prediction of the motilities of the AFMSs are less than 50%, corroborating that our theoretical treatment of the acoustic actuation for an AFMS in the previous chapters is sensible.

6.2 Suggestions for future work

A further study on steering characteristics of the AFMSs under a complex acoustic field will be conducive to the control of trajectories. Note that the current empirical method for the determination of K in the CRFT model is tedious and ungeneralizable to the scenarios beyond the parametric space studied in this thesis, as it requires FSI simulations. An analytical expression of K as a function of geometric, materials, and actuation parameters of an AFMS (i.e., without simulation) is desired, which will be our effort in future work. In addition, the effectiveness of the CRFT model for steering has not been examined in experiments (we have only examined the straight-line motion). It is necessary to fabricate AFMSs embedded with magnetic nanoparticles to determine their motility and magneto-acoustic turning performance to verify our model. As the final remark, we stress that this work only analyzed the propulsion caused by oscillations of the head of an AFMS. The effect of acoustic streaming on the tip of a flagellum, as discussed in [13, 16], was not analyzed. Such a tip force field may also induce the wiggling of a flagellum. In our model, it may also be simplified to be the external force, $\mathbf{F}_0$, acting on the tip. The detailed expression of such tip-induced propulsion is worth exploring in future work.

Although our experiments for the straight-line propulsion of an AFMS have been demonstrated in this thesis, there exists a huge gap between laboratory studies and practical applications. The study of the strategies for precise and robust manipulation of artificial micro-swimmers is still in its infancy, which should be the pivotal factor

for enabling their applications. Our studies in Chapter 4 theoretically realized the steering of an AFMS under external actuation. Further investigations could focus on the trajectory planning for the demanded application. For example, how to make the swimmer stagnate to implement some targeted missions (e.g., drug release or thermotherapy), how to preciously control its trajectory to pass through a complex biological duct, etc. The strategy we proposed, which is to propel by acoustic waves and turn by a magnetic field, may be a feasible scheme to realize steering. To enhance their practical engineering applications, it is necessary to further explore more complex fluid environments and consider the mechanical properties of the AFMSs. For instance, the influence of dynamic flow and uneven boundaries on the actuation of the micro-swimmers, as well as the nonuniform stiffness of the micro-swimmer need to be studied. In addition, the functionality of the acoustically actuated micro-swimmers needs to be further improved to achieve specific biomedical applications.

The next studies should focus on the experimental implementation of swimmer navigation using an experimental platform shown in Figure 6-1. It comprises a PDMS channel, acoustic transducers, electromagnetic coils, a needle hydrophone, an inverted microscope, a high-speed camera, and an optical thermometer. The PDMS channel, for simulating a crooked or branched biological duct, can be fabricated through a replication process (cf., Ref. [268]). An organic fluid with a viscosity of 0.01~0.1 Pa.s (cf. the gastric fluid [235]) can be employed, which leads to a low Re (10^{-3}~10^{-2}) for a 100-µm flagellum with a speed of 1 mm/s. The motion of the micro-simmer in the fluid can be recorded using the inverted microscope and the high-speed camera. For acoustic steering, as suggested in Chapter 4, only stationary acoustic transducers are required. For a rotating acoustic field, contactless ultrasound transducers (cf. [269]) placed on a rotary stage must be employed. The induced sound pressure can be recorded using the

hydrophone. In addition, an induction-heating coil may be employed to demonstrate the heating performance of micro-swimmers loaded with magnetic nanoparticles, simulating thermotherapy.

The visualization and precious steering of AFMSs *in vivo* may be further considered when it comes to a medical application. It is not straightforward to overcome these interdisciplinary challenges. Scientists in various fields should cooperate to achieve the leap from laboratory trials to practical applications.
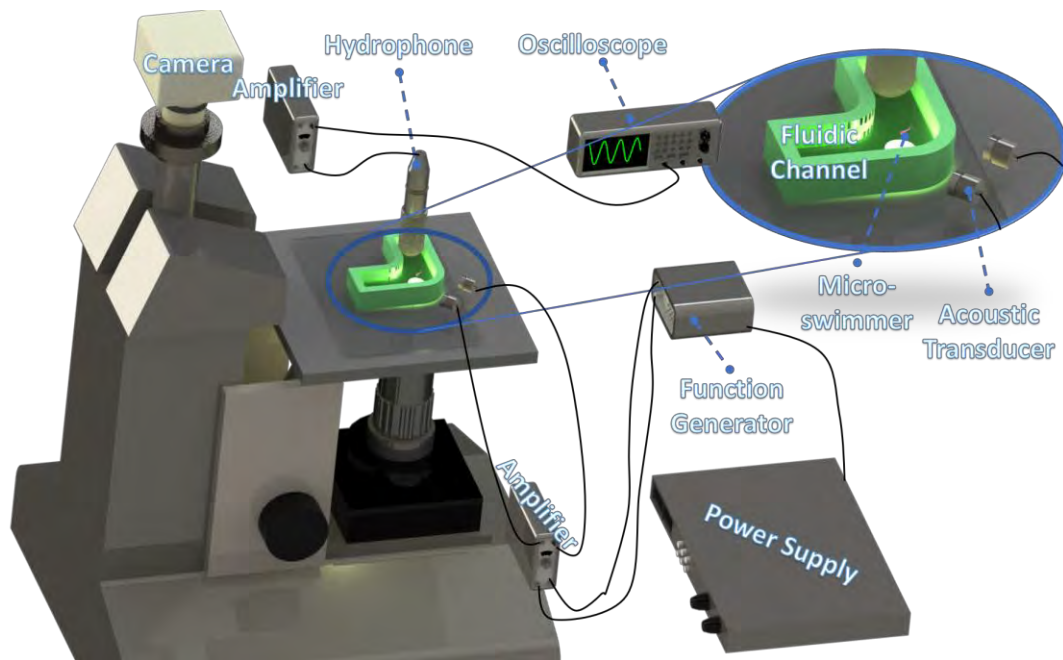
Figure 6-1. Experimental platform for validating and demonstrating steering strategies (the micro-swimmer and fluid channel are exaggerated for clarity).

Appendices

A. Analytical solutions of massless elastic flagellum for 1D propulsion

For a massless elastic flagellum, i.e. $\rho_s = 0$ and $\eta = 0$, we will have $H = 0$ and $\gamma = 0$ based on Eq. (3.23). Then, a dimensionless diffusion equation with boundary conditions is formulated as:

$$\begin{cases} Z\dfrac{\partial \xi_c}{\partial \tilde{t}} + \dfrac{\partial^2}{\partial X^2}\left(J\dfrac{\partial^2 \xi_c}{\partial X^2} \right) = 0 \ , \ 0 \le X \le 1 \ ; \\[2mm] \text{at } X = 0 : \ \xi_c = \xi_{0a}\sin 2\pi\tilde{t} \ , \ \dfrac{\partial \xi_c}{\partial X} = \theta_{0a}\sin\left(2\pi\tilde{t} + \varphi_h \right) \ ; \\[2mm] \text{at } X = 1 : \ \dfrac{\partial^2 \xi_c}{\partial X^2} = 0 \ , \ \dfrac{\partial^3 \xi_c}{\partial X^3} = 0 \ . \end{cases} \tag{A.1}$$

We prescribe that the diameter of the cross-section of the flagellum varies according to the linear function Eq. (3.53). The substitution of Eq. (3.53) into Eq. (A.1) gives the expression of J as:

$$J = J(0)h^4, \tag{A.2}$$

where $J(0) = \pi d_s^4(0)\big/\left(64L^4\right)$ and $h = 1 - \lambda X$. If $\lambda = 0$, Eq. (A.1) will be reduced to a simple diffusion equation as mentioned before [35, 38]. If $\lambda \ne 0$, we can consider Z as a constant $(f/E) \cdot \int_0^1 c_\perp(X)\,\mathrm{d}x$, then we can substitute the independent variable X with h to transform the governing equation into a Cauchy–Euler equation of order 4, expressed as:

$$\begin{cases} Z\dfrac{\partial \xi_c}{\partial \tilde{t}} + J(0)\lambda^4 h^4 \dfrac{\partial^4 \xi_c}{\partial h^4} + 8J(0)\lambda^4 h^3 \dfrac{\partial^3 \xi_c}{\partial h^3} + 12J(0)\lambda^4 h^2 \dfrac{\partial^2 \xi_c}{\partial h^2} = 0 \ ; \\[2mm] \text{at } h = 1 : \ \xi_c = \xi_{0a}\sin 2\pi\tilde{t} \ , \ \dfrac{\partial \xi_c}{\partial h} = -\dfrac{\theta_{0a}}{\lambda}\sin\left(2\pi\tilde{t} + \varphi_h \right) \ ; \\[2mm] \text{at } h = 1 - \lambda : \ \dfrac{\partial^2 \xi_c}{\partial h^2} = 0 \ , \ \dfrac{\partial^3 \xi_c}{\partial h^3} = 0 \ . \end{cases} \tag{A.3}$$

The general solution can be expressed as:

$$\xi_c(\tilde{t}, h) = \sum_{n=1}^{4} G_n h^{r_{\text{PDE}n}} e^{-i2\pi\tilde{t}} , \tag{A.4}$$

where i denotes the imaginary unit, and the eigenvalues $r_{\text{PDE}n}$ denote the four roots of the characteristic polynomial which is given by

$$r_{\text{PDE}n}{}^4 + 2r_{\text{PDE}n}{}^3 - r_{\text{PDE}n}{}^2 - 2r_{\text{PDE}n} - i\frac{2\pi Z}{J(0)\lambda^4} = 0. \tag{A.5}$$

According to the convention that we use only the real part of the complex number as a representation of the physical quantity, we will reach the four coefficients G_n based on the four boundary conditions in (A.3), formulated as:

$$\begin{cases} \sum_{n=1}^{4} G_n = i\xi_{0a} \\ \sum_{n=1}^{4} r_{\text{PDE}n} G_n = -i\frac{\theta_{0a}}{\lambda} e^{-i\varphi_h} \\ \sum_{n=1}^{4} r_{\text{PDE}n} (r_{\text{PDE}n} - 1)(1-\lambda)^{r_{\text{PDE}n}-2} G_n = 0 \\ \sum_{n=1}^{4} r_{\text{PDE}n} (r_{\text{PDE}n} - 1)(r_{\text{PDE}n} - 2)(1-\lambda)^{r_{\text{PDE}n}-3} G_n = 0 \end{cases} . \tag{A.6}$$

Note that we need to recall $h = 1 - \lambda X$ to restore Eq. (A.4) with respect to X. Ultimately, we should substitute the real part of Eq. (A.4) into Eq. (3.31) to reach the non-dimensional terminal velocity.

B. Expressions of the EOM for the bar-joint model for steering

The EOM (Eq. (4.38)) is a set of $(3N + 3)$ ODEs, in which the velocity vectors are:

$$\dot{\mathbf{X}} = \begin{bmatrix} \dot{\mathbf{X}}_1 & \dot{\mathbf{X}}_2 & ... & \dot{\mathbf{X}}_i & ... & \dot{\mathbf{X}}_n \end{bmatrix}^{\mathrm{T}},$$ (B.1)

where

$$\dot{\mathbf{X}}_i = \begin{bmatrix} \dot{x}_i & \dot{y}_i & \dot{\theta}_i \end{bmatrix}^{\mathrm{T}},$$ (B.2)

and the velocity vector of the head:

$$\dot{\mathbf{X}}_0 = \begin{bmatrix} \dot{x}_0 & \dot{y}_0 & \dot{\theta}_0 \end{bmatrix}^{\mathrm{T}}.$$ (B.3)

The $3 \times 3n$ resistive matrix of the flagellum is expressed as:

$$\mathbf{A} = \begin{bmatrix} \mathbf{A}_1 & \mathbf{A}_2 & ... & \mathbf{A}_i & ... & \mathbf{A}_n \end{bmatrix},$$ (B.4)

where

$$\mathbf{A}_i = \begin{bmatrix} A_{i11} & A_{i12} & A_{i13} \\ A_{i21} & A_{i22} & A_{i23} \\ A_{i31} & A_{i32} & A_{i33} \end{bmatrix},$$ (B.5)

and the 9 components of $\mathbf{A}_i$ are respectively expressed as:

$$\begin{aligned}
A_{i11} &= -2l\left(c_{\perp i}\sin^2\theta_i + c_{\|i}\cos^2\theta_i\right), \\
A_{i12} &= 2l\left(c_{\perp i} - c_{\|i}\right)\sin\theta_i\cos\theta_i, \\
A_{i13} &= 0, \\
A_{i21} &= 2l\left(c_{\perp i} - c_{\|i}\right)\sin\theta_i\cos\theta_i, \\
A_{i22} &= -2l\left(c_{\perp i}\cos^2\theta_i + c_{\|i}\sin^2\theta_i\right), \\
A_{i23} &= 0, \\
A_{i31} &= 2l\left[c_{\perp i}\sin\theta_i\left(x_i\cos\theta_i + y_i\sin\theta_i\right) + c_{\|i}\cos\theta_i\left(y_i\cos\theta_i - x_i\sin\theta_i\right)\right], \\
A_{i32} &= -2l\left[c_{\perp i}\cos\theta_i\left(x_i\cos\theta_i + y_i\sin\theta_i\right) + c_{\|i}\sin\theta_i\left(x_i\sin\theta_i - y_i\cos\theta_i\right)\right], \\
A_{i33} &= -\frac{2}{3}l^3 c_{\perp i}.
\end{aligned}$$ (B.6)

The resistive matrix of a head, as given in Eq. (4.27), is expressed as:

$$
\mathbf{A}_0 = \begin{bmatrix} -c_H & 0 & 0 \\ 0 & -c_H & 0 \\ c_H y_0 & -c_H x_0 & -c_{HR} \end{bmatrix}.
$$

(B.7)

The matrix of kinematic constraints of neighboring bars is expressed in the form of:

$$
\mathbf{T}_V = \begin{bmatrix} -\mathbf{T}_{V1}(2l) & \mathbf{T}_{V2}(0) & \mathbf{0} & \dots & \mathbf{0} & \mathbf{0} \\ \mathbf{0} & -\mathbf{T}_{V2}(2l) & \mathbf{T}_{V3}(0) & \dots & \mathbf{0} & \mathbf{0} \\ \mathbf{0} & \mathbf{0} & -\mathbf{T}_{V3}(2l) & \dots & \mathbf{0} & \mathbf{0} \\ \dots & \dots & \dots & \dots & \dots & \dots \\ \mathbf{0} & \mathbf{0} & \mathbf{0} & \dots & \mathbf{T}_{V(n-1)}(0) & \mathbf{0} \\ \mathbf{0} & \mathbf{0} & \mathbf{0} & \dots & -\mathbf{T}_{V(n-1)}(2l) & \mathbf{T}_{Vn}(0) \end{bmatrix},
$$

(B.8)

where

$$
\mathbf{T}_{Vi}(2l) = \begin{bmatrix} 1 & 0 & -l\sin\theta_i \\ 0 & 1 & l\cos\theta_i \end{bmatrix},
$$

(B.9)

$$
\mathbf{T}_{V(i+1)}(0) = \begin{bmatrix} 1 & 0 & l\sin\theta_{i+1} \\ 0 & 1 & -l\cos\theta_{i+1} \end{bmatrix}.
$$

(B.10)

The $3 \times 3N$ matrix $\mathbf{B}$, obtained from the kinematic constraint between the first bar and the head, is expressed as:

$$
\mathbf{B} = \begin{bmatrix} \mathbf{B}_0 & \mathbf{0} & \mathbf{0} & \dots & \mathbf{0} & \mathbf{0} \end{bmatrix},
$$

(B.11)

where

$$
\mathbf{B}_0 = \begin{bmatrix} 1 & 0 & (R_H + l)\sin\theta_1 \\ 0 & 1 & -(R_H + l)\cos\theta_1 \\ 0 & 0 & 1 \end{bmatrix}.
$$

(B.12)

The matrix of torque balance related to the joints $\mathbf{D}$ is expressed in the form as:

$$
\mathbf{D} = \begin{bmatrix}
\mathbf{D}_{11} & \mathbf{D}_{12} & \mathbf{0} & \ldots & \mathbf{0} & \ldots & \mathbf{0} \\
\mathbf{D}_{21} & \mathbf{D}_{22} & \mathbf{D}_{23} & \ldots & \mathbf{0} & \ldots & \mathbf{0} \\
\ldots & \ldots & \ldots & \ldots & \ldots & \ldots & \ldots \\
\mathbf{D}_{i1} & \mathbf{D}_{i2} & \mathbf{D}_{i3} & \ldots & \mathbf{D}_{ij} & \ldots & \mathbf{0} \\
\ldots & \ldots & \ldots & \ldots & \ldots & \ldots & \ldots \\
\mathbf{D}_{(n-1)1} & \mathbf{D}_{(n-1)2} & \mathbf{D}_{(n-1)3} & \ldots & \mathbf{D}_{(n-1)j} & \ldots & \mathbf{D}_{(n-1)n}
\end{bmatrix},
\tag{B.13}
$$

where i runs from 1 to $(N-1)$, and j from 1 to $(i+1)$. The expression of row vector $\mathbf{D}_{ij}$ is dependent on the relation between i and j: when $j < i$, $\mathbf{D}_{ij}$ is expressed as:

$$
\mathbf{D}_{ij} = \begin{bmatrix}
(x_i + l\cos\theta_i)A_{j21} - (y_i + l\sin\theta_i)A_{j11} - A_{j31} \\
(x_i + l\cos\theta_i)A_{j22} - (y_i + l\sin\theta_i)A_{j12} - A_{j32} \\
(x_i + l\cos\theta_i)A_{j23} - (y_i + l\sin\theta_i)A_{j13} - A_{j33}
\end{bmatrix}^{\mathrm{T}},
\tag{B.14}
$$

when $j = i$, $\mathbf{D}_{ij}$ is expressed as:

$$
\mathbf{D}_{ij} = \begin{bmatrix}
(x_i + l\cos\theta_i)A_{i21} - (y_i + l\sin\theta_i)A_{i11} - A_{i31} \\
(x_i + l\cos\theta_i)A_{i22} - (y_i + l\sin\theta_i)A_{i12} - A_{i32} \\
(x_i + l\cos\theta_i)A_{i23} - (y_i + l\sin\theta_i)A_{i13} - A_{i33} + \eta(I_i + I_{i+1})/4l
\end{bmatrix}^{\mathrm{T}},
\tag{B.15}
$$

when $j = i + 1$, $\mathbf{D}_{ij}$ is expressed as:

$$
\mathbf{D}_{ij} = \begin{bmatrix}
0 \\
0 \\
-\eta(I_i + I_{i+1})/4l
\end{bmatrix}^{\mathrm{T}}.
\tag{B.16}
$$

The matrix of torque balance related to the head is expressed as:

$$
\mathbf{D}_0 = \begin{bmatrix}
\mathbf{D}_{01} \\
\mathbf{D}_{02} \\
\ldots \\
\mathbf{D}_{0i} \\
\ldots \\
\mathbf{D}_{0(n-1)}
\end{bmatrix},
\tag{B.17}
$$

158

where the row vector $\mathbf{D}_{0i}$ is expressed as:

$$\mathbf{D}_{0i} = \begin{bmatrix} c_H \left(y_i + l\sin\theta_i - y_0 \right) \\ c_H \left(x_0 - x_i - l\cos\theta_i \right) \\ c_{HR} \end{bmatrix}^{\mathrm{T}}.$$

(B.18)

The vector of velocity-independent torques is expressed as:

$$\mathbf{F}_E = \begin{bmatrix} F_{E1} & F_{E2} & \cdots & F_{Ei} & \cdots & F_{E(n-1)} \end{bmatrix}^{\mathrm{T}},$$

(B.19)

where the ith component F_{Ei} is expressed as:

$$F_{Ei} = E\frac{I_i + I_{i+1}}{2}\frac{\theta_{i+1} - \theta_i}{2l} + \left(y_i + l\sin\theta_i - y_H \right)F_{\mathrm{ext}x}$$
$$+ \left(x_H - x_i - l\cos\theta_i \right)F_{\mathrm{ext}y} + \tau_{\mathrm{ext}}.$$

(B.20)

When a micro-swimmer suspends in a non-static fluid circumstance, e.g., in a plane acoustic field with the velocity of the fluid at the location of the ith bar $\mathbf{u}_i = (u_{ix}, u_{iy}, 0)^{\mathrm{T}}$ (it is $\mathbf{u}_0$ at the head), then for the relative velocity $\mathbf{U} = \mathbf{u} - \mathbf{V}$, the equations of local fluid forces will be recast as $f_{f\parallel}(s) = c_\parallel u_\parallel(s) - c_\parallel V_\parallel(s)$ and $f_{f\perp}(s) = c_\perp u_\perp(s) - c_\perp V_\perp(s)$. Eventually, the governing equations Eq. (4.38) will maintain the form except that the right-hand side non-homogenous terms must be revised to:

$$\mathbf{F}_0 = \begin{bmatrix} F_{\mathrm{ext}x} \\ F_{\mathrm{ext}y} \\ \tau_{\mathrm{ext}} + x_0 F_{\mathrm{ext}y} - y_0 F_{\mathrm{ext}x} - c_H y_0 u_{0x} + c_H x_0 u_{0y} \end{bmatrix} - \sum_{i=1}^{n} \mathbf{A}_i \mathbf{u}_i,$$

(B.21)

$$F_{Ei} = E\frac{I_i + I_{i+1}}{2}\frac{\theta_{i+1} - \theta_i}{2l} + \left(y_i + l\sin\theta_i - y_H\right)F_{\text{extx}}$$
$$+\left(x_H - x_i - l\cos\theta_i\right)F_{\text{exty}} + \tau_{\text{ext}}$$
$$+\sum_{j=1}^{i}u_{ix}\left[\left(x_i + l\cos\theta_i\right)A_{j21} - \left(y_i + l\sin\theta_i\right)A_{j11} - A_{j31}\right]$$
$$+u_{0x}c_H\left(y_i + l\sin\theta_i - y_0\right)$$
$$+\sum_{j=1}^{i}u_{iy}\left[\left(x_i + l\cos\theta_i\right)A_{j22} - \left(y_i + l\sin\theta_i\right)A_{j12} - A_{j32}\right]$$
$$+u_{0y}c_H\left(x_0 - x_i - l\cos\theta_i\right)$$

. (B.22)

C. Non-dimensional terms of the bar-joint model for steering based on the Buckingham π theorem

The Buckingham π theorem [259] is employed for non-dimensionalization. We assume that the set of ODEs of the bar-joint model (i.e., Eq. (4.38)) can be written as:

$$g\left(l, f, \mu, x, u, t, s, I, E, \eta, c, c_H, c_{HR}, R_H, F, \tau\right) = 0, \tag{C.1}$$

where x represents x_i and y_i, u represents u_{ix} and u_{iy}, c represents $c_{\parallel}$ and $c_{\perp}$, and F and τ indicate all the forces and torques. If the 3 fundamental dimensions are denoted by:

M = dimensions of mass,

L = dimensions of length,

T = dimensions of time,

then, the 16 physical variables and their dimensions can be expressed as:

$[l] = \text{L}$, $[f] = \text{T}^{-1}$, $[\mu] = \text{ML}^{-1}\text{T}^{-1}$, $[x] = \text{L}$, $[u] = \text{LT}^{-1}$, $[t] = \text{T}$, $[s] = \text{L}$, $[I] = \text{L}^4$, $[E] = \text{ML}^{-1}\text{T}^{-2}$, $[\eta] = \text{ML}^{-1}\text{T}^{-1}$, $[c] = \text{ML}^{-1}\text{T}^{-1}$, $[c_H] = \text{MT}^{-1}$, $[c_{HR}] = \text{ML}^2\text{T}^{-1}$, $[R_H] = \text{L}$, $[F] = \text{MLT}^{-2}$, $[\tau] = \text{ML}^2\text{T}^{-2}$. (C.2)

We take the half-length of each bar l, the frequency of acoustic actuation f, and the fluid viscosity μ as reference variables, then there will be 13 dimensionless Π products:

$$f\left(\Pi_1,\Pi_2,\Pi_3,\Pi_4,\Pi_5,\Pi_6,\Pi_7,\Pi_8,\Pi_9,\Pi_{10},\Pi_{11},\Pi_{12},\Pi_{13}\right)=0,\tag{C.3}$$

where

$$\Pi_1=f_1\left(l,f,\mu,x\right),\ \Pi_2=f_2\left(l,f,\mu,u\right),\ \Pi_3=f_3\left(l,f,\mu,t\right),\ \Pi_4=f_4\left(l,f,\mu,s\right),$$

$$\Pi_5=f_5\left(l,f,\mu,I\right),\ \Pi_6=f_6\left(l,f,\mu,E\right),\ \Pi_7=f_7\left(l,f,\mu,\eta\right),\ \Pi_8=f_8\left(l,f,\mu,c\right),$$

$$\Pi_9=f_9\left(l,f,\mu,c_H\right),\ \Pi_{10}=f_{10}\left(l,f,\mu,c_{HR}\right),\ \Pi_{11}=f_{11}\left(l,f,\mu,R_H\right),$$

$$\Pi_{12}=f_{12}\left(l,f,\mu,F\right),\ \Pi_{13}=f_{13}\left(l,f,\mu,\tau\right).\tag{C.4}$$

We assume $\Pi_1=l^a f^b \mu^c x$, i.e., $\Pi_1=(\mathrm{L})^a(\mathrm{T}^{-1})^b(\mathrm{ML}^{-1}\mathrm{T}^{-1})^c(\mathrm{L})$; for M: $c+0=0$; for L: $a-c+1=0$; for T: $-b-c+0=0$. Then $a=-1$, $b=0$, $c=0$, thus, $\Pi_1=l^{-1}f^0\mu^0 x = x/l$.

We assume $\Pi_2=l^a f^b \mu^c u$, i.e., $\Pi_2=(\mathrm{L})^a(\mathrm{T}^{-1})^b(\mathrm{ML}^{-1}\mathrm{T}^{-1})^c(\mathrm{LT}^{-1})$; for M: $c+0=0$; for L: $a-c+1=0$; for T: $-b-c-1=0$. Then $a=-1$, $b=-1$, $c=0$, thus, $\Pi_2=l^{-1}f^1\mu^0 u = u/(lf)$.

We assume $\Pi_3=l^a f^b \mu^c t$, i.e., $\Pi_4=(\mathrm{L})^a(\mathrm{T}^{-1})^b(\mathrm{ML}^{-1}\mathrm{T}^{-1})^c(\mathrm{T})$; for M: $c+0=0$; for L: $a-c+0=0$; for T: $-b-c+1=0$. Then $a=0$, $b=1$, $c=0$, thus, $\Pi_3=l^0 f^1 \mu^0 t = ft$.

We assume $\Pi_4=l^a f^b \mu^c s$, i.e., $\Pi_8=(\mathrm{L})^a(\mathrm{T}^{-1})^b(\mathrm{ML}^{-1}\mathrm{T}^{-1})^c(\mathrm{L})$; for M: $c+0=0$; for L: $a-c+1=0$; for T: $-b-c+0=0$. Then $a=-1$, $b=0$, $c=0$, thus, $\Pi_4=l^{-1}f^0\mu^0 s = s/l$.

We assume $\Pi_5=l^a f^b \mu^c I$, i.e., $\Pi_5=(\mathrm{L})^a(\mathrm{T}^{-1})^b(\mathrm{ML}^{-1}\mathrm{T}^{-1})^c(\mathrm{L}^4)$; for M: $c+0=0$; for L: $a-c+4=0$; for T: $-b-c+0=0$. Then $a=-4$, $b=0$, $c=0$, thus, $\Pi_5=l^{-4}f^0\mu^0 I = I/l^4$.

We assume $\Pi_6=l^a f^b \mu^c E$, i.e., $\Pi_7=(\mathrm{L})^a(\mathrm{T}^{-1})^b(\mathrm{ML}^{-1}\mathrm{T}^{-1})^c(\mathrm{ML}^{-1}\mathrm{T}^{-2})$; for M: $c+1=0$; for L: $a-c-1=0$; for T: $-b-c-2=0$. Then $a=0$, $b=-1$, $c=-1$, thus, $\Pi_6=l^0 f^1 \mu^{-1} E = E/(f\mu)$.

We assume $\Pi_7 = l^a f^b \mu^c \eta$, i.e., $\Pi_9 = (L)^a (T^{-1})^b (ML^{-1}T^{-1})^c (ML^{-1}T^{-1})$; for M: $c + 1 = 0$; for L: $a - c - 1 = 0$; for T: $-b - c - 1 = 0$. Then $a = 0$, $b = 0$, $c = -1$, thus, $\Pi_7 = l^0 f^0 \mu^{-1} \eta = \eta/\mu$.

We assume $\Pi_8 = l^a f^b \mu^c c$, i.e., $\Pi_6 = (L)^a (T^{-1})^b (ML^{-1}T^{-1})^c (ML^{-1}T^{-1})$; for M: $c + 1 = 0$; for L: $a - c - 1 = 0$; for T: $-b - c - 1 = 0$. Then $a = 0$, $b = 0$, $c = -1$, thus, $\Pi_8 = l^0 f^0 \mu^{-1} c = c/\mu$.

We assume $\Pi_9 = l^a f^b \mu^c c_H$, i.e., $\Pi_{13} = (L)^a (T^{-1})^b (ML^{-1}T^{-1})^c (MT^{-1})$; for M: $c + 1 = 0$; for L: $a - c + 0 = 0$; for T: $-b - c - 1 = 0$. Then $a = -1$, $b = 0$, $c = -1$, thus, $\Pi_9 = l^{-1} f^0 \mu^{-1} c_H = c_H/(l\mu)$.

We assume $\Pi_{10} = l^a f^b \mu^c c_{HR}$, i.e., $\Pi_{14} = (L)^a (T^{-1})^b (ML^{-1}T^{-1})^c (ML^2 T^{-1})$; for M: $c + 1 = 0$; for L: $a - c + 2 = 0$; for T: $-b - c - 1 = 0$. Then $a = -3$, $b = 0$, $c = -1$, thus, $\Pi_{10} = l^{-3} f^0 \mu^{-1} c_{HR} = c_{HR}/(l^3 \mu)$.

We assume $\Pi_{11} = l^a f^b \mu^c R_H$, i.e., $\Pi_1 = (L)^a (T^{-1})^b (ML^{-1}T^{-1})^c (L)$; for M: $c + 0 = 0$; for L: $a - c + 1 = 0$; for T: $-b - c + 0 = 0$. Then $a = -1$, $b = 0$, $c = 0$, thus, $\Pi_{11} = l^{-1} f^0 \mu^0 R_H = R_H/l$.

We assume $\Pi_{12} = l^a f^b \mu^c F$, i.e., $\Pi_{12} = (L)^a (T^{-1})^b (ML^{-1}T^{-1})^c (MLT^{-2})$; for M: $c + 1 = 0$; for L: $a - c + 1 = 0$; for T: $-b - c - 2 = 0$. Then $a = -2$, $b = -1$, $c = -1$, thus, $\Pi_{12} = l^{-2} f^1 \mu^{-1} F = F/(l^2 f \mu)$.

We assume $\Pi_{13} = l^a f^b \mu^c \tau$, i.e., $\Pi_{13} = (L)^a (T^{-1})^b (ML^{-1}T^{-1})^c (ML^2 T^{-2})$; for M: $c + 1 = 0$; for L: $a - c + 2 = 0$; for T: $-b - c - 2 = 0$. Then $a = -3$, $b = -1$, $c = -1$, thus, $\Pi_{13} = l^{-2} f^1 \mu^{-1} \tau = \tau/(l^3 f \mu)$.

Based on the above procedure, the following non-dimensional terms are introduced:

$$\tilde{x} = \frac{x}{l}, \; \tilde{u} = \frac{u}{lf}, \; \tilde{t} = ft, \; \tilde{s} = \frac{s}{l}, \; \tilde{I} = \frac{I}{l^4}, \; \tilde{E} = \frac{E}{f\mu}, \; \tilde{\eta} = \frac{\eta}{\mu}, \; \tilde{c} = \frac{c}{\mu}, \; \tilde{c}_H = \frac{c_H}{l\mu}, \; \tilde{c}_{HR} = \frac{c_{HR}}{l^3\mu},$$

$$\tilde{R}_H = \frac{R_H}{l}, \; \tilde{F} = \frac{F}{l^2 f\mu}, \; \tilde{\tau} = \frac{\tau}{l^3 f\mu}. \tag{C.5}$$

The dimensionless governing equations of Eq. (4.38) can then be reached, where the three variables l, f, and μ become unity, and other physical quantities can be directly replaced according to Eq. (C.5).

References

1. Feynman, R. *There is plenty of room at the bottom: An invitation to enter a new field of physics*. in *Lecture at American Physical Society Meeting*. 1959.
2. Toumey, C., *The literature of promises.* Nature Nanotechnology, 2008. **3**: p. 180.
3. Cho, S., *Mini and micro propulsion for medical swimmers.* Micromachines, 2014. **5**(1): p. 97-113.
4. Toennies, J.L., et al., *Swallowable medical devices for diagnosis and surgery: the state of the art.* Proceedings of the Institution of Mechanical Engineers, Part C: Journal of Mechanical Engineering Science, 2010. **224**(7): p. 1397-1414.
5. Lauga, E. and T.R. Powers, *The hydrodynamics of swimming microorganisms.* Reports on Progress in Physics, 2009. **72**(9): p. 096601.
6. Sitti, M., et al., *Biomedical applications of untethered mobile milli/microrobots.* Proceedings of the IEEE, 2015. **103**(2): p. 205-224.
7. Kaynak, M., et al., *Acoustic actuation of bioinspired microswimmers.* Lab on a Chip, 2017. **17**(3): p. 395-400.
8. Kadry, H., et al., *Digital light processing (DLP) 3D-printing technology and photoreactive polymers in fabrication of modified-release tablets.* European Journal of Pharmaceutical Sciences, 2019. **135**: p. 60-67.
9. Munoz, F., G. Alici, and W. Li, *A review of drug delivery systems for capsule endoscopy.* Advanced drug delivery reviews, 2014. **71**: p. 77-85.
10. Ghosh, A. and P. Fischer, *Controlled propulsion of artificial magnetic nanostructured propellers.* Nano letters, 2009. **9**(6): p. 2243-2245.
11. Zhang, L., et al., *Artificial bacterial flagella: Fabrication and magnetic control.* Applied Physics Letters, 2009. **94**(6): p. 064107.
12. Mohanty, S., I.S. Khalil, and S. Misra, *Contactless acoustic micro/nano manipulation: a paradigm for next generation applications in life sciences.* Proceedings of the Royal Society A, 2020. **476**(2243): p. 20200621.
13. Ahmed, D., et al., *Artificial swimmers propelled by acoustically activated flagella.* Nano letters, 2016. **16**(8): p. 4968-4974.
14. Ovchinnikov, M., J. Zhou, and S. Yalamanchili, *Acoustic streaming of a sharp edge.* The Journal of the Acoustical Society of America, 2014. **136**(1): p. 22-29.
15. Kaynak, M., et al., *Acoustofluidic actuation of in situ fabricated microrotors.* Lab on a Chip, 2016. **16**(18): p. 3532-3537.
16. Nama, N., et al., *Investigation of acoustic streaming patterns around oscillating sharp edges.* Lab on a Chip, 2014. **14**(15): p. 2824-2836.
17. Rorai, C., M. Zaitsev, and S. Karabasov, *On the limitations of some popular numerical models of flagellated microswimmers: importance of long-range forces and flagellum waveform.* Royal Society open science, 2019. **6**(1): p. 180745.
18. Hancock, G., *The self-propulsion of microscopic organisms through liquids.* Proceedings of the Royal Society of London. Series A. Mathematical and Physical Sciences, 1953. **217**(1128): p. 96-121.
19. Newman, J.N., *A slender-body theory for ship oscillations in waves.* Journal of Fluid Mechanics, 1964. **18**(4): p. 602-618.
20. Cox, R., *The motion of long slender bodies in a viscous fluid Part 1. General theory.* Journal of Fluid mechanics, 1970. **44**(4): p. 791-810.
21. Keller, J.B. and S.I. Rubinow, *Slender-body theory for slow viscous flow.* Journal of Fluid Mechanics, 1976. **75**(4): p. 705-714.
22. Koens, L. and E. Lauga, *The boundary integral formulation of Stokes flows includes slender-body theory.* Journal of Fluid Mechanics, 2018. **850**.
23. Rodenborn, B., et al., *Propulsion of microorganisms by a helical flagellum.* Proceedings of the National Academy of Sciences, 2013. **110**(5): p. E338-E347.
24. Zhang, T. and D.I. Goldman, *The effectiveness of resistive force theory in granular locomotion.* Physics of Fluids, 2014. **26**(10): p. 101308.
25. Gray, J. and G. Hancock, *The propulsion of sea-urchin spermatozoa.* Journal of Experimental Biology, 1955. **32**(4): p. 802-814.
26. Lighthill, J., *Flagellar hydrodynamics.* SIAM review, 1976. **18**(2): p. 161-230.
27. Gauger, E. and H. Stark, *Numerical study of a microscopic artificial swimmer.* Physical Review E, 2006. **74**(2): p. 021907.

28. Wang, W., et al., *Autonomous motion of metallic microrods propelled by ultrasound.* ACS nano, 2012. **6**(7): p. 6122-6132.
29. Ahmed, S., et al., *Density and shape effects in the acoustic propulsion of bimetallic nanorod motors.* ACS nano, 2016. **10**(4): p. 4763-4769.
30. Gray, J., *The movement of sea-urchin spermatozoa.* Journal of Experimental Biology, 1955. **32**.
31. Berg, H., *Motile behavior of bacteria.* Physics today, 2000.
32. Suarez, S.S. and A.A. Pacey, *Sperm transport in the female reproductive tract.* Human Reproduction Update, 2006. **12**(1): p. 23-37.
33. Abbott, J.J., et al., *How should microrobots swim?* The international journal of Robotics Research, 2009. **28**(11-12): p. 1434-1447.
34. Purcell, E.M., *Life at low Reynolds number.* American journal of physics, 1977. **45**(1): p. 3-11.
35. Machin, K.E., *Wave propagation along flagella.* Journal of Experimental Biology, 1958. **35**(4): p. 796-806.
36. Taylor, G.I., *Analysis of the swimming of microscopic organisms.* Proceedings of the Royal Society of London. Series A. Mathematical and Physical Sciences, 1951. **209**(1099): p. 447-461.
37. Turner, L., W.S. Ryu, and H.C. Berg, *Real-time imaging of fluorescent flagellar filaments.* Journal of Bacteriology, 2000. **182**(10): p. 2793-2801.
38. Wiggins, C.H. and R.E. Goldstein, *Flexive and propulsive dynamics of elastica at low Reynolds number.* Physical Review Letters, 1998. **80**(17): p. 3879.
39. Yu, T.S., E. Lauga, and A.E. Hosoi, *Experimental investigations of elastic tail propulsion at low Reynolds number.* Physics of Fluids, 2006. **18**(9): p. 3.
40. Al-Bdor, B., A. Sinawi, and M.N. Hamdan, *Nonlinear dynamic model of an inextensible rotating flexible arm supported on flexible base.* Journal of Sound and Vibration - J SOUND VIB, 2002. **251**: p. 767-781.
41. Friedrich, B.M., et al., *High-precision tracking of sperm swimming fine structure provides strong test of resistive force theory.* Journal of Experimental Biology, 2010. **213**(8): p. 1226-1234.
42. Saggiorato, G., et al., *Human sperm steer with second harmonics of the flagellar beat.* Nature communications, 2017. **8**(1): p. 1-9.
43. Alouges, F., et al., *Can magnetic multilayers propel artificial microswimmers mimicking sperm cells?* Soft Robotics, 2015. **2**(3): p. 117-128.
44. Dobell, C., *Antony Van Leeuwenhoek and his little animals.* 1960.
45. Berg, H.C., *The rotary motor of bacterial flagella.* Annual review of biochemistry, 2003. **72**.
46. Berg, H., *E. coli in Motion Springer*. 2004, NY.
47. Lowe, G., M. Meister, and H.C. Berg, *Rapid rotation of flagellar bundles in swimming bacteria.* Nature, 1987. **325**(6105): p. 637-640.
48. Bray, D., *Cell movements: from molecules to motility*. 2000: Garland Science.
49. Koyasu, S. and Y. Shirakihara, *Caulobacter crescentus flagellar filament has a right-handed helical form.* Journal of molecular biology, 1984. **173**(1): p. 125-130.
50. Armitage, J.P. and R. Schmitt, *Bacterial chemotaxis: Rhodobacter sphaeroide and Sinorhizobium meliloti-variations on a theme?* Microbiology, 1997. **143**(12): p. 3671-3682.
51. Krieg, N.R. and H. Manual, *Systematic bacteriology.* Williams Baltimore, 1984.
52. Buller, A.H.R., *Is Chemotaxis a Factor in the Fertilisation of the Eggs of Animals?* Quart. J. Microscop. Sci., 1903. **46**: p. 145-176.
53. Rothschild, L. and M. Swann, *The fertilization reaction in the sea-urchin: the probability of a successful sperm-egg collision.* Journal of Experimental Biology, 1951. **28**(3): p. 403-416.
54. Gray, J., *The movement of sea-urchin spermatozoa.* Journal of Experimental Biology, 1955. **32**(4): p. 775-801.
55. Rikmenspoel, R., G. Van Herpen, and P. Eijkhout, *Cinematographic observations of the movements of bull sperm cells.* Physics in Medicine & Biology, 1960. **5**(2): p. 167.
56. Rothschild, L. and M. Swann, *The fertilization reaction in the sea-urchin egg. The effect of nicotine.* Journal of Experimental Biology, 1950. **27**(3): p. 400-406.
57. Brokaw, C., *Non-sinusoidal bending waves of sperm flagella.* Journal of Experimental Biology, 1965. **43**(1): p. 155-169.
58. Brokaw, C.J., *Bending Moments in Free-Swimming Flagella.* Journal of Experimental Biology, 1970. **53**(2): p. 445-464.
59. Stearns, J. and M. Surette, *Microbiology for dummies*. 2019: John Wiley & Sons.
60. Childress, S., *Mechanics of swimming and flying*. 1981: Cambridge University Press.
61. Brennen, C. and H. Winet, *Fluid mechanics of propulsion by cilia and flagella.* Annual Review of Fluid Mechanics, 1977. **9**(1): p. 339-398.

62. Ellington, C.P., *The aerodynamics of hovering insect flight. II. Morphological parameters.* Philosophical Transactions of the Royal Society of London. B, Biological Sciences, 1984. **305**(1122): p. 17-40.

63. Vogel, E. and D. Vogel, *Kindred strangers: The uneasy relationship between politics and business in America.* Vol. 155. 1996: Princeton University Press.

64. Alexander, D.E., *Nature's flyers: birds, insects, and the biomechanics of flight.* 2002: JHU Press.

65. Dudley, R., *The biomechanics of insect flight: form, function, evolution.* 2002: Princeton University Press.

66. Vogel, S., *Comparative biomechanics: life's physical world Princeton University Press.* Princet. NJ USA, 2003.

67. Ludwig, W., *Zur theorie der flimmerbewegung (dynamik, nutzeffekt, energiebilanz).* Zeitschrift für vergleichende Physiologie, 1930. **13**(3): p. 397-504.

68. Lighthill, J., *Mathematical Biofluiddynamics.* 1975, Philadelphia: SIAM.

69. Yates, G.T., *How microorganisms move through water: the hydrodynamics of ciliary and flagellar propulsion reveal how microorganisms overcome the extreme effect of the viscosity of water.* American scientist, 1986. **74**(4): p. 358-365.

70. Taylor, G., M.S. Triantafyllou, and C. Tropea, *Animal locomotion.* 2010: Springer Science & Business Media.

71. Holwill, M.E.J., *Physical Aspects of Flagellar Movement.* Physiological Reviews, 1966. **46**(4): p. 696-785.

72. Hinch, E., *Hydrodynamics at low Reynolds numbers: a brief and elementary introduction*, in *Disorder and mixing.* 1988, Springer. p. 43-56.

73. Becker, L.E., S.A. Koehler, and H.A. Stone, *On self-propulsion of micro-machines at low Reynolds number: Purcell's three-link swimmer.* Journal of fluid mechanics, 2003. **490**: p. 15.

74. Childress, S. and R. Dudley, *Transition from ciliary to flapping mode in a swimming mollusc: flapping flight as a bifurcation in Re~ o~ m~ e~ g~ a.* Journal of Fluid Mechanics, 2004. **498**: p. 257-288.

75. Alben, S. and M. Shelley, *Coherent locomotion as an attracting state for a free flapping body.* Proceedings of the National Academy of Sciences, 2005. **102**(32): p. 11163-11166.

76. Vandenberghe, N., S. Childress, and J. Zhang, *On unidirectional flight of a free flapping wing.* Physics of Fluids, 2006. **18**(1): p. 014102.

77. Lu, X.-Y. and Q. Liao, *Dynamic responses of a two-dimensional flapping foil motion.* Physics of Fluids, 2006. **18**(9): p. 098104.

78. Lauga, E., *Continuous breakdown of Purcell's scallop theorem with inertia.* Physics of Fluids, 2007. **19**(6): p. 061703.

79. Sznitman, J., et al., *Propulsive force measurements and flow behavior of undulatory swimmers at low Reynolds number.* Physics of Fluids, 2010. **22**(12): p. 121901.

80. Bayly, P., et al., *Propulsive forces on the flagellum during locomotion of Chlamydomonas reinhardtii.* Biophysical journal, 2011. **100**(11): p. 2716-2725.

81. Maladen, R.D., et al., *Mechanical models of sandfish locomotion reveal principles of high performance subsurface sand-swimming.* Journal of The Royal Society Interface, 2011. **8**(62): p. 1332-1345.

82. Lauga, E., et al., *Swimming in circles: motion of bacteria near solid boundaries.* Biophysical journal, 2006. **90**(2): p. 400-412.

83. Chattopadhyay, S., et al., *Swimming efficiency of bacterium Escherichiacoli.* Proceedings of the National Academy of Sciences, 2006. **103**(37): p. 13712-13717.

84. Chattopadhyay, S. and X.-L. Wu, *The effect of long-range hydrodynamic interaction on the swimming of a single bacterium.* Biophysical Journal, 2009. **96**(5): p. 2023-2028.

85. Darnton, N.C., et al., *On torque and tumbling in swimming Escherichia coli.* Journal of bacteriology, 2007. **189**(5): p. 1756-1764.

86. Vogel, R. and H. Stark, *Force-extension curves of bacterial flagella.* The European Physical Journal E, 2010. **33**(3): p. 259-271.

87. Vogel, R. and H. Stark, *Motor-driven bacterial flagella and buckling instabilities.* The European Physical Journal E, 2012. **35**(2): p. 1-15.

88. Behkam, B. and M. Sitti, *Design methodology for biomimetic propulsion of miniature swimming robots.* 2006.

89. Li, H., J. Tan, and M. Zhang, *Dynamics modeling and analysis of a swimming microrobot for controlled drug delivery.* IEEE Transactions on Automation Science and Engineering, 2008. **6**(2): p. 220-227.

90. NgocSan, H., G. NamSeo, and Y. HyeonKyu, *Development of a propulsion system for a biomimetic thruster.* Chinese Science Bulletin, 2011. **56**: p. 432-438.

91. Johnson, R.E., *An improved slender-body theory for Stokes flow.* Journal of Fluid Mechanics, 1980. **99**(2): p. 411-431.

92. Cortez, R., L. Fauci, and A. Medovikov, *The method of regularized Stokeslets in three dimensions: analysis, validation, and application to helical swimming.* Physics of Fluids, 2005. **17**(3): p. 031504.

93. Garcia-Gonzalez, J., *Numerical Analysis of Fluid Motion at Low Reynolds Numbers.* 2017, The University of Manchester (United Kingdom).

94. Tabak, A.F. and S. Yesilyurt, *Computationally-validated surrogate models for optimal geometric design of bio-inspired swimming robots: Helical swimmers.* Computers & Fluids, 2014. **99**: p. 190-198.

95. Ramia, M., D. Tullock, and N. Phan-Thien, *The role of hydrodynamic interaction in the locomotion of microorganisms.* Biophysical journal, 1993. **65**(2): p. 755-778.

96. Shum, H., E. Gaffney, and D. Smith, *Modelling bacterial behaviour close to a no-slip plane boundary: the influence of bacterial geometry.* Proceedings of the Royal Society A: Mathematical, Physical and Engineering Sciences, 2010. **466**(2118): p. 1725-1748.

97. Pimponi, D., et al., *Hydrodynamics of flagellated microswimmers near free-slip interfaces.* Journal of Fluid Mechanics, 2016. **789**: p. 514-533.

98. Pimponi, D., M. Chinappi, and P. Gualtieri, *Flagellated microswimmers: hydrodynamics in thin liquid films.* The European Physical Journal E, 2018. **41**(2): p. 1-8.

99. Curatolo, M. and L. Teresi, *Modeling and simulation of fish swimming with active muscles.* Journal of theoretical biology, 2016. **409**: p. 18-26.

100. Chwang, A. and T.Y. Wu, *A note on the helical movement of micro-organisms.* Proceedings of the Royal Society of London. Series B. Biological Sciences, 1971. **178**(1052): p. 327-346.

101. Lighthill, M., *On the squirming motion of nearly spherical deformable bodies through liquids at very small Reynolds numbers.* Communications on pure and applied mathematics, 1952. **5**(2): p. 109-118.

102. Blake, J.R., *A spherical envelope approach to ciliary propulsion.* Journal of Fluid Mechanics, 1971. **46**(1): p. 199-208.

103. Blake, J., *Self propulsion due to oscillations on the surface of a cylinder at low Reynolds number.* Bulletin of the Australian Mathematical Society, 1971. **5**(2): p. 255-264.

104. Reynolds, A., *The swimming of minute organisms.* Journal of Fluid Mechanics, 1965. **23**(2): p. 241-260.

105. Tuck, E., *A note on a swimming problem.* Journal of Fluid Mechanics, 1968. **31**(2): p. 305-308.

106. Machin, K., *Wave propagation along flagella.* Journal of Experimental Biology, 1958. **35**(4): p. 796-806.

107. Machin, K., *The control and synchronization of flagellar movement.* Proceedings of the Royal Society of London. Series B. Biological Sciences, 1963. **158**(970): p. 88-104.

108. Lowe, C.P., *Dynamics of filaments: modelling the dynamics of driven microfilaments.* Philosophical Transactions of the Royal Society of London. Series B: Biological Sciences, 2003. **358**(1437): p. 1543-1550.

109. Lagomarsino, M.C., F. Capuani, and C.P. Lowe, *A simulation study of the dynamics of a driven filament in an Aristotelian fluid.* Journal of theoretical biology, 2003. **224**(2): p. 215-224.

110. Yu, T.S., E. Lauga, and A. Hosoi, *Experimental investigations of elastic tail propulsion at low Reynolds number.* Physics of Fluids, 2006. **18**(9): p. 091701.

111. Lauga, E., *Floppy swimming: Viscous locomotion of actuated elastica.* Physical Review E, 2007. **75**(4): p. 041916.

112. Kosa, G., M. Shoham, and M. Zaaroor, *Propulsion method for swimming microrobots.* IEEE Transactions on Robotics, 2007. **23**(1): p. 137-150.

113. Fu, H.C., C.W. Wolgemuth, and T.R. Powers, *Beating patterns of filaments in viscoelastic fluids.* Physical Review E, 2008. **78**(4): p. 041913.

114. Riveline, D., et al., *Elastohydrodynamic study of actin filaments using fluorescence microscopy.* Physical Review E, 1997. **56**(2): p. R1330.

115. Wiggins, C.H., et al., *Trapping and wiggling: elastohydrodynamics of driven microfilaments.* Biophysical journal, 1998. **74**(2): p. 1043-1060.

116. Dreyfus, R., et al., *Microscopic artificial swimmers.* Nature, 2005. **437**(7060): p. 862-865.

117. Singh, T.S. and R. Yadava, *Effect of tapering on elastic filament microswimming under planar body actuation.* Biomedical Physics & Engineering Express, 2017. **4**(1): p. 015019.

118. Manikantan, H. and D. Saintillan, *Buckling transition of a semiflexible filament in extensional flow.* Physical Review E, 2015. **92**(4): p. 041002.

167

119. Kantsler, V. and R.E. Goldstein, *Fluctuations, dynamics, and the stretch-coil transition of single actin filaments in extensional flows.* Physical review letters, 2012. **108**(3): p. 038103.
120. Guglielmini, L., et al., *Buckling transitions of an elastic filament in a viscous stagnation point flow.* Physics of Fluids, 2012. **24**(12): p. 123601.
121. Manikantan, H. and D. Saintillan, *Subdiffusive transport of fluctuating elastic filaments in cellular flows.* Physics of Fluids, 2013. **25**(7): p. 073603.
122. Young, Y.-N. and M.J. Shelley, *Stretch-coil transition and transport of fibers in cellular flows.* Physical review letters, 2007. **99**(5): p. 058303.
123. Wandersman, E., et al., *Buckled in translation.* Soft matter, 2010. **6**(22): p. 5715-5719.
124. Hinch, E., *The distortion of a flexible inextensible thread in a shearing flow.* Journal of Fluid Mechanics, 1976. **74**(2): p. 317-333.
125. Becker, L.E. and M.J. Shelley, *Instability of elastic filaments in shear flow yields first-normal-stress differences.* Physical Review Letters, 2001. **87**(19): p. 198301.
126. Tornberg, A.-K. and M.J. Shelley, *Simulating the dynamics and interactions of flexible fibers in Stokes flows.* Journal of Computational Physics, 2004. **196**(1): p. 8-40.
127. Munk, T., et al., *Dynamics of semiflexible polymers in a flow field.* Physical Review E, 2006. **74**(4): p. 041911.
128. Young, Y.-N., *Hydrodynamic interactions between two semiflexible inextensible filaments in Stokes flow.* Physical Review E, 2009. **79**(4): p. 046317.
129. Harasim, M., et al., *Direct observation of the dynamics of semiflexible polymers in shear flow.* Physical review letters, 2013. **110**(10): p. 108302.
130. Steinhauser, D., S. Köster, and T. Pfohl, *Mobility gradient induces cross-streamline migration of semiflexible polymers.* ACS Macro Letters, 2012. **1**(5): p. 541-545.
131. Autrusson, N., et al., *The shape of an elastic filament in a two-dimensional corner flow.* Physics of Fluids, 2011. **23**(6): p. 063602.
132. Wexler, J.S., et al., *Bending of elastic fibres in viscous flows: the influence of confinement.* Journal of fluid mechanics, 2013. **720**: p. 517-544.
133. Seifert, U., W. Wintz, and P. Nelson, *Straightening of thermal fluctuations in semiflexible polymers by applied tension.* Physical review letters, 1996. **77**(27): p. 5389.
134. Llopis, I., et al., *Sedimentation of pairs of hydrodynamically interacting semiflexible filaments.* Physical Review E, 2007. **76**(6): p. 061901.
135. Spagnolie, S.E. and E. Lauga, *The optimal elastic flagellum.* Physics of Fluids, 2010. **22**(3): p. 455.
136. Jayaraman, G., et al., *Autonomous motility of active filaments due to spontaneous flow-symmetry breaking.* Physical review letters, 2012. **109**(15): p. 158302.
137. Evans, A.A., et al., *Elastocapillary self-folding: buckling, wrinkling, and collapse of floating filaments.* Soft Matter, 2013. **9**(5): p. 1711-1720.
138. Chen, X.Z., et al., *Small‐scale machines driven by external power sources.* Advanced Materials, 2018. **30**(15): p. 1705061.
139. Parmar, J., et al., *Nano and micro architectures for self-propelled motors.* Science and technology of advanced materials, 2015. **16**(1): p. 014802.
140. Sánchez, S., L. Soler, and J. Katuri, *Chemically powered micro‐and nanomotors.* Angewandte Chemie International Edition, 2015. **54**(5): p. 1414-1444.
141. Wang, H. and M. Pumera, *Fabrication of micro/nanoscale motors.* Chemical reviews, 2015. **115**(16): p. 8704-8735.
142. Wang, W., et al., *From one to many: Dynamic assembly and collective behavior of self-propelled colloidal motors.* Accounts of chemical research, 2015. **48**(7): p. 1938-1946.
143. Katuri, J., et al., *Designing micro-and nanoswimmers for specific applications.* Accounts of chemical research, 2017. **50**(1): p. 2-11.
144. Maric, T., et al., *Black-phosphorus-enhanced bubble-propelled autonomous catalytic microjets.* Appl. Mater. Today, 2017. **9**: p. 289-291.
145. Paxton, W.F., et al., *Catalytic nanomotors: autonomous movement of striped nanorods.* Journal of the American Chemical Society, 2004. **126**(41): p. 13424-13431.
146. Fournier-Bidoz, S., et al., *Synthetic self-propelled nanorotors.* Chemical Communications, 2005(4): p. 441-443.
147. Paxton, W.F., A. Sen, and T.E. Mallouk, *Motility of catalytic nanoparticles through self‐generated forces.* Chemistry‐A European Journal, 2005. **11**(22): p. 6462-6470.
148. Sundararajan, S., et al., *Catalytic motors for transport of colloidal cargo.* Nano letters, 2008. **8**(5): p. 1271-1276.
149. Sundararajan, S., et al., *Drop‐off of colloidal cargo transported by catalytic Pt‐Au nanomotors via photochemical stimuli.* Small, 2010. **6**(14): p. 1479-1482.

150. Kagan, D., et al., *Rapid delivery of drug carriers propelled and navigated by catalytic nanoshuttles.* Small, 2010. **6**(23): p. 2741-2747.

151. Xu, T., L.-P. Xu, and X. Zhang, *Ultrasound propulsion of micro-/nanomotors.* Applied Materials Today, 2017. **9**: p. 493-503.

152. Chen, X.-Z., et al., *Recent developments in magnetically driven micro-and nanorobots.* Applied Materials Today, 2017. **9**: p. 37-48.

153. Bell, D.J., et al. *Flagella-like propulsion for microrobots using a nanocoil and a rotating electromagnetic field.* in *Proceedings 2007 IEEE international conference on robotics and automation.* 2007. IEEE.

154. Hawkeye, M.M. and M.J. Brett, *Glancing angle deposition: Fabrication, properties, and applications of micro-and nanostructured thin films.* Journal of Vacuum Science & Technology A: Vacuum, Surfaces, and Films, 2007. **25**(5): p. 1317-1335.

155. Schuerle, S., et al., *Helical and tubular lipid microstructures that are electroless‐coated with CoNiReP for wireless magnetic manipulation.* Small, 2012. **8**(10): p. 1498-1502.

156. Gao, W., et al., *Bioinspired helical microswimmers based on vascular plants.* Nano letters, 2014. **14**(1): p. 305-310.

157. Fusco, S., et al., *An integrated microrobotic platform for on‐demand, targeted therapeutic interventions.* Advanced Materials, 2014. **26**(6): p. 952-957.

158. Fusco, S., et al., *Shape-switching microrobots for medical applications: The influence of shape in drug delivery and locomotion.* ACS applied materials & interfaces, 2015. **7**(12): p. 6803-6811.

159. Huang, H.-W., et al., *Soft micromachines with programmable motility and morphology.* Nature communications, 2016. **7**(1): p. 1-10.

160. Khalil, I.S., et al., *MagnetoSperm: A microrobot that navigates using weak magnetic fields.* Applied Physics Letters, 2014. **104**(22): p. 223701.

161. Li, T., et al., *Magnetically propelled fish‐like nanoswimmers.* Small, 2016. **12**(44): p. 6098-6105.

162. Ahmed, S., et al., *Self-assembly of nanorod motors into geometrically regular multimers and their propulsion by ultrasound.* ACS nano, 2014. **8**(11): p. 11053-11060.

163. Ahmed, S., et al., *Steering acoustically propelled nanowire motors toward cells in a biologically compatible environment using magnetic fields.* Langmuir, 2013. **29**(52): p. 16113-16118.

164. Garcia-Gradilla, V., et al., *Functionalized ultrasound-propelled magnetically guided nanomotors: Toward practical biomedical applications.* ACS nano, 2013. **7**(10): p. 9232-9240.

165. Ahmed, D., et al., *Selectively manipulable acoustic-powered microswimmers.* Scientific reports, 2015. **5**(1): p. 1-8.

166. Feng, J., J. Yuan, and S.K. Cho, *Micropropulsion by an acoustic bubble for navigating microfluidic spaces.* Lab on a Chip, 2015. **15**(6): p. 1554-1562.

167. Ahmed, D., et al., *Artificial acousto‐magnetic soft microswimmers.* Advanced Materials Technologies, 2017. **2**(7): p. 1700050.

168. Ahmed, D., et al., *Artificial swimmers propelled by acoustically activated flagella.* Nano letters, 2016. **16**(8): p. 4968-4974.

169. Jiang, H.-R., N. Yoshinaga, and M. Sano, *Active motion of a Janus particle by self-thermophoresis in a defocused laser beam.* Physical review letters, 2010. **105**(26): p. 268302.

170. Ni, M., et al., *A review and recent developments in photocatalytic water-splitting using TiO2 for hydrogen production.* Renewable and Sustainable Energy Reviews, 2007. **11**(3): p. 401-425.

171. Ibele, M., T.E. Mallouk, and A. Sen, *Schooling behavior of light‐powered autonomous micromotors in water.* Angewandte Chemie, 2009. **121**(18): p. 3358-3362.

172. Duan, W., et al., *Motion analysis of light-powered autonomous silver chloride nanomotors.* The European Physical Journal E, 2012. **35**(8): p. 1-8.

173. Erdem, E.Y., et al., *Thermally actuated omnidirectional walking microrobot.* Journal of Microelectromechanical Systems, 2010. **19**(3): p. 433-442.

174. Saito, K., et al., *Miniaturized rotary actuators using shape memory alloy for insect-type MEMS microrobot.* Micromachines, 2016. **7**(4): p. 58.

175. Saito, K., et al., *Insect-type MEMS microrobot with mountable bare chip IC of artificial neural networks.* Artificial Life and Robotics, 2017. **22**(1): p. 118-124.

176. Darhuber, A.A., et al., *Microfluidic actuation by modulation of surface stresses.* Applied Physics Letters, 2003. **82**(4): p. 657-659.

177. Jiao, Z., X. Huang, and N.-T. Nguyen, *Manipulation of a droplet in a planar channel by periodic thermocapillary actuation.* Journal of Micromechanics and Microengineering, 2008. **18**(4): p. 045027.

178. Hosseinidoust, Z., et al., *Bioengineered and biohybrid bacteria-based systems for drug delivery.* Advanced drug delivery reviews, 2016. **106**: p. 27-44.

179. Schwarz, L., M. Medina-Sánchez, and O.G. Schmidt, *Hybrid biomicromotors.* Applied Physics Reviews, 2017. **4**(3): p. 031301.

180. Lu, A.X., et al., *Catalytic propulsion and magnetic steering of soft, patchy microcapsules: ability to pick-up and drop-off microscale cargo.* ACS applied materials & interfaces, 2016. **8**(24): p. 15676-15683.

181. Singh, A.K., et al., *Multimodal chemo–magnetic control of self-propelling microbots.* Nanoscale, 2014. **6**(3): p. 1398-1405.

182. Jang, B., et al., *Undulatory locomotion of magnetic multilink nanoswimmers.* Nano letters, 2015. **15**(7): p. 4829-4833.

183. Bertin, N., et al., *Propulsion of bubble-based acoustic microswimmers.* Physical Review Applied, 2015. **4**(6): p. 064012.

184. Peyer, K.E., L. Zhang, and B.J. Nelson, *Localized non-contact manipulation using artificial bacterial flagella.* Applied Physics Letters, 2011. **99**(17): p. 174101.

185. Peyer, K.E., L. Zhang, and B.J. Nelson, *Bio-inspired magnetic swimming microrobots for biomedical applications.* Nanoscale, 2013. **5**(4): p. 1259-1272.

186. Dijkink, R., et al., *The 'acoustic scallop': a bubble-powered actuator.* Journal of micromechanics and microengineering, 2006. **16**(8): p. 1653.

187. Oguz, H. and A. Prosperetti, *The natural frequency of oscillation of gas bubbles in tubes.* The Journal of the Acoustical Society of America, 1998. **103**(6): p. 3301-3308.

188. Ren, L., et al., *3D steerable, acoustically powered microswimmers for single-particle manipulation.* Science advances, 2019. **5**(10): p. eaax3084.

189. Finnie, I. and R.L. Curl, *Physics in a toy boat.* American Journal of Physics, 1963. **31**(4): p. 289-293.

190. Brokaw, C.J., *Bend propagation by a sliding filament model for flagella.* Journal of Experimental Biology, 1971. **55**(2): p. 289-304.

191. Ming, T. and Y. Ding, *Transition and formation of the torque pattern of undulatory locomotion in resistive force dominated media.* Bioinspiration & biomimetics, 2018. **13**(4): p. 046001.

192. Berg, H.C. and R.A. Anderson, *Bacteria swim by rotating their flagellar filaments.* Nature, 1973. **245**(5425): p. 380-382.

193. Thomas, D., D.G. Morgan, and D.J. DeRosier, *Structures of bacterial flagellar motors from two FliF-FliG gene fusion mutants.* Journal of bacteriology, 2001. **183**(21): p. 6404.

194. Darnton, N.C., et al., *On torque and tumbling in swimming Escherichia coli.* Journal of bacteriology, 2007. **189**(5): p. 1756.

195. Jawed, M.K., et al., *Propulsion and instability of a flexible helical rod rotating in a viscous fluid.* Physical review letters, 2015. **115**(16): p. 168101.

196. Zöttl, A. and J.M. Yeomans, *Enhanced bacterial swimming speeds in macromolecular polymer solutions.* Nature Physics, 2019. **15**(6): p. 554-558.

197. Angeles, V., et al., *Front-back asymmetry controls the impact of viscoelasticity on helical swimming.* Physical Review Fluids, 2021. **6**(4): p. 043102.

198. Zhang, J., M. Chinappi, and L. Biferale, *Base flow decomposition for complex moving objects in linear hydrodynamics: Application to helix-shaped flagellated microswimmers.* Physical Review E, 2021. **103**(2): p. 023109.

199. Mahoney, A.W., et al., *Velocity control with gravity compensation for magnetic helical microswimmers.* Advanced Robotics, 2011. **25**(8): p. 1007-1028.

200. Zeeshan, M.A., et al., *Hybrid helical magnetic microrobots obtained by 3D template‐assisted electrodeposition.* Small, 2014. **10**(7): p. 1284-1288.

201. Wang, X., et al., *3D printed enzymatically biodegradable soft helical microswimmers.* Advanced Functional Materials, 2018. **28**(45): p. 1804107.

202. Huang, H.-W., et al., *Adaptive locomotion of artificial microswimmers.* Science advances, 2019. **5**(1): p. eaau1532.

203. Shi, X., et al., *A Strain‐engineered Helical Structure as a Self‐adaptive Magnetic Microswimmer.* ChemNanoMat, 2021.

204. Maier, A.M., et al., *Magnetic propulsion of microswimmers with DNA-based flagellar bundles.* Nano letters, 2016. **16**(2): p. 906-910.

205. Dolev, A., M. Kaynak, and M.S. Sakar, *On‐Board Mechanical Control Systems for Untethered Microrobots.* Advanced Intelligent Systems, 2021: p. 2000233.

206. Tam, D. and A. Hosoi, *Optimal feeding and swimming gaits of biflagellated organisms.* Proceedings of the National Academy of Sciences, 2011. **108**(3): p. 1001-1006.

207. Kurtuldu, H., et al., *Flagellar waveform dynamics of freely swimming algal cells.* Physical Review E, 2013. **88**(1): p. 013015.

208. Hu, J., et al., *Modelling the mechanics and hydrodynamics of swimming E. coli.* Soft matter, 2015. **11**(40): p. 7867-7876.

209. Berti, L., et al., *Shapes enhancing the propulsion of multiflagellated helical microswimmers.* arXiv preprint arXiv:2103.05637, 2021.

210. Beyrand, N., et al. *Multi-flagella helical microswimmers for multiscale cargo transport and reversible targeted binding.* in *2015 IEEE/RSJ International Conference on Intelligent Robots and Systems (IROS).* 2015. IEEE.

211. Quispe, J. and S. Régnier. *Magnetic miniature swimmers with multiple rigid flagella.* in *2020 IEEE International Conference on Robotics and Automation (ICRA).* 2020. IEEE.

212. Wolgemuth, C.W., O. Igoshin, and G. Oster, *The motility of mollicutes.* Biophysical journal, 2003. **85**(2): p. 828-842.

213. Williamson, D.L., J.G. Tully, and R.F. Whitcomb, *The genus Spiroplasma.* The mycoplasmas, 2012: p. 71-112.

214. Balaramraja, V.S., et al. *Modelling the undulation patterns of flying snakes.* in *2016 International Conference on Advances in Computing, Communications and Informatics (ICACCI).* 2016. IEEE.

215. Leoni, M., et al., *A basic swimmer at low Reynolds number.* Soft Matter, 2009. **5**(2): p. 472-476.

216. Pak, O.S., et al., *Theoretical models of low-Reynolds-number locomotion*, in *Fluid-Structure Interactions in Low-Reynolds-Number Flows.* 2015, Royal Society of Chemistry. p. 100-167.

217. Dowell, E. and K. McHugh, *Equations of motion for an inextensible beam undergoing large deflections.* Journal of Applied Mechanics, 2016. **83**(5).

218. Tam, D. and A.E. Hosoi, *Optimal stroke patterns for Purcell's three-link swimmer.* Physical Review Letters, 2007. **98**(6): p. 068105.

219. Passov, E. and Y. Or, *Dynamics of Purcell's three-link microswimmer with a passive elastic tail.* The European Physical Journal E, 2012. **35**(8): p. 1-9.

220. Wiezel, O. and Y. Or, *Optimization and small-amplitude analysis of Purcell's three-link microswimmer model.* Proceedings of the Royal Society A: Mathematical, Physical and Engineering Sciences, 2016. **472**(2192): p. 20160425.

221. Grover, J., et al. *Geometric motion planning for a three-link swimmer in a three-dimensional low Reynolds-number regime.* in *2018 Annual American Control Conference (ACC).* 2018. IEEE.

222. Alouges, F., et al., *Energy-optimal strokes for multi-link microswimmers: Purcell's loops and Taylor's waves reconciled.* New Journal of Physics, 2019. **21**(4): p. 043050.

223. Moreau, C., L. Giraldi, and H. Gadêlha, *The asymptotic coarse-graining formulation of slender-rods, bio-filaments and flagella.* Journal of the Royal Society Interface, 2018. **15**(144): p. 20180235.

224. Germann, P., et al., *Simulating organogenesis in COMSOL.* arXiv preprint arXiv:1202.0428, 2012.

225. Cordovilla, F., et al., *Numerical-Experimental Study of the Consolidation Phenomenon in the Selective Laser Melting Process with a Thermo-Fluidic Coupled Model.* Materials (Basel), 2018. **11**(8).

226. Batchelor, G.K., *Slender-body theory for particles of arbitrary cross-section in Stokes flow.* Journal of Fluid Mechanics, 1970. **44**(3): p. 419-440.

227. Borker, N.S. and D.L. Koch, *Slender body theory for particles with non-circular cross-sections with application to particle dynamics in shear flows.* Journal of Fluid Mechanics, 2019. **877**: p. 1098-1133.

228. Yang, K., et al., *Modeling and simulations for fluid and rotating structure interactions.* Computer Methods in Applied Mechanics and Engineering, 2016. **311**: p. 788-814.

229. Werner, M. and L.W. Simmons, *Insect sperm motility.* Biological Reviews, 2008. **83**(2): p. 191-208.

230. Pak, O.S., et al., *Theoretical models of low-Reynolds-number locomotion*. 2015: Royal Society of Chemistry.

231. Multiphysics, C. and C.M.H.T. Module, *COMSOL multiphysics user's guide.* Version: COMSOL Multiphysics, 2014. **3**.

232. Ter, H.G., *Therapeutic ultrasound.* European Journal of Ultrasound: Official Journal of the European Federation of Societies for Ultrasound in Medicine Biology, 1999. **9**(1): p. 3.

233. Kinsler, L.E., et al., *Fundamentals of acoustics.* Fundamentals of Acoustics, 4th Edition, by Lawrence E. Kinsler, Austin R. Frey, Alan B. Coppens, James V. Sanders, pp. 560. ISBN 0-471-84789-5. Wiley-VCH, December 1999., 1999: p. 560.

234. Ludwig, G.D., *The Velocity of Sound through Tissues and the Acoustic Impedance of Tissues.* Journal of the Acoustical Society of America, 1950. **22**(6): p. 862.

235. Majewski, M., et al., *Stimulation of mucin, mucus, and viscosity during lubiprostone in patients with chronic constipation may potentially lead to increase of lubrication.* Clinical and translational gastroenterology, 2014. **5**(12): p. e66.

236. Falkovich, G., *Fluid mechanics: A short course for physicists.* 2011: Cambridge University Press.

237. Odegard, G., T. Gates, and H. Herring, *Characterization of viscoelastic properties of polymeric materials through nanoindentation.* Experimental Mechanics, 2005. **45**(2): p. 130-136.

238. Lei, Y., S. Adhikari, and M. Friswell, *Vibration of nonlocal Kelvin–Voigt viscoelastic damped Timoshenko beams.* International Journal of Engineering Science, 2013. **66**: p. 1-13.

239. Ghayesh, M.H., *Viscoelastic dynamics of axially FG microbeams.* International Journal of Engineering Science, 2019. **135**: p. 75-85.

240. Ghayesh, M.H., H. Farokhi, and S. Hussain, *Viscoelastically coupled size-dependent dynamics of microbeams.* International Journal of Engineering Science, 2016. **109**: p. 243-255.

241. Saffman, P., *The lift on a small sphere in a slow shear flow.* Journal of fluid mechanics, 1965. **22**(2): p. 385-400.

242. Dreyfus, R., et al., *Microscopic artificial swimmers.* Nature, 2005. **437**(7060): p. 862.

243. Huang, H.-W., et al., *Adaptive locomotion of artificial microswimmers.* Science Advances, 2019. **5**(1): p. eaau1532.

244. Yang, T.-Z., et al., *Microfluid-induced nonlinear free vibration of microtubes.* International Journal of Engineering Science, 2014. **76**: p. 47-55.

245. Thomson, W., *Theory of vibration with applications.* 2018: CrC Press.

246. Kuhn, L.M., et al. *Development of a Rapid First-Order Differential Equation Solver for Stiff Systems.* in *Proceedings of the International Conference on Scientific Computing (CSC).* 2019. The Steering Committee of The World Congress in Computer Science, Computer ….

247. Crompton, T.R., *Physical testing of plastics.* 2012: Smithers Rapra.

248. Satoh, M., K. Kaneto, and K. Yoshino, *Dependences of electrical and mechanical properties of conducting polypyrrole films on conditions of electrochemical polymerization in an aqueous medium.* Synthetic metals, 1986. **14**(4): p. 289-296.

249. Shuzhi, M., M.F. Du Chunjiang, and Z. Yu, *Topology Optimization of a Continuum Structure Using Multi-Island Genetic Algorithm (MIGA)[J].* Mechanical Science and Technology for Aerospace Engineering, 2009. **10**.

250. Lakes, R. and R.S. Lakes, *Viscoelastic materials.* 2009: Cambridge University Press.

251. Ferry, J.D., *Viscoelastic properties of polymers.* 1980: John Wiley & Sons.

252. Voß, J. and R. Wittkowski, *Orientation-Dependent Propulsion of Triangular Nano-and Microparticles by a Traveling Ultrasound Wave.* ACS nano, 2022.

253. Curtis, F.G., K. Ekici, and J.D. Freels. *Fluid-Structure Interaction for coolant flow in research-type nuclear reactors.* in *COMSOL CONFERENCE.* 2011.

254. Christian, J.T. and J.W. Boehmer, *Plane strain consolidation by finite elements.* Journal of the Soil Mechanics and Foundations Division, 1970. **96**(4): p. 1435-1457.

255. Winslow, A.M., *Numerical solution of the quasilinear Poisson equation in a nonuniform triangle mesh.* Journal of computational physics, 1966. **1**(2): p. 149-172.

256. Chwang, A.T. and T.Y.-T. Wu, *Hydromechanics of low-Reynolds-number flow. Part 2. Singularity method for Stokes flows.* Journal of Fluid mechanics, 1975. **67**(4): p. 787-815.

257. Duprat, C. and H.A. Shore, *Fluid-structure interactions in low-Reynolds-number flows.* 2015: Royal Society of Chemistry.

258. Huner, B. and R. Hussey, *Cylinder drag at low Reynolds number.* The Physics of Fluids, 1977. **20**(8): p. 1211-1218.

259. Buckingham, E., *On physically similar systems; illustrations of the use of dimensional equations.* Physical review, 1914. **4**(4): p. 345.

260. Shi, C., et al., *Observation of acoustic spin.* National science review, 2019.

261. Kumar, C.S. and F. Mohammad, *Magnetic nanomaterials for hyperthermia-based therapy and controlled drug delivery.* Advanced drug delivery reviews, 2011. **63**(9): p. 789-808.

262. Schenck, J.F., *The role of magnetic susceptibility in magnetic resonance imaging: MRI magnetic compatibility of the first and second kinds.* Medical physics, 1996. **23**(6): p. 815-850.

263. Hwang, K.S., et al., *Feasible Digital Light Processing Three-Dimensional Printing of a Biodegradable Porous Polymer with a High Internal Phase Emulsion Structure.* ACS Applied Polymer Materials, 2022. **4**(3): p. 1570-1575.

264. Chartoff, R.P., J.D. Menczel, and S.H. Dillman, *Dynamic mechanical analysis (DMA).* Thermal analysis of polymers: fundamentals and applications, 2009: p. 387-495.

265. Williams, M.L., R.F. Landel, and J.D. Ferry, *The temperature dependence of relaxation mechanisms in amorphous polymers and other glass-forming liquids.* Journal of the American Chemical society, 1955. **77**(14): p. 3701-3707.

266. Leibacher, I., S. Schatzer, and J. Dual, *Impedance matched channel walls in acoustofluidic systems.* Lab on a Chip, 2014. **14**(3): p. 463-470.

267. Wang, J., et al., *Investigating relaxation of glassy materials based on natural vibration of beam: A comparative study of borosilicate and chalcogenide glasses.* Journal of Non-Crystalline Solids, 2018. **500**: p. 181-190.
268. Dai, B., et al., *Programmable artificial phototactic microswimmer.* Nature nanotechnology, 2016. **11**(12): p. 1087-1092.
269. Louf, J.F., et al., *Hovering microswimmers exhibit ultrafast motion to navigate under acoustic forces.* Advanced Materials Interfaces, 2018. **5**(16): p. 1800425.